Karlsruhe Institute of Technology

Renewable Energy Systems in a Changing Climate

Master's Thesis of

Tim Reimus

At the KIT Department of Physics
Institute of Meteorology and Climate Research - Tropospheric Research (IMKTRO)

in Cooperation with Institute for Industrial Production (IIP) and Institute for Automation and Applied Informatics (IAI)

First examiner: TT-Prof. Dr. Martina Klose-Albinger
Second examiner: Prof. Dr. Veit Hagenmeyer

July 2025 – June 2026

Karlsruher Institut für Technologie
Fakultät für Physik
Wolfgang-Gaede-Str. 1
76131 Karlsruhe

Renewable Energy Systems in a Changing Climate (Master's Thesis)

I declare that I have developed and written the enclosed thesis completely by myself. I have not used any other than the aids that I have mentioned. I have marked all parts of the thesis that I have included from referenced literature, either in their original wording or paraphrasing their contents. I have followed the by-laws to implement scientific integrity at KIT.

Karlsruhe, June 2026

. . . . . .

(Tim Reimus)

Abstract

The deployment of solar photovoltaic and wind power across Europe at an increasing pace introduces feedback processes that are rarely addressed in integrated energy-system analyses: The same climate change that motivates the transition to renewables simultaneously alters the meteorological resource base on which that transition depends. This study aims to analyze the temporal and spatial changes in renewable-energy-relevant meteorological variables from 2020 to 2049 and to evaluate their implications for future energy markets and systems. To do this, a modelling workflow was developed that links global climate projections with electricity market simulation and power flow analysis, covering Europe under two CMIP6 scenarios (SSP2-4.5 and SSP5-8.5) as well as a Present-day scenario. Climate simulations were run with ICON-SmART, a global model that couples the ICON atmospheric model with hte ART module simulating mineral dust, a land-surface model, and an ocean component. This setup allows for an explicit representation of how dust affects radiation and how the changing land surface interacts with the atmosphere. With this new model setup, the aim is to simulate the resulting solar energy yields under changing climate conditions with the highest possible accuracy. The resulting meteorological data were then processed using the Python package atlite to calculate wind and solar capacity factors, which are used as inputs for the agent-based electricity market model PowerACE. In addition, case studies were carried out to examine how key weather conditions — including dark doldrums (low wind and low solar irradiance simultaneously) and light breeze events (high wind and high solar irradiance simultaneously) — evolve over time and co-occur across different parts of Europe. The resulting meteorological fields are post-processed with the Python module atlite to derive wind and photovoltaic capacity factors, which serve as inputs for the agent-based electricity market model PowerACE. Furthermore, case studies of the meteorological fields have been conducted to examine the spatio-temporal evolution of energy-system-relevant meteorological conditions, including dark doldrum events, light breeze events, and their spatial co-occurrence patterns across Europe.

The results show that trends in near-surface wind speed and solar irradiance vary considerably by region and scenario. Wind speeds decline in most areas under both SSP scenarios, with exceptions in southern Europe (SSP2-4.5) and eastern Europe (SSP5-8.5). Present-day trends are mostly positive, except in northern and eastern Europe. Solar irradiance trends are generally positive under the SSP scenarios, with exceptions in western, central, and southern Europe (SSP2-4.5) and eastern Europe (SSP5-8.5); present-day trends again follow a similar pattern. The direct radiative effect of mineral dust on incoming solar radiation intensifies under both future scenarios. Dark doldrum conditions become more frequent in certain regions, with the strongest signal under SSP5-8.5 over the Iberian Peninsula, south-western France, and northern Germany. Light breeze frequencies shift regionally but

show no clear overall trend. In the energy market simulations, the climate signal shows up mainly as increased variability in renewable power output and a growing tendency for electricity prices to spike in winter. Differences between the two scenarios are relatively small, since dispatch is primarily driven by the installed capacity assumed for each country — though some connections to the simulated climate trends can be identified. Finally, a first integration of all three modelling components into a power flow analysis using DIgSILENT PowerFactory demonstrates that the overall workflow is feasible, while also revealing fundamental tensions between market-based modelling approaches and the physics of AC power networks. This points to a clear path for future work on more tightly coupled market-grid frameworks. Taken together, this study lays a methodological foundation for integrated climate and energy system analysis under changing atmospheric conditions.

Zusammenfassung

Der zunehmende Ausbau von Photovoltaik- und Windkraftanlagen in Europa bringt nicht nur energietechnische und energiewirtschaftliche Zusammenhänge mit sich, sondern aufgrund des Klimawandels auch meteorologische Felder, die in integrierten Energiesystemanalysen bislang kaum berücksichtigt werden: Derselbe Klimawandel, der die Energiewende antreibt, verändert gleichzeitig die meteorologischen Grundlagen, auf die diese Energiewende angewiesen ist. Ziel dieser Arbeit ist es, die zeitlichen und räumlichen Veränderungen erneuerbaren-energie-relevanter meteorologischer Größen für den Zeitraum 2020 bis 2049 zu analysieren und deren Auswirkungen auf zukünftige Energiemärkte und -systeme zu bewerten. Dazu wurde ein Modellierungsworkflow entwickelt, der globale Klimaprojektionen mit Strommarktsimulationen und Lastflussanalysen verknüpft. Die Studie deckt räumlich Europa ab und untersucht zwei CMIP6-Szenarien (SSP2-4.5 und SSP5-8.5) sowie ein Referenzszenario für gegenwärtige atmosphärische Bedingungen. Die Klimasimulationen wurden mit ICON-SmART durchgeführt, einem globalen Klimamodell, das den atmosphärischen Kern von ICON mit dem ART-Modul zur Simulation von Mineralstaub, einem Landoberflächenmodell und einer Ozeankomponente koppelt. Dieser Aufbau ermöglicht es, explizit abzubilden, wie Staub die Strahlungsbilanz beeinflusst und wie sich ändernde Landoberflächen und die Atmosphäre miteinander wechselwirken. Ziel ist es dabei daraus resultierende Solarenergieerträge unter veränderten Klimabedingungen so exakt wie möglich abiilden zu können. Die simulierten meteorologischen Felder wurden anschließend mit dem Python-Paket atlite weiterverarbeitet, um Kapazitätsfaktoren für Wind- und Solarenergie zu berechnen, die als Eingangsdaten für das agentenbasierte Strommarktmodell PowerACE dienen. Ergänzend wurden Fallstudien durchgeführt, um die räumlich-zeitliche Entwicklung energiesystemrelevanter Wetterlagen zu untersuchen – darunter sogenannte Dunkelflauten-Ereignisse (gleichzeitig niedrige Windgeschwindigkeiten und geringe Solarstrahlung) und Hellbrise-Ereignisse (gleichzeitig hohe Windgeschwindigkeiten und hohe Solarstrahlung) sowie ein Koexistenzfall beider Ereignisse in Europa. Die Ergebnisse zeigen, dass die Trends bei bodennaher Windgeschwindigkeit und Solarstrahlung je nach Region und Szenario erheblich variieren. Unter beiden SSP-Szenarien nehmen die Windgeschwindigkeiten in den meisten Regionen ab, mit Ausnahmen in Südeuropa (SSP2-4.5) und Osteuropa (SSP5-8.5). Die Trends unter Berücksichtigung gegenwärtiger atmosphärischer Bedingungen prognostizieren eher steigende Windgeschwindigkeiten, außer in Nord- und Osteuropa. Die Solarstrahlungstrends prognostizieren unter den SSP-Szenarien mehrheitlich steigende Trends, mit Ausnahmen in West-, Mittel- und Südeuropa (SSP2-4.5) sowie Osteuropa (SSP5-8.5); das Seznario aktueller atmosphärischer Bedingungen folgt einem ähnlichen Muster. Der direkte Strahlungseffekt von Mineralstaub auf die einfallende Solarstrahlung verstärkt sich unter beiden Zukunftsszenarien. Dunkelflauten treten in bestimmten Regionen häufiger auf, wobei das stärkste Signal unter SSP5-8.5 über der

Iberischen Halbinsel, dem südwestlichen Frankreich und Norddeutschland zu verzeichnen ist. Die Häufigkeit von Hellbrisen-Ereignissen verschiebt sich regional, zeigt jedoch keinen eindeutigen Trend. In den Strommarktsimulationen äußert sich eine Klimasignal vor allem in einer erhöhten Variabilität der erneuerbaren Einspeisung und einer zunehmenden Häufung von Strompreisspitzen im Winter. Die Unterschiede zwischen den beiden Szenarien sind vergleichsweise gering, da die Einspeisung primär durch die je Land angenommenen installierten Kapazitäten bestimmt wird – wenngleich sich punktuell Zusammenhänge mit den simulierten Klimatrends erkennen lassen. Abschließend wird in einem ersten Versuch gezeigt, dass ein Klimamodell und ein Energiemarktmodell mit einer Lastflussanalyse zusammenzuführen prinzipiell umsetzbar ist. Gleichzeitig werden dabei grundlegende Spannungen zwischen marktbasierten Modellierungsansätzen und den physikalischen Anforderungen von Wechselstromnetzen sichtbar, die einen klaren Ausgangspunkt für die Weiterentwicklung stärker gekoppelter Markt-Netz-Modelle definieren. Insgesamt legt diese Arbeit eine methodische Grundlage für die kombinierte Klima- und Energiesystemanalyse in zukünftigen Studien.

Contents

List of Figures

List of Tables

1. Introduction

1.1. Motivation

The global energy system is undergoing a fundamental transformation. Driven by the urgent need to limit emitting anthropogenic greenhouse gases in line with the targets set by the Paris Agreement, the decarbonisation of electricity generation has become one of the central challenges of the 21st century (Masson-Delmotte et al., 2021). Solar photovoltaics and wind power have emerged as the two dominant technologies in this transition: Together they accounted for 16 % of global electricity supply in 2023, having more than quintupled their combined output within a single decade (institute, 2024). Within the European Union, this expansion is legally anchored in the Renewable Energy Directive (RED III, 2023/2413, see *Directive (EU) 2018/2001 of the European Parliament and of the Council of 11 December 2018 on the promotion of the use of energy from renewable sources (recast) (Text with EEA relevance.)* (2018)), which mandates a share of at least 42.5 % renewables in final energy consumption by 2030.

The very climatic conditions that make solar irradiation and wind speed the primary inputs of this new energy system are themselves subject to change. Atmospheric circulation patterns, the frequency and intensity of extreme weather events, land-surface properties, and aerosol loadings are all projected to shift under continued greenhouse gas forcing. (Masson-Delmotte et al., 2021). This creates a fundamental feedback loop that is rarely addressed in integrated energy-system analyses: The same climate change that motivates the transition to renewables simultaneously alters the renewable resource base on which that transition depends.

A particularly relevant physical property concerns atmospheric aerosols, and mineral dust in particular. Changing atmospheric and hydrological circulations also force land surfaces to change, in some regions due to increasing droughts towards less vegetation. Here mineral dust comes into place, that is emitted by dry land surfaces in the atmosphere and attenuating incoming solar radiation through scattering and absorption, and deposits on PV modules and concentrating solar power mirror surfaces, a degradation process known as soiling. Studies estimate that combined ambient aerosol and soiling effects already reduce solar energy output by 17–25 % in affected regions (Bergin et al., 2017), and these losses are expected to intensify as arid conditions expand poleward. At the same time, wind speed distributions are projected to shift across Europe, with CMIP6 multi-model ensembles indicating a broad reduction in near-surface wind speeds under high-emission pathways, alongside substantial regional and seasonal variability (Carvalho et al., 2021).

These changing impacts on the different earth components like atmosphere and land surfaces propagate directly into the economic layer of the energy system. Electricity prices on day-ahead markets are set at the margin and are therefore highly sensitive to fluctuations in renewable generation capacity. Changes in the spatio-temporal availability of solar and wind resources alter economic dynamics, price volatility, and the need for dispatchable backup capacity and storage, referring to energy output into the energy grid that can be controlled, scheduled, and adjusted by grid operators in response to system demand and supply conditions. (Heussaff and Zachmann, 2024) Another dimension arises at the network level: High and spatially heterogeneous renewable infeed alters power flows across transmission corridors, and without explicit load-flow modelling it is not possible to identify where physical grid constraints will be binding under future climate conditions (Roy et al., 2026). Taken together, this motivates an analysis that couples climate projections, energy-market simulation, and power-flow modelling into a coherent, end-to-end methodological chain.

1.2. State of Research

Research on the intersection of climate change and renewable energy has expanded rapidly over the past decade, yet important gaps remain, particularly with regard to the integrated treatment of atmospheric physics, market economics, and network constraints.

On the resource side, the transition from CMIP5 to CMIP6 climate models has materially changed the projected trajectory of renewable energy potentials in Europe. For solar irradiance, Dutta et al. (2022) find regionally differentiated changes in PV potential under SSP1-2.6, SSP2-4.5, and SSP5-8.5, with projected decreases in parts of South and East Asia but comparatively modest and uncertain effects across Europe. The study uses a multi-model ensemble and attributes regional changes to climate drivers acting on surface solar radiation and temperature; aerosol effects are represented indirectly through the climate-model radiative transfer and cloud processes rather than isolated as a separate perturbation. Hou et al. (2021) specifically examine European solar variability and highlight the dominant role of cloud cover changes. It is shown that until 2100 the total solar irradiance will increase in Europe, for the SSP5-8.5 scenario a slight decrease in Scandinavia is prognosted. For wind, Carvalho et al. (2021) demonstrate that CMIP6 and CMIP5 diverge substantially in their European wind projections where CMIP5 results in lower wind speeds than in CMIP in most of european regions. Still for most of the european regions, a decrease in wind speed is expected, except some local regions at the baltic sea, Germany, Ukraine and Turkey. A cross-resource perspective is offered by Lei et al. (2023), who show that the co-benefits of carbon neutrality could in some regions, especially Asia, enhance both solar and wind potentials, introducing an important policy feedback.

The role of aerosols as mediators between climate change and solar energy output has been addressed by a growing body of literature. C. Li et al. (2020) quantify a global reduction in solar generation efficiency attributable to ambient particulate matter and panel soiling, and in a more recent review work Benyadry et al. (2024) synthesises cleaning strategies

and performance degradation rates across climatic zones. The specific pathway from land-use change and desertification to increased mineral dust emissions and their effect on the radiation budget has been studied in the context of Earth system models (Kok et al., 2023), though its explicit coupling to energy system impacts remains an underexplored frontier. The ICON weather and climate model offers with its ART (Aerosols and Reactive Tracers) modelling framework, developed at the Karlsruhe Institute of Technology, a state-of-the-art tool for simulating the atmospheric composition, including aerosol transport, at climate-relevant timescales and at spatial resolutions capable of resolving regional energy-system patterns (D. Rieger, Bangert, et al., 2015). The new ICON seamless configuration, extended by ART in the so called SmART module, enables ICON-ART based simulations to be coupled with the ocean and land components. This allows examining potential land cover changings and their interaction with atmopsheric tracers and thus radiational components for photovoltaic energy analysis (*/www.hans-ertel-zentrum.de/Projekte/ICON-SmART.html* 2023).

At the energy-system level, the literature has devoted considerable attention to the design of electricity markets under high renewable penetration. Recent work from Zhu et al. (2025) examines multi-agent reinforcement learning approaches for market simulation and tests European market designs under full renewable scenarios. The PowerACE model, employed in the present study, provides an agent-based simulation platform for European day-ahead electricity markets (Weiskopf et al., 2026). The adequacy of the European system under future renewable build-out trajectories is systematically assessed in the ENTSO-E European Resource Adequacy Assessment (ENTSO-E, 2026), which provides an important empirical and normative benchmark.

Power flow modelling as a third analytical tier is the subject of a recent systematic review by Roy et al. (2026), which classifies optimal power flow (OPF) as the central tool for cost-free congestion management through generator redispatch and topology changes. Stochastic extensions of OPF that explicitly account for the uncertainty of intermittent renewable generation are gaining traction (X. Li and Xia, 2020), though coupling to long-term climate projections remains largely unaddressed. Nejla et al. (2025) estimate that grid congestion already causes approximately 5 % curtailment of renewable energy globally, and that integration costs rise steeply, reinforcing the practical need for spatially resolved network analysis as renewable shares increase.

In summary, while the individual components of the analysis chain pursued here – climate modelling, energy market simulation, and power flow analysis – are each well-developed fields with substantial literature, their systematic coupling under a climate-change scenario framework remains an open research problem. This thesis aims to close parts of that gap.

1.3. Onjectives and Structure of the Thesis

The goal of this study is to develop a workflow for the first time that allows using long term climatic simulation results in renewable energy market models and using their respective

outputs in order to to conduct a power flow analysis. The main research objectives of this studies are listed in the following:

1. For the meteorological simulations, one goal is to examine the changes of renewable energy system relevant variables from 2020 tot 2049 temporally and spatially.
2. This result of the meteorological simulation are used to analyze potential impacts on the future energy system.
3. The stability of the energy grids at a certain time step and the stability of the developed workflow are analyzed using a power flow model

Results of this research can be used in the future to analyze potential mitigations for the energy grid. To create a basis and a first attempt to perform such analyses in future, together with climate and market coupling, is the goal of this study.

The remainder of this thesis is structured as follows. Chapter 2 establishes the theoretical foundations, beginning with the climatic and atmospheric principles governing renewable energy resources — including socioeconomic pathways and climate scenarios, the physics of solar radiation, and atmospheric wind generation — before transitioning the atmospheric background to energy system related topics introducing the relevant renewable energy technologies and the economic and systemic principles of modern power grids, covering European energy markets and grid modelling approaches. Chapter 3 describes the model systems and analysis methods employed: Climate modelling with ICON-SmART, the post-processing of climate data to energy system quantities using the Python module atlite, energy market simulation with PowerACE, and power flow analysis with DIgSILENT Power Factory. Chapter 4 presents and discusses the results, structured along the three coupled model stages: The spatio-temporal evolution of climate characteristics relevant to future energy systems, the resulting changes in energy market properties under a changing climate, and an outlook on power flow behaviour when climate and market model outputs are coupled. Uncertainties across all three modeling stages are assessed in a dedicated subsection and some potential fields of further research are addressed. Finally a summary concludes the thesis with the key findings and summarizes an outlook on directions for future research as well.

2. From Atmosphere to Energy Grid: Theory for Climate-Responsive Energy Systems

This chapter introduces the theoretical foundations underpinning the subsequent analyses. It begins with an overview of climate change principles and climate projections, followed by a meteorological treatment of wind formation and atmospheric radiation. Building on these foundations, the connection between meteorological variables and the corresponding renewable energy technologies – wind power and photovoltaic systems – is established. The third part of the chapter addresses the principles of energy systems from both an economic and a technical perspective. Analogous to the meteorological introduction, the relevant future scenarios of energy system development are described, followed by an explanation of the liberalised electricity market and the physical characteristics of energy grids.

2.1. Climatic and Atmospheric Principles for Renewable Energy Resources

2.1.1. Socioeconomic Pathways and Climate Scenarios

Long-term assessments of renewable energy yields require consistent and physically plausible estimates of future atmospheric conditions, which in turn depend on how society develops over the upcoming decades Organization, 2025. This section first introduces the scientific foundations of anthropogenic climate change, then describes the Shared Socioeconomic Pathways (SSPs) and the Coupled Model Intercomparison Project Phase 6 (CMIP6) framework through which their climate consequences are assessed and which this study also uses.

2.1.1.1. Anthropogenic Climate Change

Earth's climate is governed by the balance between incoming shortwave solar radiation and outgoing longwave (thermal) radiation. Greenhouse gases (GHGs) such as carbon dioxide ($CO2$), methane (CH4), and nitrous oxide (N2O) absorb and re-emit outgoing infrared radiation, thereby reducing the net energy loss to space — a process known as the natural greenhouse effect (Masson-Delmotte et al., 2021), described more in detail in section 2.1.2). Atmospheric aerosols exert additional climatic effects. Depending on particle size, absorption

and scattering processes can induce both cooling and warming effects. Further information on aerosol impacts on atmospheric radiation is provided in section 2.1.2. Since the Industrial Revolution, anthropogenic emissions from fossil fuel combustion, land-use change, and agriculture have substantially increased atmospheric GHG concentrations, enhancing this effect and leading to a positive radiative forcing and thus a warming effect of the climate system (see Masson-Delmotte et al. (2021)).

2.1.1.2. Shared Socioeconomic Pathways

Scenarios are a central element of climate change research, as they enable researchers to explore different possible futures and provide a common basis for the integrated analysis of mitigation, adaptation, and physical climate change across research communities (Riahi et al., 2017). Building on a „parallel process"introduced by Moss et al. (2010), the climate change research community developed a new scenario framework that combines the *Shared Socioeconomic Pathways* (SSPs) with Representative Concentration Pathways (RCPs) from CMIP5 and other forcing targets in a Scenario Matrix Architecture. SSP scenarios describe possible future socioeconomic developments, including changes in population, economic growth, technological progress, energy use, and policy pathways. They provide internally consistent narratives and quantitative projections that are used to assess how societal changes may influence greenhouse gas emissions, climate impacts, and adaptation or mitigation challenges. RCP scenarios on the other hand describe possible future trajectories of greenhouse gas concentrations and their resulting radiative forcing levels by the year 2100.

The SSPs were developed through an iterative, multi-step community process (Riahi et al., 2017). First, five qualitative narratives (described underneath) were designed to provide the fundamental logic of each pathway, capturing socioeconomic trends that are difficult to formalise in models. These narratives were then translated into quantitative projections for population, urbanisation, and Gross Domestic Product (GDP) – the total monetary value of all final goods and services produced within a country over a specific period, typically one year – for individual countries. These projections in turn served as inputs for six Integrated Assessment Models (IAMs) to derive consistent pathways for energy systems, land use, and greenhouse gas emissions.

Generally, each scenario in the framework is identified as SSPx-y, where x denotes the socioeconomic pathway and y the target long-term global average radiative forcing in $\mathrm{W\,m^{-2}}$ by 2100. For the socioeconomic pathway, the following five narratives are designed to span a wide range of mitigation and adaptation approaches to evolving future challenges – encompassing not only climate change but also societal and political crises, technological developments, and economic conditions. SSP1 (*Sustainability*) envisions a shift towards sustainable development with investments in education and health, low material growth, and reduced inequality, resulting in low challenges to both mitigation and adaptation. SSP2 (*Middle of the Road*) describes a world in which social, economic, and technological trends continue historical patterns with moderate population growth and intermediate challenges

for mitigation and adaptation. SSP3 (*Regional Rivalry*) is characterized by resurgent nationalism, declining international cooperation, slow technological development, and high population growth in developing countries, leading to high challenges for both mitigation and adaptation. SSP4 (*Inequality*) depicts increasing disparities between an internationally connected high-tech society and fragmented lower-income populations, implying low mitigation but high adaptation challenges. SSP5 (*Fossil-fueled Development*) combines rapid economic growth and technological progress with heavy exploitation of fossil fuels and energy-intensive lifestyles, resulting in high mitigation but low adaptation challenges. (Riahi et al., 2017)

These narratives translate into markedly different quantitative outcomes. Global population ranges from approximately 7 billion in SSP1 and SSP5 to 12.6 billion in SSP3 by 2100, and the SSP baseline scenarios cover a radiative forcing range of roughly 2.6–8.5 $\mathrm{W\,m^{-2}}$ by 2100. Energy demand developments differ correspondingly: SSP5 sees a more than tripling of final energy demand driven by rapid economic growth, whereas SSP1 peaks around 2060 and declines thereafter due to efficiency measures and behavioural change. SSP3 and SSP5 rely heavily on fossil fuels with a growing coal share, while SSP1 and SSP4 show increasing deployment of renewables and low-carbon carriers. (Riahi et al., 2017)

2.1.1.3. CMIP6 and the ScenarioMIP Framework

The Scenario Model Intercomparison Project (ScenarioMIP) is the primary activity within CMIP6 providing multi-model climate projections driven by the SSP-based scenarios described above (O'Neill et al., 2016). Its central objective is to facilitate integrated research on the physical climate consequences of these scenarios and their impacts on societies, thereby informing mitigation and adaptation policy including the goals of the 2015 Paris Agreement. Secondary objectives are to address targeted science questions on specific forcings, including near-term climate forcers such as aerosols, methane, tropospheric ozone, and black carbon, as well as land-use change, and to improve the quantification of projection uncertainties from multi-model ensembles. (O'Neill et al., 2016)

The experimental design of the CMIP6 framework comprises eight 21st-century scenarios divided into two priority tiers, plus a large initial condition ensemble and long-term extensions to 2300. Tier 1 contains four required scenarios: SSP1-2.6 (low end, updating RCP2.6, global warming expected to remain well below 2 °C relative to pre-industrial levels (typically defined by the 1850–1900 baseline period), SSP2-4.5 (medium range, updating RCP4.5), SSP3-7.0 (medium-to-high end, emphasizing land-use change and NTCF emissions), and SSP5-8.5 (high end, with excessive emissions sufficient to reach this forcing level). Tier 2 adds SSP4-6.0, SSP4-3.4 (a mitigation pathway between radiative forcings of 2.6 and 4.5 $\mathrm{W\,m^{-2}}$), SSP5-3.4-OS (an overshoot pathway following SSP5-8.5 until 2040 before aggressive mitigation reduces forcing back to 3.4 $\mathrm{W\,m^{-2}}$ by 2100), and the preliminary SSP1-1.9, targeting a likely chance of staying below 1.5 °C. Two emission pathways of tier one, SSP2-4.5 and SSP5-8.5, are also used in this study to examine two climate scenarios with different radiative forcing intensities and thus different climate pathways as well as impacts on the energy system. (O'Neill et al., 2016). Figure 2.1 illustrates the Tier 1 and Tier 2 CMIP6

scenarios. With regard to this study, which only considers simulations up to 2050, it is noteworthy that the resulting radiative forcing and the differences between SSP2-4.5 and SSP5-8.5 remain relatively moderate until mid-century. One could argue that simulations covering longer time periods would result in more strongly diverging and therefore clearer signals. However, conducting reliable simulations for the energy sector over such extended time frames is highly challenging, as future installed generation capacities and energy demand are subject to considerable uncertainties.

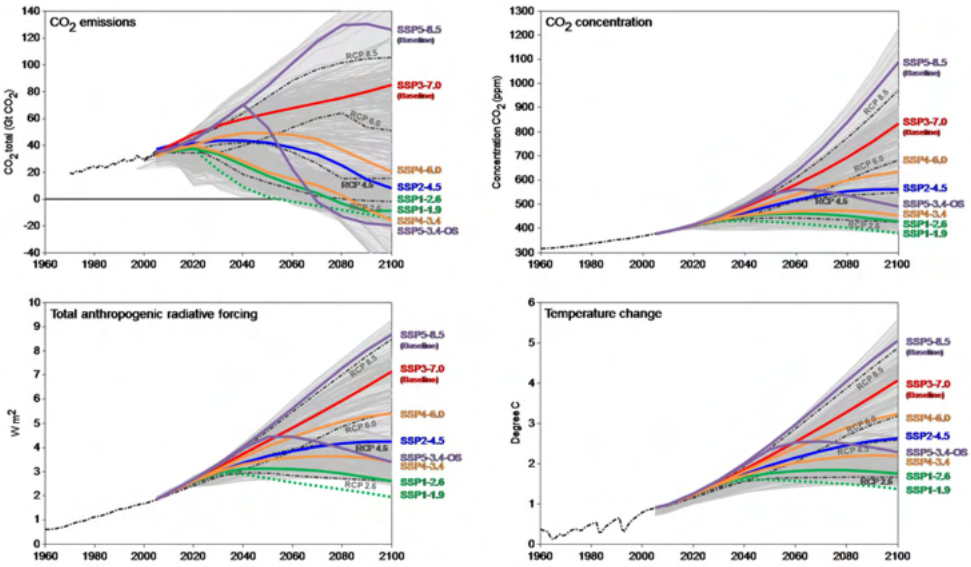

Figure 2.1.: Overview of CMIP6 Scenarios of Tier 1 and Tier 2. CO_2 emissions, concentrations, anthropogenic radiative forcing, and global mean temperature (d) until 2100 are displayed. Graphic from O'Neill et al. (2016).

2.1.2. Solar Radiation in the Atmosphere

The sun is the primary source for solar radiation in the atmosphere and thus thermal energy and electricity. To explain this source of energy further and also to explain where the photons come from, that are later important for energy production by photovoltaic energy technologies (see section 2.2.2), the production of energy and photons is quickly explained. If not stated differently, the explanations of this section are based on Wagner and Roedel (2024). The sun consists of about 92 % Hydrogen that acts as the main source from which the sun summons up its energy via a chain of transformation processes:

$$^{1}\mathrm{H} + {}^{1}\mathrm{H} \rightarrow {}^{2}\mathrm{H} + e^{+} + \nu + 1.44\,\mathrm{MeV} \tag{2.1}$$

$$^{2}\mathrm{H} + {}^{1}\mathrm{H} \rightarrow {}^{3}\mathrm{He} + \gamma + 5.49\,\mathrm{MeV} \tag{2.2}$$

$$^{3}\mathrm{He} + {}^{3}\mathrm{He} \rightarrow {}^{4}\mathrm{He} + 2\,{}^{1}\mathrm{H} + 12.85\,\mathrm{MeV} \tag{2.3}$$

In a first step two Hydrogen atoms react to a Deuterium atom, an electron and a neutrino particle. In the second step, this Deuterium atom reacts with another Hydrogen Atom to

Tritium and gamma radiation. After reaction of two Tritium atoms we receive Helium and two Hydrogen atoms. Each step of this chain reaction and thus each transformation process yields to a molecule with a higher binding energy but the mass of the resulting Helium is lower than the sum of the masses of the initial Hydrogen atoms. This is also described as mass defect and is this difference in mass is transformed in the finally produced energy by the sun that can also be calculated by the Einstein relation $E = mc^2$. This energy consists of kinetic energy of the particles as well as gamma radiation. On the inside of the sun, matter is really dense so these through gamma radiation forming photons are absorbed directly but also emitted again. Through radiative transfer they are transported through the matter of the sun to the outer layer where their wavelength is explicitly reduced and where the partricles are finally emitted as thermal radiation with an intensity of $6,33 \cdot 10^7 \frac{\mathrm{W}}{\mathrm{m}^2}$. (Vogel and Gerthsen, 1994)
This emitted solar radiation can be described with Plancks radiation law of a black radiator which is characterized that it absorbs all the incoming radiation but reflects no radiation and emits electromagnetic radiation in a broad band of wavelengths, resulting in Planck's radiation spectrum:

$$L(\lambda, T) = \frac{2\pi hc^2}{\lambda^5} \frac{1}{e^{\frac{hc}{\lambda k_B T}} - 1} \tag{2.4}$$

The Intensity of the radiation of the Planck spectrum, the spectral radiance per wavelength and temperature, can thus be described with L. Planck's constant is denoted with $h = 6,63 \cdot 10^{-31}$ Js. In equation 2.4, λ denotes the wavelength, k is the Boltzmann constant and T the absolute temperature of the radiator. The spectral radiance then has a maximum in the medium wavelengths (mainly between 400 and 700 nm) and decreases then with increasing wavelengths. The exact wavelength of the maximum intensity is temperature dependant and can be calculated with Wien's displacement law:

$$\lambda_{max} = \frac{2897,8 \mu m\, K}{T} \tag{2.5}$$

When the solar radiation enters the atmosphere (see schematic graphic in figure 2.2), parts of the radiation doesn't reach the earth's surface because it is already absorbed (described by coefficient α_{abs}), reflected (described by coefficient ρ), transmitted (described by coefficient τ) or scattered (described by coefficient α_{scat}) in higher levels of the atmosphere or it is emitted outward from the earth's surface (described by coefficient e). Responsible for these processes are on the one hand trace gases that show specific absorbing wavelength bands in which the radiation is partly or completely absorbed. That is why ozone absorbs large parts of ozone in the stratosphere and in the infrared range absorption is dominated by water vapor and carbon dioxide. On the other hand, mainly scattering processes takes place with different kinds of anthropogenic aerosols like for example nitrate aerosols tracer. Mineral dust and black carbon have both significant scattering and absorption components. All of them result in different scattering regimes due to electromagnetic waves interact with particles in qualitatively different ways depending on the size of the involved particle and the wavelength of the rays that impinge the particle. Here, the key controlling quantity is the size parameter, defined as

$$\beta = \frac{2\pi r}{\lambda} \tag{2.6}$$

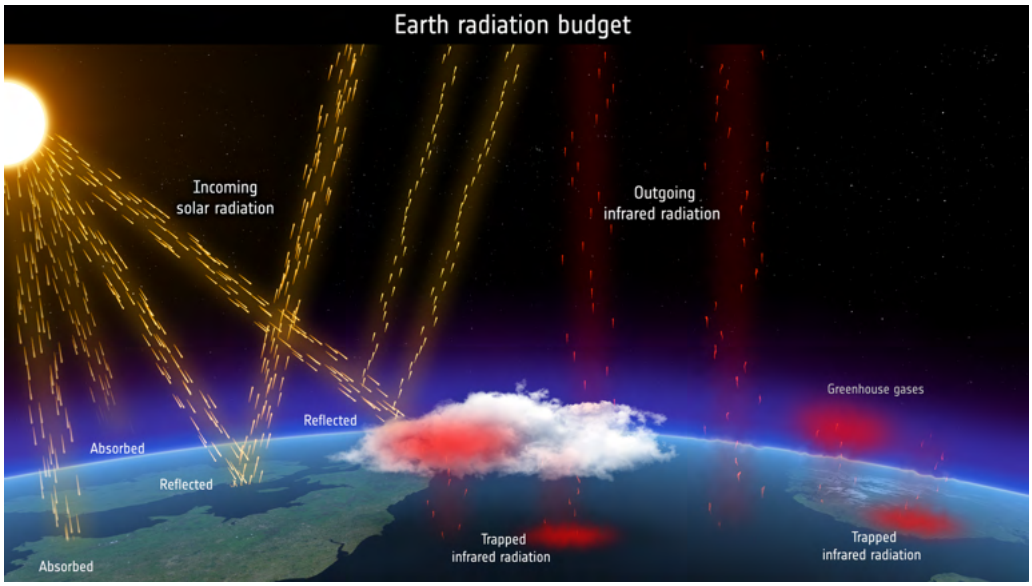

Figure 2.2.: Graphic displaying the radiation budget. Shortwave radiation is marked yellow, longwave radiation is marked red. Graphic from esa (2026).

with the radius r of the particle. If $\beta \ll 1$, particles are small compared to the wavelength and Rayleigh scattering can be observed which has a scattering intensity that is proportional to λ^{-4} , hence blue light is scattered more effective, turning the sky blue during the day. If $\beta > 1$, particles are large compared to the wavelength and Mie scattering dominates, producing diffuse, nearly non-selective scattering of electromagnetic radiation in clouds. Parts of the radiation are scattered back to space and with increasing particle forward scattering takes place. In case of $\beta \gg 1$, scattering is following the laws of geometric optics, for example big ash and ice particles or water drops.
Due to the just mentioned interaction with atmospheric constituents such as aerosols, clouds, and trace gases through scattering and absorption processes, only approximately 50–60 % of the total global incoming shortwave solar radiation at the top of atmosphere reaches the Earth's surface that can be used for solar energy. This fraction is largely absorbed by the earth's surface and partly reflected by long wave radiation. The fraction of the reflected radiation by the Earth's surface can be described by the albedo and is dependent on the material it reflects on. For example, fresh snow reflects up to 95 % of the radiation, where ocean and forests only reflect about 15 %. The radiating out long-wave radiation can be described by the Stefan-Boltzmann law:

$$E = \epsilon \sigma T^4, \tag{2.7}$$

where $\sigma = 5,67 \cdot 10^{-8} \mathrm{W\,m^{-2}K^{-4}}$ is the Stefan Boltzmann constant and T the earths surface temperature. Since the earth is not a perfect black body, an emission factor of $\epsilon = 0,95$ can be applied. Reflected long wave radiation is then partly absorbed again by trace gases in the atmosphere and back scattered to the surface which leads to the greenhouse effect that warms the earth about 33 K compared to an earth with no greenhouse gases. The Radiative Transfer Equation summarizes all the radiational intensity related processes in

one differential equation how the intensity along a path changes due to absorption, emission and scattering processes:

$$\frac{dI}{ds} = -\alpha_{abs} \cdot I + \alpha_{abs} \cdot L_\lambda(T) + \alpha_{scatt} \cdot I + \alpha_{scatt} \cdot \frac{1}{4\pi} \int_0^{4\pi} I(\Omega') P(\Omega, \Omega')\, d\Omega \tag{2.8}$$

Here, the first term on the right represents absorption of radiation along the propagation path, governed by the absorption coefficient α_{abs}. The second term accounts for thermal emission, scaled by the emission coefficient—which, invoking Kirchhoff's law, equals the absorption coefficient α_{abs}—and weighted by the blackbody spectral radiance $L_\lambda(T)$ as given by Planck's law. The third term describes out-scattering, i.e. the loss of intensity due to radiation being deflected away from the direction Ω, scaled by the scattering coefficient α_{scatt}. The fourth term captures in-scattering contributions from all incident directions Ω', integrated over the full sphere 4π, weighted by the phase function $P(\Omega', \Omega)$, which encodes the probability density of radiation being redirected from direction Ω' into direction Ω. Throughout, I_λ denotes the spectral radiance at a given wavelength λ. When we simplify the Radiative Transfer Equation such that we neglect scattering (term 1 and 2) as well as thermal emission (term 2), we receive Lambert-Beer's law that summarizes only the process of the declining intensity due to matter in the atmosphere (e.g. through aerosols):

$$\frac{dI}{ds} = -\alpha_{abs} \cdot I \quad \Leftrightarrow \quad I(s) = I_0 \cdot e^{-\alpha \cdot s} \tag{2.9}$$

The absorption coefficient is the product of the number density N and the absorption cross section σ of the object. The optical depth can then also be quantified when also taking the covered path into account, which finally yields to the transmittance $T = e^{-\tau}$. Additionally, it is defined that the sum of reflection, absorption and transmission is 1 ($\rho + \alpha + \tau = 1$) and the emissivity coefficient equals the absorptivity coefficient ($e = a$).
Summarized the total incoming short wave radiation can be separated in a direct and diffuse part. The sum also yields to the so called global irradiance.

2.1.3. Generation of Winds in the Atmosphere

Wind energy yield at a given location is governed by processes across a wide range of scales, from the large-scale atmospheric circulation down to turbulent dynamics in the surface boundary layer. This section therefore provides the physical background necessary for the analysis that follows. Starting from the large-scale atmospheric circulation, the governing equations and core concepts are introduced, from which distinct wind regimes can be derived. This framework then connects to boundary layer dynamics near the surface — the scale at which wind turbines operate and where both large-scale forcing and local processes jointly determine the available wind resource. In order to quantify wind speeds and thus wind energy yields at a certain location later in this study, it is important to understand general elements of wind formation. Therefore, in this section basic aspects are presented, how wind is formed and how it can be approximated in different regimes. For that the core concepts of the atmospheric large scale circulation is explained and basic equations

mentioned from which then different wind types can be classified. With this, a connection can be formed from the general circulation to surface near boundary layer processes that are relevant in the context of wind energy since the general wind energy yield is influenced by the general large scale circulation but also small scale processes near the surface.

Generally, atmospheric wind is induced by different strong warmings of the earth's surface at the equator and the poles and the resulting pressure gradients. Warming the surface at the equator leads to air parcels rising to higher levels, resulting in a low pressure zone near the surface region as well as a high pressure zone in the tropopause region. From here, air parcels move towards the subtropics and sink again towards the surface at higher latitudes of the subtropics, forming another high pressure zone. Due to the resulting horizontal and vertical pressure gradients, motion of air can be identified, forming the so called Hadley cell as well as the Passat winds near the surface. Due to earth rotation and the resulting Coriolis force, these low level motions equatorwards are easterly winds. In the polar regions, a similar process takes place because air parcels divert from the poles and warm at lower latitudes, which leads again to a rising motion, low pressure zones near the surface, and high pressure zones at higher atmospheric levels. Again, the air parcels diverge at the high pressure levels and sink meridionally towards the surface, forming the Polar cell. Both the Hadley cell and the Polar cell are called thermally direct cells, since they are driven by direct irradiation, which leads to thermal warming at the surface. Due to the sinking air motions in the subtropics and the rising air parcels at higher latitudes, a third thermally indirect cell is formed. This cell is called Ferell cell and induces air motions from the subtropics pole wards at surface level and equator wards at higher tropospheric levels. Taking earth rotation, and so the Coriolis force, into account, the west winds in mid-latitudes result. (Peixoto and Oort, 1992) A graphic tha depicts the various cells is given in figure 2.3.

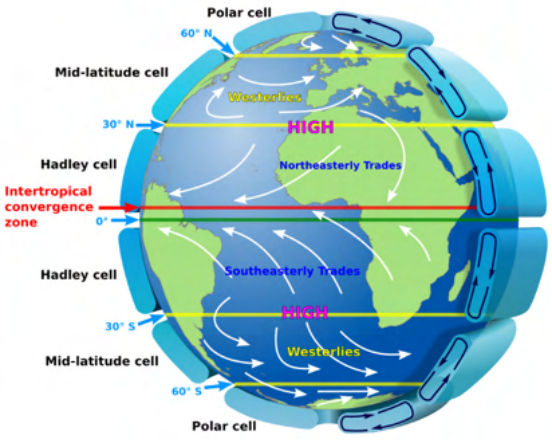

Figure 2.3.: Idealised graphic of the Earth's large-scale winds and atmospheric circulation. Graphic from *Atmospheric circulation* (2026).

These motions of air can be described by a wind vector

$$\vec{v}_{x,y,z,t} = (v_x(x,y,z,t), v_y(x,y,z,t), v_z(x,y,z,t))^T, \tag{2.10}$$

that is dependent on the zonal x-direction, he meridional y-direction and vertical z-direction in space as well as in time. On the one hand, conservation of mass is valid in the atmosphere, so that we can form the continuity equation

$$\frac{\partial \rho}{\partial t} + \nabla \cdot (\rho \vec{v}) = 0. \tag{2.11}$$

Here, ρ describes the air density, the first term the stationary change of air density in time and the second term the divergent mass flux. (Vallis, 2017)
On the other hand we can formulate a prognostic equation for $\vec{v}$ that considers all three forces that influence an air in the inertial system: Pressure gradient force $\vec{F}_p$, gravity force $\vec{F}_g$ and stress force $\vec{F}_s$.

$$\left(\frac{D\vec{v}_I}{Dt}\right)_I = \frac{\vec{F}_p + \vec{F}_g + \vec{F}_s}{\rho} = \frac{-\nabla p}{\rho} - g\vec{k} - \frac{\mu}{\rho}(\nabla^2 \vec{v} + \frac{1}{3}\nabla(\nabla \cdot \vec{v})) \tag{2.12}$$

This is the so called Navier-Stokes-equation in the inertial system of the earth, denoted by I. Here, p determines the pressure and the vector $\vec{k}$ emphasizes that the gravity g only appears in z-direction. Since $\vec{F}_s$ is defined as the divergence of a friction-tension tensor τ that is given by a 3x3-Matrix and dependent of the dynamic viscosity μ ($\tau_{ij} = \mu(\frac{\partial u_i}{\partial x_j} + \frac{\partial u_j}{\partial x_i} - \delta_{ij}\frac{2}{3}\sum_k \frac{\partial u_k}{\partial x_k})$, this stress term also contributes to shear and flow deformation processes due to external stresses. In a rotational frame, two additional forces have to be considered in this prognostic momentum equation: Centrifugal force $\vec{F}_Z$ and Coriolis force $\vec{F}_C$ so that we get:

$$\left(\frac{D\vec{v}_R}{Dt}\right)_R = \vec{F}_p + \vec{F}_s + \vec{F}_g + \vec{F}_Z + \vec{F}_C o = \left(\frac{D\vec{v}_I}{Dt}\right)_I - \vec{\Omega} \times \vec{\Omega} \times \vec{r} - 2\vec{\Omega} \times \vec{v}_R \tag{2.13}$$

Here, Ω denotes the angular velocity of the rotating coordinate system, here the earth, and v_R is the wind velocity in the rotating system. (Vallis, 2017)
Transforming this equation to spherical coordinates and applying a scale analysis with representative values of synoptic systems in the mid-latitudes to every term yields the so called primitive equations. Writing the horizontal equations in natural coordinates showcases the forces that have an effect as well as their direction on a moving air parcel. Vector $\vec{t}$ denotes here the tangent unit vector and $\vec{n}$ the normal unit vector. The coordinate in tangential direction is denoted as s and in normal direction as s.

$$\begin{array}{llll} -\frac{Dv}{Dt}\vec{t} - \frac{v^2}{R}\vec{n} - fv\vec{n} - \frac{1}{\rho}\frac{\partial p}{\partial s}\vec{t} - \frac{1}{\rho}\frac{\partial p}{\partial n}\vec{n} = \vec{0} \\ \vec{f}_t \quad + \vec{f}_z \quad + \vec{f}_c \quad + \vec{f}_p \quad = 0 \end{array} \tag{2.14}$$

This equilibrium shows that on an inertial acceleration of an air parcel, a centripetal acceleration f_z with a radius of curvature R is, a coriolis acceleration f_c with coriolis factor f and a pressure gradient acceleration is effective. From here depending on the meteorological situation and when assuming stationary conditions ($\frac{Dv}{Dt} = 0$), different flow and wind types can be derived. By defining an equilibrium of f_c and f_p, you receive the geostrophic wind that is a balance of forces that is valid for most large scale flows with low R. If R grows,

for example in case of synoptic highs and troughs, f_z can not be neglected anymore and the gradient wind balance can be derived. In case of tornados or dust devils, the flow around small-scale troughs can be cyclonically or anticyclonically and coriolis effects can be negleted, yielding to a balance between f_z and f_p. A pure balance of f_c and f_z is rather rare since this kind of flow often overlaps with other flow types but a realistic example could be a flowing parcel in a region with a very low pressure gradient. (Etling, 2008)
Except dust devils and tornadoes, all these flow types can be found in the free atmosphere on synoptical scales (in the order of 1 to 10 km horizontal length) where friction can often be neglected. When focusing on the boundary layer, that is defined as the tropospheric region that directly influenced by the Earth's surface and that responds to changes in surface forcing on relatively short timescales (about an hour or less), an atmospheric region is described where power generation by wind turbines takes place. In the boundary layer turbulent flow can be determined. If not stated differently, the following section is based on material of Stull (2009).
Turbulent flow is influenced by the large scale synoptic condition on the one hand, that was shown before, but mainly by friction at the earth's surface and convection as well, resulting in thermals through buoyancy and wind shear on the other hand. The height and structure of the boundary layer vary due to synoptic-scale influences such as large-scale pressure patterns and frontal systems, which affect stability, wind shear, and turbulence. In addition, the surface–atmosphere temperature gradient controls buoyancy, influencing eddy size and entrainment from the free atmosphere, and thereby governs boundary layer growth. During nighttime for instance, when the earth's surface cools, stable atmospheric conditions are achieved and turbulent mixing decreases significantly. With that, the wind field is a lot less influenced by surface near turbulent flows and winds are generally weaker. Nevertheless also a super geostrophic wind can form inside the boundary layer, the so called low level jet. It shows maximum wind speed in the second half of the night when the surface and the atmosphere has cooled down the most.

Since the rotors of wind turbines that contribute to the power generation, are always placed in higher altitudes over the surface than surface level, getting an estimate about height dependency of wind speeds is quite relevant. For that, we can apply the theory of similarity that yields that under neutral atmospheric conditions the wind speed changes logarithmically with height:

$$u(z) = \frac{u_\star}{\kappa} \ln\left(\frac{z-d}{z_0}\right) \tag{2.15}$$

Here, $u_\star$ denotes the friction wind speed that acts as a scaling parameter and quantifies the vertical flux of horizontal momentum $\overline{u'w'}$. Scaling the equation with the von-Karman constant κ ($\approx 0,4$) and is based on similarity theory and calibration against observations. The reference height z_0 is the aerodynamic roughness length ($z_0 = 0$) that describes how much wind speeds are reduced due to different surface structures. The displacement height is denoted with d and describes the effective zero plane of the wind profile due to obstacles in the landscape (e.g. trees). It is usually 2/3 of the obstacle height and is only applicable in regions of dense roughness coverage and not for individual roughness elements. These properties of the logarithmic wind profile under neutral conditions is also one of the key characteristics of the boundary layer when planning wind farms, since constructing wind

turbines with hub heights at higher altitudes from a meteorological point of view would lead to optimal energy yields. More details on that also from other perspectives can be found in chapter 2.2.1. The wind profile changes when atmospheric conditions shift from neutral to stable stratification. This typically occurs at night, when thermal convection weakens, reducing turbulent mixing and the associated downward momentum flux. Near-surface flow is slowed by surface roughness and obstacles. Since momentum exchange with upper-level flow is suppressed, a stronger vertical wind speed gradient develops. During e.g. a sunny day, when instable conditions take place, it is the opposite way around: Thermal convection weakens, strengthening turbulent mixing and reducing the vertical wind gradient.

2.2. Renewable Energy Technologies

This section introduces the fundamentals about the renewable energy technologies whose potential yield in a changing climate is analyzed during this study. The goal of this theoretical part is to build a bridge between meteorological processes and the technological aspects of wind turbines and photovoltaic modules, since further analysis rely on these basic principles.

2.2.1. Wind Energy

Wind has already been used for centuries as en energy source, considering windmills that were used for water pumping or grain grinding. Since the 20th century this technology has been optimized in order to use it for electricity production. (Shepherd, 1990)
The technology of wind turbines producing electricity out of wind power relies on the principle of moving air parcels due to high and low pressure regions in order to reduce pressure gradients. More on the formation of wind fields can be found in section 2.1.3. Relating these meteorological processes to their impact on energy yield, it can be stated that the logarithmic vertical wind profile leads to systematically higher wind speeds and thus increased energy yield with increasing turbine hub height. Nocturnal low-level jets can further produce pronounced nighttime wind speed maxima, resulting in corresponding peaks in energy production. In addition, strong synoptic-scale pressure gradients can generate high wind speed events that may trigger turbine cut-offs or impose extreme loads on the power grid. On shorter time scales, variations in turbulence intensity also modulate energy yield by affecting wake recovery and wake length within wind farms, thereby influencing downstream turbine performance. These implications are explained further in the following. If not stated differently, hte following explanations are based on Hau (2016).
When talking about wind power and thus creating a rotational motion at the blades in order to drive a turbine, we can distinguish between several wind turbines. Figure 2.4 depicts several types.

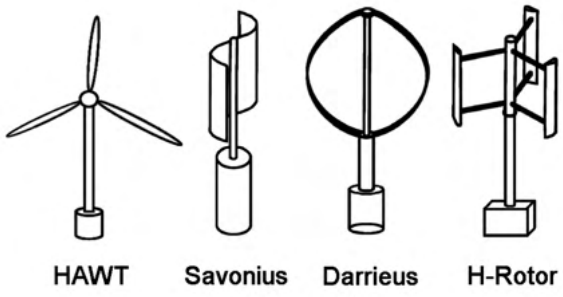

Figure 2.4.: Types of wind turbines: Horizontal axis wind turbines (HAWT), Savonius, Darrieus and H-Rotor. Graphic from Eriksson et al. (2008).

On the one hand there are drag-based wind turbines, e.g. the Savonius-Rotors, with a vertical rotation axis that can run due to a drag force on their vertical oriented surfaces with different efficiencies, depending on the geometry. However their power coefficients are relatively low, so only a few of the actual wind power can be used. On the other hand there are the mainly installed lift-based wind turbines with a horizontal rotation axis whose principle lies, like the name suggests, on a lift force occurring on one side of the blade, comparable to blades of an airplane (see figure 2.5). When placing a blade with a curved

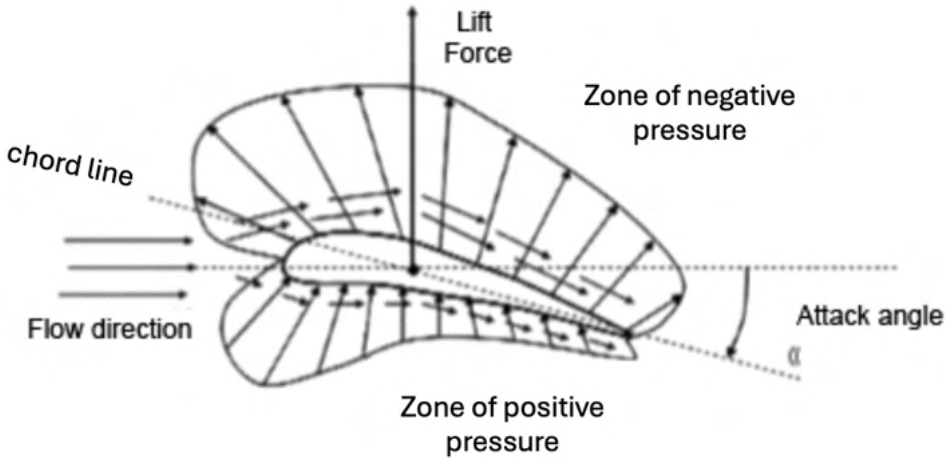

Figure 2.5.: Lift-based rotor: Shown are the resulting forces when placing in a flow that flows from the left to the right. Original graphic from Sokolovsky and Rotkin (2017), text edited.

shape into an airflow, a high pressure region at the area of the higher curvature can be determined. Near the surface of the blade's other side, lower pressure can be determined which leads the blade to a lifting towards the region of lower pressure and thus a rotation of the whole rotor . It was shown that a 3-blade rotor owns the best power coefficient of all types and provides the best compromise in efficiency, costs and wake effects. Also vertical oriented lift-based rotors exist, like the Darrieus Rotor and H-Rotor, that are not dependent on the wind direction and can be used well for extreme conditions but their power coefficient is also quite low and is mostly economically not worth to use. Further

descriptions are related to the 3-blate rotors with horizontal rotation axis since they are the most frequently used turbines in the wind industry. As the power coefficient suggests, not the whole wind can be used for wind power. By defining the Power Law, based on the on undisturbed kinetic energy ($P_o = \frac{1}{2}Mv^2 = \frac{1}{2}\rho A v_1^3$), flowing through the rotor area,

$$P(v_i, a) = C_p \frac{1}{2}\rho A v_i^3 \tag{2.16}$$

also introduces the power coefficient $C_p = 4a(1-a)^2$ and the induction factor a, that quantifies the share of the wind that is reduced due to the interaction with the inertia of the wind turbine. Index i denotes if the velocity before the wind turbine is meant ($i = 1$) or downstream behind the turbine ($i = 2$). The Power law describes the energy yield of the flow with interaction with a Wind turbine. In the Power law $M = \rho A v_i(1-a)$ can be described as the mass flow through the rotor area with the air density ρ, the rotor area A and the incident flow speed v_i. The theoretically optimal power coefficient of a lift-based wind turbine can then be calculated by putting $P(v_i, a)$ and P_0 in relation and calculating the optimized C_p by differentiating afterwards with respect to the induction factor a. This leads to a optimum induction factor of $0,33$ and to the so called Betz-Factor $C_{p,max} = \frac{16}{27}$, meaning that with an ideal 3-rotor wind turbine, the wind speed v at the rotor plane is slowed down to two thirds of the incident speed v_i. This also yields to the final optimum power law $P_{max} = \frac{16}{27}\frac{1}{2}\rho A v^3$.
When designing a wind farm, additional losses can occur. Depending on the orography of the terrain as well as the spacing and layout of multiple wind turbines, wake effects must be considered, as they can significantly influence both the energy yield and the economic performance of a wind farm. These effects arise from the extraction of kinetic energy within the wind farm, leading to downstream wake regions characterized by reduced wind speeds and modified flow conditions. Wakes also increase turbulence intensity within the farm, which enhances structural loading and oscillatory motions of turbine components, particularly the tower, thereby contributing to material fatigue and a reduced operational lifetime of the turbines. Additionally, wind turbines can cause noise emissions and, to a lesser extent, alterations in local radiation conditions in the surrounding area. Depending on national regulations, there are typically limits on permissible noise immission levels (in dB) and on shadow flicker exposure (in hours per year) for nearby settlements. If these thresholds are exceeded, wind farm operators are required to implement operational curtailment strategies, such as reduced operating modes, which consequently lead to lower energy yields. Shutdowns of certain turbines to some times of the day can also be a consequence. Additionally temporary shutdowns can occur due to too high wind speeds, bird protection sensors or because no energy can be transmitted in the energy grid at a certain time. Further information on stable grid conditions are given in chapter 2.3.3.3. Supplementary when it comes to siting of potential wind turbine locations, environmental spatial planning restrictions can cause additional losses since some places are difficult to project for permit law reasons, restricted natural areas or private parcels which can reduce the possible areas to plan and therefore wake losses. (see e.g. Aydin et al. (2010)) Deficits due to frictions in the gear as well as electrical losses have to considered by default.

2.2.2. Photovoltaic Energy

When using photovoltaic, radiation energy is converted into electrical energy when the photons of solar radiation rays hit a certain material. Here semiconductors can be used to extract the electrons through radiation from short-wave light. This process is also called the photoelectric effect. Rappaport (1959) This related effect is the so called PN junction (displayed in figure 2.6) and is triggered when bringing a p- and n-doping semiconductor into contact.

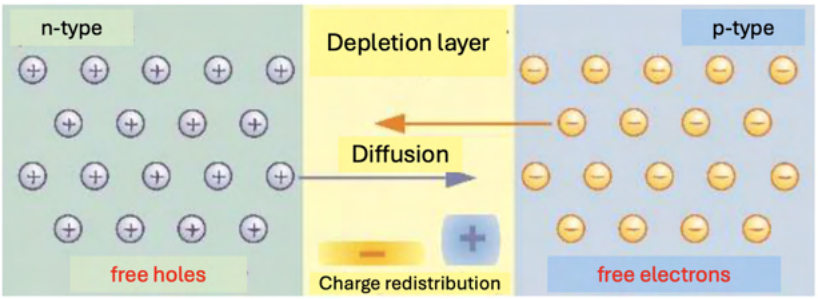

Figure 2.6.: PN junction with p-doped and n-doped semiconductors are brought into contact with depletion layer between the two materials. Original graphic from Quaschning (2025), tex edited and translated.

Doping means here that a semiconductor, consisting out of Silicon, is polluted with foreign atom. In the case of n-doping, a dopant atom with more valence electrons than the intrinsic semiconductor material, such as phosphorus, is introduced into the crystal lattice, resulting in an excess of free electrons. For p-doping, an element with fewer valence electrons than the host semiconductor, such as boron, is used, which leads to the formation of holes, i.e. effective positive charge carriers corresponding to missing valence electrons in the crystal lattice. This means for n-doping that there are more electrons in the conduction band and less holes on the valence band, resulting in a high potential to excite electrons in the conduction band due to many free valence electrons. For p-doping it is the opposite case that less electrons are on the conduction band and more holes on the valence band. Already at low temperatures the free charge carriers, like electrons and holes are thermally excited and become mobile charge carriers and are attracted to each other. With that the process of the p-n junction is starting. The effect of drifting charge carriers is called diffusion. (Quaschning, 2025). Here the electrons of the n-semiconductor are pulled towards the p-semiconductor and the holes from the n-semiconductor towards the p-semiconductor. When an electron meets a hole, it fills the hole and the two carriers recombine. The doped atoms remain in the lattice. Through that process, three regions are forming: the p-doped region, the space charge region and the n-doped region. Due to the space charges an electrical field builds up from n-doped region to p-doped region and a drift current is evolving that moves the majorities, meaning the negatively charged electrons in the n-region and the positively charged holes in the p-region. Because of this current 2 forces act in the charge carriers: First, the diffusion because of the attraction of the charge carriers, and second the electric field pushes the charge carriers back into the semiconductor where they are majorities.

That is the reason why recombination only takes place at the interface region of both semiconductors and the space charge region evolves. At the same time due to the electrical field, a diffusion voltage of $0,7\,V$ is created that is defined by the electrical potential difference at both interfaces of space charge region and p- or n-region. (Quaschning, 2025)
When connecting the n-doped semiconductor contact with the p- doped semiconductor contact by an external conductor and illuminating the whole system, additional electron-hole-pairs are formed. Short-circuit conditions are applied. Due to the space charge region electron-hole pairs are separated and transported to the contacts. Consequently, the concentration of minorities (electrons in the p-region and holes in the n-region) in the respective zones is increased. Same applies for the drift current density of the minorities: electrons drift towards the n-region and holes towards the p-region through the connected conducter. As a result a current flows through the circuit, even though no voltage is applied. The resulting so called Photo-current is flowing from n-region to p-region and can be harvested and used as electrical energy. (Quaschning, 2025)
Due to the construction of photovoltaic cells there are several losses in the process of producing electrical energy so that not all of the original power can be used. First, there are losses due to reflections on the material silicon that is metallic grey and shows a reflection coefficient of 30 %. This can be improved with an extra anti-reflection layer as well as an additional texture on the surface to increase the total path of the light rays. Then there are losses due to recombination which partly yields to no separation of electrons caused by the electric field. This can be for example due to failures in the crystal lattice or growing processes of the crystal structures. An extra SiO_2-layer on the surface and a high p-doped backside can counteract this loss. Thirdly, losses in photovoltaic (PV) systems arise from spectral mismatch related to the semiconductor band gap. Photons with energies below the band gap ΔE cannot be absorbed and therefore do not contribute to charge carrier generation, which results in a loss of approximately 23,% of the solar spectrum. Conversely, photons with energies significantly above the band gap are absorbed, but the excess energy above ΔE is dissipated as heat (thermalisation losses), accounting for an additional loss of roughly 33,% of the incident solar energy. One approach to reduce these losses is the use of multi-junction solar cells or materials such as amorphous silicon, which allow for a better spectral matching and thus improve overall conversion efficiency. Finally, shading losses occur due to the front metal grid of the solar cell, which blocks a fraction of incoming radiation. In older cell designs, these shading losses can reach up to approximately 12,%, whereas modern technologies mitigate this effect through advanced contact structures such as buried or rear contacts. (Häberlin, 2007)
Furthermore, if the solar modules are not placed on a an open field, solar radiation can always be shielded by environmental factors like trees, mountains or buildings which can be strongly site dependent. Moreover, the power of solar modules decreases with increasing temperature:

$$P_T = P_{STD} \cdot (1 + \gamma(T_C - 25)), \tag{2.17}$$

where the power P_T at module temperature T_C can be calculated by adding the fraction of additional power to a certain temperature of the rated power at standard conditions P_{STD} with help of the module dependent temperature coefficient γ. (Maysun, 2025) Additionally,

following the model by Ai et al. (2003), the overall direct short wave solar radiation reaching the photovoltaic module and the resulting energy yield is also quite dependent on the site and orientation. The overall yield of an arbitrarily oriented module surface can be calculated by multiplying the direct incoming short-wave irradiance with the cosinus of the angle between the path of irradiance and the normal of area A.

$$i_{dir,A} = i_{dir} \cdot \cos\Theta \tag{2.18}$$

To identify Θ it is necessary to identify the geographic latitude Φ, the azimuth angle γ of the surface normal of the solar cell, defined relative to due south as well as the tilt angle β, relative to the horizontal. Additionally, the declination angle δ of the earth at a certain time of the year, has to be taken into account, as well as the hour angle ω, expressed in degrees, representing the true solar time. Considering all these angles without neglects , Θ can finally be expressed with the following expression:

$$\begin{aligned} \cos\Theta = \; & \sin\delta \sin\Phi \cos\beta \\ & - \sin\delta \cos\Phi \sin\beta \cos\gamma \\ & + \cos\delta \cos\Phi \cos\beta \cos\omega \\ & + \cos\delta \cos\Phi \sin\beta \sin\gamma \cos\omega \\ & + \cos\delta \sin\beta \sin\gamma \sin\omega \\ & = f(\Phi, \beta, \gamma, \delta, \omega) \end{aligned} \tag{2.19}$$

2.3. Economic and Systemic Principles of Modern Power Grids

This chapter expands the energy meteorological topic to energy economic related topics. Similar to the section about climatic and atmospheric principles (see section 2.1), first some details about progressions are given, here related to the energy system. Further, this section creates a basis to understand how the European energy market and its related energy trading works. These principles form a basis for energy market models that are used in this study to analyze energy market effects. Further details on the energy market simulation is described in section 3.3.2. A theoretical background of the properties of energy grids is also given in section 2.3.3 which is needed for electro engineering power flow simulations .

2.3.1. Energy System Progressions - The Ten Year Net Development Plan (TYNDP)

Since 2018, ENTSO-E and ENTSOG have been producing the Ten-Year Network Development Plan (TYNDP, see ENTSO-E (2025)) as a joint undertaking, with the 2024 edition marking the fourth combined publication. The instrument was designed to give infrastructure planners and decision-makers a consistent, evidence-based picture of how the European energy system might develop over the coming decades. In practical terms, the TYNDP addresses two distinct analytical needs: it supplies the data required to evaluate

whether specific infrastructure investments are economically justified from a societal standpoint which is destinctly important in this study, and it points to where potential gaps or bottlenecks in the transmission network may arise under different future conditions.

The regulatory underpinning is provided by Regulation (EU) 2022/869 (the TEN-E Regulation), which introduced a requirement absent from previous planning cycles: the processes for developing electricity, hydrogen, and methane infrastructure must now be explicitly coordinated. This marks a shift toward a cross-carrier perspective in European network planning. The same regulation defines what the jointly developed scenarios must deliver: consistency with the energy efficiency first principle, alignment with both the Union's 2030 climate and energy objectives and the 2050 climate neutrality goal, and due consideration of the European Commission's own modelling output as well as Member States' National Energy and Climate Plans (NECPs). Throughout, the scenarios are kept carrier-, technology-, and source-neutral, meaning no particular development pathway is favoured over another.

In total, six scenarios in total make up the 2024 cycle. The first group, the National Trends+ (NT+) scenarios, covers 2030 and 2040 and is grounded in data submitted by national TSOs. The second group consists of two deviation scenarios — Distributed Energy (DE) and Global Ambition (GA) — which branch off from the NT+ 2030 results and extend projections to 2050, with an intermediate snapshot at 2035. Both deviation scenarios are committed to carbon neutrality by mid-century but rest on different assumptions about the character of the transition. Four structural dimensions set them apart: The overall level of climate ambition, whether the transition is steered from the local or the supranational level, how strongly energy efficiency and behavioral change reduce overall demand, and what mix of technologies is deployed on the supply and demand sides.

2.3.1.1. Key Methods

Energy demand is quantified using the Energy Transition Model (ETM) by Quintel Intelligence, a publicly accessible tool covering all sectors and energy carriers (see *Energy Transition Model* (2026). Because input parameters are fully published, independent parties can reconstruct and verify the calculations. The electricity system is modelled with explicit representation of prosumers and electric vehicles, both of which respond to wholesale market price signals alongside contextual factors. Offshore wind is organised into geographically defined zones connected by transmission corridors, enabling the optimisation to determine how energy is most efficiently transported — as electricity or as hydrogen. Heating demand is addressed through hybrid heat pump configurations that pair electric heat pumps with gas or hydrogen boilers, capturing interactions across energy carriers. Synthetic fuels, including e-kerosene, e-diesel, and synthetic methane, are treated as fully endogenous components, linking hydrogen demand to the broader fuel supply balance. To ensure that the scenarios reflect a broad range of expertise, external stakeholders are involved throughout the entire process. A dedicated Scenarios Stakeholder Reference Group (SRG), consisting of 22 members from various sectors, provides ongoing input at each stage of the scenario cycle. In addition, all organisations and individuals can participate through

a public consultation focused on the underlying model assumptions, as well as through in-person roundtables designed to allow for open discussion of more complex technical questions.

2.3.1.2. The National Trends+ (NT+)-Scenario

The NT+ scenario is assembled from the bottom up: each participating TSO provides national figures that reflect its own assessment of how energy supply, demand, and infrastructure will evolve in accordance with its country's policy commitments. These submissions draw on NECPs, national hydrogen strategies, and other long-term planning documents. Since data collection concluded in early 2023 — before a number of Member States had published their revised draft NECPs — a degree of divergence between the scenario figures and the plans that subsequently appeared is both expected and acknowledged.

A structural novelty of the 2024 edition is that the NT+ scenario now encompasses all energy carriers rather than being restricted to electricity and gas. This expansion makes it possible, within the TYNDP framework for the first time, to assess compliance with the Union's 2030 energy and climate objectives in a genuinely cross-carrier manner as the regulation demands which make the scenarios especially useful during the scope of this interdisciplinary study.

The EU Energy Efficiency Directive sets a binding upper limit for final energy consumption in 2030 of 763 Mtoe (approximately 8,873 TWh). When the national data submitted by TSOs were added up, the total exceeded this limit by around 8 %, corresponding to roughly 818 TWh. To bring the scenario into compliance with the EU target, a dedicated adjustment procedure was applied. This procedure exclusively reduced the projected consumption of liquid and solid fuels, so that the electricity and gas figures — and the modeling results derived from them — remained unaffected.

Once adjusted, the NT+ scenario exceeds the EU's 2030 renewable energy share target of 42.5%, reaching 45.4%. The expansion of wind and solar installations is the primary driver, with combined capacities growing to 1,127 GW by 2030 and to 1,936 GW by 2040. Against this backdrop, the proportion of renewable and low-carbon sources in electricity generation rises to 89% in 2030 and to 96% a decade later.

On the climate side, the NT+ scenario meets the EU's minimum greenhouse gas reduction requirement of 55% below 1990 levels by 2030. Projecting forward to 2040, the reduction deepens to 88%, a value that comes close to — and marginally surpasses — the 90% benchmark under discussion at EU level. Regarding gas, methane consumption contracts only slowly up to 2030, as efficiency-driven reductions in residential and industrial use are partly counterbalanced by demand arising in other applications: A steeper downward trajectory is then projected from 2030 onwards, driven by the growing uptake of hydrogen across multiple sectors. Under the national policy assumptions embedded in NT+, approximately four-fifths of EU gas output is expected to be decarbonised or renewable by 2030, with the remaining share of unabated natural gas declining further as 2040 approaches. Regarding supply, domestic extraction of conventional natural gas is set on a continuous downward

path across all scenarios, arriving at zero by 2050. Within the NT+ trajectory, biomethane is the main growth area on the renewable gas side, while electrolysis-based synthetic methane plays a comparatively minor role. The NT+ scenario additionally adds CCS deployment assumptions.

2.3.2. Energy Economical Trading on European Markets

To understand fundamental processes and aspects of the european energy market, in this section details on the liberalized market and energy trading in Europe are given. These basics are crucial to understand how the energy market simulation works, performed in this study with PowerACE.

2.3.2.1. The Liberalized European Energy Market: Structure and Pricing Principles

The organization of European electricity supply has undergone a fundamental transformation since the late 1990s. Prior to liberalization, national energy systems were dominated by vertically integrated monopolies in which generation, network operation, and retail supply were controlled by a single entity. A series of EU directives, beginning with the electricity market directive in 1996 and followed by the gas market directive in 1998, initiated a gradual transition toward competitive markets . In Germany, these directives were transposed into national law through amendments to the Energy Industry Act (Energiewirtschaftsgesetz, EnWG) in 2005, marking a decisive step toward a fully liberalized framework. The central objective of market liberalization is to establish competitive conditions for the trading of network-bound energy carriers. Several structural characteristics define this framework. First, customers are free to select their electricity or gas supplier independently of their network operator. Second, the principle of unbundling legally separates network operation from energy generation and retail activities within a single company, encompassing legal, operational, informational, and accounting dimensions. Third, non-discriminatory third-party access to transmission and distribution networks is guaranteed, meaning network operators are obligated to transport energy from any licensed supplier to the end customer. Finally, an independent regulatory authority — in Germany the Federal Network Agency (Bundesnetzagentur), BNetzA) — oversees compliance with these rules, while independent system operators, specifically four transmission system operators (TSOs) for electricity and sixteen for gas, are responsible for system stability. (P. Konstantin and M. Konstantin, 2023b)

A key pricing mechanism in the liberalized electricity market is the merit order. Power plants are dispatched in ascending order of their short-run marginal costs, that refer to costs of producing one more unit of electricity in the short term, which encompass fuel costs, emission allowance costs, and other variable operating costs. Starting from the cheapest available generation unit, typically renewables with near-zero marginal costs, progressively more expensive plants are activated until total generation meets demand. The price accepted for the last unit needed to balance supply and demand defines the

market clearing price, which all accepted suppliers receive equally. This implies that the electricity price is effectively set by the most costly plant still required to cover load. (P. Konstantin and M. Konstantin, 2023b) This is also essential to consider, concerning the energy market simulation employed in this study. A notable consequence of the rising share of renewable energy sources, which for example in Germany under the German Renewable Energy Act (EEG, see *EEG 2023 - nichtamtliches Inhaltsverzeichnis* (2026)) enjoy priority grid access and have marginal costs of essentially zero, is the so-called merit order effect: The increased feed-in of renewables displaces expensive conventional plants from the dispatch order, systematically reducing wholesale prices. However, this simultaneously creates a missing money problem: Under conditions of high renewable penetration, wholesale prices may become insufficient to cover the fixed costs of flexible peak-load plants, undermining investment incentives for the dispatchable capacity that remains necessary for grid stability. Capacity markets, in which operators receive remuneration both for delivered energy and for the mere availability of generation capacity, represent one proposed solution to this structural challenge. (Shu et al., 2025) The Energy Trilemma framework provides a useful lens for evaluating these market dynamics along three simultaneously relevant dimensions: energy security, understood as reliable access to sufficient generation capacity; energy equity, referring to the affordability and universal accessibility of supply; and environmental sustainability, capturing the transition toward low-carbon energy sources. In practice, these objectives frequently create tensions — for instance, low wholesale prices favor equity but may jeopardize the long-term security of supply by discouraging investment. (Marti and Puertas, 2022)

2.3.2.2. Electricity Trading: Markets, Instruments, and Long-Term Price Drivers

Electricity trading on European markets is organized across multiple time horizons and institutional settings. This section is based on P. Konstantin and M. Konstantin (2023b) if not stated differently. At the broadest level, a distinction is made between exchange-traded and over-the-counter (OTC) markets, each of which encompasses both spot and forward segments (Directorate-General for Energy (European Commission) and Frontier Economics, 2019).

The spot market serves the physical short-term procurement and sale of electricity, with transaction fulfillment occurring within two days of contract conclusion . Within the spot market, two segments are relevant. The day-ahead market operates as a daily auction, typically clearing at noon on the day before delivery. Participants submit hourly supply and demand bids, and the equilibrium price for each delivery hour is determined at the intersection of the aggregated supply and demand curves — closely mirroring the merit order logic described above. On the European Power Exchange (EPEX) Spot exchange, which covers the German-Luxembourg price zone among others, hourly and quarter-hourly contracts are available. Day-ahead trading accounts for approximately 20–30% of physical electricity demand, and prices are substantially influenced by short-term factors such as weather-driven renewable feed-in, seasonal demand patterns, and the momentary availability of conventional plants. The dispatch of generation units, meaning the actual activation of

power plants to produce and feed in electricity, is coordinated between market participants and TSOs on the basis of schedules derived from day-ahead auction results.

The complementary intraday market allows continuous trading throughout the day of delivery, enabling participants to correct deviations from their previously submitted schedules. This is particularly relevant for operators of wind and photovoltaic installations, whose actual generation frequently diverges from day-ahead forecasts. On platforms such as EPEX Spot, contracts are available in hourly as well as finer time resolutions down to 15-minute intervals. Since most positions are already covered through the day-ahead market, intraday volumes are comparatively small, representing only around 5 % of total physical electricity demand.

When actual generation deviates from scheduled values even after intraday corrections, TSOs must intervene through redispatch measures to restore physical balance in the transmission network. Redispatch refers to the instruction given by a TSO to increase or decrease the output of specific generation units, generally at the operator's cost, in order to relieve network congestion or compensate for system imbalances that cannot be resolved through market mechanisms alone. This is of special relevance for the Optimal Power Flow simulations, planned to be conducted within this project. Unlike dispatch, which denotes the market-driven activation of plants in merit order, redispatch is a grid-security measure imposed by the system operator outside the market framework. In Germany, the costs of redispatch have grown substantially in recent years as renewable capacity has expanded and network expansion has lagged behind, making the efficient allocation of these costs an active area of regulatory and research debate.

Beyond the spot market, the futures market, also referred to as the derivatives or forward market, enables participants to trade electricity for delivery periods ranging from the near term up to several years ahead. Futures contracts traded on the EEX are fully standardized with respect to contract size, delivery period, and underlying product specification. Alongside exchange-traded futures, bilateral OTC forward contracts are widely used; these are individually negotiated between counterparties with respect to volume, delivery profile, and price, offering greater flexibility at the cost of reduced standardization and higher counterparty risk. (Deng and Oren, 2006) The primary function of the futures market is risk management. Generators use futures to lock in revenues from future production, while suppliers and large industrial consumers hedge against procurement price volatility. A market participant purchasing electricity futures acquires the obligation — or, in the case of options, the right — to receive a fixed quantity of electricity at a predetermined price at a future date, thereby insulating itself from adverse spot price movements. (Brandkamp, 2025)

For long-term energy market projections spanning several decades — as required for infrastructure planning, regulatory design, or scenario-based research which is conducted in this study — an additional set of structural drivers becomes decisive. The price of CO_2 emission allowances under the EU Emissions Trading System (EU ETS) plays a central role, as higher carbon costs make fossil fuel power plants more expensive to operate and thus push them further back in the merit order. Similarly, the prices of primary fuels such as natural gas and coal directly determine how costly it is to run conventional power plants, and therefore what

level of wholesale electricity prices can be expected. (Liebensteiner et al., 2025) The speed at which wind and solar capacity is added to the system matters as well: a rapid expansion of renewables tends to lower average wholesale prices and increases the occurrence of hours with very low or even negative prices (P. Konstantin and M. Konstantin, 2023a). At the same time, the retirement of nuclear and coal plants and the potential addition of flexible assets such as gas turbines or battery storage will shape how much backup capacity is available when renewable output is low. Finally, overall electricity demand is set to grow in the coming decades as transport, heating, and industrial production are increasingly electrified, though efficiency gains may partially offset this trend Liebensteiner et al., 2025. All of these factors interact with one another, and any credible long-term outlook for electricity prices needs to account for them jointly. It emphasizes how volatile the market can become and that it is dependent from many boundary conditions, which is important to consider for the energy market simulation, conducted within this study.

2.3.3. Modeling Energy Grids

This section delivers some fundamental electrical engineering principles to describe energy grids as technical systems. For that, some electrodynamic definitions and basic laws are given, before the structure of energy grids can be explained.

2.3.3.1. Electrical engineering context

When analyzing and modeling the energy grid, a number of basic electrodynamic quantities are required to describe its behavior more precisely. The explanations are based on Hufschmid (2021).
First, there is the electric current that is defined by the amount of charges dQ passing a certain area at a certain time dt:

$$I = \frac{dQ}{dt} \tag{2.20}$$

The amount of work W that is carried out per charge is defined as the electric potential,

$$\Phi = \frac{W}{Q}, \tag{2.21}$$

which yields the voltage by subtracting the electric potential at two different points in space:

$$U_{12} = \Phi_1 - \Phi_2 = \frac{dW}{dQ}. \tag{2.22}$$

Since power is defined as the amount of work performed per unit time, the power can be expressed using these quantities as

$$U_{12} = \frac{dW}{dt} = U \cdot I. \tag{2.23}$$

Since in most practical cases the energy grid is operated with alternating currents (AC), both current and voltage become time-dependent. The system operates with three-phase currents, in which three coils are connected in three phases, each offset by 120°, generating a rotating magnetic field. The current continuously alternates its direction, and the voltage is then defined as

$$\begin{aligned} I(t) &= \hat{I} \cdot \sin\omega t + \phi_i = \operatorname{Im} \hat{I} \cdot e^{j(\omega t + \Phi_i} = \operatorname{Im} \underline{\hat{I}} \cdot e^{j(\omega t)} = \operatorname{Im} \underline{I}(t) \\ U(t) &= \hat{U} \cdot \sin\omega t + \phi_u = \operatorname{Im} \hat{U} \cdot e^{j(\omega t + \Phi_u} = \operatorname{Im} \underline{\hat{U}} \cdot e^{j(\omega t)} = \operatorname{Im} \underline{U}(t) \end{aligned} \tag{2.24}$$

resulting in a likewise time-dependent and complex power $\underline{S}(t) = \underline{U}(t) \cdot \underline{I}^*(t)$. In this formulation, j denotes the imaginary unit, ω the angular frequency, Φ the phase shift (subscripted i for current and u for voltage), and I^* the complex conjugate of the current. From these quantities, further variables required to describe the power flow in energy networks can be derived. The real part of the complex power yields the active power,

$$P(t) = \operatorname{Re}(\underline{S}(t)) \tag{2.25}$$

and the imaginary part the reactive power

$$Q(t) = \operatorname{Im}(\underline{S}(t)) \tag{2.26}$$

can be formulated. The active power is the portion of electric power that is actually converted into usable work, whereas the reactive power describes the portion of electrical power that oscillates between the source and reactive components like inductors and capacitors, without being converted into useful work. The total opposition to alternating current is called impedance and describes how an electrical component resists AC in magnitude and phase. It is defined as

$$Z = R + jX, \tag{2.27}$$

where $R = \operatorname{Re}(Z)$ describes resistance, that represents energy dissipation and conversion into heat or other forms of useful energy, and $X = \operatorname{Im}(Z)$ describes reactance that quantifies the ability of a component to oppose AC due to temporary storage and release of energy in electric or magnetic fields. The reciprocal of impedance is the admittance Y and is the complex measure of how easily current flows in an AC circuit:

$$Y = \frac{1}{Z} \tag{2.28}$$

Here, $G = \operatorname{Re}(Y)$ describes conductance, that represents the ability of a circuit to conduct electric current, associated with energy dissipation, and $B = \operatorname{Im}(Y)$ describes susceptance that quantifies how easily a component allows AC to flow due to the ability of a circuit to store and release of energy.

2.3.3.2. Structure of Energy Grids

When modeling the power grid, three categories of components must be considered: generators, comprising thermal and renewable power plants; consumers, encompassing industry,

commerce, public and private services, transport, and private households; and the transmission grid, responsible for conveying power between these entities. All components involved in grid control, operation, and monitoring must be accounted for, as well as the grid infrastructure itself, consisting of overhead transmission lines and underground cables. The transmission grid is structured across several voltage levels: for transmission over distances exceeding 100 km, extra-high voltage levels of 220 or 380 kV are used. Regional power distribution relies on high-voltage levels of 110 kV, and sometimes 60 kV. Power distribution within local areas such as towns or industrial zones uses medium voltage of 10 to 30 kV, while low-voltage transmission at 230 to 400 V is used inside households and smaller communities. Conventional thermal power plants typically feed in at high or extra-high voltage levels, whereas renewable energy installations connect at all voltage levels depending on the scale and application of the wind farm or photovoltaic system. (Schwab, 2017)
The energy grid is modeled as an undirected graph, consisting of nodes and edges. Every node N_i is described by the adjacent phase and amplitude of voltage U_i and the fed in power I_i. There are three types of nodes, also called buses: First there are load nodes (PQ Buses), where a certain load of active power P_i^D and reactive power Q_i^D is given. Voltage V_i and phase angle δ can evolve freely. Second, generator nodes (PV Buses) with information of a certain generator power P_i^G at a given voltage V_i. Phase angle and reactive power Q_i^G evolve freely here. Lastly, there is always one node, called the reference node (Slack Bus), that balances losses from the energy grid. With a given voltage V_i and phase angle δ, the reference node represents a controllable source with sufficient capacity to compensate for the discrepancy between scheduled generation and demand, as well as the dissipative losses in the network, in order to finally satisfy the overall system boundaries. Power Flows on every edge i and j is described by the admittance matrix Y:

$$Y_{ij} = G_{ij} + jB_{ij} \tag{2.29}$$

This also yields to the formulation for the current

$$\tilde{I} = \tilde{Y}\tilde{U}, \tag{2.30}$$

where $\tilde{I}$ and $\tilde{U}$ are both vectors representing the current and voltage at node i. The admittance $\tilde{Y} = \sum_{j=1}^{n} Y_{ij}$ is always related to an edge between a node of index i and j. This formulation can be inserted in equation 2.3.3.1 in order to calculate the power flow at a certain node. (Grainger and Stevenson, 1994)
The π-equivalent circuit (see figure 2.7) is a standard lumped-parameter representation used to approximate the distributed electrical behavior of a 3-phase transmission line in AC analysis. Physically, a real transmission line is characterized by distributed series impedance (due to resistance and inductance along the conductors) and distributed shunt admittance (primarily due to capacitance between conductors and to ground). The π-model captures these effects by concentrating them into a simple three-element network. In this representation, the total series impedance Z models the cumulative resistive and inductive effects of the line. It accounts for ohmic losses (through its real part) and for the magnetic energy storage associated with inductance (through its imaginary part). This impedance is placed between the sending end and receiving end nodes, so that the current flowing through it

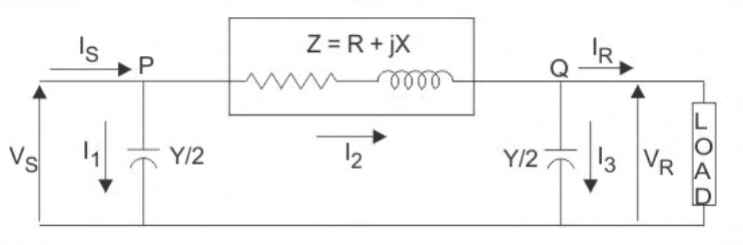

Figure 2.7.: Pi-equivalent circuit: Circuit diagram to approximate the distributed electrical behavior of transmission lines. Figure from Hagenmeyer (2024).

represents the longitudinal current along the line. The shunt elements, each represented by an admittance $Y/2$, are placed at both ends of the line. Together they represent the total capacitive effect of the line, which in reality is continuously distributed. Physically, this capacitance arises from the electric field between conductors and between conductors and ground. The reason for splitting the total admittance Y equally into two halves is to symmetrically approximate the distributed nature of the line and to ensure that both the sending and receiving ends "see" half of the capacitive charging effect. The sending-end current I_S is therefore composed of two contributions: The current flowing through the series impedance toward the receiving end, and the charging current drawn by the shunt admittance $Y/2$ at the sending side. Similarly, the receiving-end current I_R consists of the current arriving through the series impedance minus the portion that is diverted into the shunt admittance Y/2 at the receiving side. As a result, I_S and I_R are generally not equal, even in steady state, because part of the current is continuously exchanged with the electric field of the line via its capacitance. From a physical standpoint, the π-equivalent circuit therefore expresses how electromagnetic energy is both transported and temporarily stored along the line: energy is dissipated and phase-shifted by the series impedance Z, while it is alternately stored and released in the electric field represented by the shunt admittances Y/2. This model provides an accurate approximation for medium-length transmission lines and forms the basis for power flow and stability analyses in electrical power systems. More details on that can be found in chapter 3.4.1. (Kundur and Malik, 2022)

2.3.3.3. Operation Requirements and Control Objectives

The reliable operation of an electric power system requires satisfying several fundamental conditions simultaneously. Generation must continuously match consumption, the power quality must be maintained, meaning both voltage and frequency should remain constant at 50 Hz, and the system must exhibit a sufficient level of reliability in the presence of varying loads and unexpected disturbances. The key physical variables that characterize the state of a power system are voltage, frequency, and power. Each of these variables is the target of dedicated control mechanisms operating on different time scales and degrees of centralization. (Kundur and Malik, 2022)

In the European context, frequency control is organized according to a three-level hierarchy defined by ENTSO-E. Primary control (droop control) is a fully decentralized, proportional

feedback scheme that reacts within seconds to frequency deviations, stabilizing the system and restoring an active power balance. Secondary control operates on a longer timescale and uses distributed, integral-action-based communication to eliminate residual steady-state frequency errors and to balance power flows between interconnected control areas. Finally, tertiary control (minute reserve) is activated to replace the secondary reserve in the event of sustained power imbalances. (ENTSO-E, 2009)

To analyze how a power network evolves over time, a suitable dynamic model is required. For conventional power systems, the dynamics of each generator bus are commonly described by the swing equation, a second-order ordinary differential equation that captures the rotational mechanics of synchronous generators:

$$M_i\dot{\omega}_i = -D_i\omega_i + P_{G,i} - P_{L,i} - P_i, \quad i = 1, \ldots, n_G, \tag{2.31}$$

Even though in this study only quasi-stationary conditions are simulated, meaning changes over time are small and slow enough that the AC grid can be assumed as stationary, the swing equation shows mathematically very well of which power components a power grid is put together. Here, ω_i denotes the frequency deviation relative to the synchronous reference frame, but differentiated with respect to time, denoted by the dot. The parameter $M_i > 0$ is the inertia constant of the generator. A large inertia implies slower frequency changes in response to power imbalances. $D_i > 0$ models frequency-dependent damping, $P_{G,i}$ and $P_{L,i}$ are the generated and consumed active power at bus i, respectively. (Bergen and Hill, 1981) Here, under the assumption of lossless transmission ($G_{ij} = 0$) and with voltage magnitudes normalized to one per unit, the active power flow from bus i to its neighbors simplifies to

$$P_i = \sum_j B_{ij} \sin(\theta_i - \theta_j) \tag{2.32}$$

Here, θ_i is the voltage phase angle at bus i and $B_{ij} \leq 0$ describes the susceptance of the line connecting buses i and j. The coupling term $\sum_j B_{ij} \sin(\theta_i - \theta_j)$ represents the active power flowing into bus i from the rest of the network. The reactive power flow is then given as $Q_i = \sum_j B_{ij} U_i U_j$. This simplified form decouples active and reactive power flows, making the system analytically more tractable while still capturing the essential nonlinear coupling between buses through phase angle differences. When not neglecting G_{ij} and normalizing the voltage, the regular Power Flow Equations are valid, explained in the following. (Kundur and Malik, 2022) The power flow equations describe the steady-state relationship between voltage magnitudes, phase angles, and the active and reactive power injected or consumed at every bus of the network. They follow directly from Kirchhoff's laws applied to the network admittance matrix $\mathbf{Y}$, whose off-diagonal elements are $Y_{ik} = G_{ik} + jB_{ik}$. Writing bus voltages in polar form as $|U_i|e^{j\theta_i}$ as well as considering generated and consumed active

power separated from the residual active power like in equation, the nodal power balance yields two real equations per bus i:

$$P_i(\mathbf{U}, \boldsymbol{\theta}) = \sum_{j=1}^{N} |U_i|\,|U_j|\big(G_{ij}\cos(\theta_i - \theta_j) + B_{ij}\sin(\theta_i - \theta_j)\big), \tag{2.33}$$

$$Q_i(\mathbf{U}, \boldsymbol{\theta}) = \sum_{j=1}^{N} |U_i|\,|U_j|\big(G_{ij}\sin(\theta_i - \theta_j) - B_{ij}\cos(\theta_i - \theta_j)\big), \tag{2.34}$$

These equations describe the injected active and reactive power per bus i. Solving this nonlinear system for the unknown state vector $x_i = (\theta_i, |U_i|, P_i, Q_i)^\top$ at every bus constitutes the Power Flow (PF) problem, described further in section–3.4. (Grainger and Stevenson, 1994)

3. Description of used model systems and analysis methods

This chapter provides a detailed, description of the workflow developed to link climate simulations with agent-based energy market simulations and, ultimately, with power flow models.
First, a climate simulation with ICON-SmART covering the period 2020 to 2049 under three climate scenarios is conducted. The model output is subsequently post-processed in two ways. One approach applies the newly developed regional tracking algorithm, which identifies specific meteorological events defined by threshold values of selected variables in both space and time. In this study, the system is used to identify dark doldrums and light breezes. In addition, the ICON-SmART meteorological output is used to calculate capacity factors with the Python library *atlite*, which then serve as meteorological input profiles for the energy market simulation with PowerACE. Energy yields representing the actual renewable power generation at a given time step and location are also computed with *atlite*. On this basis, a market simulation is performed for all three climate scenarios. Finally, all outputs are mapped onto substation nodes so that the combined data can be used to carry out a power flow analysis.

3.1. Climate Modeling with ICON-SmART

This section describes the ICON-SmART model system and its configuration for the long-term simulations conducted in this study. Particular attention is paid to the simulation of mineral dust during the climate projection and to its interaction with the ocean and interactively evolving land surfaces, which change in response to the surrounding climatic conditions over the course of the simulation. This coupled setup allows a more accurate representation of aerosol abundances affecting atmospheric radiation and thus solar energy yields.

3.1.1. The ICON model system

The ICOsahedral Nonhydrostatic (ICON) model (see Zängl et al. (2015)) is a numerical weather prediction and climate model developed jointly by the Deutscher Wetterdienst (DWD), the Max Planck Institute for Meteorology (MPIM), the German Climate Computing Center (DKRZ), the Karlsruhe Institute of Technology (KIT) and the Center for Climate

Systems Modeling (C2SM). It is designed for weather forecasting and climate simulations and has been operationally used for weather prediction at the DWD since 2015.
The main feature of ICON is the simulation of weather and climate on an icosahedral triangular grid that has the advantage to prevent singularities at the poles. The horizontal resolution of this grid is formulated in the notation RnBk. Here, n represents the number of elements into which the sides of one of the base triangles are divided. The resulting triangles are then recursively divided into four triangles k times. Figure 3.1 shows an example of an RnBk grid with $n = 2$ and $k = 3$. (see Wan et al. (2013) and Zängl et al. (2015)) As shown in

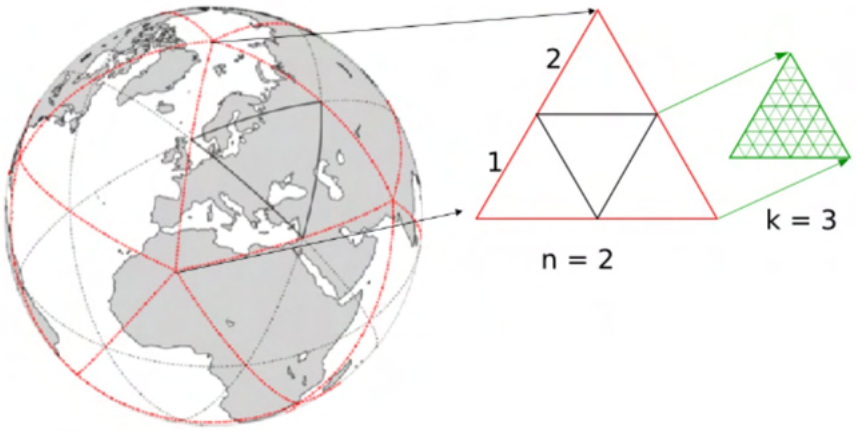

Figure 3.1.: Horizontal ICON grid in resolution R2B03: The figure shows the division of the base triangles (in red) into n parts, which are recursively divided by k. Figure from Reinert et al. (n.d.).

Zängl et al. (2015), the distance between the sides of a triangle can be calculated using the formula

$$\bar{\Delta x} = \sqrt{\frac{\pi}{5}} \frac{R_{Earth}}{n2^k} \tag{3.1}$$

where R_{Earth} denotes the radius of the Earth assuming a sphere. The number of grid cells can be calculated using the following formula:

$$n_{cells} = 20n^2 4^k. \tag{3.2}$$

Table 3.1 lists some examples of different resolutions, including grid width and number of cells and figure 3.1 shows the grid structure and how the base triangles are separated the for an exemplary grid resolution of R2B03.

Table 3.1.: Examples of different resolutions with corresponding grid point spacing $\bar{\Delta x}$ and associated number of grid cells. Table from Zängl et al., 2015.

Resolution	$\bar{\Delta x}$ (in km)	Number of grid cells
R2B04	157.8	20480
R2B05	78.9	81920
R2B06	39.5	327680
B2B07	19.7	1310720
B3B07	13.9	2949120

The vertical coordinates used in ICON are the Smooth LEvel VErtical coordinates (SLEVE) according to Leuenberger et al. (2010). Here, 90 levels are introduced as height coordinates, with the lower layers following the orography and the upper layers having a significantly more homogeneous structure. Figure 3.2 shows the longitudinal structure of these. The

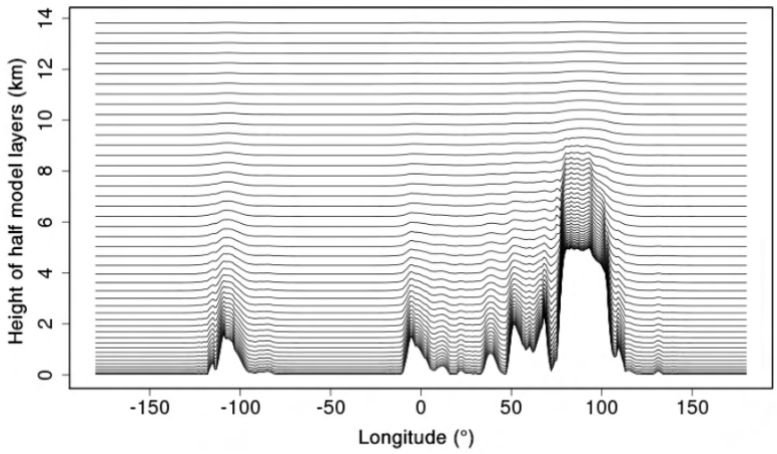

Figure 3.2.: Vertical ICON grid in Smooth LEvel VErtical coordinates: The figure shows the different vertical model levels in dependence of the longitude. Figure from Weimer et al. (2017).

dynamic core (see Zängl et al. (2015)) of ICON solves the aforementioned continuity equation (equation 3.5) as well as the Navier-Stokes equation (equations 3.3 and 3.4) and the first law of thermodynamics (equations 3.6 and 3.7). It is based on a system of equations in non-hydrostatic formulation according to Gassmann and Herzog (2008). The system of equations can be expressed as follows:

$$\frac{\partial v_n}{\partial t} + \frac{\partial K_h}{\partial n} + (\zeta + f)v_t + w\frac{\partial v_n}{\partial z} = -c_{pd}\Theta_v\frac{\partial \pi}{\partial n} + F(v_n) \tag{3.3}$$

$$\frac{\partial w}{\partial t} + \vec{v_h}\cdot\nabla w + w\frac{\partial w}{\partial z} = -c_{pd}\Theta_v\frac{\partial \pi}{\partial z} - g \tag{3.4}$$

$$\frac{\partial \rho}{\partial t} + \nabla\cdot(\vec{v}\rho) = 0 \tag{3.5}$$

$$\frac{\partial \rho \Theta_v}{\partial t} + \nabla \cdot (\vec{v} \rho \Theta_v) = \tilde{Q} \tag{3.6}$$

$$\frac{\partial \pi}{\partial t} + \frac{R_d}{c_{vd}} \frac{\pi}{\rho \Theta_v} \nabla \cdot (\vec{v} \rho \Theta_v) = \hat{Q} \tag{3.7}$$

Here, π denotes the Exner function:

$$\pi = \left(\frac{R_d}{p_{00}} \rho \Theta_v \right)^{\frac{R_d}{c_{vd}}} \tag{3.8}$$

An explanation of the variables and physical constants appearing in the equations described above can be found in Table 3.2.

Table 3.2.: Explanation of variables from the ICON dynamic core equation set

Symbol	Description
$\vec{v}$	3-dimensional wind
$\vec{v_h}$	2-dimensional horizontal wind
v_n	horizontal wind, normal direction
v_t	horizontal wind, tangential direction
w	vertical wind
ζ	vertical relative vorticity
K_h	horizontal kinetic energy
f	Coriolis parameter
Θ_v	virtual potential temperature
ρ	Air density
p	Pressure
V	Volume
c_{pd}	Heat capacity ($p = const.$)
c_{vd}	Heat capacity ($V = const.$)
R_d	Gas constant of dry air (def.: $c_{pd} - c_{vd}$)
p_{00}	Reference pressure of 1000 hPa
$\tilde{Q}$, $\hat{Q}$	Diabatic processes
$F(v_n)$	Source term of horizontal momentum
t	Time
n	Normal direction (in natural coordinates)
z	Geometric height

From a numerical perspective, to make sure that for example mass conservation is satisfied, ICON employs a combination of finite-volume and finite-difference discretization to solve the governing equations on the computational grid (see Borchert et al. (2019) and Staniforth and Wood (2008)). In addition, semi-Lagrangian advection schemes are applied, combining Eulerian and Lagrangian concepts for the transport of atmospheric quantities (see Miura and Skamarock (2013) and D. Rieger, Bangert, et al. (2015)). In this approach, the fields are

evaluated on a fixed Eulerian grid at the new time level t_{n+1}, while air parcel trajectories are traced backward to their departure points at time t_n.

3.1.2. The SmART Model extension

In this section, a general overview of the ICON-SmART model is provided. There is no published reference of this model extension yet since it is still in development, only a description of the project is available to call up (see */www.hans-ertel-zentrum.de/Projekte/ICON-SmART.html* (2023)). Further details regarding the specific configuration of the ICON-SmART simulation run conducted in this study are given in section 3.1.3.
Generally, ICON-SmART is an extension of ICON-XPP (see Müller et al. (2025)). It combines the seamless ICON configuration including the Aerosol and Reactive Trace gases (ART, see section 3.1.2.1) module with the ocean component (ICON-O, see 3.1.2.2) and the land surface model JSBACH (Jena Scheme for Biosphere-Atmosphere Coupling in Hamburg, see 3.1.2.3). This model setup is specifically designed to enable simulations on climate time scales while retaining the representation of ART-related processes within the coupled system. In this study the ART module simulates mineral dust as the only aerosol. Considering all the features the model system offers, ICON-SmART is suitable for applications involving atmospheric tracer analysis on decadal time scales, where land surface changes must also be considered as part of the evolving boundary conditions. In turn, the quantification of the radiative properties of the atmosphere can be conducted more precisely since it is influenced by the aerosol emissions and thus changing land surface types as well. Since this study investigates also photovoltaic yields besides wind power yields, these coupled interactions between land surface changes, resulting aerosol emissions and atmospheric radiation interactions may have a relevant impact on the results.

3.1.2.1. Dust modeling with the ART module

The ART module was developed at the Karlsruhe Institute of Technology (KIT) and extends the existing ICON modeling system by providing the capability to simulate atmospheric aerosols and other chemical tracers, thereby contributing to a better understanding of atmospheric composition. In this context, aerosols and chemical processes of trace gases can be incorporated into global modeling. Still the dust modeling done within ICON-ART, as described in this section, are coupled with the other ICON-SmART model components. The emission of mineral dust in ICON-ART, follows the implementation of Daniel Rieger et al. (2017). Generally, the underlying physical process is wind-driven surface erosion, which is represented through a two-step mechanism. In the first step, saltation is computed, which describes the near-surface hopping motion of soil particles driven by wind shear. In the second step, the momentum transferred by impacting saltating particles to the soil surface is sufficient to mobilize finer dust particles, which are subsequently injected into the atmosphere. More details on the emission scheme are given in the following.

The central premise of the emission scheme is that saltation and hence dust emission can only occur when the surface friction velocity u_* surpasses a threshold value $u_{*t}(d_p)$ that

varies with particle diameter. This threshold arises from the balance of aerodynamic lift, gravitational settling, and interparticle cohesion, and is expressed following Shao and Lu (2000) as:

$$u_{*t}(d_p) = f_r \cdot f_\eta \cdot \sqrt{A_n \cdot \left(\frac{\rho_s}{\rho} \cdot g \cdot d_p + \frac{\gamma_n}{\rho \cdot d_p}\right)}, \tag{3.9}$$

where $A_n = 0.0123$ and $\gamma_n = 3 \times 10^{-4}\ \mathrm{kg\,s^{-2}}$ are empirical constants, ρ denotes the air density, $\rho_s = 2650\ \mathrm{kg\,m^{-3}}$ the soil particle density, and g the gravitational acceleration. The bare-soil threshold is modified by two correction factors reflecting surface conditions.

The factor f_r captures the sheltering effect of vegetation and other roughness elements on particle mobilization (Raupach, 1993):

$$f_r = \sqrt{1 - 0.5 \cdot \lambda} \cdot \sqrt{1 + 0.5 \cdot 90 \cdot \lambda}, \quad \text{with} \quad \lambda = -0.35 \cdot \ln(1 - p_p), \tag{3.10}$$

where p_p is the fractional plant coverage within a grid cell.

The factor f_η reflects the role of soil moisture in suppressing erosion. Increasing gravimetric soil moisture η strengthens the adhesive bonds between soil particles, thereby elevating the erosion threshold. The parametrization of (Fécan et al., 1999) is adopted:

$$f_\eta = \sqrt{1 + 1.21 \cdot (\eta - \eta_0)^{0.68}}, \quad \text{with} \quad \eta_0 = a_z \cdot (0.0014 \cdot p_c^2 + 0.17 \cdot p_c), \tag{3.11}$$

where p_c is the clay content of the soil in percent and η_0 represents the residual soil moisture below which no additional adhesion correction is applied. The factor $a_z = 5$ is introduced to compensate for a systematic overestimation of modeled soil moisture (Zender et al., 2003).

The soil particle size distribution $n_s(d_p)$ constitutes a fundamental input to the emission scheme. Its shape is sensitive to the degree of soil dispersion, which itself depends on the wind conditions. Two end-member distributions are defined: a minimally dispersed state $n_{s,m}(d_p)$, applicable under gentle erosion, and a fully dispersed state $n_{s,f}(d_p)$, characteristic of vigorous erosion. The effective distribution is obtained as a linear combination of these end members, weighted by the dispersion factor γ_d (Shao, 2001):

$$n_s(d_p) = \gamma_d \cdot n_{s,m}(d_p) + (1 - \gamma_d) \cdot n_{s,f}(d_p), \tag{3.12}$$

$$\gamma_d = e^{-0.5 \cdot (u_* - u_{*t,m})^3}, \tag{3.13}$$

where $u_{*t,m}$ is the global minimum of the threshold friction velocity over all particle diameters. For low values of u_*, γ_d tends toward unity, so that the minimally dispersed distribution prevails; for high values of u_*, γ_d approaches zero and the fully dispersed distribution becomes dominant. The two limiting distributions are presented from (Shao, Fink, et al., 2010) and cover 12 soil types classified according to the United States Department of Agriculture (USDA) system. The global distribution of soil types is taken from the Harmonized World Soil Database (HWSD; see Nachtergaele and Batjes (2012)).

Once the friction velocity surpasses the threshold, saltation is initiated. The saltation flux $F_h(d_p)$ as a function of particle diameter is computed following White (1979):

$$F_h(d_p) = C_{\text{white}} \cdot \frac{\rho}{g} \cdot u_*^3 \cdot \left(1 + \frac{u_{*t}(d_p)}{u_*}\right) \cdot \left(1 - \frac{u_{*t}^2(d_p)}{u_*^2}\right), \tag{3.14}$$

where $C_{\text{white}} = 0.7$ serves as a tuning parameter to bring the modeled emission flux into agreement with observational data. The total saltation flux F_{th} is derived by integrating $F_h(d_p)$ across all particle diameters, with each diameter bin weighted by its contribution to the total soil cross-sectional area, and summing over the four log-normal soil particle size distributions (indexed by s):

$$F_{th} = fr_e \cdot \sum_{s=1}^{4} \int_{-\infty}^{\infty} F_h(d_p) \cdot \frac{\frac{\pi}{4} d_p^2 \cdot n_s(d_p)}{\int_{-\infty}^{\infty} \frac{\pi}{4} d_p^2 \cdot n_s(d_p)\, \mathrm{d}\ln d_p} \mathrm{d}\ln d_p, \tag{3.15}$$

where fr_e is the erodible soil fraction within a grid cell, derived from GlobCover2009 land-use data (Arino et al., 2008). It is defined as the aggregate of fractional coverages $fr_{b,i}$ across five land-use classes: bare areas, sparse vegetation, closed to open grassland, closed to open shrub-land, and mosaic grassland/forest-shrub-land. The four log-normal soil particle size distributions describe the typical representation of atmospheric aerosols as a superposition of four distinct modes, each characterized by a log-normal distribution in particle size. These modes usually include nucleation, accumulation, coarse, and giant particles, which differ in their median radii and geometric standard deviations. Each mode represents a specific source and physical behavior: nucleation and accumulation modes are typically associated with secondary particle formation and long-range transport, while coarse and giant modes are mainly linked to mechanical processes such as dust uplift and soil erosion. The log-normal formulation allows an efficient and flexible description of the strongly skewed particle size spectrum observed in atmospheric dust and soil aerosol populations.

The kinetic energy transferred by saltating particles upon impact with the soil surface is capable of dislodging finer aerosol particles whose binding energies are overcome. This sandblasting mechanism is parametrized following (Alfaro and Gomes, 2001). The vertical emission flux for each dust aerosol mode l is given by:

$$F_{v,l}(d_p) = \frac{\pi}{6} \cdot \rho_p \cdot d_{3,l}^3 \cdot \frac{p_l(d_p) \cdot \beta_{\text{kin}} \cdot F_h(d_p)}{e_l}, \tag{3.16}$$

where $\beta_{\text{kin}} = 163\ \mathrm{m\,s^{-2}}$ is the kinetic energy transfer coefficient, e_l denotes the binding energy characteristic of particles in mode l, and p_l is the share of kinetic energy allocated to the release of particles in mode l. The allocation is structured such that particles in the coarsest mode are mobilized first upon exceeding the threshold, while finer particles, which are more tightly bound, require progressively higher friction velocities for their release. The total emission flux for mode l is obtained by integrating equation (3.16) over all saltation particle diameters, weighted by cross-sectional area:

$$F_{tv,l} = fr_e \cdot \sum_{s=1}^{4} \int_{-\infty}^{\infty} F_{v,l}(d_p) \cdot \frac{\frac{\pi}{4} d_p^2 \cdot n_s(d_p)}{\int_{-\infty}^{\infty} \frac{\pi}{4} d_p^2 \cdot n_s(d_p)\, \mathrm{d}\ln d_p} \mathrm{d}\ln d_p. \tag{3.17}$$

Individual grid cells frequently encompass several distinct soil types. This subgrid-scale variability is addressed through a tile approach, in which the emission flux $F_{tv,l,i}$ is evaluated independently for each soil type i, and the grid-cell emission is assembled as the area-weighted average:

$$F_{tv,l} = \sum_{i=1}^{13} f_{s,i} \cdot F_{tv,l,i}, \tag{3.18}$$

where $f_{s,i}$ is the areal fraction of soil type i within the grid cell, subject to the constraint $\sum_{i=1}^{14} f_{s,i} = 1$, with the 14th fraction reserved for water bodies, rock, and urban surfaces. Although the soil particle size distributions $n_{s,i}(d_p)$ vary between soil types, the gravimetric soil moisture η and the residual moisture threshold η_0 are treated as uniform grid-cell quantities. The effective clay content entering the calculation of η_0 is the area-weighted mean over all soil types present in the cell:

$$p_c = \sum_{i=1}^{13} f_{s,i} \cdot p_{c,i}. \tag{3.19}$$

Removal processes including sedimentation, dry deposition, and washout are accounted for, whereas coagulation and chemical aging of dust particles are not considered in this configuration (Hoshyaripour et al., 2026).

3.1.2.2. Ocean modeling with ICON-O

With ICON-O (see Korn et al. (2022)) the ocean and the sea ice is modeled. It is implemented in the ICON-SmART coupling configuration and developed at the Max Planck Institute for Meteorology. ICON-O solves the hydrostatic Boussinesq equations of large-scale ocean dynamics with a free surface, also referred to as the primitive equations of large-scale ocean dynamics. The prognostic state vector consists of a horizontal velocity field, the sea surface elevation, as well as potential temperature and practical salinity from which all other quantities are derived. The model operates on an unstructured icosahedral triangular grid with an Arakawa C-type variable staggering and a classical z-coordinate in the vertical that ranges from 8 m near the surface to 200 m near the bottom. Horizontal momentum dissipation is parametrized through a biharmonic operator scaled with local grid resolution, while vertical mixing of momentum and tracers is governed by a prognostic turbulent kinetic energy (TKE) equation, from which vertical viscosity and diapycnal diffusivity are derived. Surface boundary conditions are provided by prescribed atmospheric reanalysis forcing, from which turbulent heat fluxes are calculated. Shortwave and longwave radiation, precipitation, sea level pressure, 2 m temperature, dew point temperature, cloud cover, and 10 m wind speed and stress are read from the forcing datasets, while evaporation and latent and sensible heat fluxes are computed internally.

3.1.2.3. JSBACH land model

JSBACH (Jena Scheme for Biosphere Atmosphere Coupling in Hamburg, see Schneck et al. (2022)) is a land surface model developed at the Max Planck Institute for Meteorology (MPI-M). It serves as the land component of ICON-SmART, providing surface boundary conditions to the atmosphere. JSBACH simulates a range of land surface processes operating on timescales of seconds to years. These include the surface energy balance, terrestrial water budget and runoff, surface exchange fluxes of moisture, heat, and carbon, phenology, surface albedo and roughness, radiation within the canopy, and plant productivity via gross

and net primary production (GPP and NPP). JSBACH provides several land surface variables to the ART module at each model time step, enabling the mentioned dynamic and physically consistent coupling between the land surface state and the aerosol processes simulated by ART. The depth of the first soil layer (`dz_soil`) sets the geometrical reference for the uppermost soil horizon from which dust can be emitted. With the first layer, the surface layer closest to the atmosphere is meant. Soil moisture (`w_so`), representing the total water content of this first layer, enters the calculation of the threshold friction velocity: higher soil moisture increases interparticle cohesion and thus suppresses dust emission. Similarly, the ice content of the first soil layer (`w_so_ice`) acts as a binary control — the presence of frozen soil water prevents dust emission entirely. Snow cover height (`h_snow`) serves the same function, as dust emission is not triggered over snow-covered surfaces. Plant cover fraction (`plcov`) modulates the aerodynamic roughness length, which in turn affects the near-surface wind shear relevant for dust mobilization. Of particular scientific relevance in the context of this coupled simulation are the fractional land cover classes provided by JSBACH like bare soil, desert, grass, trees, shrubs, crops, and pasture. These fractions are used to scale the dust emission flux according to local land cover. Crucially, while the land cover in standalone ICON-ART is static and based on a climatology, the JSBACH-coupled configuration used here provides *dynamically evolving* land cover fractions that change annually in response to the prescribed LUH2v2h land-use change scenario. A transition from bare soil to forested area, for example, directly reduces the dust emission potential in the affected grid cells. Beyond dust, JSBACH additionally supplies plant functional type information (`jsbach_pft`) required for the computation of biogenic aerosol emissions within ART which is not used in this simulation setup Coupling to the atmospheric model occurs through the exchange of albedo, surface roughness, and turbulent fluxes of sensible and latent heat, embedded within the implicit vertical diffusion scheme of the host atmosphere model.

3.1.3. ICON-SmART model settings

3.1.3.1. Experiment Overview and General Configuration

As described in section 3.1.2, the simulation was performed with the ICON-SmART-dust configuration. The experiment targets a 30-year long-term integration starting on 1 January 2020, organized in six consecutive five-year chunks. Three experiment members were simulated in parallel, corresponding to the climate scenarios SSP2-4.5 and SSP5-8.5 (O'Neill et al., 2016) as well as a present-day control member, allowing for a comparison of climate responses across different radiative forcing pathways. The two SSP scenarios are chosen to analyze one extreme scenario and one more optimistic scenario. Due to the current mitigation strategies, Tier 1 scenario SSP1-2.6 seems too unrealistic. In general, all experiment members were run using auto-icon (Baer et al., 2025), a workflow manager developed for ICON simulations that automatically submits the corresponding jobs to the HPC cluster and additionally supports input data retrieval as well as pre- and post-processing operations. The following description used Zängl (2023) as a basis.

The simulation was run on 80 compute nodes on the Levante HPC-System (*Levante HPC System — DKRZ Documentation documentation* 2026), with 30% of available tasks allocated to the ocean component. The model time step with atmospheric physics operates on a 5-minute time step, while both the ocean and the atmosphere-ocean coupling use a 10-minute time step. Physical parametrization schemes are called at longerintervals: radiation is updated every 3600 s, while convection, sub-grid-scale orographic drag (SSO), and gravity wave drag (GWD) schemes are invoked every 1800 s.

The atmospheric component uses the ICON R2B05 triangular grid, while the ocean employs the higher-resolution R2B06 grid. The atmosphere uses 90 vertical levels while the ocean uses 72 vertical levels. The land surface is represented by JSBACHv4, initialized from a pre-computed soil spin-up state referenced to the pre-industrial year 1850, with boundary conditions for soil properties, and sub-grid-scale orography.

The atmospheric initial state is derived from the Integrated Forecasting System (IFS) from the European Centre for Medium-Range Weather Forecasts (ECMWF), a global numerical weather prediction model that couples a spectral atmospheric dynamical core with a four-dimensional variational data assimilation scheme (4D-Var) (R Owens, 2018). IFS analysis fields valid at 00 UTC on 1 January 2020 are interpolated onto the ICON triangular grid at resolution R2B05 (grid number 0030) using the `ifs2icon` remapping tool, providing three-dimensional fields of wind, temperature, specific humidity, and surface pressure as the atmospheric initial state. (Prill et al., 2025)

The ocean component is initialized from a restart file of the predecessor experiment `slo1624`, valid on 1 January 2000, which provides a dynamically consistent, thermodynamically adjusted ocean state and avoids the need for a prolonged spin-up phase. As a supplementary reference and relaxation target, the file `ts_phc3.0_annual.L72sml.nc` provides ocean temperature and salinity fields from the Polar Science Center Hydrographic Climatology version 3.0 (Steele et al., 2001). PHC3.0 is a globally gridded climatology that merges the World Ocean Atlas 1998 (Antonov et al., 1998) with Arctic regional data from the joint US–Russian Arctic Ocean Atlas (Environmental Working Group, 1997), yielding an observationally well-constrained hydrographic background particularly in the Arctic Ocean. For this simulation, the climatology is vertically interpolated to 72 model levels and remapped to the ICON ocean grid.

Surface boundary conditions for the atmospheric grid (R2B05) are provided through an external parameter file generated by the EXTPAR software system (*External Parameters for Numerical Weather Prediction and Climate Application*), developed at DWD and MeteoSwiss. EXTPAR aggregates globally observed surface datasets — including orographic height, soil type, land–sea mask, fractional plant cover, leaf area index, and sub-grid orography parameters — onto the target triangular grid. (Prill et al., 2025).

The ocean grid file employs a modified bathymetry (`modsills`), in which the depth and width of critical ocean passages - including the Denmark Strait, the Faroe-Iceland Ridge, and the Strait of Gibraltar – have been manually adjusted to their observed geometry.

3.1.3.2. Physics Parametrizations

The atmospheric component applies the NWP physics package of ICON, a suite of parametrization schemes developed for operational numerical weather prediction at DWD and subsequently extended for climate-scale applications (Prill et al., 2025). Deep, shallow, and mid-level convection are parametrized using the Tiedtke–Bechtold mass-flux scheme, described in Tiedtke (1989) and Bechtold et al. (2001), in which cloud-base mass flux is determined by a CAPE-based closure and entrainment rates depend on environmental relative humidity. Boundary-layer turbulence and vertical diffusion are handled by TURBDIFF, a prognostic turbulent kinetic energy (TKE) scheme with additional source terms for horizontal wind shear and subgrid-scale orographic gravity wave breaking, which are particularly relevant for tracer mixing in the upper troposphere and lower stratosphere (Mellor and Yamada, 1982). Grid-scale cloud microphysics follow a single-moment bulk scheme (Seifert and Beheng, 2001) predicting mass mixing ratios of cloud water, cloud ice, rain, and snow, while sub-grid orographic and non-orographic gravity wave drag are parametrized after Lott and Miller (1997) and Orr et al. (2010), respectively.

Cloud cover is determined diagnostically at each radiation call using the Köhler scheme, which combines fractional cloud contributions from three independent sources: stratiform clouds diagnosed from the large-scale saturation state of the single-moment microphysics scheme, convective cloud cover provided by the Tiedtke–Bechtold scheme, and boundary-layer cloud cover from the TURBDIFF turbulence scheme. No prognostic equation for cloud fraction is solved; instead, the cloud cover field is reconstructed at every radiation time step from the current thermodynamic and dynamical state of the model. The radiative coupling is fully interactive: ecRad (Hogan and Bozzo, 2018) uses the prognostic cloud liquid and ice water mixing ratios from the microphysics scheme, together with the diagnosed cloud fraction, to compute cloud optical properties and their effects on shortwave and longwave radiation at every radiation time step. The resulting radiative heating and cooling rates feed back into the model's thermodynamic equation, thereby completing the cloud–radiation feedback loop. Aerosol-Cloud interactions are considered in this simulation (see section 3.1.3.5).

3.1.3.3. Radiation Scheme and Forcing

Gaseous radiative transfer is handled by the Rapid Radiative Transfer Model (RRTMC) for Global Circulation Models (GCMs), a correlated-*k* distribution scheme in which spectrally varying gas absorption coefficients are grouped into a compact set of quadrature points. RRTMG is embedded within ecRad (Hogan and Bozzo, 2018), the modular radiation framework adopted as the standard scheme for ICON (D. Rieger, Köhler, et al., 2019), whose flexible design allows cloud and aerosol optical properties to be supplied interactively from the model's prognostic fields, making radiation fully coupled to the simulated cloud and aerosol state at each call (here every 3600 s). The concentrations of all major greenhouse gases — CO_2, CH_4, N_2O, CFC-11, and CFC-12 — are prescribed from scenario-specific time series. The corresponding concentrations are read at each model time step from an external

NetCDF file, which provides the GHG trajectories of the respective scenario as harmonized for CMIP6 (see Kriegler et al. (2014) and O'Neill et al. (2016)). The data is available on *ESGF MetaGrid* (2026). This approach ensures that the radiative forcing evolves continuously and consistently with the prescribed SSP pathway throughout the 30-year simulation, rather than relying on a fixed or annually stepped concentration. In the third scenario that is calculated during this study, the Present-Day scenario, fixed concentrations for the greenhouse gases are given instead of a given NetCDF-timeseries. Stratospheric ozone is supplied interactively from the Linearized Ozone scheme (LINOZ) parametrization within the ART module, so that ozone responds to changes in transport and stratospheric dynamics over the simulation period. The solar zenith angle is computed with full astronomical accuracy including the Earth–Sun distance correction. Aerosol-radiation interactions are considered (see section 3.1.3.4).

3.1.3.4. ICON-ART Setup for Aerosol–Radiation Interactions

As described in section 3.1.2 ICON-ART extends ICON with emissions, transport, gas-phase chemistry, and aerosol dynamics in both the troposphere and stratosphere. Photolysis rates are computed using the Fast-JX scheme (Wild et al., 2000), which solves the solar UV radiative transfer equation with an eight-stream multiple-scattering algorithm across 18 wavelength bins (177–850 nm), accounting for the optical effects of gases, clouds, and aerosols. The required input files include wavelength-resolved absorption cross-sections and quantum yields, photolysis reaction mappings, and scattering property tables for aerosol and cloud particles.

Stratospheric ozone is parametrized with the LINOZ scheme (McLinden et al., 2000), which represents stratospheric chemical rates as a first-order Taylor expansion around the local ozone mixing ratio, temperature, and overhead ozone column, and is applied above approximately 10 km altitude. The coefficient file additionally incorporates bromine chemistry, relevant for heterogeneous lower-stratospheric ozone depletion.

As already motivated in the introduction of this section as well as in the introduction of this study (see chapter 1 and 3.1.2), the scientific focus of the experiment is the prognostic simulation of mineral dust and its radiative effects. Dust tracer classes are defined through the XML configuration file, while aerosol–radiation interaction is handled via the `DUST_RAD` module and a prescribed optical property file. The coupling to ecRad is realized through the ART aerosol interface, through which mass extinction coefficients, single scattering albedos, and asymmetry parameters are computed from prognostic aerosol mass concentrations at each grid point and model level. The ART module (Hoshyaripour et al., 2026) is activated and configured for the prognostic simulation of mineral dust aerosol and its direct and indirect radiative effects. Dust emission, transport, and size distribution are defined through XML configuration files, which specify the emitted size modes, their optical properties, and the emission flux parametrization. The direct aerosol–radiation interaction is activated, meaning that the dust optical properties computed from the prognostic mass concentrations are passed to ecRad at each radiation call and affect the shortwave and longwave radiative fluxes. A key diagnostic feature is the multi-call radiation approach, in which ecRad is

invoked twice per radiation time step — once with the full aerosol field and once without — to quantify the dust direct radiative effect (DDRE) at each grid point and time step. This approach allows the aerosol radiative effect to be separated cleanly from the background radiative state without running additional offline calculations.

Optical properties for background aerosol species not explicitly simulated by ART (see Section 3.1.2.1) are prescribed from the MACv2 aerosol climatology (*Max Planck Institute Aerosol Climatology version 2*) of (Kinne, 2019). MACv2 provides monthly global fields of aerosol optical depth, single scattering albedo, and asymmetry parameter for fine-mode (radius $< 0.5\,\mu$m) and coarse-mode particles (radius $> 0.5\,\mu$m), constrained by multi-year AERONET and Maritime Aerosol Network observations.

3.1.3.5. Aerosol–Cloud Interaction: Coupling to Convection and Microphysics

The namelist switch `icpl_aero_gscp = 1` enables aerosol–microphysics coupling, through which the cloud droplet number concentration (CDNC) is derived from the 2D aerosol optical depth based on prescribed vertical profiles by climatology of (Tegen et al., 1997). An increase in CDNC at fixed liquid water content results in a larger number of smaller droplets, which increases the cloud optical depth and albedo. This process is known as the first aerosol indirect effect, or the Twomey effect (Twomey, 1977). An increase in aerosol loading leads to a higher CDNC, which in turn results in smaller cloud droplet effective radii r_{eff}. As a consequence, the cloud albedo is enhanced. The parameter `icpl_aero_conv = 1` extends the aerosol–cloud interaction to the Tiedtke–Bechtold convection scheme, where the aerosol-modulated CDNC affects the autoconversion of cloud water to rain within convective updrafts. A higher CDNC reduces the autoconversion rate, suppressing precipitation formation and potentially prolonging the lifetime of convective cloud systems. This mechanism corresponds to the second indirect aerosol effect (Albrecht effect, Albrecht (1989)): The reduction in droplet size decreases collision–coalescence efficiency, which delays the onset of warm rain and can increase cloud liquid water path and cloud fraction. Wet deposition in turn removes dust from the atmosphere. The coupling of aerosol to ozone chemistry is also activated, which couples the LINOZ stratospheric ozone parametrization to the tropopause position diagnosed in the NWP physics, ensuring a consistent ozone distribution near the tropopause.

3.1.3.6. JSBACH: Land Surface, Biogeochemistry, and Land-Use Change

The land surface component is JSBACHv4 (see Schneck et al. (2022) and Reick et al. (2021)), integrated as a module within ICON-SmART and exchanging surface energy fluxes, albedo, and roughness length with the atmospheric physics at every model time step. Vegetation is represented through eleven plant functional types (PFTs), with fractional PFT coverage prescribed from the Land-Use Harmonization project LUH2 (Hurtt et al., 2020) and a full vegetation albedo scheme responding to PFT composition and leaf area index. Soil thermodynamics and hydrology include dynamic snow processes, soil freezing, and full river-routing via the hydrological discharge model, which delivers surface runoff as a freshwater flux to

the ocean and thereby closes the global water cycle. Plant phenology is computed prognostically using a logistic growth model, and photosynthesis is represented interactively and is calculated using a two-stream radiation approximation for canopy light absorption, with C3 and C4 carbon fixation pathways treated separately following the Farquhar et al. (1980) and Collatz et al. (1992) formulations. The terrestrial carbon cycle is fully active in this simulation, with carbon tracked across multiple pools — living biomass, litter, and soil organic matter — and net primary production computed from the interactive assimilation module. Heterotrophic respiration is temperature- and moisture-dependent, allowing the terrestrial carbon balance to respond dynamically to the evolving climate. This enables a first-order representation of the carbon–climate feedback, although the atmospheric CO_2 concentration entering the radiation scheme remains prescribed from the SSP time series rather than being coupled to the prognostic land carbon flux. Dynamic land-use change is enabled through the NLCC module (`jsb_nlcc_nml`), which updates the fractional PFT coverage of each grid cell annually according to the LUH2 land-use change maps. For the respective SSP scenario, these maps encode a moderate intensification of agricultural land use alongside regional afforestation, consistent with the mitigation trajectory of that scenario. Changes in PFT fractions directly affect local surface albedo, roughness length, evapotranspiration, and the carbon budget. Soil hydrology is resolved across five layers extending approximately 9.8 m below the surface, and JSBACHv4 additionally incorporates frozen soil water and a five-layer snow scheme.

3.1.4. Temporal and Spatial Postprocessing analysis with Region Tracking Algorithm

3.1.4.1. Overview

In order to detect the temporal and spatial evolution of specific atmospheric events that can be expressed through a certain criteria or threshold, an algorithm is developed. A typical application is the identification of *dark doldrums* – periods during which renewable energy capacity factors fall below a given threshold across coherent geographic areas. The developed Region Tracking algorithm detects contiguous spatial regions in gridded hourly time-series data where the user-defined criterion is satisfied. These detected regions are tracked across consecutive time steps and across year boundaries, so that events spanning the turn of the year are handled correctly and assigned persistent identifiers. The workflow is implemented in five files: a scenario configuration file, a computation file with helping functions, a main orchestration script, and two SLURM shell scripts for cluster submission.

3.1.4.2. Configuration and Job Submission

Each case that is examined with its own criteria to detect is represented by its own configuration file. The `SCENARIO` variable, referring to the respective climate scenario that is being analysed, acts as the central identifier and determines the output subdirectory and appearing in every output filename so that results from different scenarios are kept strictly separate. Up to

four input paths of different climate data with diverse variables (`INPUT1`–`INPUT4`) can be specified. With these Inputs a mask expression, defining the evaluation criteria and being a free-form Python expression, can be indicated. The submit script (`submit_Region_Tracking.sh`) chains one SLURM job per year using `--dependency=afterok:<jobid>`, so that year $n + 1$ starts only after year n has successfully written its state file.

3.1.4.3. Tracking Process

Before the mask expression is evaluated, all loaded data arrays are brought to a common grid via `xr.align(..., join="outer")`. This step is critical when inputs have different spatial coverages (e.g. capacity factor fields for different countries): without alignment, the mosaic step may produce grids of different sizes for different variables, causing a dimension mismatch that silently yields zero detected regions. After alignment, cells outside a given input's coverage carry `NaN`, which is treated as `False` in the mask, so a pixel is flagged as active only if all referenced inputs carry valid data there. The mask expression (`MASK_EXPR`) in the configuration file is then evaluated on the aligned arrays. The resulting boolean array has dimensions (time, y, x). All subsequent steps derive their reference grid from the computed mask, ensuring full dimensional consistency.

Grid-cell areas are computed analytically, accounting for the spherical geometry of the Earth:

$$A_{ij} \;=\; R^2 \,|\cos\varphi_i|\,|\Delta\varphi_i|\,|\Delta\lambda_j|,$$

where $R = 6371\,\text{km}$ is the Earth's radius (Vidmachenko, 2026), φ_i is the latitude of cell i in radians, and $\Delta\varphi_i$, $\Delta\lambda_j$ are the angular extents, so height and width, of the cell using latitude and longitude in radians. Spatial connectivity is defined using 8-connectivity (the 3×3 structuring element with all entries set to one).

The mask produces a grid of `True`/`False` values at each time step, `True` where the criterion is met. The labeling step then answers the question which of those `True` pixels belong together spatially. This is accomplished using `scipy.ndimage.label`, which traverses the grid and assigns a unique integer to each connected cluster of `True` pixels, where connectivity is defined in the 8-neighbourhood sense (direct and diagonal neighbours). The result is a label array of the same spatial dimensions as the mask, with zero at inactive pixels and a positive integer identifying each distinct cluster. A simple example illustrates the idea: if the mask is `True` in three geographically separated areas at a given hour, the labeling algorithm assigns the integers 1, 2, and 3 to those three clusters, with the boundaries between them determined purely by spatial adjacency. These integer labels are assigned freshly and independently at every time step. They carry no meaning across time: the same integer appearing in two consecutive time steps does not imply that the underlying pixels belong to the same physical event. Resolving that question which cluster at one time step is the continuation of which cluster at the next is the sole purpose of the tracking step that follows. The labeling itself is purely a spatial operation performed one time step at a time. Because loading all 8760 hourly time steps of a full year simultaneously would require a prohibitive amount of memory, the computation is split into chunks of 168 time steps, corresponding to one week

of hourly data. Each chunk is processed independently and the results are concatenated before the tracking step begins.

The core challenge of tracking is to assign persistent identifiers to regions that evolve from one time step to the next. This is solved using the *Intersection over Union* (IoU, Jaccard index, see e.g. Ataş (2023)), which measures spatial overlap between two regions A and B:

$$\mathrm{IoU}(A, B) \;=\; \frac{|A \cap B|}{|A \cup B|}.$$

IoU = 0 indicates no shared pixels; IoU = 1 indicates identical pixel sets. At each time step, every current region is compared against all regions active in the previous step. That means that at each time step the amount of shared pixels with the previous time step in a certain region is put into relation with the total amount of pixels that are marked `True` at both time steps. If that value meets or exceeds `IOU_THRESHOLD` (here set to 0.1), the current region is treated as a continuation and inherits the predecessor's global identifier. Otherwise, the region is treated as a new cluster.

Regions are stored as sets of flat pixel indices (`frozenset`), making set intersection and union operations fast and keeping memory usage proportional to the number of active pixels rather than to the total grid size. At the end of each year, the active region sets and the identifier counter are saved to a pickle state file; the following year's job loads this state, enabling seamless cross-year tracking. Each completed year produces three files:

- **Statistics file** (`region_track_<COUNTRY>_<SCENARIO>_<year>.nc`): per-region time series of area (`area_km2`), pixel count (`size_pixels`), and centroid coordinates (`lat_c`, `lon_c`), plus scalar summaries (lifetime, maximum area, mean area). Dimensions: (region, time).
- **Label field** (`..._labels.nc`): integer region identifier at every grid cell and time step, zero where no event is active. Dimensions: (time, y, x). Allows the exact spatial footprint of any region at any moment to be reconstructed.
- **State file** (`state_<COUNTRY>_<SCENARIO>_<year>.pkl`): internal transfer object passing active pixel sets and the identifier counter to the following year.

In this study, the Region tracking algorithm is applied to onshore dark doldrums where the capacity factors for wind and photovoltaic drops below the threshold off 0,1 and light breezes when the capacity factors exceed 0.9 (see section 4.1.2.1 and 4.1.2.2).

3.2. Post-Processing Climate Data to Energy System Quantities with Python Atlite

Now that the ICON-SmART data is simulated, it can be post-processed and the input data for the energy market model PowerACE can be prepared. For the input data, capacity factors per time step, per market area and per technology (wind onshore, wind offshore and photovoltaic) are needed and a table with all these information have to be prepared

to be usable as PowerACE input. For further input preparations for the power flow model, renewable energy yields per predefined substation region have to be calculated. This can also be achieved using atlite as decribed in this section.

3.2.1. The Python module atlite

The module „atlite“ (see Hofmann et al. (2021) and *Introduction — atlite 0.6 documentation* (2026)) is an open-source Python software package designed to convert historical weather data into power generation potentials and time series for a range of renewable energy technologies, including solar photovoltaic (PV) panels, wind turbines, hydropower systems, and solar thermal collectors. Originally developed by the Renewable Energy Group at the Frankfurt Institute for Advanced Studies, atlite has since evolved into a community-driven library with a substantially expanded feature set. The central abstraction of atlite is the Cutout class, which represents a spatio-temporal subset of one or more weather datasets and forms the basis for all subsequent preparation and conversion steps. atlite natively supports multiple meteorological data sources, including ERA5 reanalysis data from the European Centre for Medium-Range Weather Forecasts and the satellite-based SARAH-2 dataset, while an abstraction layer for weather datasets additionally enables the integration of custom or preprocessed input data (Botha et al., 2025). By leveraging the Python packages xarray, dask, and rasterio, atlite achieves memory-efficient and parallelized processing, making it performant even on large spatio-temporal datasets. Beyond power generation, atlite also provides conversion functions for demand-side variables such as building heating demand and heat pump performance coefficients. The software's design prioritizes extensibility, customizability, and reproducibility, distinguishing it from web-based alternatives such as renewables.ninja, which neither expose their underlying datasets nor their conversion methods. These properties make atlite a suitable tool for a wide range of applications in renewable energy research and planning, from generating aggregated regional time series for large-scale energy system models to identifying optimal installation sites under specific climatic and geographic conditions, as demonstrated for the case of South Africa by Botha et al. (2025).

3.2.2. Climate Data Transformation to Capacity Factors

Generally, a capacity factor is defined as the energy yield E (in kWh) of a certain renewable technology i at a given site j and time frame k (in hours), divided by the maximum possible rated power of that technology i (in kW) and the calculation time frame (in hours) t:

$$CF = \frac{E_{ijk}}{R_i \cdot t} \tag{3.20}$$

When calculating capacity factors for every hour, this simplifies to $CF = \frac{E_{ijk}}{R_i}$. (Mignacca and Locatelli, 2020) The computation of capacity factor relies on the atlite library, which provides power-curve- and irradiance-based conversion routines for wind and solar technologies.

In the following the pipeline is described how to calculate capacity factors for a certain country and a certain renewable technology (wind onshore, wind offshore and photovoltaic) at a certain time step. Since the input data originates from the ICON-SmART model rather than from ERA5 data (ECMWF Reanalysis data, generation 5) from ECMWF, the dataset cannot be passed to atlite through its native data retrieval interface; instead, the model fields must be carefully prepared so that they exactly match the variable naming conventions, attribute structure, and coordinate layout that Atlite internally expects. The preparation of the dataset therefore constitutes a critical first step. From the raw model output, the relevant atmospheric variables are extracted. In table 3.3, the necessary variable names and corresponding ICON variables are explained. After merging all variables into

Table 3.3.: Expected variables from meteorological dataset comitted to atlite

Variable (atlite)	Variable (ICON)	Descriptionn
u10	u_10m	10 m wind (u-comp.)
v10	v_10m	10 m wind (v-comp.)
wnd100	(via Power Law)	10 m wind vector
temperature	t_2m	2 m temperature
influx_toa	sob_t + sou_t	total short wave downward irradiance (TOA)
influx_diffuse	sodifd_s	diffusive short wave downward irradiance (surface)
influx_direct	sob_s + sou_s	total short wave downward irradiance (surface)
albedo	albdif	diffuse short wave albedo
roughness	gz0	roughness length

a single `xarray.Dataset`, the spatial coordinate names are changed from `lon/lat` to `x/y`, and global dataset attributes `module = "era5"` and `Conventions = "CF-1.6"` are set. These naming conventions and attributes are not optional: Atlite uses them internally to identify which data source to apply and which physical conversion routines to invoke. At the variable level, each field must carry a `module` and a `feature` attribute. The wind variables receive `feature = "wind"`, the radiation field `feature = "solar"`, and the temperature field `feature = "temperature"`. To account for the hub height of offshore turbines, the 10 m wind speed magnitude is extrapolated to 100 m using the empirical power law

$$\vec{v}_{100\mathrm{m}} = \sqrt{u_{10\mathrm{m}}^2 + v_{10\mathrm{m}}^2} \cdot \left(\frac{100}{10}\right)^{\alpha}, \tag{3.21}$$

where $\alpha = 0.14$ is the Hellmann exponent for neutral stratification, and the resulting field is stored as `wnd100m` within the dataset. Here, the 10m wind speed has been used for calculation speed and RAM reasons. An interpolation to direct model levels is more expensive to calculate. Once the dataset is correctly formatted, two spatially restricted subsets are derived from it. A land mask is constructed using `regionmask.mask_geopandas` applied to the Natural Earth country boundary geometries, and an offshore mask is obtained analogously from the EEZ shapefile, with the land area subtracted so that only open-sea grid points are retained. The full dataset is then split into a land subset (`ds_landarea`) and a sea subset (`ds_seaarea`). These subsets are subsequently wrapped into atlite `Cutout` objects.

A cutout defines a spatially and temporally bounded data cube; its spatial extent is set to the bounding box of the country geometry, and its temporal axis spans the extend of the dataset. In this case of using custom climate data, preparing a cutout also means preparing the netCDF-Dataset inside of atlite such that further analysis with atlite methods are enabled afterwards. Rather than triggering atlite's internal ERA5 download, the pre-processed model data is injected directly by assigning it to the `cutout.data` attribute. Two cutouts are created: `cutout_on` receives `ds_landarea` and is used for all onshore calculations, while `cutout_off` receives `ds_seaarea` and is used exclusively for offshore wind.

The actual capacity factor time series are then computed by calling Atlite's built-in conversion methods `cutout.wind()` and `cutout.pv()` on the respective cutouts as well as by calling the argument `capacity_factor_timeseries=True)` and selecting a certain wind turbine with the argument (here e.g) `turbine="Vestas_V112_3MW"` or panel type as well as their orientation with the arguments (here e.g.) `panel="CSi", orientation=dict(slope=30, azimuth=180)`. The last expression would model a south-facing crystalline-silicon panels at a fixed tilt of 30°. All methods return `xarray.DataArray` objects with dimensions `(time, x, y)`, i.e. a full hourly capacity factor field at the spatial resolution of the input grid. Country-level representative time series are then derived by averaging each field uniformly over all spatial grid points.

3.2.3. Energy Yield calculation

In the following it is described how hourly energy yield time series for photovoltaic (PV) and wind power are computed for a given geographic region using Python `atlite`. Exactly like when quantifying capacity factors, the calculation uses the ICON-SmART climate model output as meteorological forcing data and on plant-level capacity records to determine how much installed capacity exists within the target region and where it is located. The meteorological input data is loaded using `xarray` with Dask-based chunking to keep memory usage manageable. After loading, the dataset is clipped to the bounding box of the target region, which is defined by a polygon shapefile. If the region is smaller than a single grid cell, the nearest grid point is selected automatically. If only one grid point falls within the bounding box per spatial axis, it is expanded to include an adjacent point formally, since `atlite` requires at least two grid points in each dimension to construct a valid cutout. For the actual yield calculation this extra cell is neglected since atlite only considers the installed capacity within the predefined shape file that then doesn't correlate with the adjacent cell. From the clipped dataset, all variables required by `atlite` are derived and assembled into a new `xarray.Dataset` with the valid Era5 variable naming convention (see section 3.2.2). The meteorological data and its spatial extent are then passed to `atlite` through a `Cutout` object.

Once the meteorological data is prepared, the installed capacity within the target region is read from a CSV file (separate files exist for wind and solar plants). For this study open source files from *Home | Global Energy Monitor* (2026) are used. Each row in the file corresponds to one power plant and contains its latitude, longitude, capacity in MW, and commissioning year. The plants are spatially filtered to retain only those falling inside

the target polygon, and the result is reformatted into a `pandas.DataFrame` with columns that contain at least those variables described in table 3.4. Note that atlite only needs the variables "x", "y", "capacity" for the energy yield calculation, if information about the other columns are missing, these fields can be filled randomly. Similar to the meteorological data where ERA5 data is expected, here atlite expects columns like in the now discontinued "Anlagenregister" from *EnergyMap - Auf dem Weg zu 100% EE* (2026). With the cutout in

Table 3.4.: Expected columns from capacity dataset comitted to atlite

Variable	Expected Input
installation date	date (e.g. 01.01.2025)
plz	postal code (e.g. 76135)
city	city name (e.g. Karlsruhe)
capacity	capacity in MW (e.g. 27,2)
level	voltage level (e.g. 03 (HS))
y	latitude of site (e.g. 49,0)
x	longitude of site (e.g. 8,4)
validation	commissioning status (e.g. OK)

place, a spatial capacity layout is constructed from the renewable plant data using:

```
layout = cutout.layout_from_capacity_list(cap_df, col="capacity")
```

This function interpolates the point-level plant capacities onto the cutout's spatial grid, producing a weighted map that `atlite` uses to spatially aggregate the power output across the region. The actual yield calculation then uses one of two `atlite` functions, `pv` or `wind` depending on the technology. For Photovoltaic one could write:

```
ts = cutout.pv( panel="CSi", orientation="slope":  30.0, "azimuth":  180.0, lay-
out=layout, ).squeeze().to_series()
```

Here, `panel="CSi"` selects crystalline silicon as the panel technology. After calculating the yields, the output is converted to a `pandas.Series` with an hourly `DatetimeIndex`, representing aggregated power output in MW across all plants in the region for the full timeframe. If no plants are found within the target polygon, a zero-valued time series is written directly without invoking any `atlite` function.

3.3. Energy Market Simulation with PowerACE

The data of the climate simulation climate data are now available and they have also been transformed to capacity factors for wind onshore, wind offshore and photovoltaic so that the climate data can be used as renewable profile inputs in the energy market simulations with PowerACE.

3.3.1. Model System PowerACE

PowerACE is an established agent-based electricity market simulation model developed between 2004 and 2007 through a joint effort of researchers at the University of Karlsruhe, the Fraunhofer Institute for Systems and Innovation Research, and the University of Mannheim (see e.g. Sensfuß (2007)). Since its inception, the model has been continuously extended to address an expanding set of research questions, including the merit-order effect of renewables, market power in liberalized electricity markets, and the long-term effects of capacity remuneration mechanisms (CRMs) in interconnected European markets. The model is built around five core dimensions: (1) an agent-based modeling approach, (2) short-term market simulation, (3) long-term planning and investment, (4) multi-area representation with cross-border effects, and (5) capacity remuneration mechanisms. The description is based on material from Fraunholz (2021) and Zimmermann (2024), if not stated differently.

3.3.1.1. Agent-Based Modeling Approach

The most fundamental design choice underlying PowerACE is its agent-based modeling (ABM) paradigm. In contrast to traditional optimization models — which adopt the perspective of a central planner and minimize total system costs subject to given constraints — agent-based simulation models take a so called explorative approach. Each agent follows its own decision rules under imperfect information, allowing system-level behavior to emerge from individual, decentralized decisions. The agents representing utility companies make both short-term dispatch decisions and long-term investment decisions based on their individual expectations. A regulator agent sets the framework conditions, including price caps and CRM parameters. Demand traders represent electricity consumers, renewable traders manage the bidding of variable renewable generation profiles, and storage agents optimize storage dispatch. This structure allows for the representation of path dependencies, strategic behavior, and imperfect foresight — phenomena that optimization models typically cannot capture — making PowerACE well-suited for analyzing how market designs shape long-term system development.

3.3.1.2. Short-Term Market Simulation

PowerACE simulates short-term electricity markets at an hourly temporal resolution, covering all 8760 hours of each simulation year. The market design is closely aligned with the European day-ahead spot market. In each hour, supply-side agents submit price-quantity bids for individual power plant units, based on variable costs encompassing fuel costs, CO_2 certificate prices, and plant efficiency parameters. Start-up costs are computed for plants transitioning from off-line status and incorporated into the bid price. Mark-ups above variable costs are applied between minimum and maximum generation levels to recover fixed and capital costs. On the demand side, a demand trader submits a price-inelastic bid reflecting the given load profile. Variable renewable energy (RE) sources are represented by a renewable trader that bids at zero price, consistent with priority dispatch status and

negligible variable costs. Together with defined installed capacities and given capacity factors that describe the possible usage of a certain renewable technology at a certain time step based on the respective meteorological conditions, the renewable energy dispatch is calculated. The Storage agents — primarily representing pumped-hydro storage — optimize dispatch over a 24-hour horizon, accounting for round-trip efficiency, fill levels, and power constraints. Market clearing is performed by the market operator agent through the intersection of the aggregated merit-order supply curve and residual demand, i.e., total demand net of renewable infeed and cross-border imports. A single spot market serves as an approximation of all short-term energy markets, with a price cap aligned to the day-ahead market maximum. Balancing markets are represented in simplified form through an annual capacity auction covering primary, secondary, and tertiary reserve requirements.

3.3.1.3. Long-Term Planning and Investment

At the end of each simulation year, investment planner agents evaluate new generation capacity options through a net present value (NPV) calculation. Investments are only undertaken if individually profitable under prevailing market conditions — with no guarantee that sufficient capacity will always be built to cover peak demand. This distinguishes PowerACE from optimization models and enables the study of adequacy implications under different market designs. In addition to these endogenous, market-driven investment decisions, long-term capacity trajectories, particularly for RE sources, can alternatively be provided through exogenous input tables, for example based on scenarios from the ENTSO-E TYNDP, allowing the model to reflect policy-driven expansion pathways directly.

3.3.1.4. Separation into Different Market Areas and Cross-Border Effects

A defining feature of PowerACE is its multi-area architecture, which represents the major national electricity markets of Europe as distinct but interconnected market areas. Each market area implements the full set of agents described above independently. Adjacent areas are linked via modeled interconnector capacities, allowing for cross-border electricity exchange. For each simulation hour, the clearing of all coupled market areas is formulated as a welfare-maximizing linear optimization problem. Inputs are the full set of supply and demand bids from all areas together with the net transfer capacities (NTCs) between adjacent areas. The result is a market price per area, associated cross-border electricity flows, and an acceptance rate for each bid. This mechanism captures the fundamental economics of cross-border trade: in the absence of transmission congestion, prices converge across areas; when interconnectors are binding, areas decouple and price differences reflect transmission scarcity (market splitting). These effects have important implications both for short-term resource allocation efficiency and for long-term investment incentives. For the investment dimension, a novel algorithm iteratively determines a stable Nash equilibrium of investment decisions across all market areas, and endogenous price forecasts account for expected cross-border flows. This spatial coupling dimension enables the analysis of how national market designs affect neighboring countries, including free-rider dynamics,

import dependency, and the cross-border displacement of investment between energy-only markets (EOMs) and markets with CRMs.

3.3.2. PowerACE model settings

In the following the simulation settings of the electricity market simulation with PowerACE are described. An overview of the key simulation parameters is given in Table 3.5. A map with the market areas included in this simulation is given in figure 3.3.

Table 3.5.: Overview of key PowerACE simulation parameters.

Parameter	Value / Source
Simulation horizon	30 years (from 2020)
Temporal resolution	Hourly
Scenarios	SSP2-4.5, SSP5-8.5, Present-day
Market regions	DE_LU, FR, BE, NL, AT, CH, PL, PT
Demand profiles	TYNDP 2024, National Trends
Fuel prices	TYNDP 2024, National Trends
CO_2 prices	TYNDP 2024, National Trends
Net transfer capacities	TYNDP 2024
Capacity factors (VRE)	ICON-SmART via *atlite*
Hydro inflows	PECD 2025
Investment module	Disabled (exogenous capacity)
Strategic reserve	Disabled

In each simulated hour, the model clears a competitive day-ahead market by dispatching conventional thermal power plants, renewable generators, and storage units based on their marginal costs, subject to capacity and inter-regional transmission constraints as well as general demand per market area.

Each simulation covers a period of 30 years starting from the base year 2020, producing a continuous hourly output time series for the entire horizon. The three scenario variants of the climate simulation with ICON-SmART (see chapter 3.1.3) are again considered: a moderate climate change trajectory following the Shared Socioeconomic Pathway SSP2-4.5, a high-emission pathway under SSP5-8.5, and a Present-day reference scenario representing contemporary climate conditions without anthropogenic climate change trends. This three-scenario design allows for a systematic assessment of how progressively altered climatic conditions affect renewable energy availability and, consequently, electricity market outcomes over multi-decadal timescales.

The simulation encompasses eight interconnected market regions in Central and Western Europe: Germany–Luxembourg (DE_LU), France (FR), Belgium (BE), the Netherlands (NL), Austria (AT), Switzerland (CH), Poland (PL), and Portugal (PT). Each region is represented

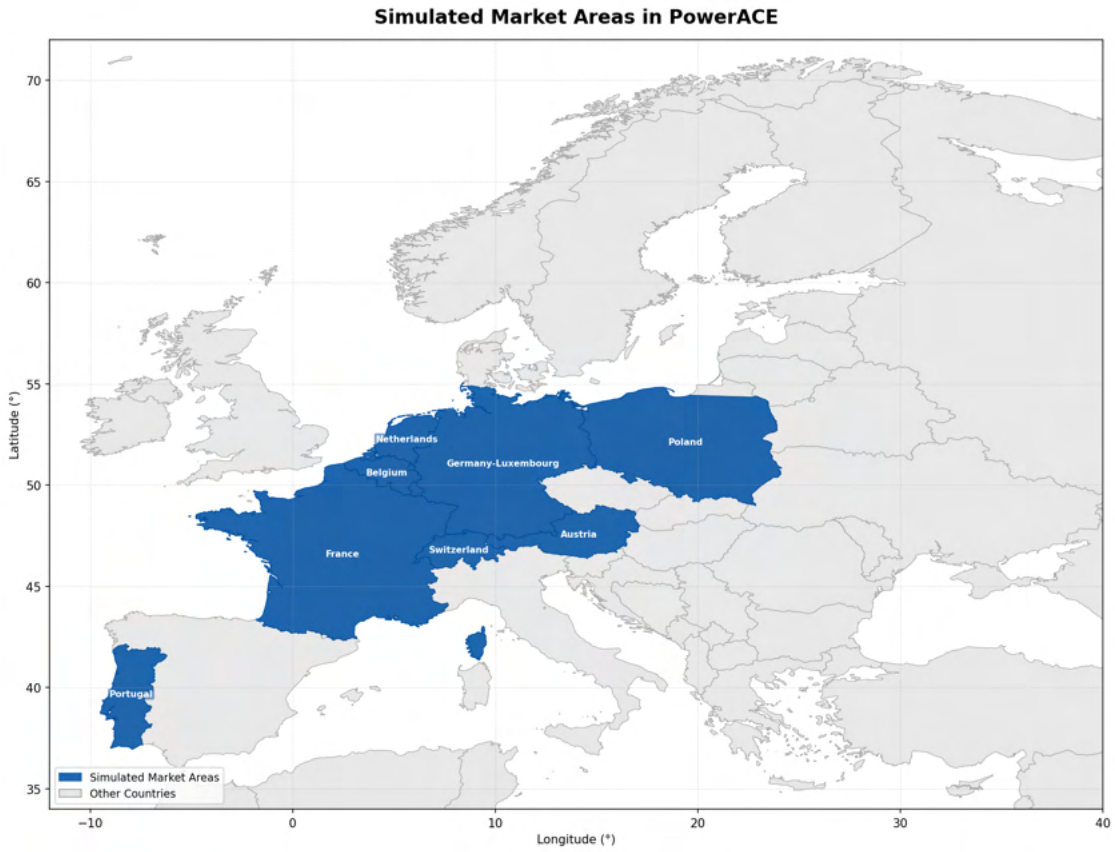

Figure 3.3.: Map of market areas included in PowerACE Simulation (marked blue).

as a single bidding zone with its own power plant fleet, demand profile, and renewable generation portfolio. Cross-border exchange between regions is governed by NTCs drawn from the TYNDP 2024, ensuring a scenario-consistent representation of transmission constraints over the simulation horizon; historical NTC values from ENTSO-E serve as the basis for the initial calibration period. Internal grid losses within individual market areas are neglected. The module for interactive investment decisions is disabled throughout as well, meaning the installed capacity fleet is treated as exogenously given for every simulation year and no endogenous capacity additions or retirements are triggered during the run. Instead, renewable and thermal power plant- as well as grid capacities are given by the pre-calculated capacities of the TYNDP at support years 2030, 2040 and 2050. A separate self developed script adjusts an already given power plant list of present-day capacities as well as commissioning and decommissioning dates so that the by the TYNDP given capacity values are met in the support years. To keep transitions between decades and their respective capacities per country smoother, the script also adjusts the capacities every two years if there are large amounts of capacity extensions so that the capacities between the support years are interpolated. Market clearing is performed without strategic price markups, and no strategic reserve mechanism is activated in any of the modeled regions. All major exogenous input data are drawn from publicly available European planning datasets to ensure consistency and reproducibility. Hourly electricity demand profiles for all eight

market regions are also taken from the TYNDP 2024 National Trends scenario, which provides country-level load projections aligned with current national energy and climate policies. Fuel cost trajectories for all relevant energy carriers—including natural gas, hard coal, lignite, and uranium—are likewise sourced from the TYNDP 2024 National Trends scenario and applied at daily resolution throughout the simulation. CO_2 allowance prices follow the same TYNDP 2024 source and are updated at a semi-annual frequency to capture gradual carbon price trajectories. For the initial years of the simulation, historical CO_2 price data from futures markets are used to anchor the model to observed conditions.

Hourly capacity factors for variable renewable energy sources—wind onshore, wind offshore, and utility-scale solar photovoltaics—are derived from the output of the ICON-SmART regional climate model using the open-source Python toolkit *atlite* (see section 3.2.2). This workflow converts gridded meteorological fields into technology-specific generation time series by applying turbine power curves and PV conversion models, thereby providing a physically consistent link between the climate scenario and the simulated renewable resource availability. Hydro power is treated separately: run-of-river and reservoir inflow data are sourced from the Pan-European Climate Database (PECD) 2025, while pump-storage operation is modeled explicitly. The seasonal storage dispatch is solved iteratively within each simulation step, with ten inner iterations to ensure numerical convergence of long-duration storage operation.

3.4. Power Flow Analysis

Climate and energy market data have now been simulated. To evaluate grid capacities, grid stability, and the adjustments required under a future climate, a power flow model can be employed by combining all pre-simulated quantities. The operating principles of such a model and a first approach to linking all three models are described in this section. Section 2.3.3.3 describes power flow through energy grids. Note that in this study only a power flow simulation is employed that describes the stationary conditions of the energy grid. While this can be used for modeling the grid itself, it leaves open the important question of how generators should be dispatched in the first place. Since this is an important point that is picked up in this thesis for future studies, the usage of an extended Optimal Power Flow (OPF) model is explained in the following to create a basis for that.
As described in section 3.3, electricity markets and their models determine generator set-points based on economic criteria. The simplifications made in such models render market clearing tractable, but they ignore the finite capacity of transmission lines and the requirement that electricity obeys the laws of physics. As a result, the schedule produced by the market may cause certain lines to become overloaded. Grid operators must then intervene manually, instructing some generators to increase their output while others reduce theirs – a process known as redispatch. The central question underlying the OPF problem is therefore: how can generator outputs be chosen such that generation costs are minimised, the power flow equations are satisfied at every bus, and all physical limits in the network are respected?

This question can be stated precisely as a constrained optimization problem, based on Frank et al. (2012). In its general form, such a problem seeks to minimize an objective function $f(x)$ over a set of variables x from a domain X, subject to two types of constraints. Equality constraints $g_i(x) = 0$ must be satisfied exactly, while inequality constraints $h_j(x) \leq 0$ define limits that must not be exceeded. The set of all points that satisfy both types of constraints is called the feasible set S. A solution $x^* \in S$ is called a global optimum if no other feasible point achieves a lower objective value. If this only holds within a local neighborhood of x^*, it is called a local optimum—a distinction that becomes particularly important when the problem is non-convex.

$$\min_{x \in X} \; f(x) \quad \text{s.t.} \quad g_i(x) = 0, \; i = 1, \ldots, n_g, \qquad h_j(x) \leq 0, \; j = 1, \ldots, n_h. \tag{3.22}$$

In the AC OPF, the optimization variables x at each bus i collect the phase angle θ_i, the voltage magnitude v_i, and the generated active and reactive power P_i^G and Q_i^G. The objective function typically represents the total generation cost, expressed as a linear or quadratic function of the active power outputs:

$$f(x^G) = \sum_{k \in \mathcal{G}} \left(a_k (P_k^G)^2 + b_k P_k^G + c_k \right), \tag{3.23}$$

where $\mathcal{G}$ is the set of generator buses and $a_k, b_k, c_k \geq 0$ are cost coefficients. The equality constraints of the OPF are precisely the power flow equations (2.33)–(2.34), which enforce that Kirchhoff's laws are satisfied at every bus. They ensure that the chosen generation schedule is physically realizable. On top of that, the inequality constraints capture the operational limits of the system. Voltage magnitudes must stay within acceptable bounds $\underline{v}_k \leq v_k \leq \bar{v}_k$, generator outputs are bounded between a minimum and maximum value $\underline{P}_k \leq P_k^G \leq \bar{P}_k$, and the apparent power flow on each transmission line (k, l) must not exceed its thermal capacity $|s_{kl}|$:

$$P_{kl}^2 + Q_{kl}^2 \leq |s_{kl}|^2. \tag{3.24}$$

A key challenge when solving the AC OPF is that the power flow equations contain trigonometric and bilinear terms, which make the feasible set non-convex. This means that a locally optimal solution found by a numerical solver is not necessarily globally optimal. In energy systems, convexity is almost never guaranteed, so care must be taken when interpreting the results of OPF solvers.
Note also that this represents a mathematically optimal solution. In practice, when selecting power plants for redispatch, energy market factors must again be taken into account to determine which plants should provide additional generation and which should reduce output.

3.4.1. Used Power Flow Model in DIgSILENT Power Factory

The power flow analysis described in the preceding sections relies on a static representation of the network. To capture the dynamic behaviour arising from generation outages, load

imbalances, or switching events, a transient-dynamic Root-Mean-Square (RMS) simulation model is employed. (U. Kühnapfel and Hagenmeyer, 2025) The model used in this work was developed at the Institute for Automation and Applied Informatics (IAI) at the Karlsruhe Institute of Technology (KIT) within the framework of the Kopernikus-ENSURE project (U. G. Kühnapfel, 2025). It is implemented in the DIgSILENT PowerFactory and covers the synchronous interconnected transmission network of Continental Europe (ENTSO-E CE region), incorporating data from the Ten-Year Network Development Plan (TYNDP 2018/2028) as well as planned grid extensions such as NordLink and additional generation units from the German Network Development Plan (NEP) up to 2037. The model encompasses more than 461 700 individual network elements and includes 654 power plants equipped with dynamic controllers representing four primary generation technologies: nuclear, conventional thermal, gas turbine, and hydroelectric. These controllers implement frequency and voltage regulation in accordance with the reserve hierarchy, covering frequency containment reserves (FCR) and frequency restoration reserves (FRR), thereby enabling realistic simulation of inertia-driven transients and inter-area oscillations.

To allow integrated studies across all voltage levels, the transmission model is vertically coupled with distribution grid sub-models. The 110 kV overlay network covering all four German transmission control zones has been fully implemented, structured according to the respective TSO zones and georeferenced using administrative boundaries. Renewable generation units are aggregated and assigned to the corresponding network nodes, while load profiles are derived from population statistics. At the sub-transmission and distribution level, medium-voltage (10/20 kV) and low-voltage (0.4 kV) grid models are coupled to the 110 kV layer via boundary transformers, covering both urban residential areas and industrial supply zones. This hierarchical, multi-voltage model structure enables the simulation of phenomena that span voltage levels, such as the propagation of frequency deviations from the transmission grid into distribution networks, or the collective impact of distributed renewable generation on transmission-level power flows.

3.4.2. Power Flow Analysis with climate data and energy market progression inputs

One objective of this study is to develop a workflow that links climate models such as ICON-SmART and agent-based energy market models such as PowerACE in order to perform a power flow analysis using all pre-calculated results. Summarising the state of the data after a successful climate simulation and energy market simulation: on the one hand, a dataset of hourly modelled climate variables at a global kilometre-scale resolution is available; on the other hand, hourly information on spot market prices and power plant dispatches have been computed, aggregated for each pre-selected country. The goal is now to map the PowerACE results onto nodes compatible with the transient-dynamic Root-Mean-Square (RMS) simulation model in DIgSILENT PowerFactory. To model a particular time step in PowerFactory, profiles for load, renewable generation (broken down into photovoltaic and wind energy), and conventional generation (broken down into gas, hard coal, lignite, nuclear, and oil) are required for each node and time step.

In this study, the load data are aggregated over node regions of the Institute for Industrial Production (IIP), a member institute of the Karlsruhe Institute of Technology (KIT). The key to connecting PowerACE with PowerFactory is to scale these loads such that the sum of all loads in node regions belonging to a given country matches the total load simulated by PowerACE for that country. All conventional power plant generation values, which are georeferenced in PowerACE, must also be assigned to the IIP nodes. Renewable generation can be calculated from the ICON-SmART output via *atlite*. Once every necessary dataset has been mapped onto the IIP nodes using a nearest-neighbour method in a dedicated script, all values can be transferred from the IIP node regions to the nodes used in PowerFactory. The residual load – defined as the load minus renewable generation – is then computed for each node. After the data have been correctly mapped, the power flow model can be applied to display the calculated dispatch.
In the following details are given how the IIP nodes are defined, how the load data is calculated for every of these node regions - both examined in the study of (Slednev, 2024) - and how the calculation of the renewable generation can be managed.

3.4.2.1. Definition of IIP nodes

The approach draws on OpenStreetMap (OSM) data to approximate the topology of the underlying 110 kV high-voltage distribution grid, a methodology established in earlier work by Slednev et al. (2017). While OSM coverage is available across the entire model region, data quality varies considerably by country. The extracted distribution grid topology is sufficiently detailed to support DC optimal power flow (DC-OPF) computations at least within central and western European countries. In the present model, however, only the graph structure of this distribution grid is used, rather than its electrical parameters, with the sole purpose of delineating supply areas for the transmission grid nodes. Concretely, supply areas are determined by constructing so called Voronoi polygons over the nodes of the high- and partially medium-voltage distribution grid. Each distribution node is then assigned to the nearest substation at which a transformation to the extra-high voltage transmission level takes place. As a result, every electricity-consuming or electricity-generating process in the model can be allocated to a specific node of the transmission network based on its geographic location. The boundaries between adjacent polygons are therefore drawn exactly halfway between neighboring nodes, meaning that the resulting regions are entirely determined by the spatial configuration of the underlying grid topology. Applied to a map, this produces a mosaic of non-overlapping polygons that together cover the entire model region without gaps. The resulting supply areas therefore reflect the actual underlying grid topology rather than administrative boundaries.

3.4.2.2. Load data

The approach for computing energy demand data is built around a clear conceptual distinction: Rather than estimating time series of energy carrier-specific final energy demand (FED) directly, the methodology first derives an energy carrier-agnostic useful energy demand

(UED) for heating and cooling applications, and then, in a second step, calculates FED values for individual energy carriers based on conversion efficiencies. This separation allows the model to endogenously optimize the choice of conversion technology — for example, switching from a gas boiler to a heat pump — while keeping the underlying thermal demand fixed. The starting point for the regional demand computation is a complete national energy balance for a historic reference year (currently 2019), supplemented by external scenario frameworks such as the TYNDP or the World Energy Outlook. Heating and cooling demands are given special attention: At a spatial resolution of 100 m, raster data on heated and cooled floor areas (drawn from the hotmaps database) are combined with national building statistics on age- and type-specific energy intensities as well as NUTS(Nomenclature of Territoral Units for Statistics) 3-level (referring tot regional Unities like cities) dwelling statistics from Census 2011. Since various statistical datasets are typically inconsistent with one another, a series of quadratic optimization problems is solved to reconcile population counts and energy quantities across hierarchical spatial levels — first at NUTS 3, then at the 100 m pixel level — while ensuring that national totals are matched exactly. Once the spatially resolved UED is established, the corresponding FED values for all modelled energy carriers are derived by accounting for local infrastructure availability (e.g., gas grid access) and technology-specific efficiencies. For heat pump-based processes, hourly temperature-dependent coefficients of performance (COPs) are computed for each weather event; for conventional boilers, static efficiency values from the JRC-IDEES database (*JRC Data Catalogue - Collection - European Commission* 2026) are applied. District heating supply is addressed through a layout optimization at high spatial resolution that considers existing and potential heat sources such as combined heat and power (CHP) plants. For the industrial sector, large heat consumers (e.g., from the chemical or paper industries) are modelled individually using plant-level data from the hotmaps database and the EU Emissions Trading System (ETS), while the residual industrial demand is distributed via downscaled GDP rasters and NUTS 2-level (referring to larger regional unities) employment statistics. Sectors such as transport, agriculture, and the energy sector are regionalized using infrastructure-related proxies (e.g., road and rail lengths, freight volumes, registered vehicles) or biological indicators (e.g., manure and crop residue potentials). Non-heating-related electricity demand in the residential and tertiary sectors, covering appliances, lighting, and similar end uses, is approximated using population and floor area distributions at 100 m resolution.

3.4.2.3. Calculation of renewable generation per IIP region node

The renewable generation can be calculated directly with atlite (see section 3.2.3). For that, the shape-files of every IIP node region are needed, in order to cut the climate dataset in a way spatially, that only the grid cells located in a certain node domain are considered. By using a dataset of the installed renewable capacity as additional inputs, iteratively the renewable energy yield can then be calculated for every node region. The data of the installed capacity is obtained by global-solar-power-tracker.org, an open-source platform for worldwide energy data, in case of renewable energy with data of installed capacity on site scale.

3.4.2.4. Spatial Matching of IAI and IIP Substation Datasets

To integrate substation-level attributes from the two European power system datasets of IIP and IAI, a nearest-neighbor spatial matching procedure is applied. Both datasets describe high-voltage substations across continental Europe but differ in their spatial resolution, coverage, and the attributes they provide. The matching enables the combination of generation and load capacities available in the IIP dataset with the detailed grid topology encoded in the IAI dataset.

The matching itself is performed as a bidirectional nearest-neighbor spatial join, executed separately for each country to avoid cross-border mismatches. For every substation in the IAI dataset, the geographically closest substation in the IIP dataset is identified, and vice versa. To limit erroneous long-distance assignments, a maximum matching radius of 100 km is enforced; substation pairs exceeding this threshold are discarded. The script yields a list of every IAI substation node with the resulting residual load.

4. Results and Analysis

This chapter presents the evolution of meteorological variables that are relevant for renewable energy systems like wind speed, solar irradiance and surface near dust concentrations temporally and spatially, simulated with ICON-SmART. Based on the calculated capacity factors (see Section 3.2.2), several case studies are carried out to investigate meteorological situations that may lead to challenging conditions for regional energy transmission and the ability to meet energy demand. Also the resulting energy market circumstances, simulated with PowerACE, are presented. A focus is put here on the evolving energy mix and the role of renewable energies. The results of the workflow connecting the climate model ICON-SmART, the energy market model PowerACE, and the power flow model PowerFactory are presented afterwards. After presenting and describing these results, the evolutions are discussed and limitations, potential challenges as well as areas for further research are pointed out.

4.1. Spatio-Temporal Climate Characteristics Shaping Future Energy Systems

This section directly addresses one of the central questions of this study: how meteorological fields will evolve temporally and spatially under a changing climate. In this section, meteorological fields relevant to the renewable energy sources wind power and photovoltaic, simulated with ICON-SmART, are described. First, the raw climate data are analysed across different European climate zones to identify spatially dependent trends. In a second part, several case studies of characteristic atmospheric conditions are conducted to examine specific energy-system-relevant patterns and their future evolution. For this analysis, the Regional Tracking System developed during this study is applied, together with capacity factor fields calculated using the Python library *atlite* and ICON raw output as input data.

4.1.1. Evolution of climate characteristics in European climate zones

In this section, the anomalies obtained from the detrended ICON-SmART simulations are analyzed and used to compare the different scenarios. In every timeseries bright colours indicate the mean values and darker colours representing the associated linear trends.
As an introduction into this section, in figure 4.1 the global mean detrended temperature

evolution until 2049 is shown. Here, the expected increase in temperature can be noted, with the highest increase for SSP5-8.5, then SSP2-4.5 and lastly for the Present-day scenario.

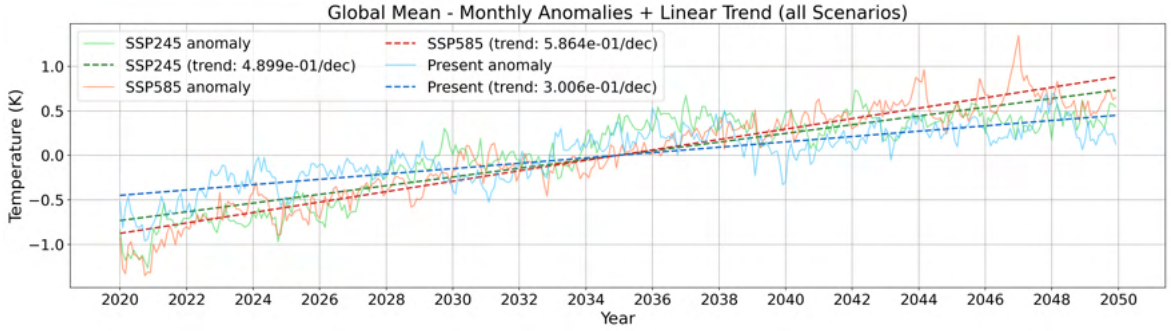

Figure 4.1.: Global mean temperature (K) from 2020 to 2049, considering the scenarios SSP2-4.5, SSP5-8.5 and Present-day.

For all variables, detrended time series with monthly and annual means are used to display the simulation results, potential trends, and their statistical significance. Trends for the 5-year mean are also shown. In a respective table of the section all results are summarized. For the wind vector, probability density functions (PDFs) are also presented, as these are a common approach for characterising wind conditions at a given site. To distinguish between different regions, several climate zones are defined, following the classification of Schneider et al. (2013). Note that for simplification reasons this classification is approximated into square regions. The defined zones are summarised in table 4.1 and displayed on the map in figure 4.2.

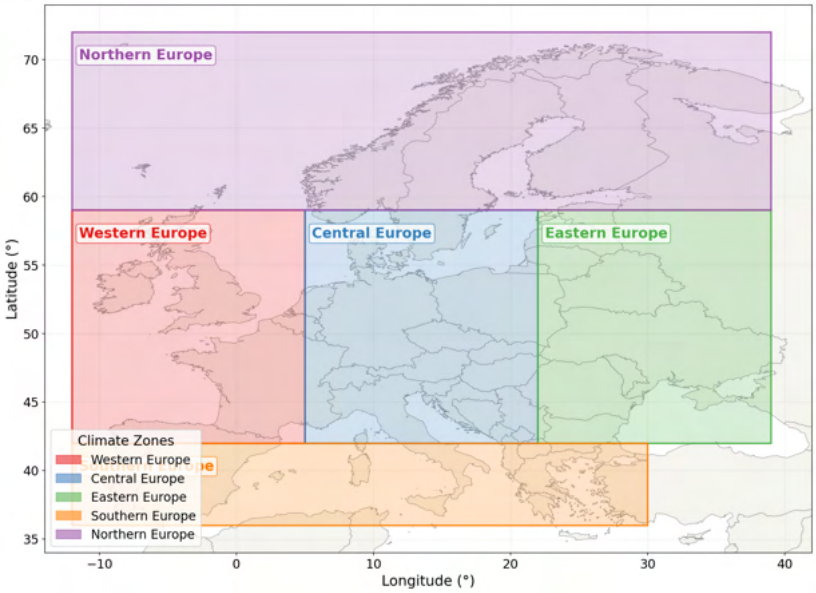

Figure 4.2.: Map of defined climate zones for this study, based on classification of Schneider et al. (2013).

Table 4.1.: Defined climate zones for this study, following the classification of Schneider et al. (2013).

Region	Lat_{min}	Lat_{max}	Lon_{min}	Lon_{max}
Western Europe	42°N	59°N	12°W	5°E
Central Europe	42°N	59°N	5°E	22°E
Eastern Europe	42°N	59°N	22°E	39°E
Southern Europe	36°N	42°N	12°W	30°E
Northern Europe	59°N	72°N	12°W	39°E

4.1.1.1. 10 m Wind Speed

In the following, the 10 m wind speed is analyzed, first the global mean is shown, european means of the depicted european zones afterwards. For the 10 m wind speed global mean (see figure 4.3), all three scenarios display pronounced interannual variability throughout the 2020–2049 period, with monthly anomalies ranging approximately from −0.35 to +0.25 m s^{-1}. The SSP2-4.5 scenario exhibits the strongest negative linear trend (-1.460×10^{-2} m s^{-1} decade^{-1}), while SSP5-8.5 and the Present-day simulation show comparatively weak negative trends (-2.875×10^{-3} and -2.238×10^{-3} m s^{-1} decade^{-1}, respectively). Overall, the linear trends of SSP5-8.5 and Present-day scenarios remain close to zero, indicating no substantial long-term change in global mean wind speed over the period. SSP2-4.5 shows a slightly stronger negative trend.

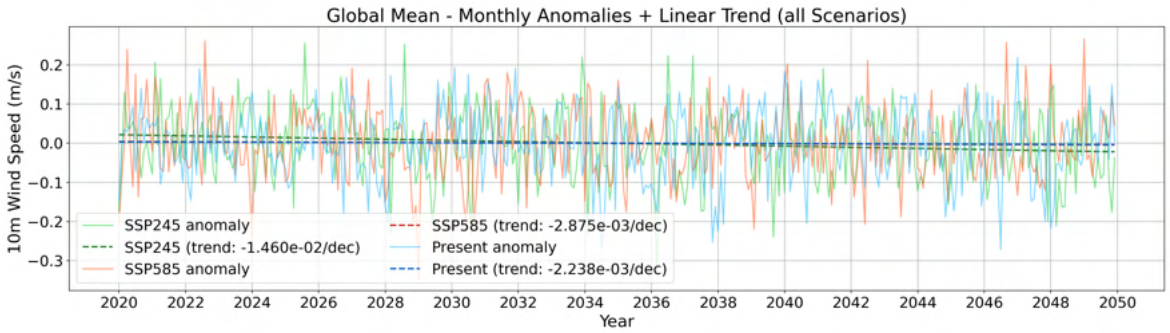

Figure 4.3.: Global mean monthly anomalies of 10 m wind speed (m s^{-1}) for the three model scenarios (SSP2-4.5, SSP5-8.5, Present-day), covering the period 2020–2049.

Figure 4.4 shows the monthly mean evolution for each defined climate zone in Europe. In addition, annual means and 5-year running means were calculated for each region. The trends for all time series, including averaged values and their significance analysis, are summarized in Table 4.2. Furthermore, Probability Density Functions (PDFs) for all regions are shown in Figure 4.5, with wind speed on the x-axis and probability density on the y-axis. All averaged detrended timeseries (e.g. Figs. 4.4 as well as PDFs 4.5) reveal substantial differences in climatological wind speed between regions. In the PDFs (Fig. 4.5), Northern Europe and western Europe have the highest wind speeds, southern, central and eastern Europe are progressively calmer. They are which are unimodal and right-skewed across all

regions, consistent with a Weibull-type distribution shape. The full-period PDFs of SSP2-4.5, SSP5-8.5, and Present-day largely overlap in every region, indicating that the overall wind speed distribution is not strongly scenario-dependent when averaged over the full 30-year period.

In western Europe, inter-annual variability in wind speed is the largest of all five regions: Monthly mean anomalies (Fig. 4.4a) frequently exceed $\pm 1\,\mathrm{m\,s^{-1}}$, with isolated months reaching ± 2–$2.5\,\mathrm{m\,s^{-1}}$. Against this background of high variability, the linear trend signals are small. At the monthly level, SSP2-4.5 and SSP5-8.5 are weakly negative (-6.6×10^{-3} and $-4.2 \times 10^{-2}\,\mathrm{m\,s^{-1}\,yr^{-1}}$, respectively) while Present-day is slightly positive ($+1.1 \times 10^{-2}\,\mathrm{m\,s^{-1}\,yr^{-1}}$); the monthly trend magnitudes are consistent with these annual estimates. The 5-year rolling means (Fig. A.2a) make the scenario behavior clearer: SSP5-8.5 starts above SSP2-4.5 around 2020 but declines throughout the period ($-5.5 \times 10^{-2}\,\mathrm{m\,s^{-1}\,yr^{-1}}$), converging towards the more slowly declining SSP2-4.5 by the 2040s, while Present-day rises weakly ($+2.8 \times 10^{-2}\,\mathrm{m\,s^{-1}\,yr^{-1}}$). The full-period PDF (Fig. 4.5a) peaks near $5\,\mathrm{m\,s^{-1}}$ with a maximum density of approximately 0.23 and extends to roughly $16\,\mathrm{m\,s^{-1}}$; the three scenario curves are nearly coincident. The PDF difference (Fig. not shown) shows a positive feature near $4\,\mathrm{m\,s^{-1}}$ and a compensating negative region near 5.5–$6\,\mathrm{m\,s^{-1}}$ for SSP2-4.5 and Present-day, suggesting a slight shift of probability mass towards lower wind speeds from the 2020s to the 2040s; SSP5-8.5 exhibits a stronger positive peak near $5\,\mathrm{m\,s^{-1}}$, indicating a different redistribution pattern.

Southern Europe shows the smallest wind speed anomaly amplitudes among all five regions. Monthly anomalies (Fig. 4.4b) rarely exceed $\pm 1\,\mathrm{m\,s^{-1}}$. The scenario trends at the annual level (Fig. A.1b) are of opposite sign: SSP2-4.5 is weakly positive ($+3.5 \times 10^{-2}\,\mathrm{m\,s^{-1}\,yr^{-1}}$) while SSP5-8.5 is weakly negative ($-3.8 \times 10^{-2}\,\mathrm{m\,s^{-1}\,yr^{-1}}$). This divergence is confirmed in the rolling means (Fig. not shown), where SSP5-8.5 starts above SSP2-4.5 around 2020 and declines, while SSP2-4.5 increases, resulting in the two means crossing around 2030–2035. Present-day remains nearly flat throughout. The full-period PDF (Fig. 4.5b) is narrower than in other regions, peaked near 3–$3.5\,\mathrm{m\,s^{-1}}$ with a maximum density of 0.40–0.41. SSP2-4.5 and SSP5-8.5 show a marginally higher peak than Present-day, indicative of a slight concentration of probability at lower speeds under the high-radiative forcing scenario. The PDF difference (Fig. not shown) shows the largest amplitudes of all regions: SSP5-8.5 exhibits a strong positive feature near $3\,\mathrm{m\,s^{-1}}$ and a pronounced negative trough between 4 and $5\,\mathrm{m\,s^{-1}}$, consistent with a shift towards lower wind speeds in the 2040s under this scenario, while SSP2-4.5 shows a positive peak near $5\,\mathrm{m\,s^{-1}}$, in line with its positive annual trend.

Northern Europe features the largest scenario divergence among all regions for wind speed. The monthly anomaly time series (Fig. 4.4c) shows variability up to $\pm 2\,\mathrm{m\,s^{-1}}$ with a notable spread between scenario curves. The monthly trend under SSP2-4.5 is clearly negative ($-6.4 \times 10^{-2}\,\mathrm{m\,s^{-1}\,yr^{-1}}$), while SSP5-8.5 is weakly positive ($+2.9 \times 10^{-2}\,\mathrm{m\,s^{-1}\,yr^{-1}}$); the monthly trends are consistent with these values. In the 5-year rolling means (Fig. A.2c), SSP2-4.5 declines persistently while SSP5-8.5 rises. The full-period PDF (Fig. 4.5c) peaks near 4.5–$5\,\mathrm{m\,s^{-1}}$ with a density of 0.27–0.28; the Present-day curve shows a slightly higher peak than SSP2-4.5 and SSP5-8.5. The PDF difference (Fig. not shown) reveals the most

pronounced decadal change under SSP2-4.5, with a strong positive peak near 4.5–5 $\mathrm{m\,s^{-1}}$ and a compensating negative region between 6 and 9 $\mathrm{m\,s^{-1}}$, indicating that the distribution narrows and shifts downward, with moderate-speed events becoming more frequent at the expense of stronger ones. SSP5-8.5 and Pr show smaller, more irregular differences.

Central Europe presents a consistent picture across all temporal representations. Monthly anomalies (Fig. 4.4d) remain within approximately $\pm 1.2\,\mathrm{m\,s^{-1}}$. The monthly trend lines are under SSP2-4.5 negative ($-1.5 \times 10^{-2}\,\mathrm{m\,s^{-1}\,yr^{-1}}$), while Present-day is weakly positive ($+2.4 \times 10^{-2}\,\mathrm{m\,s^{-1}\,yr^{-1}}$), SSP5-8.5 has a quite negligible trend. The rolling means (Fig. A.2d) oscillate within a narrow band ($\sim$ 2.3–2.6 $\mathrm{m\,s^{-1}}$) without pronounced directional change or scenario separation. The full-period PDF (Fig. 4.5d) is the one of tthe narrowest, with a maximum near 3 $\mathrm{m\,s^{-1}}$ at a density of 0.37–0.38; the three scenario curves are nearly indistinguishable. In the PDF difference (Fig. not shown), SSP2-4.5 and SSP5-8.5 both show an increase in probability near 1.5–2 $\mathrm{m\,s^{-1}}$ and a decrease near 3 $\mathrm{m\,s^{-1}}$, indicating a shift towards the lower tail of the distribution from the 2020s to the 2040s, while Present-day shows a broadly similar but lower-amplitude pattern.

Eastern Europe stands out for its strong scenario dependence of its decadal wind speed evolution. Annual anomalies (Fig. A.1e) rarely exceed $\pm 0.2\,\mathrm{m\,s^{-1}}$, and monthly anomalies (Fig. 4.4e) remain within $\pm 0.75\,\mathrm{m\,s^{-1}}$. Despite the low variability, the scenario trends diverge clearly: SSP2-4.5 shows a moderately negative annual trend ($-5.2 \times 10^{-2}\,\mathrm{m\,s^{-1}\,yr^{-1}}$), confirmed in the monthly analysis ($-5.1 \times 10^{-2}\,\mathrm{m\,s^{-1}\,yr^{-1}}$), while SSP5-8.5 and Present-day are near trend-neutral at both timescales. In the 5-year rolling means (Fig. A.2e), SSP2-4.5 declines persistently and clearly separates from the essentially flat SSP5-8.5 and Present-day means from around 2035 onward, with the separation continuing to grow through the end of the period. The full-period PDF (Fig. 4.5e) has the highest peak density of all regions ($\sim$ 0.46–0.48) near 2.5–3 $\mathrm{m\,s^{-1}}$; the SSP2-4.5 curve shows a slightly higher and narrower peak than the other two scenarios. The PDF difference (Fig. not shown) shows that SSP5-8.5 has the largest amplitude differences, with alternating positive and negative features between 1.5 and 4 $\mathrm{m\,s^{-1}}$; all scenarios converge to near-zero differences beyond approximately 5 $\mathrm{m\,s^{-1}}$, indicating that decadal changes are confined to the core of the distribution.

Table 4.2 summarises the linear trends across the European sub-regions. The most statistically significant signal in the entire dataset is found in Eastern Europe under SSP2-4.5, where a consistent negative trend is detected across all three temporal aggregations: at monthly resolution $p < 0.01$ and $p_{\mathrm{MK}} < 0.01$ (with p^* also significant at < 0.01), at annual resolution $p < 0.01$ and $p_{\mathrm{MK}} < 0.05$, and at the 5-year level all three tests agree at $p < 0.01$. The absence of any comparable signal under SSP5-8.5 and in the Present-day run points to a forcing-specific dynamical response confined to the moderate emissions pathway. Northern Europe under SSP2-4.5 shows a marginally significant negative trend at annual resolution ($p^* < 0.05$, $p_{\mathrm{MK}} < 0.10$), which strengthens at the 5-year level ($p < 0.01$, $p_{\mathrm{MK}} < 0.01$), suggesting a low but consistent wind speed decline under moderate future forcing. A physically noteworthy feature is found in Southern Europe, where the trend signs are opposite between scenarios at 5-year resolution: SSP2-4.5 yields a significant positive trend ($p < 0.01$, $p_{\mathrm{MK}} < 0.01$) while SSP5-8.5 produces a comparably significant negative trend ($p < 0.01$, $p_{\mathrm{MK}} < 0.01$). This scenario divergence in both sign and significance warrants

further investigation in the context of scenario-dependent large-scale circulation changes. The trends of Western and Central Europe are largely non-significant, with only isolated signals at the 5-year level that do not survive the AR1 correction (p^*), and should therefore be interpreted with caution.

Table 4.2.: Wind Speed trends per region, temporal average and scenario. Slope in $\mathrm{m\,s^{-1}}\ yr^{-1}$.p: $rawp - value$–p*: AR1-corrected p-value (Santer et al. 2000) - p_{MK}: Mann-Kendall p-value.

Region	Average	Scenario	Slope/yr	p	p^*	p_{MK}
Western	Monthly	SSP2-4.5	-6.65e-03	0.8720	0.9002	0.9584
		SSP5-8.5	-4.24e-02	0.2979	0.3809	0.3613
		Present-day	1.06e-02	0.8019	0.8496	0.8743
	Yearly	SSP2-4.5	-4.35e-03	0.9351	0.9297	0.8584
		SSP5-8.5	-4.30e-02	0.3472	0.3844	0.1751
		Present-day	1.76e-02	0.7303	0.6778	0.6174
	5-year	SSP2-4.5	-1.54e-03	0.4810	0.9029	0.4537
		SSP5-8.5	-5.54e-02	0.0025	0.3329	0.0031
		Present-day	2.78e-02	0.0847	0.4379	0.1435
Central	Monthly	SSP2-4.5	-1.53e-02	0.5455	0.6425	0.3467
		SSP5-8.5	-4.90e-05	0.9982	0.9984	0.8017
		Present-day	2.37e-02	0.3448	0.4484	0.2310
	Yearly	SSP2-4.5	-1.68e-02	0.6095	0.6251	0.4978
		SSP5-8.5	-1.67e-03	0.9438	0.9396	0.9148
		Present-day	2.79e-02	0.2653	0.1876	0.3008
	5-year	SSP2-4.5	-2.54e-02	0.0862	0.7936	0.1751
		SSP5-8.5	-6.12e-03	0.5516	0.8824	0.5207
		Present-day	2.93e-02	0.0026	0.3817	0.0092
Eastern	Monthly	SSP24-4.5	-5.06e-02	0.0013	0.0053	0.0004
		SSP5-8.5	2.54e-03	0.8761	0.8802	0.9633
		Present-day	-6.01e-03	0.7221	0.7477	0.8646
	Yearly	SSP2-4.5	-5.15e-02	0.0062	0.0000	0.0204
		SSP5-8.5	1.09e-03	0.9505	0.9363	0.6947
		Present-day	-4.39e-03	0.7933	0.7723	0.7212
	5-year	SSP2-4.5	-5.08e-02	0.0000	0.0000	0.0000
		SSP5-8.5	-3.72e-03	0.4417	0.6743	0.2535
		Present-day	-4.73e-03	0.5304	0.8995	0.5207
Southern	Monthly	SSP2-4.5	3.50e-02	0.0780	0.1009	0.0952
		SSP5-8.5	-3.67e-02	0.1027	0.1337	0.0705
		Present-day	6.81e-03	0.7346	0.7459	0.5456
	Yearly	SSP2-4.5	3.56e-02	0.0842	0.0632	0.1989
		SSP5-8.5	-3.79e-02	0.1637	0.1463	0.1249
		Present-day	6.38e-03	0.6435	0.5662	0.8305
	5-year	SSP2-4.5	3.63e-02	0.0002	0.3011	0.0009
		SSP5-8.5	-3.50e-02	0.0017	0.3365	0.0022
		Present-day	6.13e-03	0.0502	0.2744	0.1640
Northern	Monthly	SSP2-4.5	-6.43e-02	0.0723	0.1316	0.2105
		SSP5-8.5	2.96e-02	0.3501	0.3715	0.5685
		Present	-3.71e-02	0.2347	0.2896	0.1834
	Yearly	SSP2-4.5	-6.80e-02	0.1312	0.0155	0.0540
		SSP5-8.5	2.78e-02	0.4696	0.4845	0.5207
		Present-day	-2.75e-02	0.4240	0.3941	0.2844
	5-year	SSP2-4.5	-5.89e-02	0.0003	0.2910	0.0001
		SSP5-8.5	2.24e-02	0.1251	0.5768	0.0688
		Present-day	-2.45e-02	0.0520	0.4854	0.1249

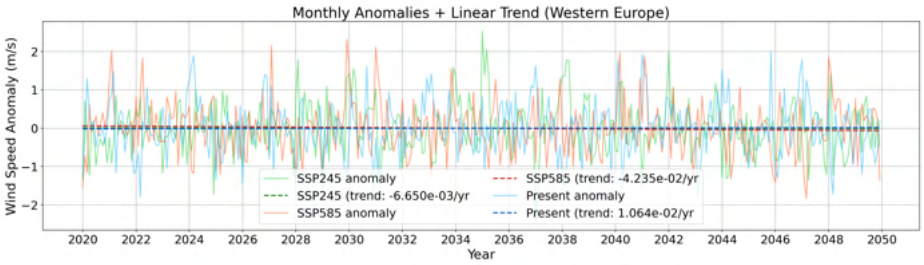

(a) Western Europe

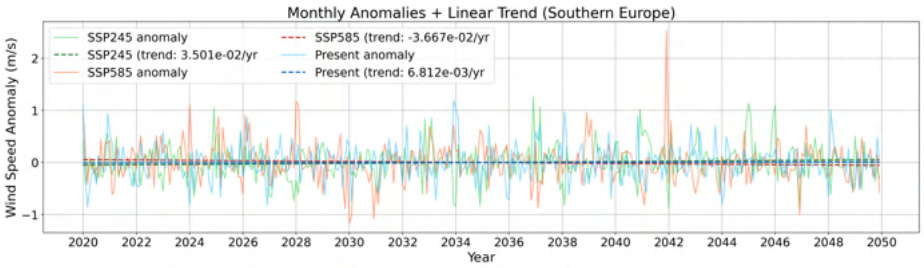

(b) Southern Europe

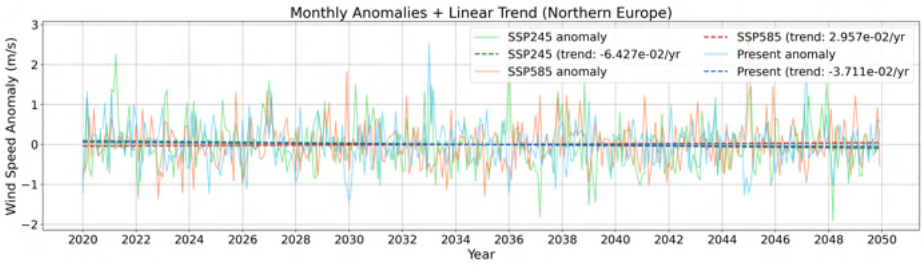

(c) Northern Europe

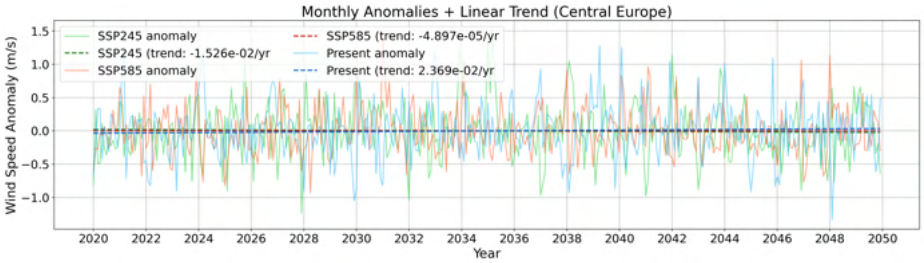

(d) Central Europe

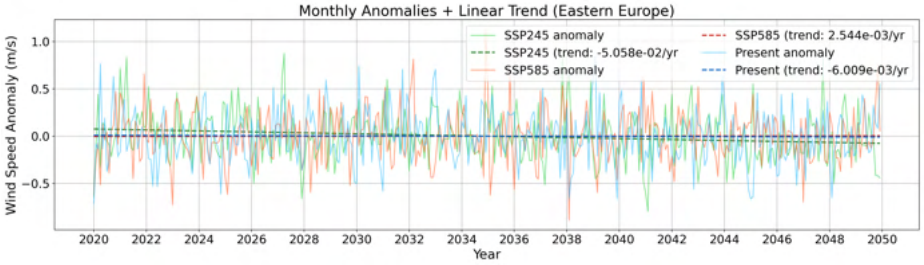

(e) Eastern Europe

Figure 4.4.: Monthly anomalies and linear trends of 10 m wind speed ($m\,s^{-1}$) in different climate zones, 2020–2050.

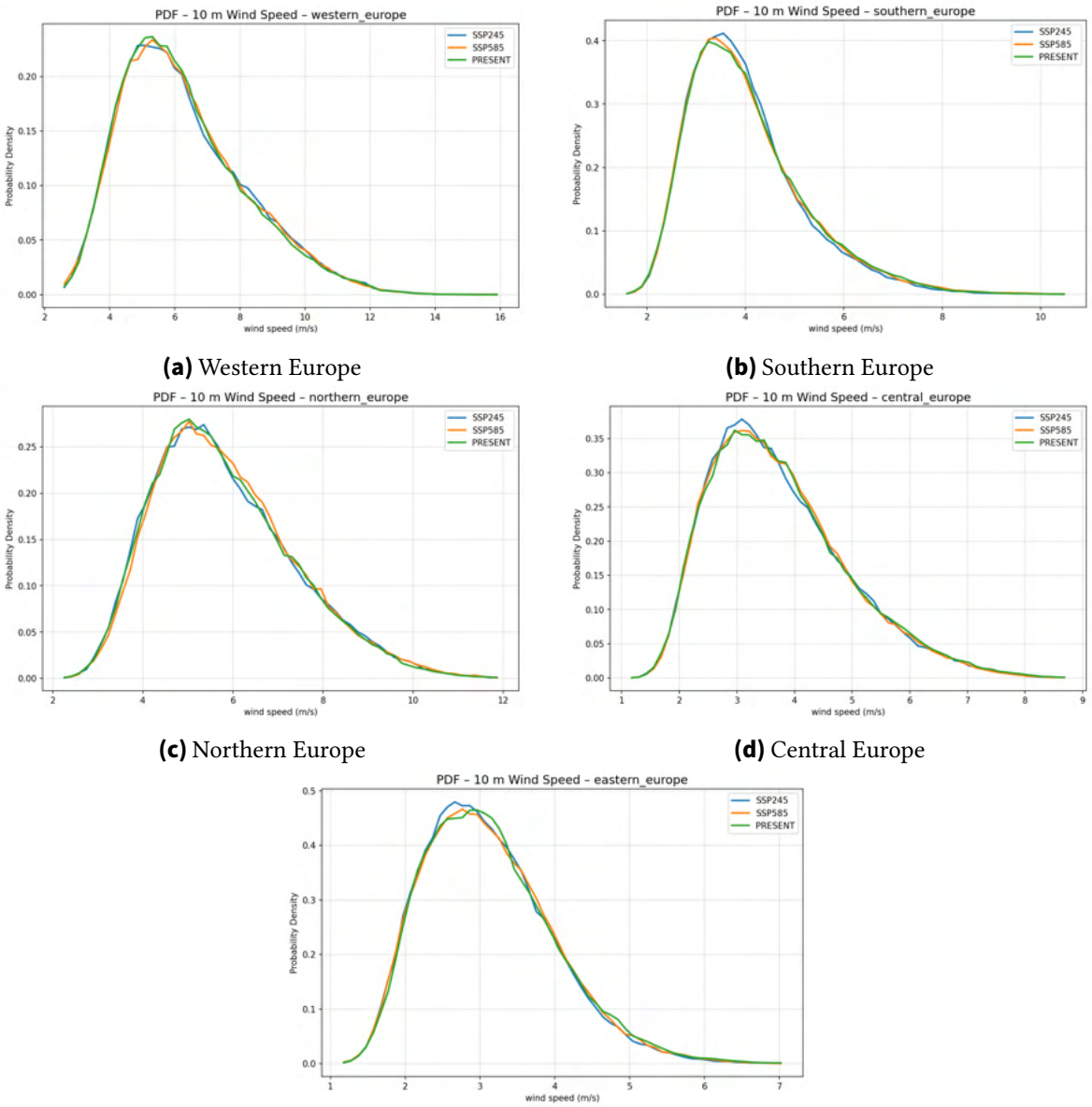

(a) Western Europe

(b) Southern Europe

(c) Northern Europe

(d) Central Europe

(e) Eastern Europe

Figure 4.5.: density functions of 10 m wind speed in different climate zones, 2020–2049.

4.1.1.2. Shortwave Irradiance

In the following, shortwave irradiance is examined, first the global mean, afterwards the regional means of the european zones. For the global mean shortwave irradiance (see figure 4.6), all three scenarios display pronounced interannual variability throughout the 2020–2049 period, with monthly anomalies ranging approximately from −3 to +2 $\mathrm{W\,m^{-2}}$. The SSP5-8.5 scenario exhibits the strongest negative linear trend ($-3.540 \times 10^{-1}\,\mathrm{W\,m^{-2}\,decade^{-1}}$), while SSP2-4.5 shows a comparatively weak negative trend ($-8.845 \times 10^{-2}\,\mathrm{W\,m^{-2}\,decade^{-1}}$). In contrast, the Present-day simulation yields a slightly positive

trend ($+1.658 \times 10^{-1}$ W m^{-2} decade^{-1}), resulting in a divergence between the scenario and Present-day trajectories that becomes more pronounced towards the end of the period.

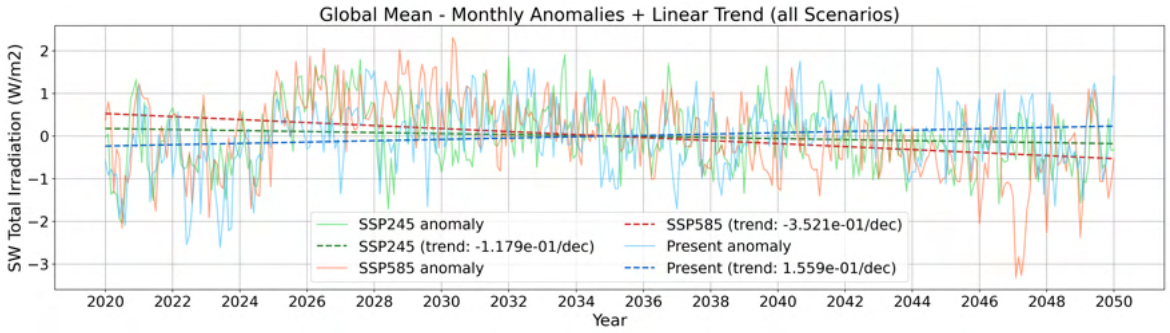

Figure 4.6.: Global mean monthly anomalies of total short-wave irradiation at the surface (W m^{-2}) for three model scenarios (SSP2-4.5, SSP5-8.5, Present-day), covering the period 2020–2049.

Figure 4.7 presents the monthly mean evolution for each defined climate zone in Europe. Furthermore, annual means and 5-year running means were computed for each region. The trends of all time series, together with the corresponding averaged values and significance analyses, are listed in Table 4.3. The figures illustrating the annual and 5-year means are included in the Appendix (see Figure A.3 and A.4).

When examining the incoming shortwave irradiance regionally, it exhibits pronounced latitudinal gradients in its climatological mean. The 5-year rolling means (Fig. A.4) confirm that southern Europe receives the highest annual mean irradiance ($\sim$ 192–200 W m^{-2}), followed by eastern ($\sim$ 142–148 W m^{-2}), central ($\sim$ 138–144 W m^{-2}), and western Europe ($\sim$ 132–137 W m^{-2}), with northern Europe at the low end ($\sim$ 93–97 W m^{-2}). Inter-annual and monthly variability in irradiance is large across all regions, reflecting the sensitivity of the variable to cloud cover and atmospheric composition. The scenario-dependent trend signals are more pronounced than for wind speed in several regions, and the rolling means make the long-term scenario divergence particularly visible.

In western Europe, the annual anomaly time series (Fig. A.3a) shows a clear divergence between SSP2-4.5 and the other two scenarios: SSP2-4.5 exhibits a distinctly negative trend (-6.8×10^{-1} W m^{-2} yr^{-1}) that pulls its anomaly curve towards increasingly negative values, while SSP5-8.5 is slightly positie ($+7.4 \times 10^{-2}$ W m^{-2} yr^{-1}) and as wll as Present-day ($+5.5 \times 10^{-1}$ W m^{-2} yr^{-1}). Individual annual anomalies reach up to ± 5 W m^{-2}. The monthly series (Fig. 4.7a) confirms this ordering, with monthly trend values consistent with the annual estimates. The three scenario curves diverge progressively from around 2035. In the rolling means (Fig. A.4a), this divergence becomes clearly visible: SSP2-4.5 declines from approximately 136 W m^{-2} in 2020 to below 134 W m^{-2} by the late 2040s, crossing below the nearly flat SSP5-8.5 mean around 2030, while Present-day rises to end as the highest of the three scenarios, producing a total spread of approximately 4 W m^{-2} by 2048.

Southern Europe is characterized by the largest irradiance anomaly amplitudes of all regions, with individual annual deviations exceeding ± 6 W m^{-2} (Fig. A.3b) and monthly

values reaching approximately $\pm 25\,\mathrm{W\,m^{-2}}$ (Fig. 4.7b). In contrast to western Europe, both future scenarios show positive trends here, with SSP5-8.5 exhibiting the stronger signal ($+1.2\,\mathrm{W\,m^{-2}\,yr^{-1}}$ annually; $+7.4 \times 10^{-2}\,\mathrm{W\,m^{-2}\,yr^{-1}}$ monthly) and SSP2-4.5 also positive ($+9.3 \times 10^{-1}$ and $+6.8 \times 10^{-2}\,\mathrm{W\,m^{-2}\,yr^{-1}}$, respectively). A gradual upward drift is discernible in the monthly curves in the second half of the record. The rolling means (Fig. A.4b) display an interesting crossover: SSP5-8.5 starts below SSP2-4.5 in 2020 but increases more rapidly, overtaking it around 2032, while Present-day shows the slowest increase and remains below both future scenarios throughout most of the period.

Northern Europe is the most scenario-insensitive region for shortwave irradiance. The annual anomaly series (Fig. A.3c) shows all three scenarios with weakly positive trends of comparable magnitude (SSP2-4.5: $+6.6 \times 10^{-1}$; SSP5-8.5: $+4.7 \times 10^{-1}$; Present-day: $+2.2 \times 10^{-1}\,\mathrm{W\,m^{-2}\,yr^{-1}}$), and the monthly curves (Fig. 4.7c) are largely overlapping throughout. Annual anomaly amplitudes are smaller than in southern regions ($\lesssim \pm 4\,\mathrm{W\,m^{-2}}$), and monthly values remain within roughly $\pm 10\,\mathrm{W\,m^{-2}}$. The rolling means (Fig. A.4c) confirm the broad agreement between scenarios, with all three means increasing at comparable rates; only the Present-day run shows larger decadal-scale fluctuations.

Central Europe exhibits the largest scenario divergence in shortwave irradiance of all regions. The annual anomaly series (Fig. A.3d) already shows the two SSP scenarios on clearly opposing trajectories — SSP2-4.5 strongly negative ($-1.4\,\mathrm{W\,m^{-2}\,yr^{-1}}$) and SSP5-8.5 weakly positive ($+3.5{\times}10^{-1}\,\mathrm{W\,m^{-2}\,yr^{-1}}$) — with year-to-year anomaly amplitudes frequently exceeding $\pm 6\,\mathrm{W\,m^{-2}}$. The monthly series (Fig. 4.7d) reinforces this picture, with trend values of -1.5 and $+2.7 \times 10^{-1}\,\mathrm{W\,m^{-2}\,yr^{-1}}$ for SSP2-4.5 and SSP5-8.5, respectively; monthly amplitudes frequently exceed $\pm 20\,\mathrm{W\,m^{-2}}$ and the two future scenario curves are visually separated in the second half of the record. In the rolling means (Fig. A.4d), the divergence is most striking: SSP2-4.5 declines from approximately $143\,\mathrm{W\,m^{-2}}$ in 2020 to below $138\,\mathrm{W\,m^{-2}}$ by the late 2040s ($-1.93\,\mathrm{W\,m^{-2}\,yr^{-1}}$), while SSP5-8.5 increases to approximately $141.5\,\mathrm{W\,m^{-2}}$ ($+5.0 \times 10^{-1}\,\mathrm{W\,m^{-2}\,yr^{-1}}$), resulting in a total separation of approximately $5\,\mathrm{W\,m^{-2}}$ between the two future scenarios by 2049.

Eastern Europe shares the pattern seen in central Europe but with even larger anomaly amplitudes. Individual annual anomalies reach up to $10\,\mathrm{W\,m^{-2}}$ (Fig. A.3e), making this the most variable region in terms of irradiance. At the annual level, SSP2-4.5 shows a clearly negative trend ($-1.6\,\mathrm{W\,m^{-2}\,yr^{-1}}$), while SSP5-8.5 is close to neutral ($-8.1 \times 10^{-2}\,\mathrm{W\,m^{-2}\,yr^{-1}}$) and Present-day is weakly positive ($+7.1 \times 10^{-1}\,\mathrm{W\,m^{-2}\,yr^{-1}}$). Monthly anomaly amplitudes exceed $\pm 20\,\mathrm{W\,m^{-2}}$ in individual months (Fig. 4.7e), and the monthly trend for SSP2-4.5 ($-1.8\,\mathrm{W\,m^{-2}\,yr^{-1}}$) is consistent with the annual estimate; the slight divergence between SSP2-4.5 and the other two scenarios is apparent in the monthly record from approximately 2035. The rolling means (Fig. A.4e) show SSP2-4.5 declining from approximately $147.5\,\mathrm{W\,m^{-2}}$ to $143\,\mathrm{W\,m^{-2}}$, while SSP5-8.5 remains near-neutral and Present-day increases.

Table 4.3 summarizes the linear trends in downwelling shortwave (SW) surface radiation across European sub-regions for the same scenarios and temporal aggregations as described above. The most consistent and statistically robust signal is found in Central Europe under SSP2-4.5, where a negative trend is detected across all three temporal aggregations. At monthly resolution, both p and p_{MK} are significant at the < 0.01 level, with p^* confirming

significance at < 0.05, demonstrating that the signal survives autocorrelation correction. The annual and 5-year means corroborate this finding ($p < 0.05$ and $p < 0.01$, respectively). Strikingly, the corresponding SSP5-8.5 trend in Central Europe is near-zero and non-significant throughout, implying a scenario-dependent radiative response that may be linked to differential aerosol emission trajectories between the two pathways. A similar pattern is seen in Eastern Europe under SSP2-4.5, where significant negative trends emerge at monthly ($p < 0.05$, $p^* < 0.10$, $p_{\mathrm{MK}} < 0.05$) and 5-year resolution ($p < 0.01$, $p_{\mathrm{MK}} < 0.01$), while SSP5-8.5 and Present-day remain largely non-significant. In Southern Europe, a positive trend is detected under SSP5-8.5 at monthly resolution ($p < 0.05$, $p_{\mathrm{MK}} < 0.05$).

Table 4.3.: SW Surface Radiation trends per region, temporal average and scenario. Slope in $\mathrm{W\,m^{-2}}\ yr^{-1}$.p= $rawp - value$;p* = AR1-corrected p-value (Santer et al. 2000); p_{MK} = Mann-Kendall p-value.

Region	Average	Scenario	Slope/yr	p	p^*	p_{MK}
Western	Monthly	SSP2-4.5	-6.83e-02	0.0883	0.1078	0.0981
		SSP5-8.5	7.39e-04	0.9912	0.9919	0.8984
		Present-day	5.58e-01	0.1828	0.1978	0.1132
	Yearly	SSP2-4.5	-4.01e-01	0.1322	0.0918	0.1010
		SSP5-8.5	1.22e-01	0.9488	0.9498	0.8073
		Present-day	6.59e-02	0.2029	0.0870	0.0878
	5-year	SSP2-4.5	-4.97e-01	0.0029	0.6349	0.0077
		SSP5-8.5	1.41e-01	0.9969	0.9990	0.9551
		Present-day	6.24e-01	0.0021	0.2930	0.0282
Central	Monthly	SSP2-4.5	-1.57e-00	0.0029	0.0151	0.0046
		SSP5-8.5	2.72e-02	0.3895	0.4724	0.5841
		Present-day	2.24e-02	0.4190	0.5057	0.5860
	Yearly	SSP2-4.5	-1.36e-00	0.0314	0.0437	0.0505
		SSP5-8.5	3.52e-01	0.5664	0.6349	0.7784
		Present-day	3.52e-01	0.3795	0.3668	0.3201
	5-year	SSP2-4.5	-1.38e-00	0.0000	0.1817	0.0000
		SSP5-8.5	3.30e-01	0.1686	0.8251	0.0688
		Present-day	4.00e-01	0.0303	0.6332	0.2525
Eastern	Monthly	SSP2-4.5	-1.81e-01	0.0137	0.0844	0.0133
		SSP5-8.5	-6.08e-02	0.6136	0.6977	0.6168
		Present-day	5.74e-01	0.3062	0.3814	0.2215
	Yearly	SSP2-4.5	-1.56e-00	0.0972	0.0707	0.1607
		SSP5-8.5	8.12e-02	0.6969	0.7296	0.8659
		Present-day	7.10e-01	0.2860	0.3287	0.4644
	5-year	SSP2-4.5	-1.45e-00	0.0000	0.1261	0.0001
		SSP5-8.5	-9.52e-02	0.5041	0.8618	0.4418
		Present-day	7.26e-01	0.0013	0.3447	0.0073
Southern	Monthly	SSP2-4.5	7.17e-01	0.2407	0.2856	0.2421
		SSP5-8.5	1.09e-00	0.0474	0.1618	0.0449
		Present-day	1.57e-01	0.8052	0.8581	0.7465
	Yearly	SSP24-4.5	9.29e-01	0.3348	0.2210	0.4179
		SSP5-8.5	1.18e-00	0.1646	0.3737	0.1287
		Present-day	3.67e-01	0.8287	0.8559	0.8659
	5-year	SSP2-4.5	7.40e-01	0.0088	0.1739	0.0553
		SSP5-8.5	1.03e-00	0.0677	0.7765	0.0950
		Present-day	4.15e-01	0.4971	0.9162	0.7784
Northern	Monthly	SSP2-4.5	6.25e-01	0.3275	0.4905	0.4669
		SSP5-8.5	1.09e-01	0.5939	0.6393	0.8030
		Present-day	3.91e-01	0.5282	0.6518	0.4671
	Yearly	SSP2-4.5	6.63e-01	0.4783	0.5777	0.4179
		SSP5-8.5	2.18e-01	0.6052	0.5643	0.8365
		Present-day	4.66e-01	0.7186	0.8051	0.7215
	5-year	SSP2-4.5	6.57e-01	0.0805	0.7819	0.0313
		SSP5-8.5	2.13e-01	0.0833	0.6436	0.0447
		Present-day	4.89e-01	0.2074	0.8449	0.1709

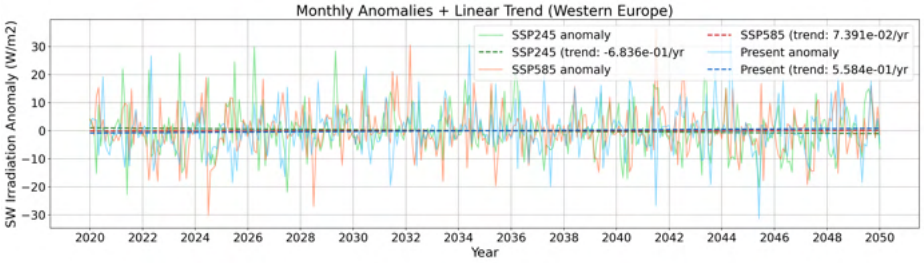

(a) Western Europe

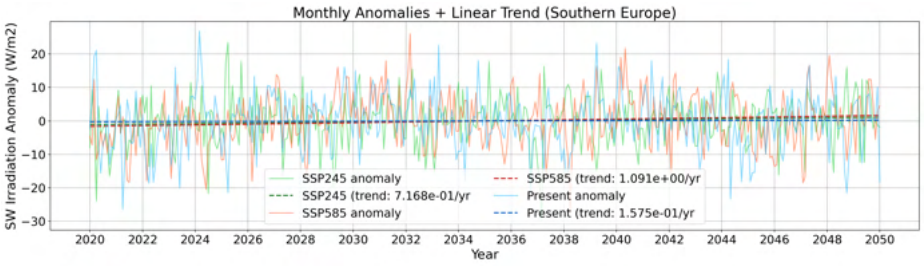

(b) Southern Europe

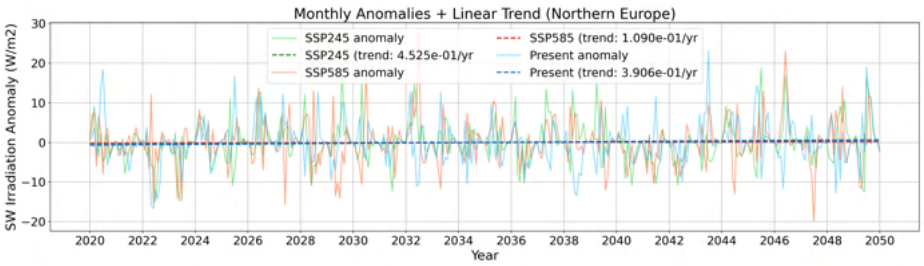

(c) Northern Europe

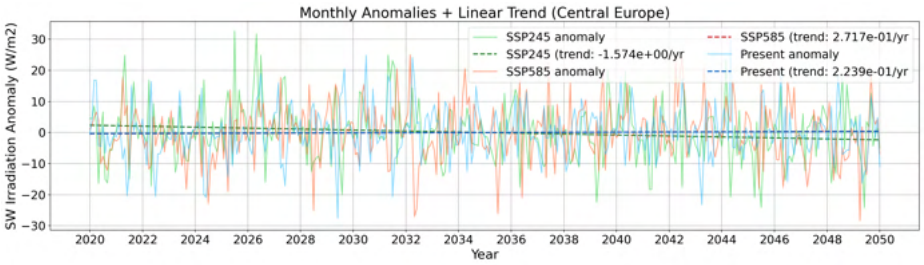

(d) Central Europe

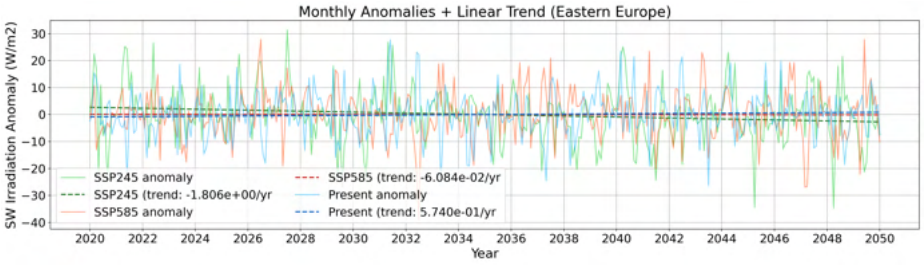

(e) Eastern Europe

Figure 4.7.: Monthly anomalies and linear trends of shortwave irradiance (W m^{-2}) in different climate zones, 2020–2050.

4.1.1.3. Near-Surface Dust Mass Concentration

In the following, the dust mass concentration at model level 90, which corresponds to the lowest near-surface level in ICON, is analyzed. Again, first the global mean is presented and afterwards european regional means. For the global mean near-surface mineral dust mass concentration (see figure 4.8), all three scenarios display pronounced interannual variability throughout the 2020–2049 period, with monthly anomalies ranging approximately from -1.5×10^{-8} to $+2.5\times10^{-8}$ kg m^{-3}. All scenarios exhibit consistent negative linear trends: SSP2-4.5 shows the strongest decrease (-3.232×10^{-9} kg m^{-3} decade^{-1}), followed by the Present-day simulation (-2.884×10^{-9} kg m^{-3} decade^{-1}) and SSP5-8.5 (-2.490×10^{-9} kg m^{-3} decade^{-1}). The trend lines converge closely across all three scenarios, suggesting that the projected decline in global mean dust burden is largely independent of the emission pathway.

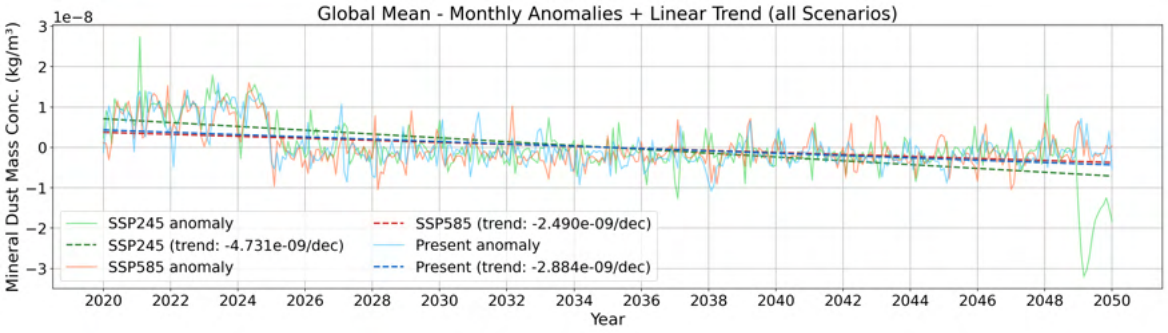

Figure 4.8.: Global mean monthly anomalies of near-surface mineral dust mass concentration (kg m^{-3}) for three model scenarios (SSP2-4.5, SSP5-8.5, Present-day), covering the period 2020–2049.

Figure 4.11 shows the detrended monthly mean evolution for each defined climate zone in Europe. In addition, annual means and 5-year running means were calculated for each region. The trends of all time series, together with the corresponding averaged values and significance analyses, are summarized in Table 4.4. The figures for the annual and 5-year means are provided in the Appendix (see Figure A.5 and A.6).
The anomalies of near-surface mineral dust mass concentration is displayed of order 10^{-8} kg m^{-3} in western, southern, eastern and central Europe, while northern Europe is displayed in the 10^{-7} kg m^{-3} range due to higher values in the beginning oof the simulation. The variable exhibits a broadly decreasing tendency across most regions and scenarios over the 2020–2049/2050 period, though the character of this decrease — whether gradual or abrupt, monotonic or episodic — differs substantially between regions. A particularly prominent feature is a step-like reduction in dust loading observed synchronously across all scenarios in northern and eastern Europe which dominates the linear trend estimates for these regions.

Western Europe shows a consistent negative trend in dust concentration across all three scenarios at both the annual and monthly timescale. In the annual anomaly series (Fig. A.5a), SSP2-4.5 declines most strongly (-8.4×10^{-10} kg m^{-3} yr^{-1}), followed by SSP5-8.5 (-6.3×10^{-10} kg m^{-3} yr^{-1}) and Present-day (-3.0×10^{-10} kg m^{-3} yr^{-1}); the scenario anomaly curves

overlap considerably, reflecting the high inter-annual variability relative to the trend. The monthly series (Fig. 4.9a) confirms these trends (SSP2-4.5: -8.1×10^{-10}; SSP5-8.5: -6.6×10^{-10}; Present-day: $-3.2\times10^{-10}\,\mathrm{kg\,m^{-3}\,yr^{-1}}$) and additionally reveals isolated positive spikes in the early part of the record reaching up to $\sim 2.5\times10^{-8}\,\mathrm{kg\,m^{-3}}$, likely associated with episodic dust transport events. In the 5-year rolling means (Fig. A.6a), the decline is steady and visible across all scenarios, from approximately $1.3–1.4\times10^{-8}\,\mathrm{kg\,m^{-3}}$ at the start to around $1.1–1.2\times10^{-8}\,\mathrm{kg\,m^{-3}}$ by the 2040s, with SSP2-4.5 and SSP5-8.5 declining more rapidly than Present-day.

Southern Europe is the only region where both future scenarios do not show a decrease in near-surface dust loading. Annual anomalies (Fig. A.5b) exhibit large inter-annual swings, and the fitted trends for SSP2-4.5 and SSP5-8.5 are near-zero or weakly positive ($+1.5\times10^{-10}$ and $+1.2\times10^{-10}\,\mathrm{kg\,m^{-3}\,yr^{-1}}$, respectively), while Present-day shows a moderately negative slope ($-6.6\times10^{-10}\,\mathrm{kg\,m^{-3}\,yr^{-1}}$). The monthly series (Fig. 4.9b) confirms these near-neutral future scenario trends and additionally highlights large episodic positive spikes throughout the record reaching up to $4\times10^{-8}\,\mathrm{kg\,m^{-3}}$, without obvious temporal clustering. In the rolling means (Fig. A.6b), SSP5-8.5 and SSP2-4.5 remains increases slightly, while Present-day declines. This diverging scenario behaviour contrasts with the largely concurrent decline seen in most other regions.

Northern Europe displays the most distinctive dust concentration anomaly signal of all five regions. The annual anomaly series (Fig. A.5c) shows large positive values in the early part of the simulation, followed by a sharp step-change around 2024–2025 after which anomalies become persistently negative. This transition is synchronous across all three scenarios. The resulting trend estimates are strongly negative and among the largest of any region (SSP24-4.5: -10.0×10^{-9}; SSP5-8.5: $-6.7\times10^{-9}\,\mathrm{kg\,m^{-3}\,yr^{-1}}$). The monthly series (Fig. 4.9c) reveals the full extent of this feature: an intense cluster of high-amplitude positive anomalies (order $10^{-7}\,\mathrm{kg\,m^{-3}}$) concentrated in 2020–2025, followed by an abrupt reduction to near-zero or negative values. All three monthly trend lines are strongly negative (SSP2-4.5: -9.9×10^{-9}; SSP5-8.5: -6.7×10^{-9}; Present-day: $-7.6\times10^{-9}\,\mathrm{kg\,m^{-3}\,yr^{-1}}$), largely driven by this early episode. The 5-year rolling means (Fig. A.6c) make the step change most clearly visible: all three scenario means decline steeply from around $3–4.5\times10^{-8}\,\mathrm{kg\,m^{-3}}$ in 2020 to approximately $1.5–1.7\times10^{-8}\,\mathrm{kg\,m^{-3}}$ around 2027, after which they stabilise at the lower level.

Central Europe shows no clear dominant trend in dust concentration. Annual anomalies (Fig. A.5d) exhibit high inter-annual variability with no obvious directional change, and the trend estimates are small and of mixed sign (SSP2-4.5: -4.3×10^{-10}; SSP5-8.5: $+3.0\times10^{-10}\,\mathrm{kg\,m^{-3}\,yr^{-1}}$). The monthly series (Fig. 4.9d) likewise shows no systematic change in frequency or amplitude of dust events over time, with positive spikes occurring throughout the record without temporal preference (SSP2-4.5: -4.0×10^{-10}; SSP5-8.5: $+3.3\times10^{-10}\,\mathrm{kg\,m^{-3}\,yr^{-1}}$). In the rolling means (Fig. A.6d), SSP2-4.5 fluctuates with decadal-scale oscillations around $1.9\times10^{-8}\,\mathrm{kg\,m^{-3}}$, while SSP5-8.5 starts lower and gradually increases, with the two scenario means converging and subsequently remaining closely aligned from around 2033–2035 onward. Present-day occupies an intermediate position. The

overall picture for this region is thus one of limited systematic change over the projection period.

Eastern Europe shows a pattern broadly similar to northern Europe, though less abrupt. All three scenarios converge on a moderate negative trend in the annual anomaly series (Fig. A.5e): SSP2-4.5 at $-3.7 \times 10^{-9}\,\mathrm{kg\,m^{-3}\,yr^{-1}}$, SSP5-8.5 at $-2.3 \times 10^{-9}\,\mathrm{kg\,m^{-3}\,yr^{-1}}$, and Present-day at $-2.6 \times 10^{-9}\,\mathrm{kg\,m^{-3}\,yr^{-1}}$, with the anomaly curves overlapping substantially. The monthly series (Fig. 4.9e) reveals that the highest monthly anomalies are concentrated in the early 2020s, after which a gradual decrease in amplitude is visible toward the 2040s (SSP2-4.5: -3.6×10^{-9}; SSP5-8.5: -2.2×10^{-9}; Present-day: $-2.6 \times 10^{-9}\,\mathrm{kg\,m^{-3}\,yr^{-1}}$). This is reflected clearly in the 5-year rolling means (Fig. A.6e), where all three scenario means decline in a step-like fashion from approximately $2.0–2.4 \times 10^{-8}\,\mathrm{kg\,m^{-3}}$ around 2020–2022 to $1.3–1.5 \times 10^{-8}\,\mathrm{kg\,m^{-3}}$ by the mid-2030s, after which the decline slows and the three curves run nearly parallel at the lower level.

Table 4.4 summarizes linear trends in dust aerosol burden across the five European subregions under two future climate scenarios (SSP2-4.5 and SSP5-8.5) and a Present-day reference simulation. Trends were derived from a linear regression applied to monthly means, annual means, and 5-year rolling means, and statistical significance was assessed using the raw linear regression p-value (p), an AR1-corrected p-value (p^*; Santer et al. 2000), and the non-parametric Mann-Kendall test (p_{MK}). The most pronounced and spatially consistent signals emerge in Eastern and Northern Europe, where strongly negative trends are detected under all three scenarios and across all temporal aggregations. At monthly and annual resolution, p, p^*, and p_{MK} agree at the < 0.01 level, confirming that these trends are robust and not attributable to serial autocorrelation. Western Europe also exhibits significant negative trends under SSP2-4.5 and SSP5-8.5 at monthly and annual resolution; however, p^* loses significance at the 5-year level, indicating that the underlying signal, while genuine, is partially obscured by interannual variability when the time series is smoothed. In contrast, Central and Southern Europe show no significant trends across any scenario or aggregation, suggesting either negligible long-term forcing or the presence of compensating regional processes.

Table 4.4.: Dust Burden trends per region, temporal average and scenario. Slope in kg m^{-2} yr^{-1}.p= $rawp - value$;p* = AR1-corrected p-value (Santer et al. 2000); p_{MK} = Mann-Kendall p-value.

Region	Average	Scenario	Slope/yr	p	p^*	p_{MK}
Western	Monthly	SSP2-4.5	-8.12e-10	0.0017	0.0203	0.0007
		SSP5-8.5	-6.57e-10	0.0098	0.0504	0.0016
		Present-day	-3.17e-10	0.2465	0.4040	0.2251
	Yearly	SSP2-4.5	-8.41e-10	0.0082	0.0144	0.0323
		SSP5-8.5	-6.30e-10	0.0324	0.0251	0.0295
		Present-day	-2.97e-10	0.3284	0.3134	0.3535
	5-year	SSP2-4.5	-8.62e-10	0.0000	0.3756	0.0000
		SSP5-8.5	-6.63e-10	0.0000	0.4448	0.0006
		Present-day	-2.84e-10	0.0402	0.6371	0.1435
Central	Monthly	SSP-4.5	-4.00e-10	0.3205	0.3930	0.6540
		SSP5-8.5	3.34e-10	0.3813	0.4749	0.1603
		Present-day	3.79e-10	0.2458	0.2537	0.3810
	Yearly	SSP2-4.5	-4.34e-10	0.4256	0.5257	0.4978
		SSP5-8.5	2.95e-10	0.5617	0.6951	0.6947
		Present-day	3.05e-10	0.3259	0.4124	0.1989
	5-year	SSP2-4.5	-4.97e-09	0.0804	0.7897	0.0497
		SSP5-8.5	2.63e-09	0.3943	0.8968	0.3724
		Present-day	2.95e-	0.0848	0.7927	0.0804
Eastern	Monthly	SSP2-4.5	-3.65e-09	0.0000	0.0000	0.0000
		SSP5-8.5	-2.25e-09	0.0000	0.0000	0.0000
		Present-day	-2.59e-09	0.0000	0.0000	0.0000
	Yearly	SSP2-4.5	-3.68e-09	0.0000	0.0296	0.0000
		SSP5-8.5	-2.31e-09	0.0005	0.1013	0.0153
		Present-day	-2.65e-09	0.0000	0.0799	0.0002
	5-year	SSP2-4.5	-3.66e-09	0.0000	0.4068	0.0000
		SSP5-8.5	-2.28e-09	0.0000	0.5075	0.0012
		Present-day	-2.62e-09	0.0000	0.4354	0.0000
Southern	Monthly	SSP2-4.5	1.80e-10	0.6822	0.7217	0.7924
		SSP5-8.5	9.20e-10	0.8563	0.8805	0.7750
		Present-day	-6.72e-10	0.1454	0.1754	0.1554
	Yearly	SSP2-4.5	1.50e-10	0.7805	0.8238	0.8028
		SSP5-8.5	1.18e-10	0.8689	0.8878	0.7481
		Present-day	-6.56e-10	0.1605	0.2531	0.2535
	5-year	SSP2-4.5	1.11e-10	0.6453	0.9225	0.8305
		SSP5-8.5	2.26e-10	0.5124	0.9206	0.3724
		Present-day	-6.54e-10	0.0052	0.5464	0.0204
Northern	Monthly	SSP2-4.5	-9.92e-09	0.0000	0.0001	0.0000
		SSP5-8.5	-6.71e-09	0.0000	0.0023	0.0000
		Present-day	-7.59e-09	0.0000	0.0001	0.0000
	Yearly	SSP2-4.5	-9.99e-09	0.0000	0.1473	0.0000
		SSP5-8.5	-6.70e-09	0.0013	0.2593	0.2390
		Present-day	-7.69e-09	0.0000	0.0813	0.0002
	5-year	SSP2-4.5	-9.75e-09	0.0000	0.4433	0.0000
		SSP5-8.5	-6.67e-09	0.0001	0.5539	0.1164
		Present-day	-7.47e-09	0.0000	0.4491	0.0000

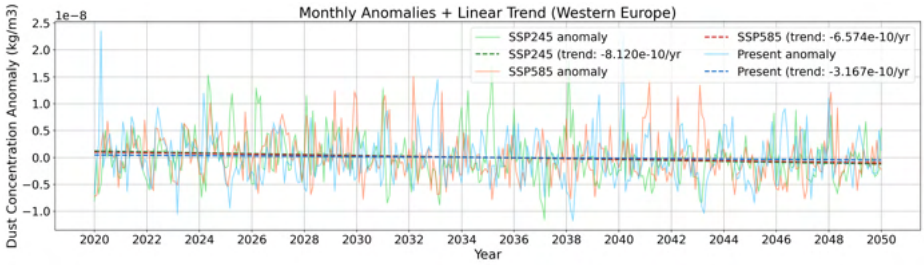

(a) Western Europe

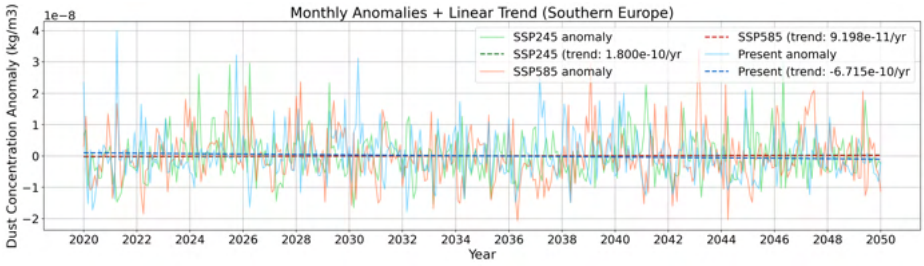

(b) Southern Europe

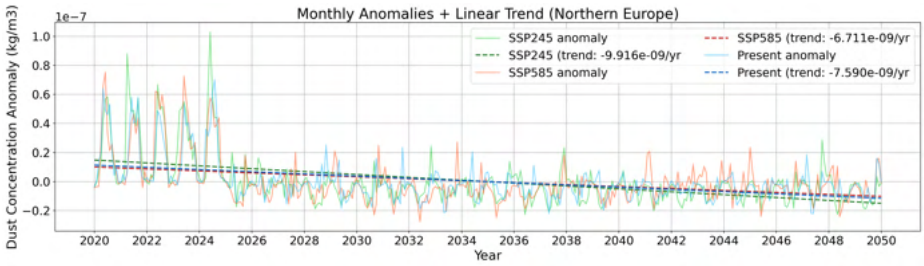

(c) Northern Europe

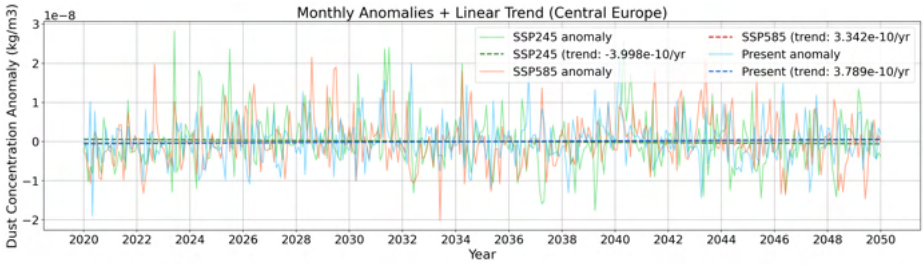

(d) Central Europe

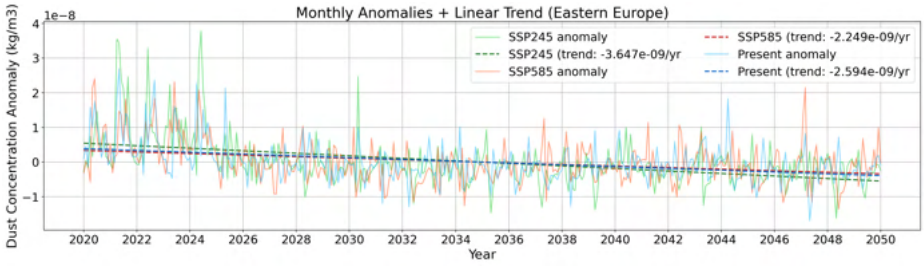

(e) Eastern Europe

Figure 4.9.: Monthly anomalies and linear trends of near-surface dust mass concentration ($\mathrm{kg\,m^{-3}}$) in different climate zones, 2020–2050.

Shortwave Direct Radiative Effect of Mineral Dust

The shortwave direct radiative effect (SW DRE) of mineral dust quantifies the perturbation to the downwelling shortwave flux at the surface caused by dust aerosol scattering and absorption, and thus provides a direct link between the near-surface dust mass concentration discussed above and its impact on the surface radiation budget. Monthly SW DRE anomalies and their linear trends are shown for the full simulation period 2020–2050 (Fig. 4.10) and for the sub-period starting in 2025, with the first five years excluded (Fig. 4.11). The exclusion of the early period is motivated by the pronounced negative anomaly clusters visible in all regions during 2020–2024, which are consistent with an initialisation artefact in the model rather than a physically meaningful signal, and which strongly influence the trend estimates when retained.

When the full period is included (Fig. 4.10), the SW DRE anomaly time series in all five regions are dominated by a cluster of large negative values in the early part of the record (2020–2025), coinciding with the elevated dust concentration episode identified in northern and eastern Europe (see Fig. 4.9e and 4.9c) and consistent with the strongly negative radiative effect expected from anomalously high dust loading. After approximately 2025, the anomalies in all regions transition to a regime of lower amplitude and become centered near zero. This transition mirrors the step-change in dust concentration described for northern and eastern Europe, and confirms that the early dust episode exerts a detectable negative perturbation on surface shortwave radiation across all regions.

Because of these large negative values in the first years, the fitted trend lines over 2020–2050 are positive in all five regions and all three scenarios, reflecting the recovery from the early negative anomalies rather than any sustained long-term increase in the radiative effect. Trend magnitudes range from approximately +0.04 to +0.07 $\mathrm{W\,m^{-2}\,yr^{-1}}$ (SSP2-4.5 and Present-day) with SSP5-8.5 generally showing smaller slopes, consistent with the weaker dust loading signal under the high-emission scenario in some regions.

In western Europe (Fig. 4.10a), the early-period negative anomalies are relatively moderate (down to $\sim -5\,\mathrm{W\,m^{-2}}$), and the transition to near-zero conditions occurs around 2025. The three scenario curves are closely overlapping after this transition, and the positive trend slopes are small (+0.042–+0.051 $\mathrm{W\,m^{-2}\,yr^{-1}}$), reflecting the weaker and less spatially coherent dust signal in this region.

Southern Europe (Fig. 4.10b) shows a particularly strong negative outlier in 2026 under SSP2-4.5 (reaching approximately $-11\,\mathrm{W\,m^{-2}}$), which stands out as an isolated event against otherwise moderate variability. Trend slopes are broadly positive across all scenarios (+0.038–+0.047 $\mathrm{W\,m^{-2}\,yr^{-1}}$), and after the early period the three scenario anomaly curves become closely aligned, consistent with the near-neutral and scenario-insensitive dust trends found for this region.

Northern Europe (Fig. 4.10c) displays the most pronounced early-period negative anomalies of all five regions, with individual months reaching below $-10\,\mathrm{W\,m^{-2}}$ in 2024–2025. This is directly attributable to the exceptionally high near-surface dust concentrations observed in northern Europe during this period. Following the abrupt dust decrease around 2025, the

DRE anomalies recover rapidly and the series shows a persistent positive trend (+0.057–+0.068 $\mathrm{W\,m^{-2}\,yr^{-1}}$), the largest of all regions, driven by the large baseline offset created by the early anomalies. The three scenario curves are nearly indistinguishable after 2026.

Central Europe (Fig. 4.10d) presents a moderate early-period signal with anomalies reaching around $-6\,\mathrm{W\,m^{-2}}$ in isolated months. The recovery to near-zero conditions is gradual over the first decade, and the subsequent anomalies are centred close to zero with relatively limited amplitude ($\lesssim \pm 3\,\mathrm{W\,m^{-2}}$). Trend slopes are positive across all scenarios (+0.037–+0.050 $\mathrm{W\,m^{-2}\,yr^{-1}}$) but lower in magnitude than in northern Europe, consistent with the less pronounced dust step-change in this region.

Eastern Europe (Fig. 4.10e) shows a clear early-period negative episode with several months below $-4\,\mathrm{W\,m^{-2}}$ concentrated between 2020 and 2025, followed by a gradual recovery. The trend slopes are positive and broadly consistent across scenarios (+0.049–+0.064 $\mathrm{W\,m^{-2}\,yr^{-1}}$), with SSP2-4.5 exhibiting the steepest slope, which can be linked to the stronger dust decline under this scenario discussed in Section 4.1.1.3. After approximately 2032, the three scenario curves converge and the anomaly amplitudes decrease progressively towards the end of the period.

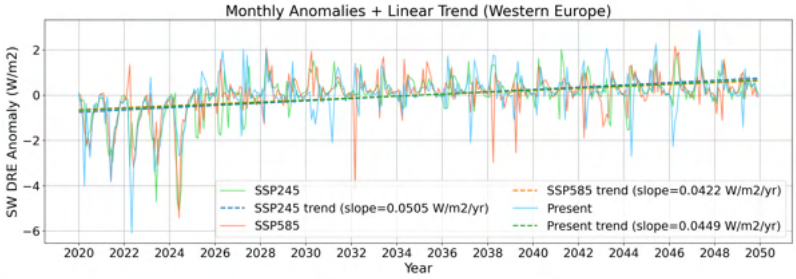

(a) Western Europe

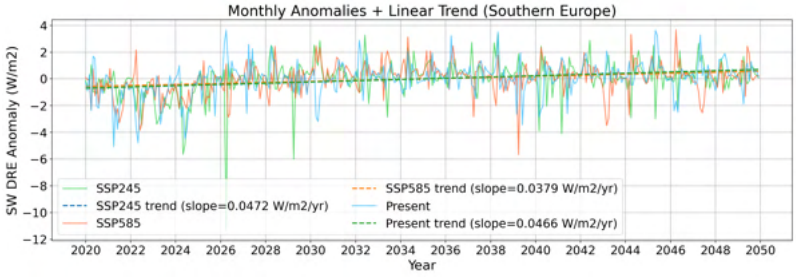

(b) Southern Europe

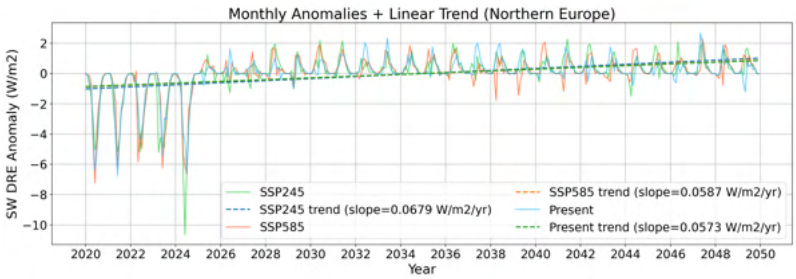

(c) Northern Europe

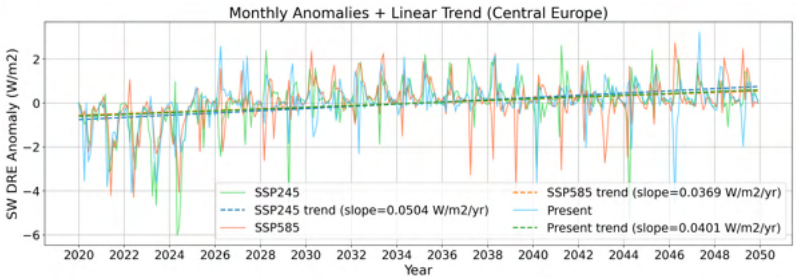

(d) Central Europe

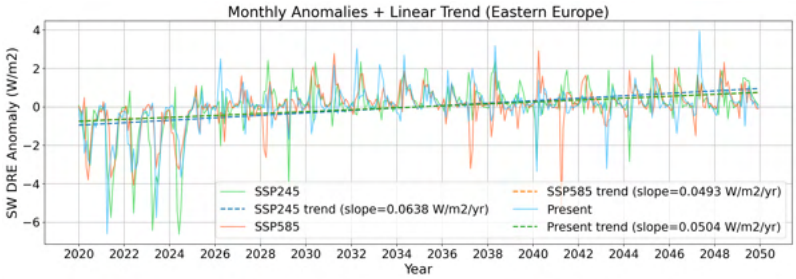

(e) Eastern Europe

Figure 4.10.: Monthly SW DRE anomalies (W m^{-2}) and OLS linear trends, full period 2020–2050. All three scenarios are shown; dashed lines indicate OLS trends.

Restricting the analysis to the period starting in 2025 (Fig. 4.11) eliminates the influence of the suspected initialisation artefact and reveals the underlying scenario-dependent SW DRE signal in this period. The most immediate consequence of this restriction is that all trend slopes change substantially: where the full-period analysis yielded uniformly positive trends driven by recovery from the early anomalies, the 2025–2050 trends are considerably smaller in magnitude and in some regions close to zero. The three scenario curves also become more closely overlapping after the exclusion of the early period, confirming that much of the apparent scenario spread in the full-period analysis was attributable to timing differences in the early dust episode. Mostly, the SSP signals are stronger than the Present-day signal.

In western Europe (Fig. 4.11a), the removal of the early period leaves a time series with anomaly amplitudes generally within $\pm 2\,\mathrm{W\,m^{-2}}$ and trend slopes that are near-zero and closely aligned across scenarios ($+0.007$–$+0.018\,\mathrm{W\,m^{-2}\,yr^{-1}}$) with slightly steeper trends for the SSP scenarios. The three scenario curves are largely superimposed throughout, consistent with the low scenario sensitivity of dust loading identified in this region.

Southern Europe (Fig. 4.11b) likewise shows markedly reduced trend slopes after exclusion of the early period ($+0.007$–$+0.016\,\mathrm{W\,m^{-2}\,yr^{-1}}$), and the isolated deep negative event of 2026 under SSP2-4.5 is the most prominent feature of the remaining record. After this event, the anomalies remain centred near zero and the scenario curves are closely overlapping. A slightly positive trend for all scenarios can be detected.

Northern Europe (Fig. 4.11c) shows the most striking change upon exclusion of the early period. The positive trend that dominated the full-period analysis is largely eliminated, with sub-period slopes of only $+0.003$–$+0.011\,\mathrm{W\,m^{-2}\,yr^{-1}}$, and the anomaly amplitudes ($\lesssim \pm 2\,\mathrm{W\,m^{-2}}$) are substantially smaller than in the full record. The three scenario curves are nearly indistinguishable throughout, reflecting the scenario-insensitive dust behaviour in northern Europe after the initial step-change has concluded. Inly SSP2-4.5 has a stronger signal.

For central Europe (Fig. 4.11d), the sub-period shows monthly anomalies within approximately $\pm 3\,\mathrm{W\,m^{-2}}$ with trend slopes that are small and broadly similar across scenarios ($+0.004$–$+0.016\,\mathrm{W\,m^{-2}\,yr^{-1}}$). The three scenario trends are again slighly poositive with again a tendency towards a higher DRE with respect to mineral dust in the future.

Eastern Europe (Fig. 4.11e) retains the most discernible positive signal of all regions in the 2025–2050 sub-period, with trend slopes of $+0.013$–$+0.013\,\mathrm{W\,m^{-2}\,yr^{-1}}$ for SSP2-4.5 and SSP5-8.5 and $+0.006\,\mathrm{W\,m^{-2}\,yr^{-1}}$ for Present-day - marking again steeper trends for the SSP scenarios. Anomaly amplitudes decrease gradually from the early part of the sub-period towards the 2040s, broadly consistent with the continued gradual decline in dust concentration described for eastern Europe (Sect. 4.1.1.3). The scenario curves are more tightly clustered than in the full-period analysis, though SSP2-4.5 retains a slightly higher trend slope.

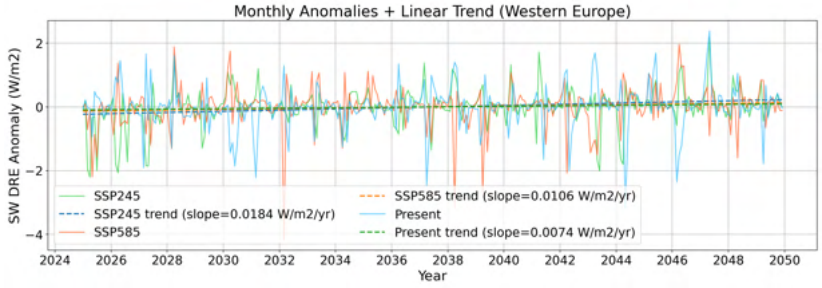

(a) Western Europe

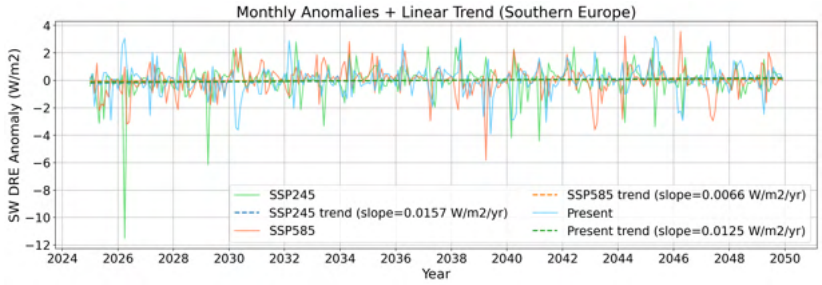

(b) Southern Europe

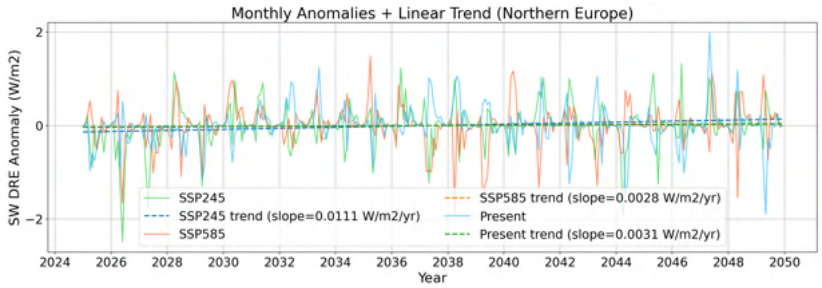

(c) Northern Europe

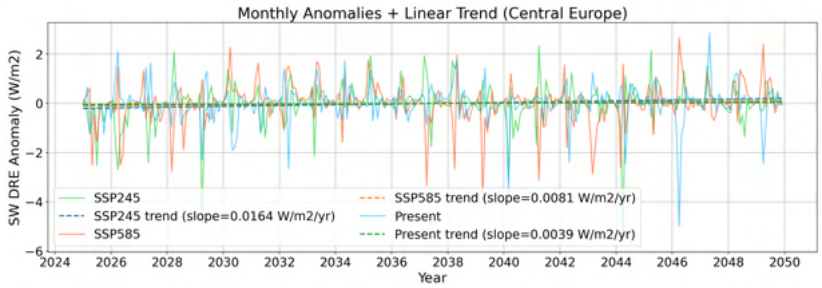

(d) Central Europe

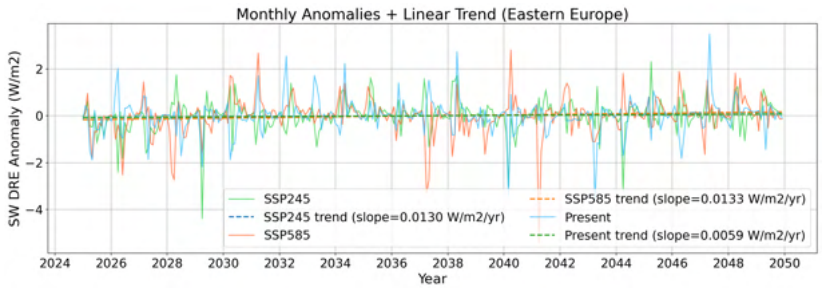

(e) Eastern Europe

Figure 4.11.: Monthly SW DRE anomalies ($\mathrm{W\,m^{-2}}$) and OLS linear trends, sub-period 2025–2050 (model spin-up excluded). Dashed lines indicate OLS trends per scenario.

4.1.2. Case Studies of Energy System Relevant and Spatio-Temporally Differing Scenarios

In this section, several case studies are conducted using the Region Tracking System described in Section 3.1.4. The scope of this section is to analyse the occurrence of weather conditions in a changing climate that are relevant to the energy system, specifically the energy grid. With *energy system relevant conditions*, situations are meant in which the meteorological variables, and thus the renewable energy yields, reach unusual high or low values such that the stability of the energy grid may become problematic when the share of renewables in the overall energy mix is high and redispatch actions must be applied in certain regions. At Present-day, gaps in electricity supply can, for example, be compensated by coal-fired or gas-fired power plants. In addition, the expansion of the power grid, as well as the use of energy storage systems, can help to mitigate these situations. For the continuing goal of a transformation towards a climate-neutral society and therefore the increased deployment of renewable technologies, solutions must be found to bridge such periods. Meteorologically, it is also relevant to examine the occurrence of certain weather events in order to better understand both the effects of climate change and atmospheric interactions. Throughout this study, the main spatial target is the western European region that is also analysed with the energy market model (see Section 3.3.2).

4.1.2.1. Case 1: Dark Doldrums

The first case scenario deals with the occurrence of dark doldrums. In the literature, numerous definitions of dark doldrums exist, but no single definition is universally valid across all studies. According to the definition of the German Federal Ministry for Economic Affairs and Energy (see *Glossar - energieforschung.de* (2026), dark doldrums combine the concepts of low wind conditions and a lack of sunlight. The term refers to a weather situation in which wind turbines receive insufficient wind and photovoltaic systems receive insufficient solar radiation to generate adequate electricity, or in some cases any electricity at all. Depending on the scope of the study, it can also be useful to take energy demand into account when defining dark doldrums, since only when there is a certain level of demand can an insufficient amount of demand be quantified due to insufficient renewable dispatching. When taking energy demand into account, the definition of dark doldrums should also be adjusted according to the season, since in winter the overall energy consumption tends to be higher than in summer, for example due to colder temperatures and shorter periods of solar irradiance.

Other studies use definitions based on capacity factors, which is also the approach adopted here, since capacity factors are already calculated to link the meteorological climate model ICON-SmART with the energy market model PowerACE. Here, several thresholds are applied, depending on the intensity of dark doldrums that are to be emphasised in the respective study. A medium-to-average threshold for both photovoltaic and wind energy capacity factors of

$$\mathrm{CF} < 0.1 \tag{4.1}$$

is used. (Ohlendorf and Schill, 2020) With this, the Region Tracking Algorithm (see Section 3.1.4) searches for time frames and locations in which capacity factors fall below this threshold, and also records how long these regions persist, whether there are neighbouring grid cells that can be assigned to an overall cell of a certain event, and what total size these cells reach during their persistence. The results of this analysis are presented in the following paragraphs.

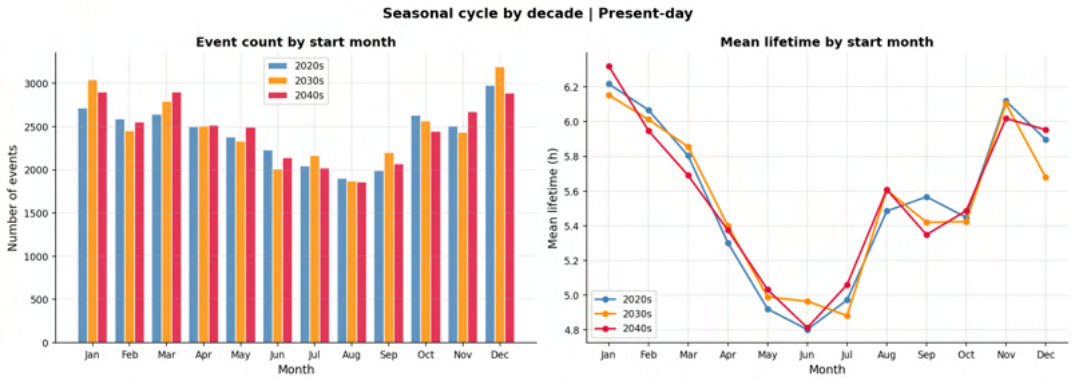

(a) Present-day

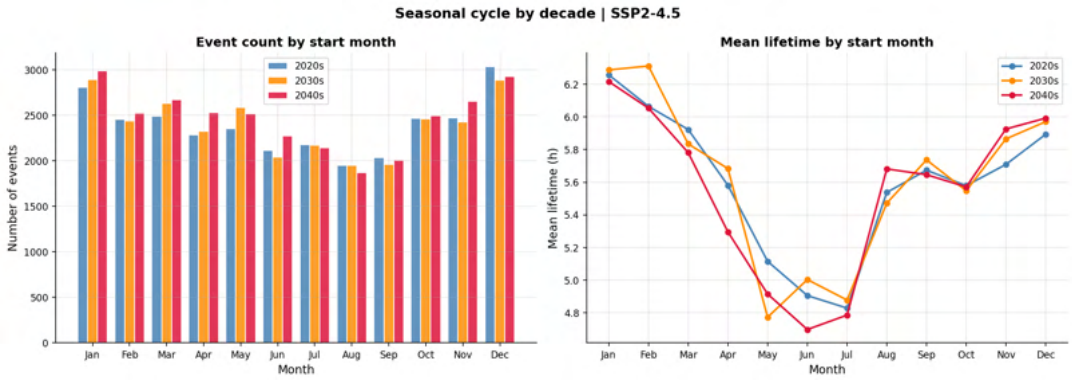

(b) SSP2-4.5

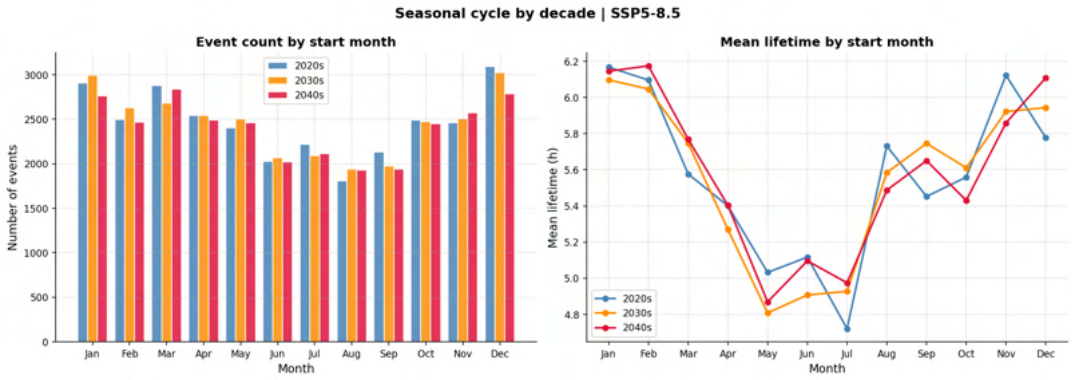

(c) SSP5-8.5

Figure 4.12.: Seasonal cycle of dark doldrum events by decade for each scenario.

In Figure 4.12, the seasonal structure of dark doldrum events and their duration is illustrated which break the seasonal cycle down by decade within each scenario. In all three scenarios, dark doldrum events follow a pronounced annual cycle in which event counts peak during the winter months, particularly December and January, and reach their minimum during summer, with the lowest counts occurring in June, July, and August. This pattern is physically consistent with the reduced solar irradiance during northern European winters, which systematically pushes capacity factors below the threshold of 0.1. The mean lifetime of individual events exhibits the inverse pattern: events starting in winter persist for roughly 6.0–6.2 h on average, whereas summer events are markedly shorter, dropping to approximately 4.8 h in June and July. This contrast reflects the diurnal solar cycle, which limits the duration of low-irradiance periods in summer. Across all three scenarios, the scenario comparisons show very similar event counts and lifetimes for Present-day, SSP2-4.5, and SSP5-8.5, indicating that the seasonal structure is largely preserved under both warming scenarios and that differences between scenarios are comparatively small in the seasonal dimension.

Within individual scenarios, Figure 4.12 reveals subtle but consistent decadal shifts. Under Present-day forcing, the decadal spread in event counts is modest and shows no strong directional tendency, while lifetimes remain broadly stable across the 2020s, 2030s, and 2040s. Under SSP2-4.5, the winter months show a slight increase in event counts from the 2020s to the 2040s, except December, whereas under SSP5-8.5 the winter counts tend to decrease slightly into the 2040s. For mean lifetimes, both future scenarios exhibit a tendency towards slightly shorter summer lifetimes in the later decades thereby reducing the frequency of prolonged low-production periods.

The temporal evolution of de-seasoned monthly anomalies in event count, mean peak area, and mean lifetime is shown in Figure 4.13. These anomaly time series are again computed by removing the long-term monthly climatology in order to isolate interannual variability and potential long-term trends from the seasonal signal already discussed above.

Regarding event count anomalies (Figure 4.13a), the raw monthly signal exhibits pronounced variability of ±100 events in individual months across all three scenarios, reflecting the strong year-to-year variability of atmospheric circulation patterns. The 12-month running means reveal that SSP2-4.5 carries a statistically marginally significant positive trend of $+0.32\,\text{events}\,\text{yr}^{-1}$ ($p = 0.044$), suggesting a slight increase in the number of dark doldrum events over the simulation period. In contrast, SSP5-8.5 exhibits a weak negative trend of $-0.22\,\text{events}\,\text{yr}^{-1}$ ($p = 0.207$), which is not statistically significant, and the Present-day simulation shows no discernible trend ($p = 0.472$). These results indicate that under the moderate mitigation scenario SSP2-4.5 a marginally significant but small upward tendency in event frequency may emerge.

The mean peak area anomaly (Figure 4.13b) exhibits considerably smaller variability in relative terms, with monthly excursions generally remaining within $\pm\, 0.075 \times 10^6\,\text{km}^2$. All three linear trends are statistically insignificant (all $p > 0.09$), demonstrating that the spatial extent of individual dark doldrum events at their maximum development does not change systematically under either warming scenario, still a slight negative trend for Present-day and SSP2-4.5 can be shown a s well as a slight positive trend for SSP5-8.5. Similarly, the

mean lifetime anomaly (Figure 4.13c) shows no significant trend in any scenario (all $p > 0.5$), with trend magnitudes on the order of 0.002 h yr^{-1}. Taken together, these results suggest that while the total number of dark doldrum events may shift slightly under SSP2-4.5, the characteristic size and persistence of individual events remain largely unaffected by the projected climate change over the 2020–2050 period.

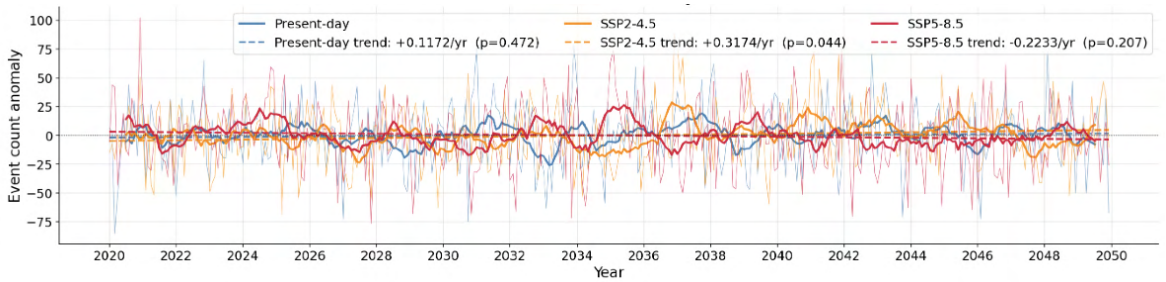

(a) Event count anomaly.

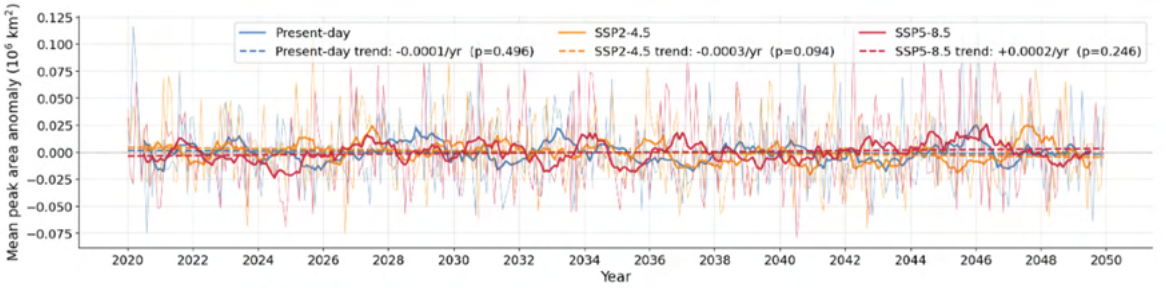

(b) Mean peak area anomaly (10^6 km^2).

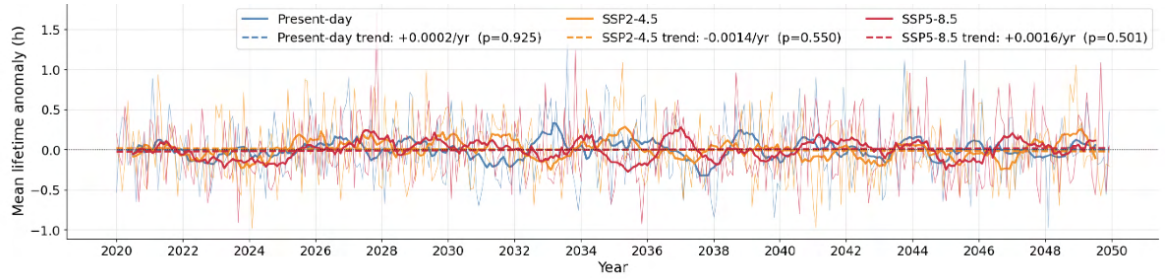

(c) Mean lifetime anomaly (h).

Figure 4.13.: Monthly de-seasoned anomalies and linear trends for dark doldrum events, 2020–2049.

The spatial distribution of dark doldrum frequency, expressed as the percentage of time steps in which the capacity factor criterion is met at each grid cell, is presented in Figure 4.14. Across all scenarios and all decades, the criterion frequency exhibits a spatially coherent pattern with two distinct hotspot regions: a broad central-south European area in Austria, soouthern Germany, Switzerland and southern France as well as Poland, where frequencies reach values of 30–50%, and a secondary southern hotspot over the Iberian Peninsula, particularly concentrated in the interior of Spain and Portugal, where frequencies locally exceed 40–50%. The North Sea coastal areas, consistent with the high wind resource in these regions.

Comparing the three scenarios, the spatial patterns are strikingly similar across Present-day, SSP2-4.5, and SSP5-8.5. Within each scenario, the decadal evolution from the 2020s through the 2040s reveals modest changes in the spatial extent and intensity of the hotspots, as described below.

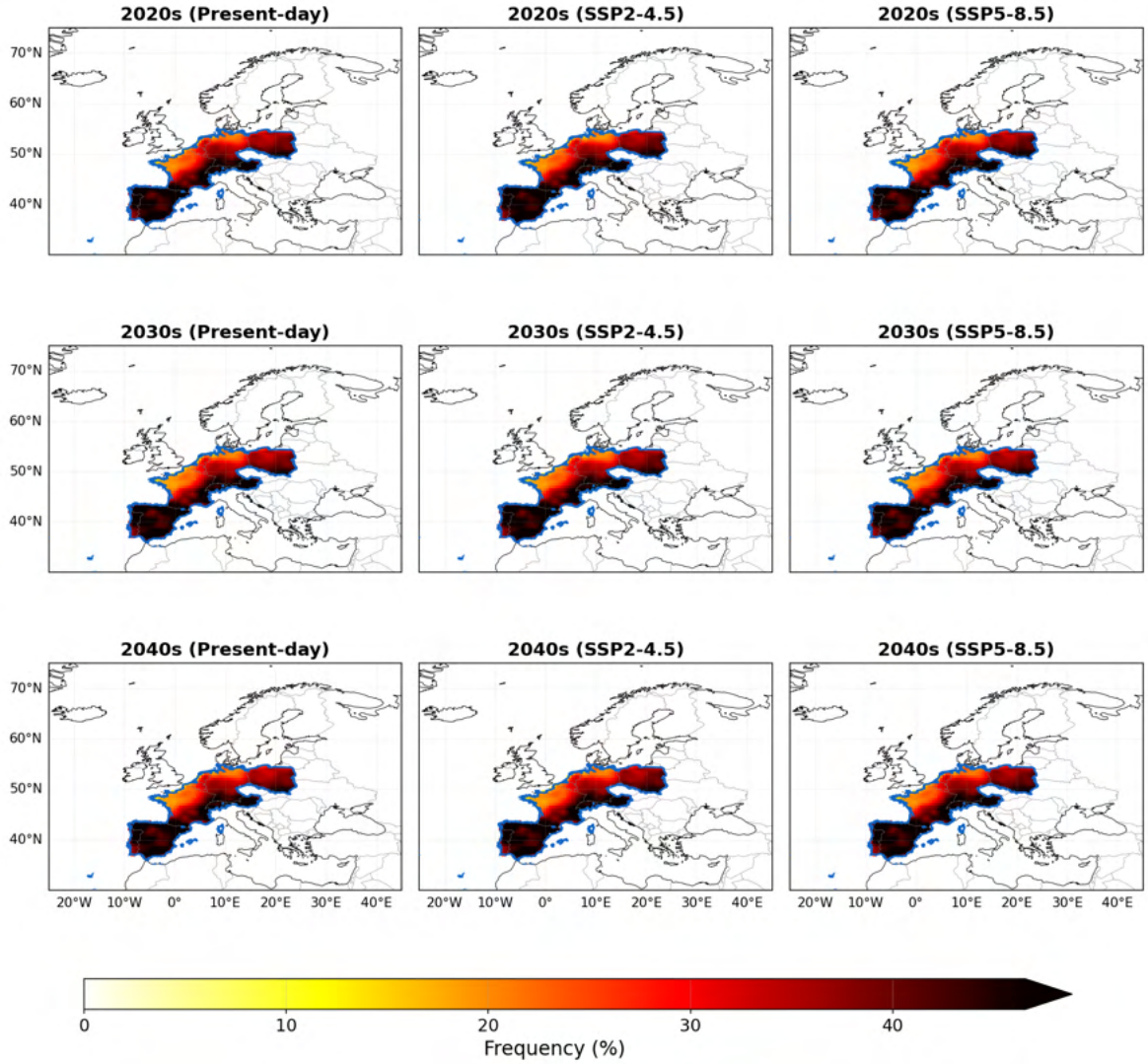

Figure 4.14.: Criterion frequency (%) of dark doldrum conditions by decade for each climate scenario. Blue outlines determine analysis region boundaries.

The decadal change in criterion frequency relative to the 2020s baseline is depicted in Figure 4.15. Under Present-day forcing, the 2030s minus 2020s difference shows a widespread decrease in frequency over France and parts of Germany, while the 2040s minus 2020s panel reveals a persistent and spatially extended negative anomaly across western and central Europe, including the Iberian Peninsula. This suggests that internal variability in the Present-day simulation produces a systematic multi-decadal oscillation in the occurrence of dark doldrum conditions.

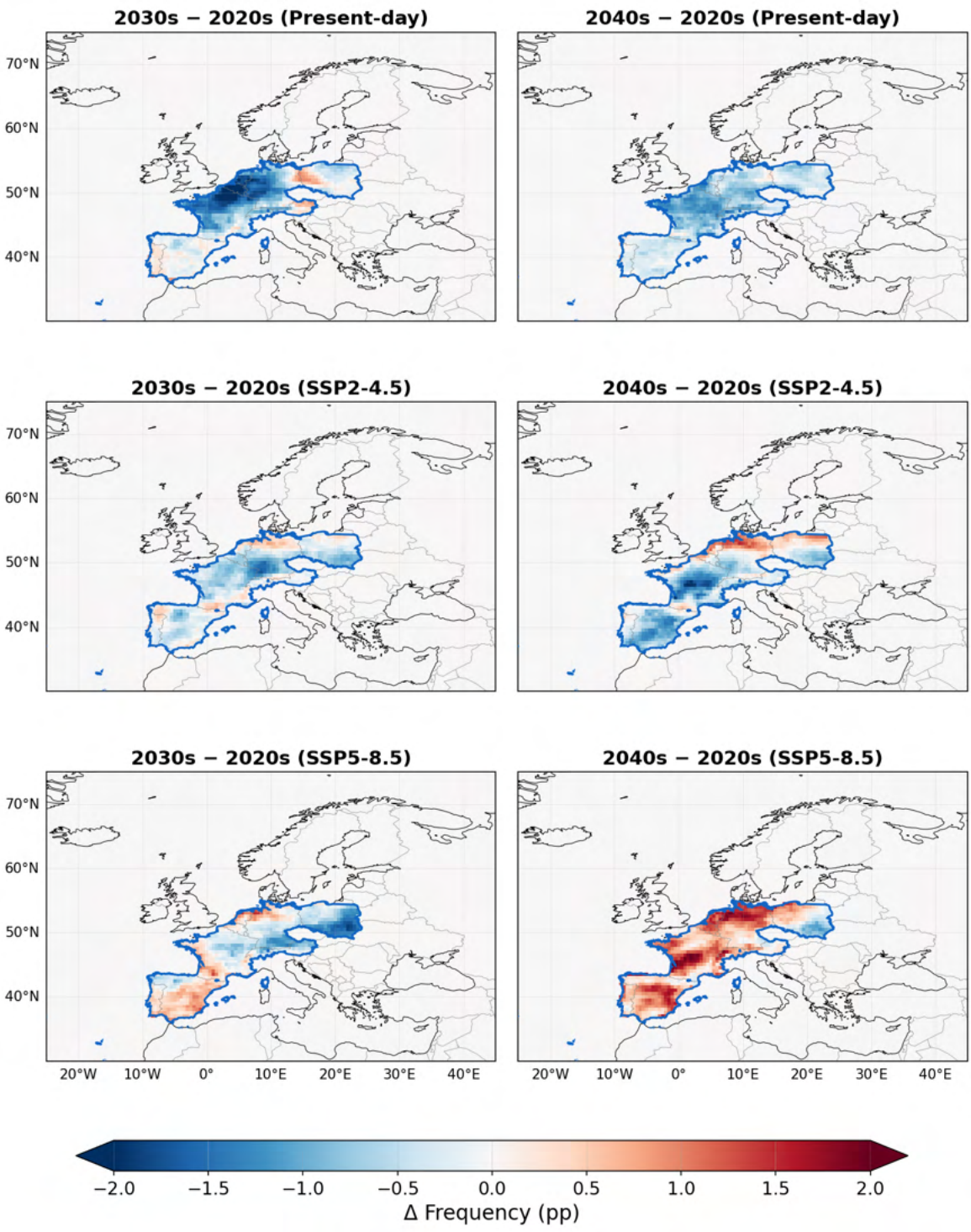

Figure 4.15.: Decadal change in dark doldrum criterion frequency relative to the 2020s baseline for each climate scenario. Blue outlines determine analysis region boundaries.

Under SSP2-4.5, the decadal evolution is markedly different: the 2030s show an increase in frequency relative to the 2020s, particularly over north-western Germany and Benelux, while the 2040s display a strong positive anomaly over a broad region encompassing northern

regions near the North sea and Baltic sea, with values exceeding +1 pp in some areas. The Iberian Peninsula also shows decreasing frequencies in the later decades. Under the high-emission pathway SSP5-8.5, the 2030s minus 2020s panel exhibits a dipole pattern, with frequency decreases over western central Europe and modest increases over the Iberian Peninsula. By the 2040s, however, a strong and spatially coherent increase in dark doldrum frequency emerges across the Iberian Peninsula and parts of southern France, alongside increases in eastern Europe, while central European frequencies also rise. The magnitude of the changes under SSP5-8.5 in the 2040s is notably larger than under SSP2-4.5, pointing towards a stronger intensification of dark doldrum conditions in the higher-emission pathway, particularly over the Iberian Peninsula.

The overall frequency difference between each future scenario and the Present-day simulation, disaggregated by decade, is shown in Figure 4.21. For the SSP245 scenario (Figure 4.16a), the full-period map reveals a modest dipole structure: a slight increase in dark doldrum frequency over parts of the Baltic and eastern Europe as well as the Iberian Pensula, and a slight decrease over north western Europe and. The decade-by-decade panels show that during the 2020s the two scenarios are nearly indistinguishable in spatial pattern, while in the 2030s a positive anomaly emerges around eastern Europe. By the 2040s, the eastern positive anomaly strengthens further while a modest increase also appears over Iberia. Magnitudes throughout remain below ±2 pp, indicating a moderate scenario-induced signal.

For SSP5-8.5 (Figure 4.16b), the full-period difference is spatially more expressive. The 2020s are already characterized by a positive anomaly over eastern Europe and a negative anomaly over western Europe, suggesting early divergence from the Present-day trajectory. In the 2030s, the pattern partially inverts, with decreases over western areas and strong increases over the central European corridor. By the 2040s, the SSP5-8.5 minus Present-day difference shows pronounced positive values of up to +2 pp or more over much of the Iberian Peninsula and eastern Europe, indicating a clear intensification of dark doldrum conditions under the high-radiative forcing scenario relative to Present-day climate. The contrast between the 2020s and 2040s panels for SSP5-8.5 illustrates the progressive divergence of the climate signal, which becomes increasingly pronounced with time and is spatially concentrated in the central and eastern region of the study domain.

Also comparing the two scenario comparisons during the same century leads to the result that the intensity of the dark doldrum tendencys increases in most regions for the SSP5-8.5 scenario, except for the 2030s.

Especially in tthe 2040s, SSP5-8.5 seems like an intensified version of SSP2-4.5 with stronger positive tendencies in the respective regions.

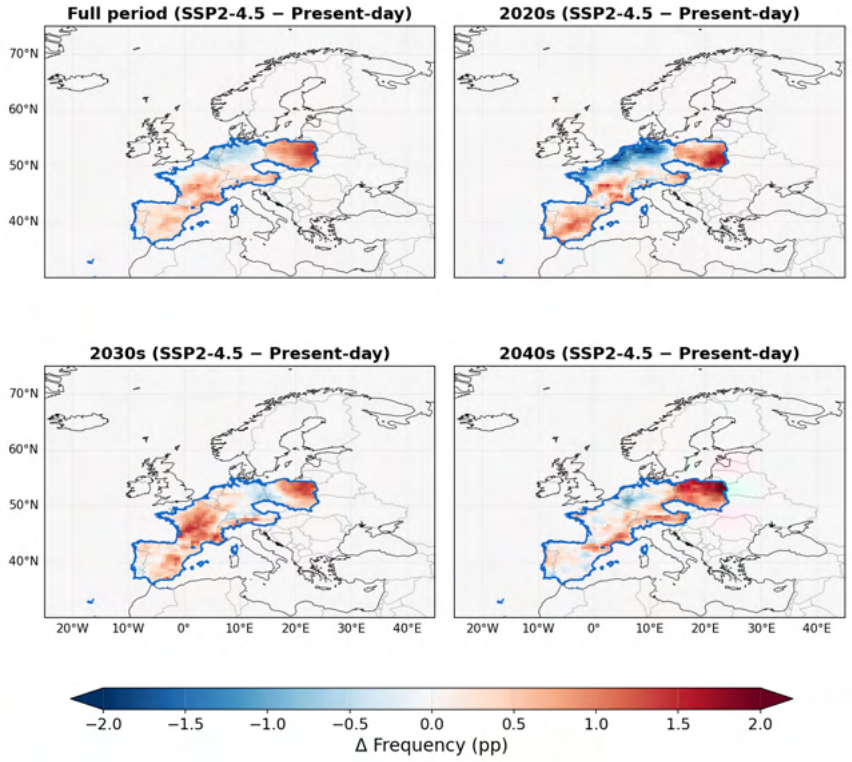

(a) SSP2-4.5 minus Present-day

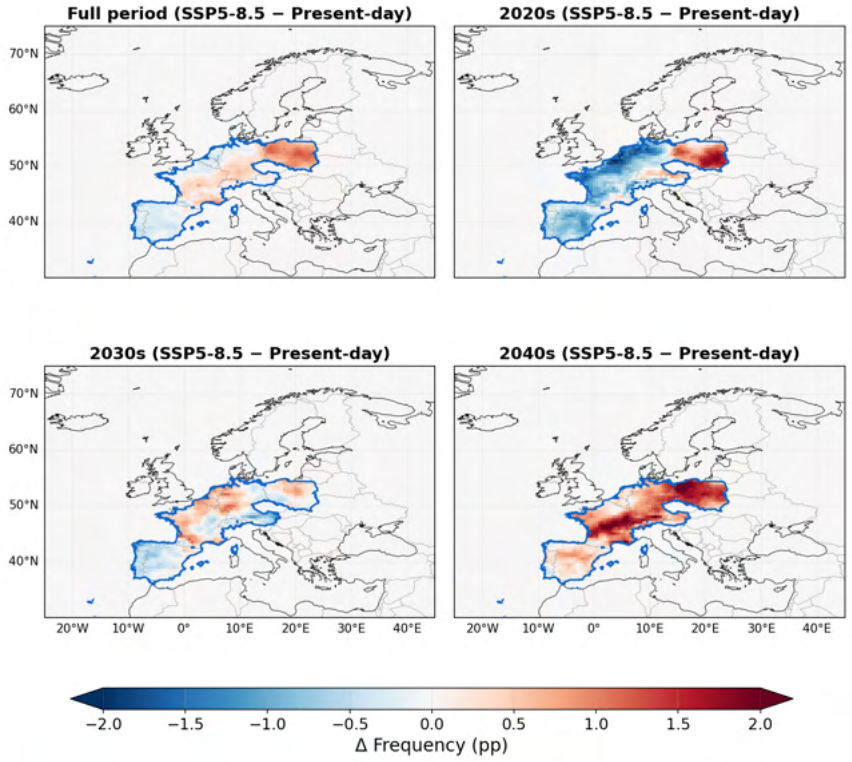

(b) SSP5-8.5 minus Present-day

Figure 4.16.: Frequency difference of dark doldrum conditions between future scenarios and Present-day, by decade. Blue outlines determine analysis region boundaries.

4.1.2.2. Case 2: Light Breezes

The second case scenario deals with the occurrence of light breezes, which represent the meteorological opposite of dark doldrums. In general, light breeze conditions are characterized by simultaneously high wind energy and photovoltaic yields. Light breezes have not been the subject of many scientific studies, and consequently no clear quantitative definition exists in the literature. If energy demand data are taken into account, low demand values would be expected to coincide with high renewable energy dispatching at a given location. As a consequence, low contributions from other energy technologies would be needed, the distribution grids would require high capacities to transmit the surplus renewable energy to areas with greater demand, or certain renewable installations would need to be curtailed. To maintain consistency with the analysis of dark doldrums (see Section 4.1.2.1), a capacity factor threshold of

$$\mathrm{CF} > 0.9 \tag{4.2}$$

for both wind and photovoltaic energy capacity factors has been chosen. With this, the Region Tracking Algorithm (see Section 3.1.4) searches for time frames and locations in which capacity factors exceed this threshold, and also records how long these regions persist, whether there are neighboring grid cells that can be assigned to an overall cell of a certain event, and what total size these cells reach during their persistence. The results of this analysis are presented in the following paragraphs.

The seasonal cycle of light breeze events is presented in Figure 4.17. In stark contrast to dark doldrums, light breeze events exhibit a pronounced spring-centred seasonal maximum: Event counts peak sharply in March and remain elevated through April and May, before declining to their lowest values in summer and recovering modestly in late autumn. This pattern reflects the combination of high solar irradiance angles in spring and frequent synoptic wind events, which together drive simultaneous high capacity factors for both wind and photovoltaic generation. The mean lifetime of events, shown in the right-hand panels, displays the inverse pattern relative to event count: lifetimes are shortest in winter (around 2.5 h) and reach their maximum in May and June (approximately 4.0–4.2 h), consistent with the longer daylight hours during which high photovoltaic yields can be sustained.

The scenario comparison in Figure 4.17 reveals that Present-day, SSP2-4.5, and SSP5-8.5 produce nearly identical seasonal distributions of both event count and mean lifetime, indicating that the seasonal structure of light breezes is robust across scenarios. Decadal differences within each scenario are modest overall, though under SSP2-4.5 the 2030s show a slight elevation in March event counts compared to the 2020s, while under SSP5-8.5 the 2040s decade exhibits an increase in mean lifetime for summer months. Under Present-day forcing, the decadal spread remains the smallest of the three scenarios, consistent with the absence of a long-term forcing trend.

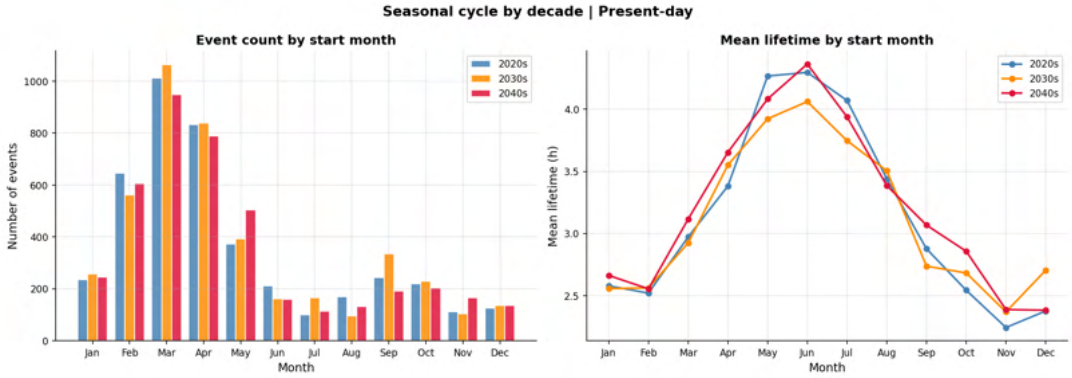

(a) Present-day

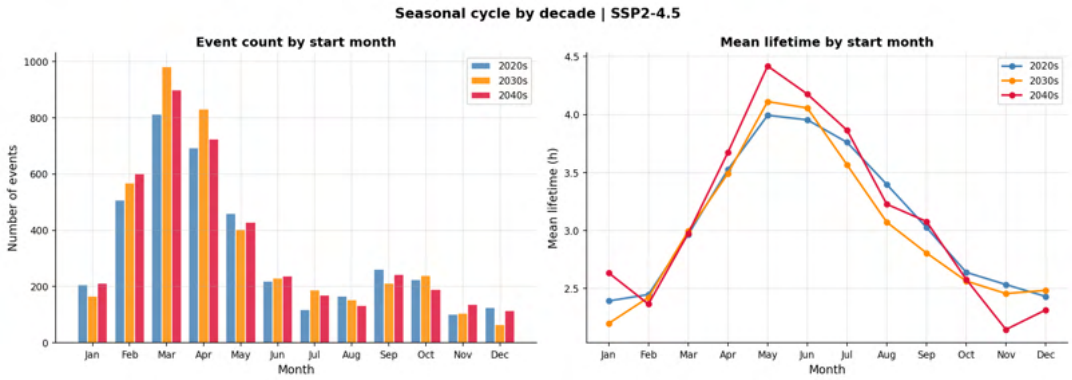

(b) SSP2-4.5

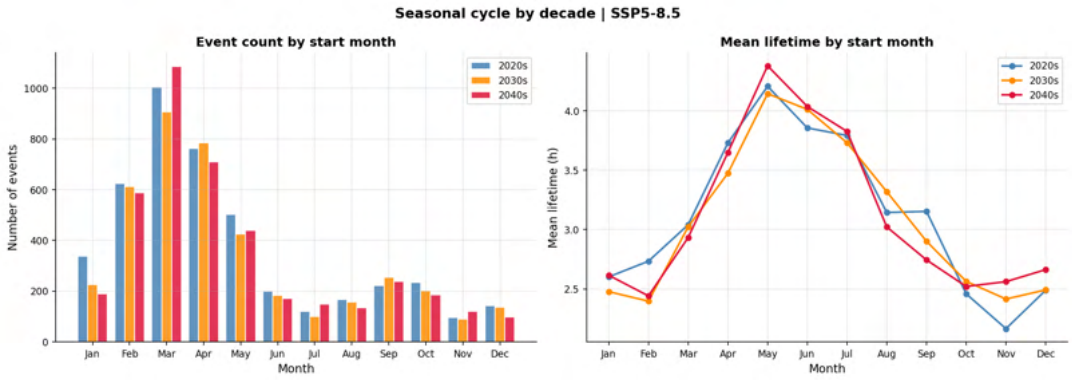

(c) SSP5-8.5

Figure 4.17.: Seasonal cycle of light breeze events by decade for each scenario.

The monthly de-seasoned anomaly time series for light breeze event count, mean peak area, and mean lifetime are displayed in Figure 4.18. For the event count anomaly (Figure 4.18a), the month-to-month variability is considerably smaller than for dark doldrums, with individual monthly anomalies remaining within roughly ±60 events. None of the three linear trends reaches statistical significance: Present-day shows a slight negative tendency (-0.06 events yr^{-1}, $p = 0.456$), SSP2-4.5 a marginal positive tendency ($+0.07$ events yr^{-1}, $p = 0.379$), and SSP5-8.5 a moderate negative tendency (-0.14 events yr^{-1}, $p = 0.103$). The absence of statistically significant trends in any scenario implies that the total number

of light breeze events is not systematically altered by the projected warming over the 2020–2050 period.

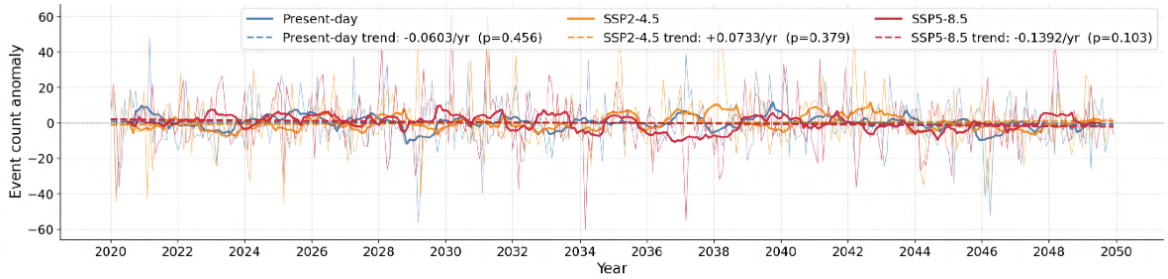

(a) Event count anomaly

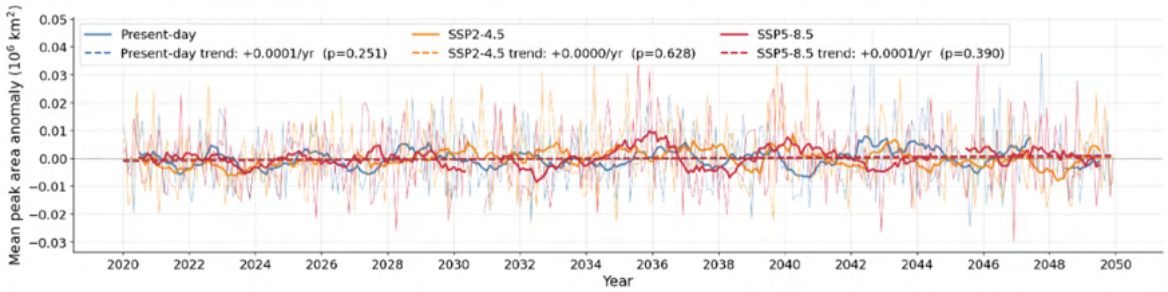

(b) Mean peak area anomaly (10^6 km^2)

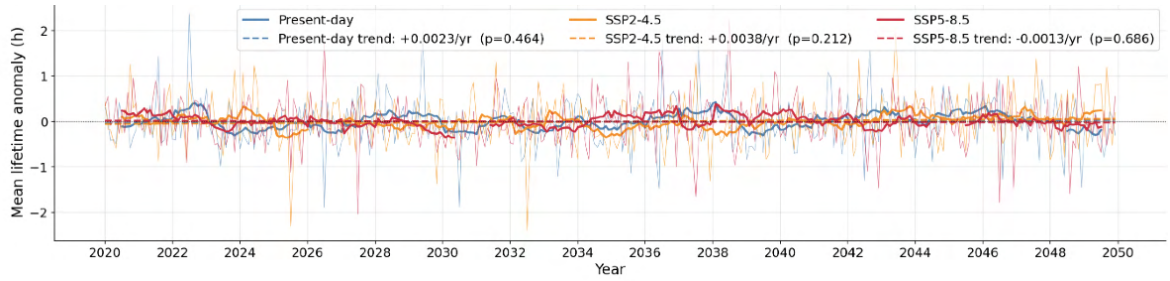

(c) Mean lifetime anomaly (h)

Figure 4.18.: Monthly de-seasoned anomalies and linear trends for light breeze events, 2020–2050.

The mean peak area anomaly for light breezes (Figure 4.18b) exhibits very small variability, with anomalies confined to $\pm 0.04 \times 10^6$ km^2. All trend slopes are negligibly small and statistically insignificant with quite high p-values, indicating that the spatial extent of light breeze events at their peak development is stable across all scenarios. Likewise, the mean lifetime anomaly (Figure 4.18c) shows no significant trend in any scenario, though it is notable that the interannual variability in lifetime anomaly is slightly larger for light breezes than for dark doldrums. Overall, the anomaly analysis for Case 2 reinforces the picture obtained from the seasonal analysis: Light breeze events are characterised by a stable frequency, size, and duration across the entire study period and across all three climate scenarios.

The spatial distribution of light breeze criterion frequency across all three scenarios and decades is shown in Figure 4.14. The overall frequency of light breeze conditions is substan-

tially lower than that of dark doldrums, typically not exceeding 2% at any grid cell, which is consistent with the stricter threshold applied. Spatially, the highest frequencies are concentrated along a narrow band spanning the Franco-Belgian coastline and extending into the southern parts of France and a secondary cluster over north-eastern Iberia. These regions benefit from a favourable combination of frequent synoptic wind events and relatively high solar resource, making simultaneous exceedance of the high capacity factor threshold most likely.

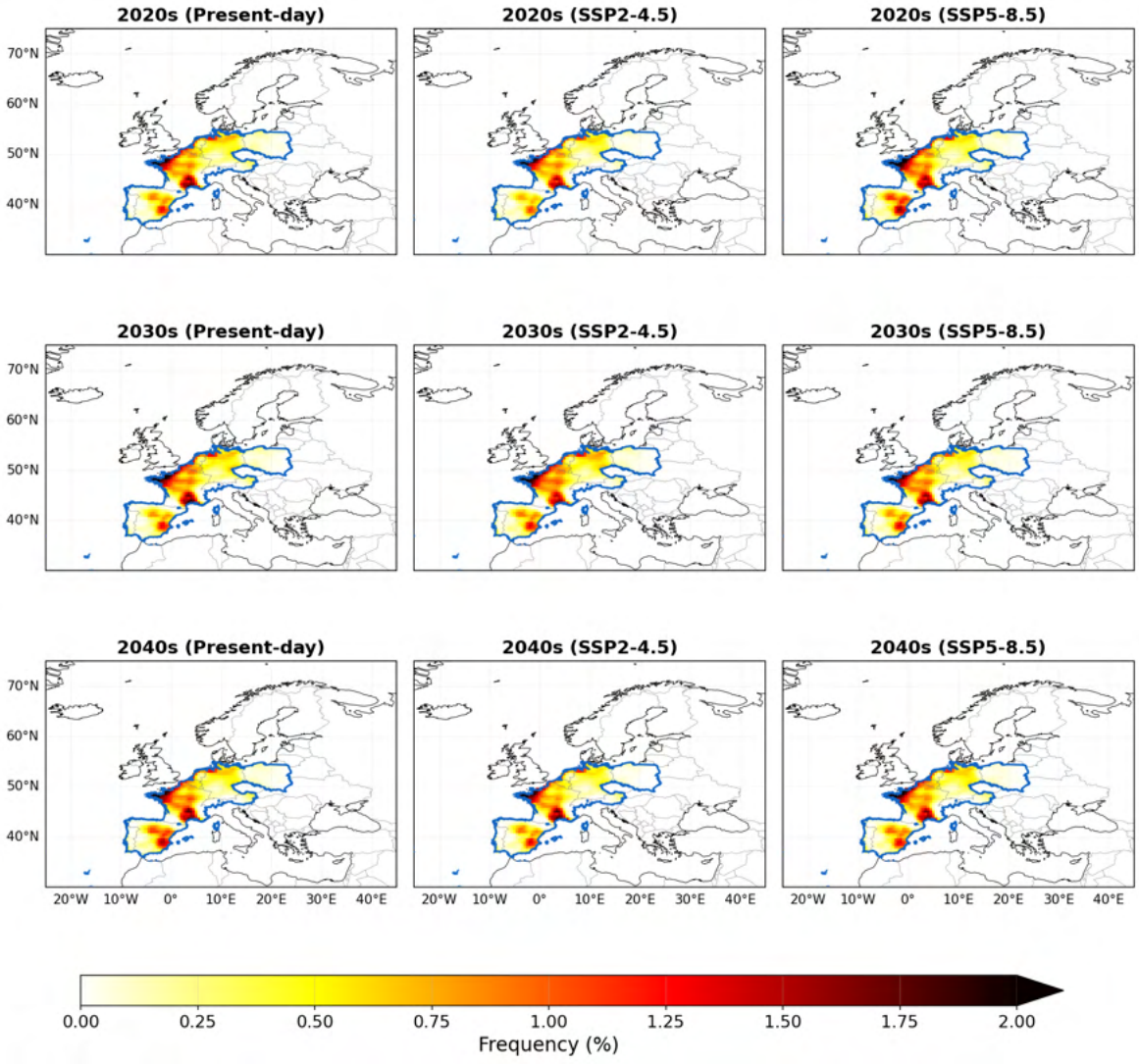

Figure 4.19.: Criterion frequency (%) of light breeze conditions by decade for each climate scenario. Blue outlines determine analysis region boundaries.

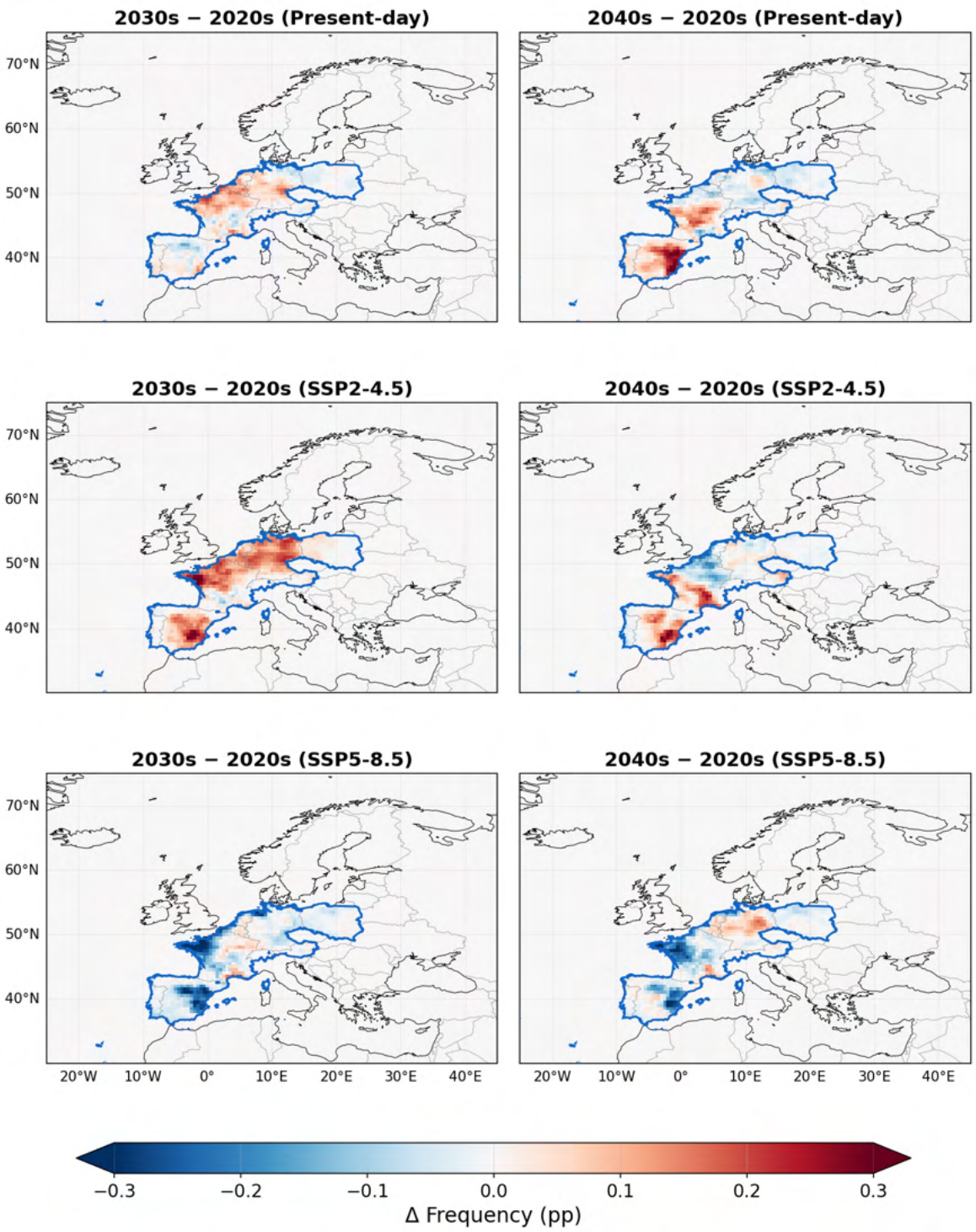

Figure 4.20.: Decadal change in light breeze criterion frequency relative to the 2020s baseline for each climate scenario. Blue outlines determine analysis region boundaries.

Across all three scenarios and all three decades, the spatial pattern is remarkably consistent, with virtually no perceptible shift in the location or spatial extent of the hotspots from the 2020s to the 2040s. Only small changes between the scenarios and ceries can be noted directly

(e.g. over the Iberian Peninsula or in northern Germany). The maximum frequencies in the hotspot regions remain in the range of 1.5–2.0% throughout, and no systematic increase or decrease is directly apparent between scenarios.

The decadal changes in light breeze criterion frequency relative to the 2020s are presented in Figure 4.20. Under Present-day forcing, both decadal difference maps show a mix of modest positive and negative anomalies without a clear spatial structure or direction, consistent with internal variability. Under SSP2-4.5, the 2030s minus 2020s panel shows a widespread positive anomaly across north-western and central Europe, suggesting an increase in light breeze frequency in the intermediate decade. However, by the 2040s this signal partially reverses over France and Germany, while positive values persist over soutth-western areas oof France and parts of Iberia. The interplay of positive and negative anomalies in the SSP2-4.5 2040s panel suggests that internal variability continues to dominate over any forced trend signal, consistent with the non-significant linear trends identified in the anomaly time series.

Under SSP5-8.5, the decadal evolution is more pronounced: the 2030s minus 2020s difference is dominated by a strong negative anomaly, particularly over western France and the western Iberian Peninsula, indicating a marked decrease in light breeze frequency during the 2030s relative to the 2020s. This negative anomaly largely remains by the 2040s, with a broad positive signal emerging over parts of Germany and southern France.

The difference in light breeze criterion frequency between each SSP scenario and the Present-day simulation is shown in Figure 4.21a and 4.21b. For SSP2-4.5 (Figure 4.21a), the full-period panel reveals a predominantly negative frequency difference across central Europe and the Iberian Peninsula, The decadal panels show that during the 2020s the two scenarios are close, while in the 2030s positive signals develop over central and south Europe. By the 2040s, a strong negative anomaly develops across the Iberian Peninsula and southern France, reaching values approaching −0.3 pp, suggesting that light breeze conditions in these regions become relatively less frequent under SSP2-4.5 compared to the Present-day reference. It is important no note that 0.3 pp still does not show extreme changes, but still measurable.

For SSP5-8.5 (Figure 4.21b), the differences with respect to Present-day are more spatially structured and of larger magnitude. The 2020s already show positive differences over the North Sea coastal region and parts of western France and Iberia, alongside negative values over northern Germany and Poland. In the 2030s, this pattern shifts, with a prominent negative anomaly over the Franco-Belgian border and a negative signal over central Europe. By the 2040s, the SSP5-8.5 minus Present-day difference becomes negative across parts of Iberia and parts of southern France, while positive differences return near the North Sea.

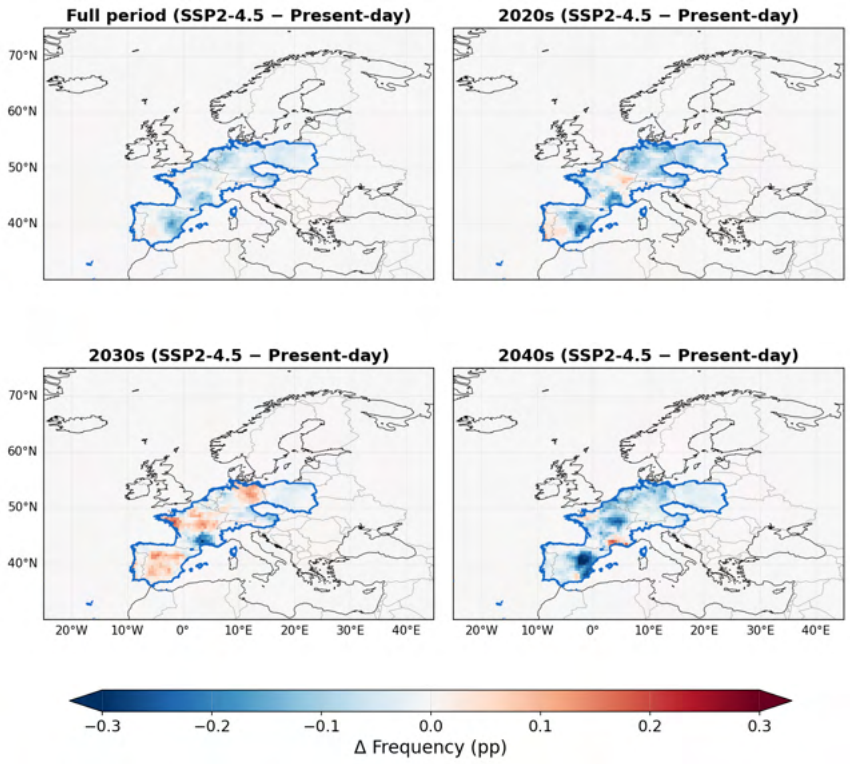

(a) SSP2-4.5 minus Present-day

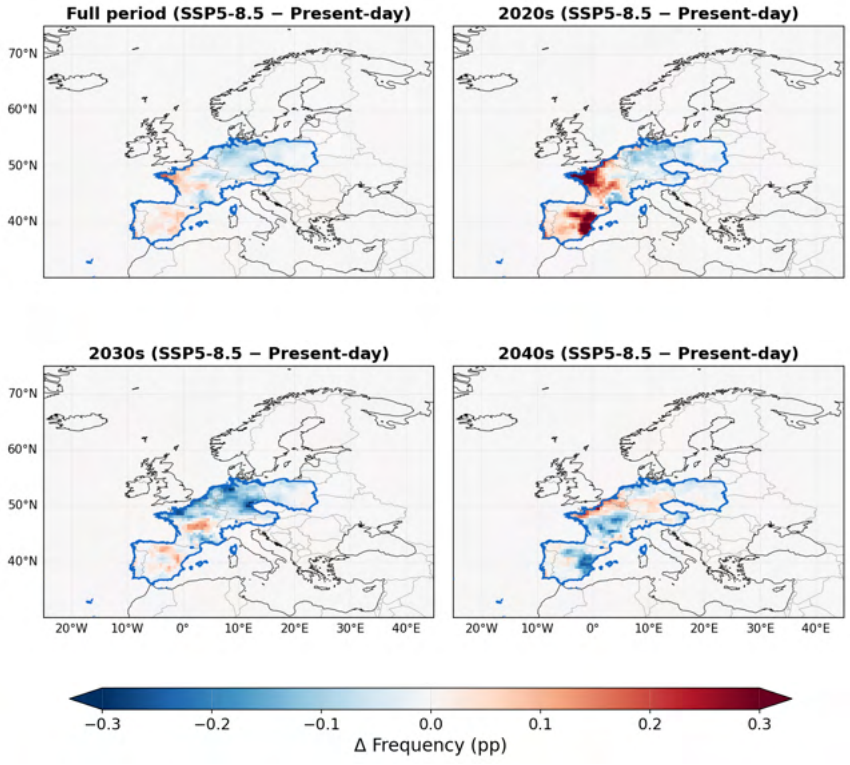

(b) SSP5-8.5 minus Present-day

Figure 4.21.: Frequency difference of light breeze conditions between future scenarios and Present-day, by decade. Blue outlines determine analysis region boundaries.

4.1.2.3. Case 3: Coexistence of Dark Doldrums over Central Europe and Light Breezes over the Iberian Peninsula

The third case scenario analyses a situation in which light breeze conditions, as defined in Section 4.1.2.2, are simultaneously detected over the Iberian Peninsula (comprising Portugal and Spain, denoted as bright areas) while dark doldrum conditions, as defined in Section 4.1.2.1, prevail in the central European region (denoted as dark areas). This scenario is of particular relevance when considering that energy grid connections between the Iberian Peninsula and the rest of Europe exhibit relatively low interconnection capacities. The scenario therefore aims to identify whether there may be a potential risk of overloading the transmission grids in the Pyrenean area under intensifying climate change conditions. Overloading could occur when it becomes economically attractive to transmit large quantities of renewable energy surplus from light breeze areas towards dark doldrum areas. It should be noted that this case study analyses the general occurrence of the simultaneous presence of light breezes and dark doldrums in the depicted regions and does not impose a minimum area threshold on the detected events. The results of this analysis are presented in the following paragraphs.

The temporal evolution of the monthly de-seasoned anomaly in the combined area of co-occurrence (i.e. the sum of the bright-country area in Iberia and the dark-country area in central Europe) is shown in Figure 4.22. The anomaly signal is characterized by high interannual variability, with monthly excursions reaching up to $\pm\,0.1{\times}10^6$ km^2. Linear trends in all three scenarios are negligibly small and statistically insignificant: the Present-day simulation yields $+0.0001\,\mathrm{km^2\,yr^{-1}}$ ($p = 0.626$), SSP2-4.5 gives $-0.0004\,\mathrm{km^2\,yr^{-1}}$ ($p = 0.122$), and SSP5-8.5 shows essentially no trend ($p = 0.913$).

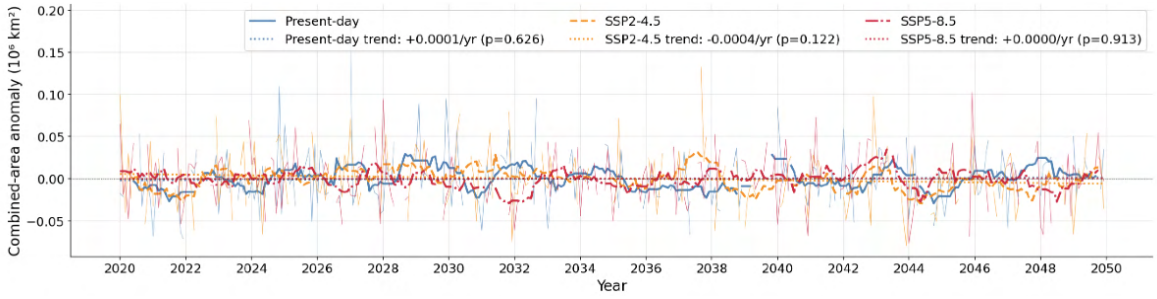

Figure 4.22.: Monthly de-seasoned combined-area anomaly (10^6 km^2) of co-occurring light breezes and dark doldrums, 2020–2050.

The seasonal distribution of co-occurrence events and the mean bright-country area during co-occurrence hours are presented in Figure 4.23. Panel (a) shows that co-occurrence events are strongly concentrated in the first half of the year, with a pronounced peak in March (approximately 340–440 co-occurrence hours across scenarios), a secondary peak in April, and elevated values in January, February, and December. The summer months (June–August) exhibit very few co-occurrence events, with total hours dropping below 40 across all scenarios. This seasonal structure mirrors that of light breezes (Section 4.1.2.2), reflecting

the dominant role of the spring irradiance maximum over the Iberian Peninsula in driving simultaneous high photovoltaic and wind capacity factors. Comparing the three scenarios, SSP5-8.5 tends to show slightly higher co-occurrence totals in the spring months, particularly in March, where it exceeds both Present-day and SSP2-4.5 by approximately 10–20%, while SSP2-4.5 produces the lowest counts in some months, suggesting that the moderate scenario may slightly suppress certain synoptic configurations that favour co-occurrence.

Panel (b) shows the mean bright-country area during co-occurrence hours as a function of month. All three scenarios exhibit a bimodal structure with peaks in February–March and a secondary maximum in July–August, separated by a relative minimum in May–June. The SSP2-4.5 and SSP5-8.5 scenarios tend to produce slightly larger mean bright areas than the Present-day reference, particularly in autumn and winter, indicating that when co-occurrence events do occur in the future scenarios, the Iberian light breeze region tends to be spatially more extensive. The Present-day scenario shows the most pronounced summer minimum in mean bright area, reaching approximately 0.022×10^6 km^2 in June, compared to 0.038×10^6 km^2 for SSP2-4.5 and 0.015×10^6 km^2 for SSP5-8.5.

The mean dark-country area per month, broken down by scenario, is displayed in Figure 4.24. The seasonal cycle of dark-country area exhibits a bimodal structure with peaks in January–March and a relative maximum in July, alongside a pronounced minimum in May and August. The Present-day simulation consistently shows the largest mean dark areas in winter and spring (up to 0.073×10^6 km^2 in January and March), while SSP5-8.5 displays a strong suppression in July, reaching values as low as 0.033×10^6 km^2. The SSP2-4.5 scenario tends to follow an intermediate trajectory throughout most of the year but shows the highest values in December, partly exceeding both other scenarios. These differences point towards scenario-dependent shifts in the frequency and spatial extent of the dark doldrum conditions prevailing over central Europe during co-occurrence episodes.

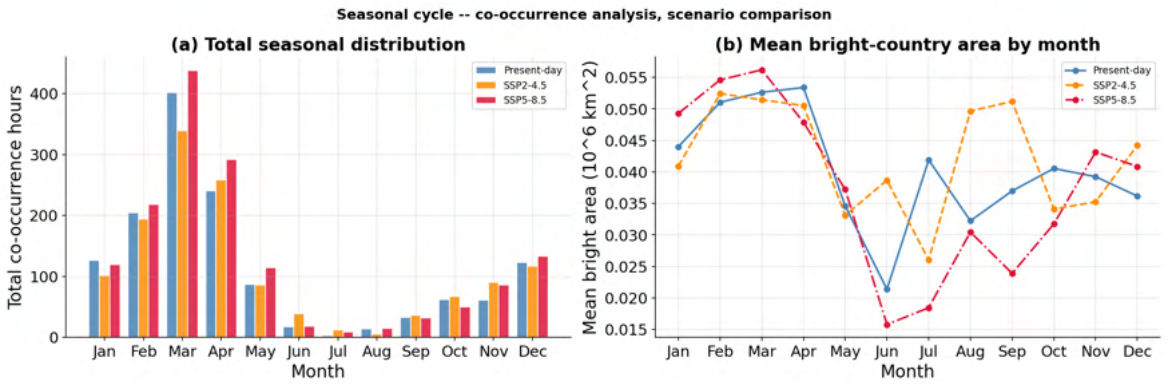

Figure 4.23.: Seasonal cycle of co-occurrence events: (a) total co-occurrence hours and (b) mean bright-country area by month – scenario comparison.

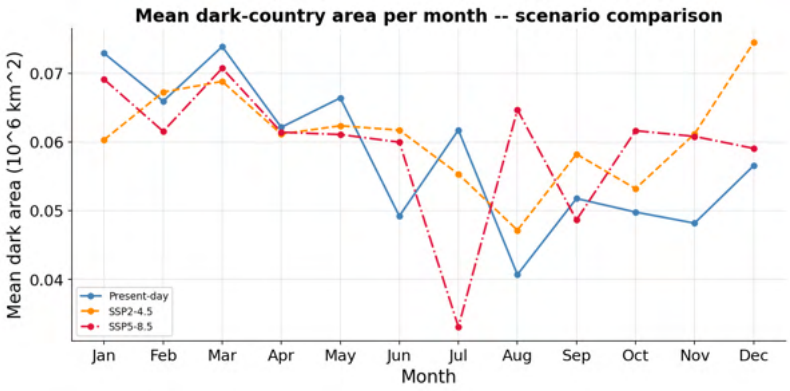

Figure 4.24.: Mean dark-country area per month during co-occurrence events – scenario comparison.

The annual number of co-occurrence hours in each year, grouped by decade and scenario, is presented in Figure 4.25. In all three scenarios, strong year-to-year variability is evident, with annual totals ranging from as few as 20 hours in some years to nearly 90 hours in others, reflecting the dominant role of internal atmospheric variability. Under Present-day forcing, the decade-to-decade show a increasing trend in co-occurrence hours per year; the 2020s and 2030s exhibit comparable variability, while the 2040s show a slight tendency towards higher annual totals in several years. Under SSP2-4.5, the 2020s are broadly similar to the Present-day simulation, while the 2030s show a moderate increase in the frequency of years with high co-occurrence totals. By the 2040s, some of the highest individual annual totals are reached under SSP2-4.5, though the interannual spread remains wide. Under SSP5-8.5, the 2020s are already characterized by a wider range of annual totals than under Present-day, with several years exceeding 60–80 hours. The 2030s show a partial reduction, while the 2040s again feature several years with elevated totals. Overall, the picture across all scenarios is one of high variability and no robust monotonic trend, consistent with the anomaly analysis.

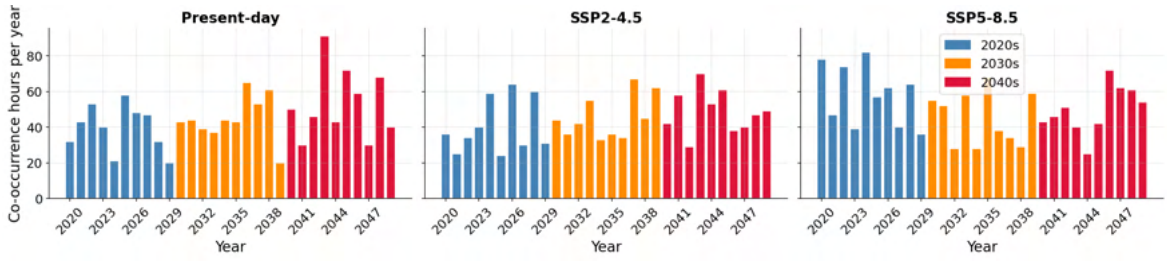

Figure 4.25.: Annual co-occurrence hours by decade for all scenarios (Present-day, SSP2-4.5, SSP5-8.5).

The probability density distributions of bright-country area and dark-country area during co-occurrence events, estimated via kernel density estimation (KDE) and stratified by decade and scenario, are shown in Figure 4.26, respectively.

For the bright-country area (Figure 4.26a), all three scenarios exhibit positively skewed distributions with the mode located near $0.02–0.03 \times 10^6$ km^2. Under Present-day forcing, a clear decadal shift is visible: the 2020s peak is the sharpest and tallest, while the 2030s and especially the 2040s show a flatter and broader distribution, indicating an increase in the occurrence of events with larger bright areas in later decades. This shift is less pronounced under SSP2-4.5 and SSP5-8.5, where the distributions for the three decades are more similar to each other, with only a slight broadening in the 2040s. Interestingly, the SSP scenarios show a lower probability density at the mode compared to Present-day, combined with more probability mass in the tail at larger areas.

For the dark-country area (Figure 4.26b), the distributions are bimodal across all scenarios, with a first peak near zero and a dominant secondary peak around $0.07–0.08 \times 10^6$ km^2. This bimodality likely reflects two distinct regimes of dark doldrum conditions during co-occurrence: one in which the dark area is spatially limited (small events along the periphery of the central European region) and one dominated by large-scale events covering much of the defined dark-country domain. The decadal shift within Present-day is modest, with the three decade curves nearly overlapping. Under SSP2-4.5, the 2030s show a notably higher and sharper secondary peak than the 2020s and 2040s, while under SSP5-8.5 the 2020s exhibit the highest secondary peak, with the 2030s and 2040s showing progressively lower density at the modal value but heavier tails.

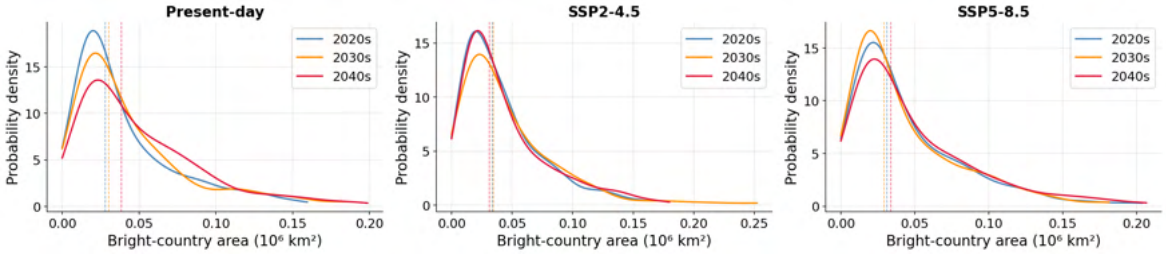

(a) Bright-country area (Iberian Peninsula).

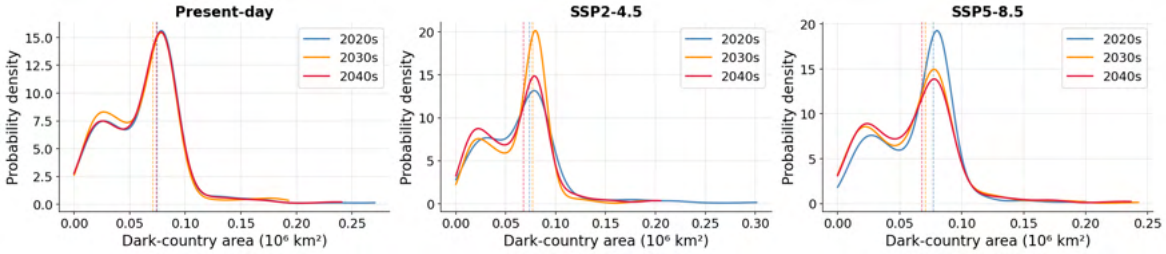

(b) Dark-country area (central Europe).

Figure 4.26.: KDE of bright- and dark-country areas during co-occurrence events by decade and scenario.

The spatial distribution of co-occurrence frequency for the full simulation period across all three scenarios is shown in Figure 4.27. Co-occurrence frequency is defined here as the fraction of time steps in which the simultaneous bright-in-Iberia and dark-in-central-Europe criterion is met at each grid cell. The spatial pattern is broadly consistent across all three

scenarios: the highest frequencies are found along the North sea coast and in the western and southern parts of France, extending into the Benelux region and northern Germany, with maximum values reaching approximately 0.5%. The Iberian interior shows another maximum, consistent with the role of the south-western Iberian Peninsula in contributing to high photovoltaic and wind capacity factors during co-occurrence events. Again, 0.5 pp do not refer to frequent events but still measurable.

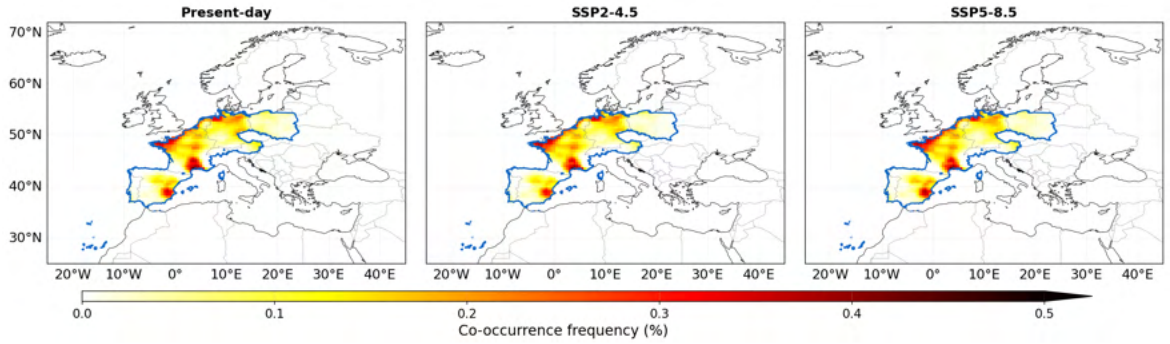

Figure 4.27.: Co-occurrence frequency (%) over the full simulation period for all three scenarios. Blue outlines determine analysis region boundaries.

The change in co-occurrence frequency relative to the Present-day reference for SSP2-4.5 and SSP5-8.5 is presented in Figure 4.28. For SSP2-4.5 (left panel), the difference map reveals a mixed pattern of modest positive and negative anomalies. Positive values of up to approximately +0.04 pp are found over the western coast of France and parts of eastern Germany, indicating a slight increase in co-occurrence frequency in these regions under the moderate scenario. Conversely, negative values appear over southern Germany, southern France, Poland and parts of Austria, suggesting a slight decrease in co-occurrence frequency there. Over the Iberian Peninsula, a weakly positive signal is visible in the south-western part of Spain and Portugal, while the north-eastern Iberian region shows slightly negative differences.

For SSP5-8.5 (right panel), the spatial pattern shares some similarities with SSP2-4.5 but exhibits a more pronounced positive signal over western France, the Benelux region, and north-western Germany, with values reaching up to +0.04 pp. The negative anomaly over central Germany and Austria is also present under SSP5-8.5, though it is slightly more spatially extended. Over Iberia, the SSP5-8.5 signal is broadly positive, particularly in the interior, indicating an increase in co-occurrence frequency under the high-radiative forcing scenario.

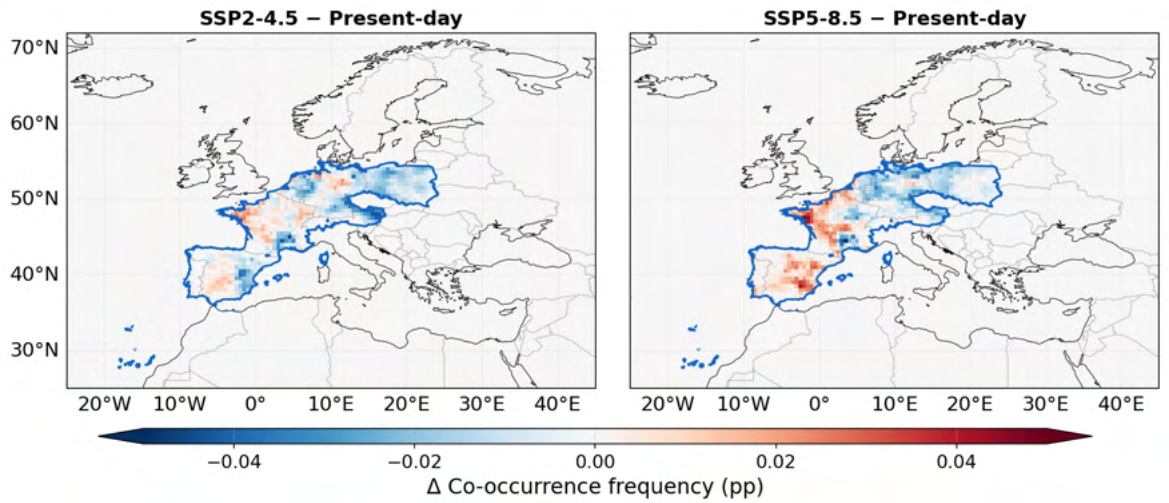

Figure 4.28.: Change in co-occurrence frequency relative to Present-day for SSP2-4.5 (left) and SSP5-8.5 (right). Blue outlines determine analysis region boundaries.

4.2. Energy Market Properties in a Changing Climate

In this chapter the results of the three energy market simulations with PowerACE, including a Present-day scenario (in the following market as „present“) and two scenarios that consider climate change effects, resulting in differing renewable profiles. As described in section 2.1.1, SSP2-4.5 considers an intermediate radiative forcing and SSP5-8.5 a stronger radiative forcing. Results are shown for the developing market prices, in the chosen market areas, as well as the annual energy generation mix per market area. An emphasis always also lays on the renewable generation.
This section particularly answers one of the central questions of this study, how the energy system will evolve in a changing climate and what impact renewable energies have on that. Even though the expansion of the energy system is externally driven, some differences in the dispatch can be found.

4.2.1. Market Prices

4.2.1.1. Annual Mean Day-Ahead Price – All Market Areas

Figure 4.29 presents the annual mean day-ahead electricity prices for all eight modeled market areas across the three scenarios SSP2-4.5, SSP5-8.5, and Present-day for the period 2020 to 2049.

Across the majority of countries, prices exhibit a broadly consistent pattern regardless of the scenario: A relatively stable or slightly declining phase during the early 2020s, followed by a pronounced upswing beginning around 2027–2030, and sustained elevated levels thereafter. The scenario spread remains modest in the near term but widens noticeably from the early

2030s onward, reflecting the increasing divergence in climatic forcing and the resulting differences in renewable resource availability and residual demand patterns.

Austria and Switzerland stand out with the steepest absolute price increases, reaching average annual values in the range of 200–250 €/MWh by the mid-2040s. France displays a distinctive trajectory, with strongly negative or near-zero average prices in the late 2020s before recovering to positive levels in the range of 50–100 €/MWh by 2045–2049. Portugal exhibits unusually high average prices in the period around 2028–2032, peaking at values exceeding 1 500 €/MWh. These spikes subside substantially after 2033, converging back towards 500–800 €/MWh. Poland and the Netherlands show moderate but steady price growth, remaining mostly within 100–200 €/MWh over the projection horizon. Germany-Luxembourg and Belgium display intermediate price levels, generally between 50–200 €/MWh, with considerable inter-annual variability. Note that partly very high prices occur when the by the TYNDP given demand can not be fulfilled. More on that can be found in the discussion of future energy system evolutions (see 4.3.2.2).

The three scenarios track each other closely for most countries, with Present-day and SSP2-4.5 often yielding near-identical results and SSP5-8.5 occasionally departing more strongly from the other two, particularly in the 2030s and 2040s, and showing slightly more extreme values in certain years, e.g. 2037 in Germany-Luxembourg, the Netherlands as well as Belgium, or in the second half of the 2040s in Austria, Switzerland and France.

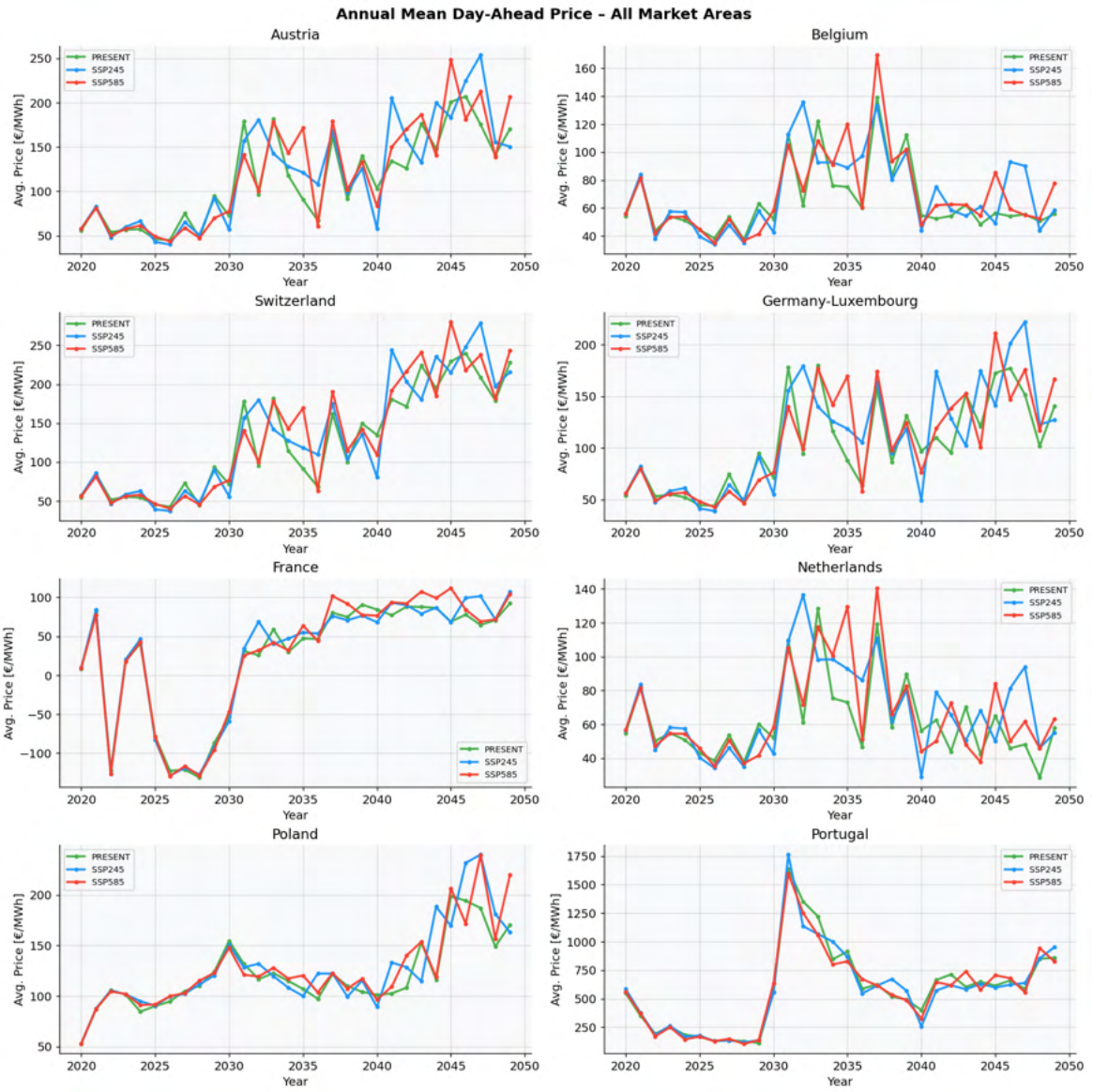

Figure 4.29.: Annual mean day-ahead electricity price for all modelled market areas (2020–2049). Each panel shows the three scenarios SSP2-4.5 (blue), SSP5-8.5 (red), and Present-day (green). Prices are averaged over all hours of each calendar year.

4.2.1.2. Daily Price Time Series – Germany-Luxembourg

Focusing a little more on the market area Germany-Luxembourg, here Figure 4.30 shows the full daily price time series (in faint colour) for Germany-Luxembourg from 2020 to 2049, smoothed with a 30-day rolling mean. All three scenarios are overlaid, with the raw daily values displayed as semi-transparent bands and the rolling mean as opaque lines.

During the first half of the 2020s, prices remain comparatively low and stable across all scenarios, broadly in line with observed market conditions. From approximately 2027

onwards, episodic price spikes become increasingly frequent and intense, reflecting the growing penetration of variable renewables and the associated periods of scarcity when wind and solar output is low. The spike events are characterized by sharp, narrow peaks in the daily series reaching 500–2 500 €/MWh, superimposed on a baseline that rises steadily over the decades. By the 2040s, the underlying 30-day rolling mean fluctuates regularly between roughly 50 and 400 €/MWh, with the three scenarios showing broadly similar magnitudes but differing timing and intensity of individual events. SSP5-8.5 tends to exhibit somewhat more pronounced peaks in certain years, consistent with greater climatic variability under the higher-emission pathway. Also a seasonal variability becomes apparent since the spikes mainly appear during the winter months.

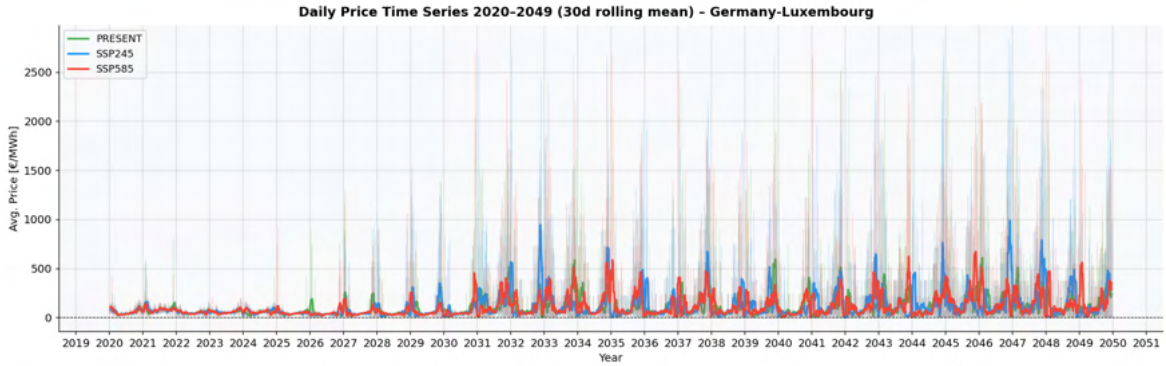

Figure 4.30.: Daily price time series for Germany-Luxembourg (2020–2049), 30-day rolling mean. Faint lines indicate raw daily averages; bold lines show the smoothed rolling mean. Scenario colours: Present-day (green), SSP2-4.5 (blue), SSP5-8.5 (red).

Figure 4.31 complements the time series by displaying the rolling 30-day price difference between Present-day and each of the two climate scenarios (Present-day–SSP2-4.5 in purple; Present-day–SSP5-8.5 in orange). In the early 2020s, the differences are small and centred around zero, indicating near-identical market outcomes under all three forcing conditions. Starting from approximately 2027, the amplitude of the difference series grows substantially, with excursions regularly reaching ±200 €/MWh and occasionally exceeding ±600 €/MWh in both directions. This bidirectional character reflects the stochastic nature of weather-driven generation: in some periods Present-day yields higher prices than the climate scenarios (positive difference), while in others the reverse holds. No strong systematic directional bias towards one scenario is apparent, though individual years can show prolonged stretches of predominantly positive or negative differences. The divergence between the two difference series (purple vs. orange) remains moderate, suggesting that the price response to climate is more strongly governed by inter-annual weather variability than by the specific emission pathway. The overall tendency though seems that differences between Present-day and SSP5-8.5 are slightly higher over the course of the time while differences between Present-day and SSP2-4.5 show higher extremes in price differences, like in year 2029, 2033, 2034, 2042, 2044, 2046 or 2048.

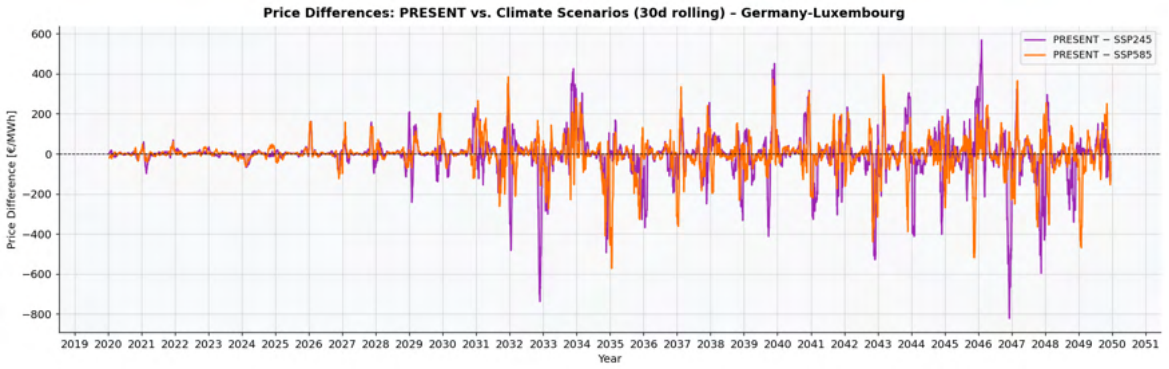

Figure 4.31.: Price differences Present-day–SSP2-4.5 (purple) and Present-day–SSP5-8.5 (orange) for Germany-Luxembourg, 30-day rolling mean. Shaded areas indicate the sign of the difference; positive values indicate higher prices in the Present-day scenario.

4.2.2. Annual Generation Mix

Figures 4.32 to 4.39 Present-day the annual generation mix for each of the eight modeled market areas. Each figure is structured identically: the top row shows absolute annual generation in GWh for SSP2-4.5, SSP5-8.5, and resent on a shared y-axis; the bottom row displays the differences Present-day–SSP2-4.5 and Present-day–SSP5-8.5 on a shared difference axis. Positive (above zero) contributions in the difference plots indicate that Present-day generates more from a given carrier in that year, whereas negative contributions indicate the opposite.

A cross-cutting observation applicable to virtually all countries and scenarios is the progressive decline of fossil thermal generation (natural gas, coal, lignite, and fuel oil) and the concurrent strong expansion of wind and solar capacity over the 30-year projection horizon, irrespective of the specific climate scenario. The scenario differences are generally smaller than the overall trend magnitudes, confirming that the strategies towards a darcarbonization of the energy sector of each market area dominates over the climate-pathway-sensitive.

4.2.2.1. Austria

Austria's generation mix (Figure 4.32) undergoes one of the more dramatic absolute expansions in the dataset, with total annual generation growing from roughly 15 000 GWh in 2020 to above 50 000 GWh by 2049, driven almost entirely by the buildout of solar PV (yellow) and wind onshore (light blue). In 2020, natural gas Combined Cycle Gas Turbine (CCGT) (orange) and natural gas gas turbines together constitute a non-negligible share of around 5 000–8 000 GWh, serving as the primary dispatchable backup. This contribution declines steadily over the 2020s and becomes marginal by the early 2030s, after which gas generation is largely confined to occasional peaking roles. A small contribution from unknown steam turbines and waste CCGT is visible in the early years but effectively disappears before 2030.

Solar PV expands continuously and becomes the dominant generation carrier by the late 2020s, ultimately reaching an estimated 30 000–40 000 GWh annually by 2045–2049. Wind onshore follows a similar growth trajectory, though at somewhat lower absolute levels. Pumped hydro storage (teal) provides a persistent and growing negative contribution in the charging domain, reaching values of around −10 000 GWh per year by 2035–2040, reflecting the increasing need for intraday flexibility as solar penetration rises. The three scenarios are very similar in their overall composition and magnitude throughout the projection period, with the main differences confined to individual years. The hard coal CCGT, which appears as a minor contributor in the first few years, is completely absent by the mid-2020s.

The difference panels (Present-day–SSP2-4.5 and Present-day–SSP5-8.5) show alternating positive and negative deviations in the range of ±3 000–4 500 GWh, concentrated in solar and wind, reflecting inter-annual weather variability rather than any systematic scenario divergence. In several years around 2037–2042, the Present-day–SSP2-4.5 difference is characterised by a notable positive solar surplus alongside a simultaneous negative pumped hydro deviation in the charge domain. In some years like 2036, 2040, 2041, 2044 and 2047 the hydrogen contribution tends to result in higher deviation during SSP2-4.5 conditions but in both SSP scenarios in total with higher hydrogen dispatches in most of the years than in the Present-day scenario. Solar power is slightly less contributed in the SSP scenarios compared to Present-day conditions. For wind power no clear trend can be identified.

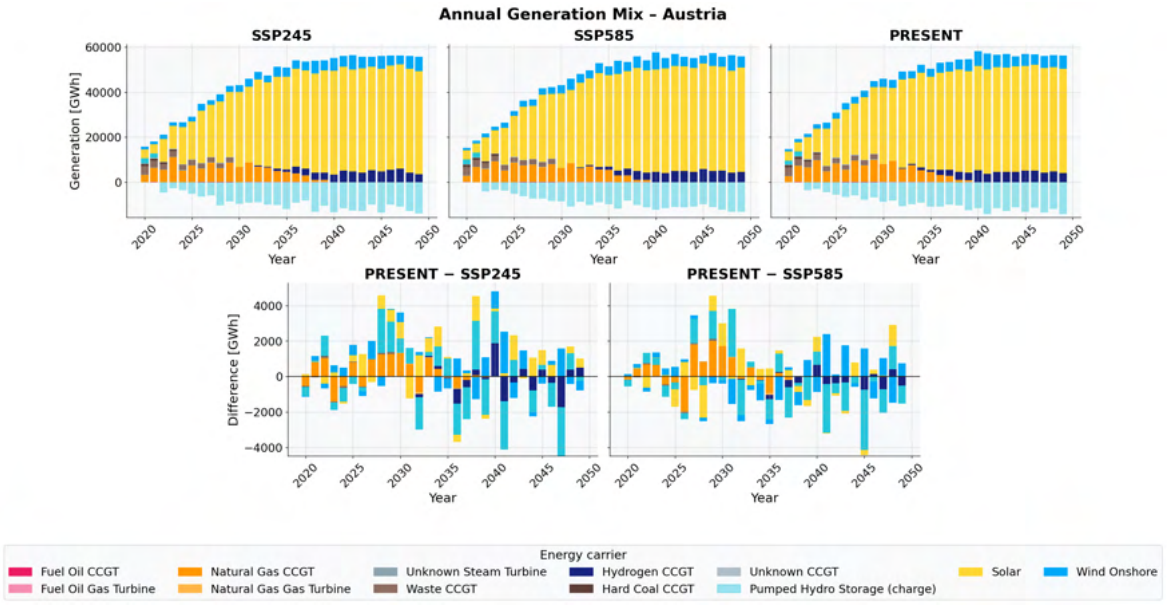

Figure 4.32.: Annual generation mix for Austria (2020–2049). Top row: absolute generation by carrier and scenario. Bottom row: annual differences between the Present-day scenario and each climate scenario. Pumped hydro storage appears in the negative domain due to charging load.

4.2.2.2. Belgium

Belgium (Figure 4.33) begins the projection period with a generation portfolio that is heavily shaped by two dominant technologies: nuclear (uranium steam turbine, purple) and natural gas CCGT (orange), together accounting for the bulk of the approximately 90 000 GWh produced annually in the early 2020s. A smaller but visible contribution from hard coal steam turbines is Present-day in the first few years and is essentially phased out by the mid-2020s, consistent with Belgium's early coal exit. Fuel oil gas turbines appear only as a negligible sliver in the first years and vanish swiftly thereafter.

The nuclear fleet begins declining from the late 2020s and falls steeply through the early 2030s as reactors are progressively decommissioned, in line with Belgium's nuclear phase-out policy. Natural gas CCGT follows a broadly similar downward trajectory, though the decline is more gradual and extends into the 2040s. The combined effect is a substantial reduction in total annual generation to approximately 65 000–75 000 GWh by the mid-2030s. Solar PV (yellow), wind onshore (light blue), and wind offshore (dark blue) expand steadily to compensate, with offshore wind becoming a particularly notable contributor from the 2030s onwards as Belgium continues to develop its North Sea resources. Hydrogen CCGT (dark navy) appears from approximately 2033–2035 as a low-carbon dispatchable substitute for gas, growing to a modest but non-trivial share by the late 2040s. Waste CCGT provides a small but stable baseload contribution throughout the entire period. Pumped hydro storage is visible as a minor negative charging contribution.

The difference plots between Present-day and the two climate scenarios are characterized by large deviations, on- and offshore wind fluctuations (up to ±8 000 GWh) resulting in differing gas and from approximately 2035 hydrogen dispatches. Despite the fluctuations, in SSP5-8.5 the overall wind dispatch seems to be lower in the late 2030s and early 2040s compared to Present-day than in SSP2-4.5. The differences in solar in terms of amount are not differing a lot, while around 2030 Present-day has slightly more solar energy dispatched than SSP2-4.5, except in the late 2030s and early 2040s, when slghtly more solar energy is dispatched , especially during SSP5-8.5 conditions, compared to SSP2-4.5.

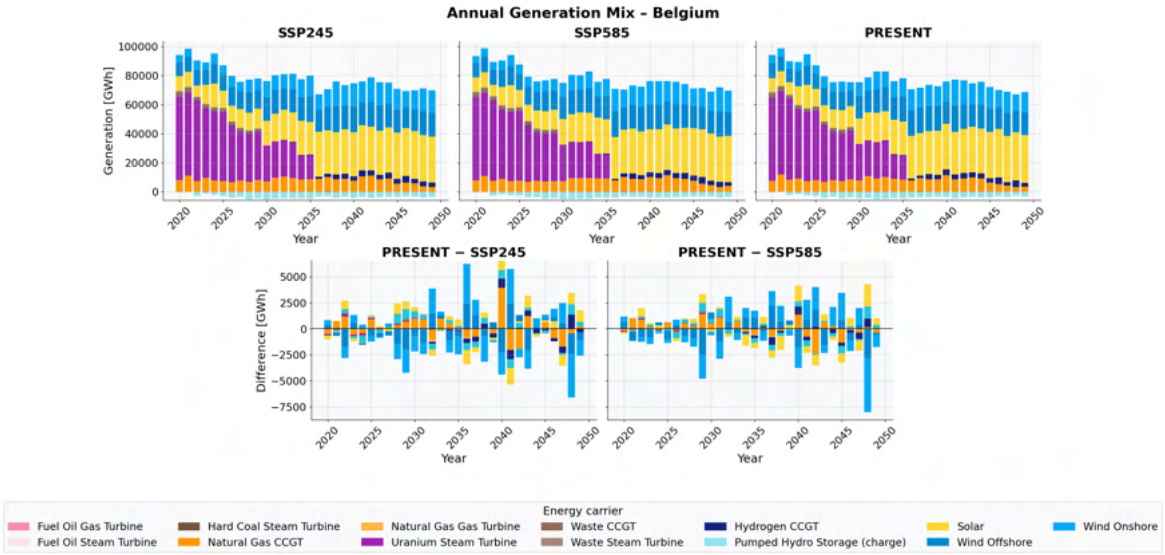

Figure 4.33.: Annual generation mix for Belgium (2020–2049). The large initial nuclear share (purple) declines progressively; solar, wind, and hydrogen CCGT expand. Difference panels highlight inter-annual variability dominated by nuclear and offshore wind deviations.

4.2.2.3. Switzerland

Switzerland (Figure 4.34) presents one of the structurally most distinctive generation mix profiles in the model domain. For the first roughly two decades of the simulation, the mix is dominated by two carriers: nuclear (uranium steam turbine, purple), contributing approximately 25 000–35 000 GWh annually, and solar PV (yellow), which grows steadily from a comparatively modest base in 2020. Natural gas CCGT and natural gas gas turbines are present as minor contributors in the early 2020s, providing backup capacity, but their combined share rarely exceeds 2 000–3 000 GWh and declines to near zero by the late 2020s. Waste CCGT and waste steam turbines provide a small but steady baseload contribution throughout much of the projection period, in the range of 2 000–4 000 GWh.. A negligible contribution from fuel oil gas turbines is visible only in the very first simulation years.

The most visually striking feature of the Swiss generation mix is the abrupt step-down in nuclear generation occurring in the 2030s. This reduces nuclear output to below 10 000 GWh within one to two years, and nuclear generation is essentially absent from the mix by 2040. Solar PV expands strongly to compensate, ultimately reaching estimated values of 30 000–35 000 GWh by 2045–2049 and accounting for the vast majority of positive generation. Wind onshore contributes a very small but slightly growing share, while pumped hydro storage (teal) maintains a persistent and substantial (charging) contribution throughout the entire period, fluctuating between approximately −5 000 and −12 000 GWh.

The difference plots between Present-day and the two climate scenarios are modest relative to the overall generation levels, with deviations primarily in the range of ±1 000–3 500 GWh. The dominant source of these differences is solar PV and pumped hydro storage, with pumped hydro differences in the charge domain occasionally reaching −2 000 GWh. In most

of the years time frames when Present-day provides more solar irradiance than the SSP scenarios. Another more pronounced positive deviation concentrated around 2028–2030 reflects a period where Present-day conditions generate more from both solar and pumped hydro discharge relative to the climate scenarios.

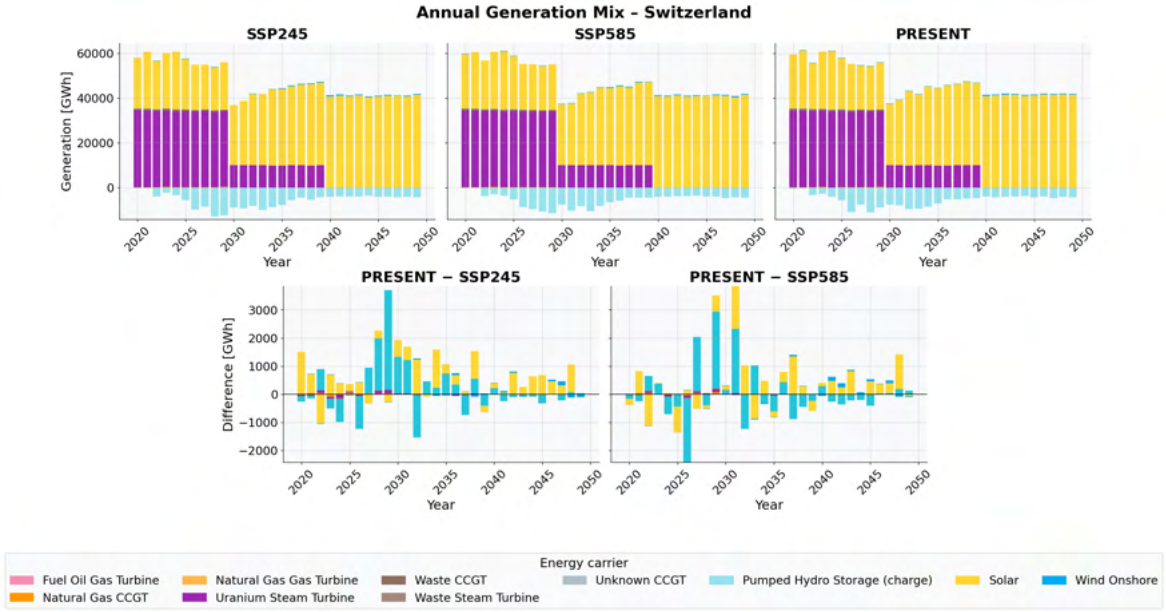

Figure 4.34.: Annual generation mix for Switzerland (2020–2049). The abrupt step-down in nuclear generation around 2038 is clearly visible across all scenarios. Solar PV expands strongly thereafter, while pumped hydro storage remains a consistent negative contributor.

4.2.2.4. Germany-Luxembourg

Germany-Luxembourg (Figure 4.35) represents the largest market in the dataset and accordingly the most complex generation mix. In 2020, the portfolio spans a broad range of carriers: hard coal steam turbines, natural gas CCGT (orange) and natural gas gas turbines, lignite CCGT and lignite steam turbines (dark brown), uranium steam turbines (nuclear, purple), as well as already significant wind onshore and solar PV contributions. Minor contributors in the early years include biofuel internal combustion engines and biofuel CCGT, both of which disappear within the first five years of the simulation as they are pushed out of merit order. Waste CCGT and waste steam turbines provide a small but stable contribution of approximately 10 000–15 000 GWh throughout the entire period.

The fossil phase-out proceeds in a broadly consistent sequence across all three scenarios: hard coal exits first, with its contribution declining from roughly 50 000–70 000 GWh in 2020 to near zero by 2030. Lignite follows a slightly slower trajectory, persisting at 20 000–40 000 GWh into the early 2030s before dropping sharply. Natural gas CCGT maintains a more resilient role through the 2030s as a dispatchable backup for variable renewables, declining more gradually to a minor peaking share by the mid-2040s. Nuclear, which contributes around 20 000–30 000 GWh in the early years, is phased out completely by the

mid-2020s in line with Germany's nuclear exit. Hydrogen CCGT emerges as a growing dispatchable contributor from the late 2030s, reaching an estimated 20 000–40 000 GWh by 2049; under some scenarios this generation level nearly rivals that of natural gas plants, as H_2-ready power plants are progressively converted to hydrogen in the 2030s.

Wind onshore and solar PV grow to jointly dominate the generation mix from the mid-2030s onwards, with solar PV ultimately reaching approximately 150 000–200 000 GWh and wind onshore a comparable magnitude. Wind offshore adds a further 30 000–60 000 GWh. Pumped hydro storage and Li-Ion battery storage (both in the charge domain) expand steadily in line with the growing flexibility requirement, jointly reaching −10 000 to −20 000 GWh per year by the 2040s.

The difference plots for DE-LU are notable for the relatively large absolute magnitudes of individual-year deviations, up to ±40 000 GWh, driven primarily by wind onshore and solar. SSP5-8.5 differences are generally more moderate in absolute terms for DE-LU, suggesting closer overall agreement between Present-day and the high-radiative forcing driven climate for wind resource in this region. For both SSP scenarios around 2030, less wind power is dispatched in the Present-day scenario, while in late 2030s and the 2040s in most of the years less wind power is dispatched for the SSP scenarios than the Present-day scenarios with exceptions especially in for example 2040. For the SSP5-8.5 scenario this effect is even stronger. In most of the years from 2035, more solar energy is dispatched, especially for the SSP5-8.5 scenario. The lignite and coal contributions to the difference plots are non-zero only in the early years, where SSP2-4.5 shows the highest coal dispatches, disappearing entirely once these carriers exit the mix.

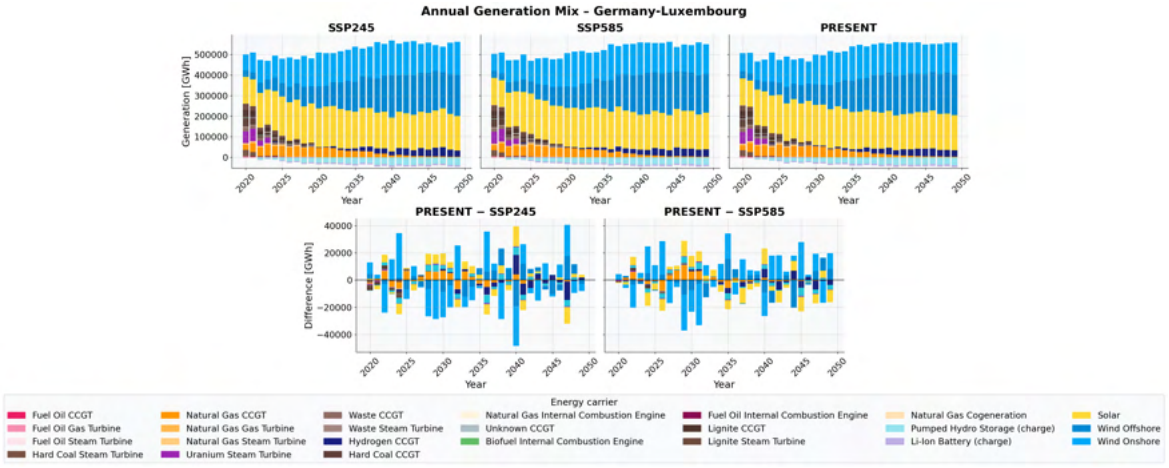

Figure 4.35.: Annual generation mix for Germany-Luxembourg (2020–2049). The transition away from coal and lignite towards wind and solar is clearly visible. Difference plots show high inter-annual variability driven primarily by wind and solar deviations of up to ±40 000 GWh.

4.2.2.5. France

France (Figure 4.36) is the largest producer in absolute terms across all modeled countries, with annual generation in the range of 400 000–580 000 GWh. The defining structural feature is the overwhelming dominance of nuclear power (uranium steam turbine, purple), which accounts for approximately 300 000–400 000 GWh per year in the early 2020s and constitutes the large majority of total French generation. The residual mix in this period includes natural gas CCGT (orange), fuel oil CCGT, fuel oil gas turbines, and fuel oil cogeneration – the latter three being minor carriers present only in the first few simulation years before being displaced by renewables. Hard coal steam turbines contribute a small but visible share of roughly 5 000–10 000 GWh in the early 2020s and are absent by 2025. Natural gas gas turbines and natural gas steam turbines add minor contributions that persist somewhat longer but decline steadily through the late 2020s.

Beginning around 2026–2028, the nuclear fleet enters a rapid decline phase as ageing reactors are progressively decommissioned without replacement. This decline is among the structurally most significant transitions in the entire model domain: nuclear output falls from roughly 350 000 GWh to approximately 100 000–150 000 GWh within a decade, and by the early 2040s, nuclear generation stabilises at this lower level, representing the contribution of a reduced number of newer or life-extended units. The simultaneous expansion of solar PV (yellow) and wind onshore and offshore only partially compensates for this loss, resulting in a net reduction in total annual generation towards 400 000–450 000 GWh by 2049. Hydrogen CCGT begins to appear from the mid-2030s as a dispatchable, low-carbon replacement for the departing gas capacity. Pumped hydro storage (teal) remains present throughout the period as a charging load, albeit at modest absolute levels compared to the overall generation volumes.

The difference plots between Present-day and the two climate scenarios are notable for the unusually large deviations visible in the mid-2030s, reaching values of ±10 000–15 000 GWh in individual years, with nuclear dispatch and wind generation the primary contributors. A strong negative excursion in Present-day–SSP2-4.5 around 2036 of approximately −15 000 GWh, dominated by nuclear and natural gas, indicates a year in which Present-day climate is less favorable for nuclear utilization than SSP2-4.5. Differences between the climate scenarios become more apparent from the late 2030s and particularly in the 2040s, especially for wind energy. From 2037 onwards, wind energy contributions under both SSP scenarios tend to be lower than under Present-day conditions in most years – with the exception of 2039, 2040, 2048, and 2049 – and the effect is more pronounced under SSP5-8.5. In years with comparably low or high wind contributions, nuclear and partly solar dispatch tends to follow a similar pattern. As a result, solar contributions are to some degree dependent on wind feed-in levels; however, in general – and again with year-to-year exceptions due to climate variability – there is a tendency towards more dispatched solar energy in the late 2030s and 2040s under SSP5-8.5 in particular. Under SSP2-4.5, the positive and negative deviations largely balance out over the years.

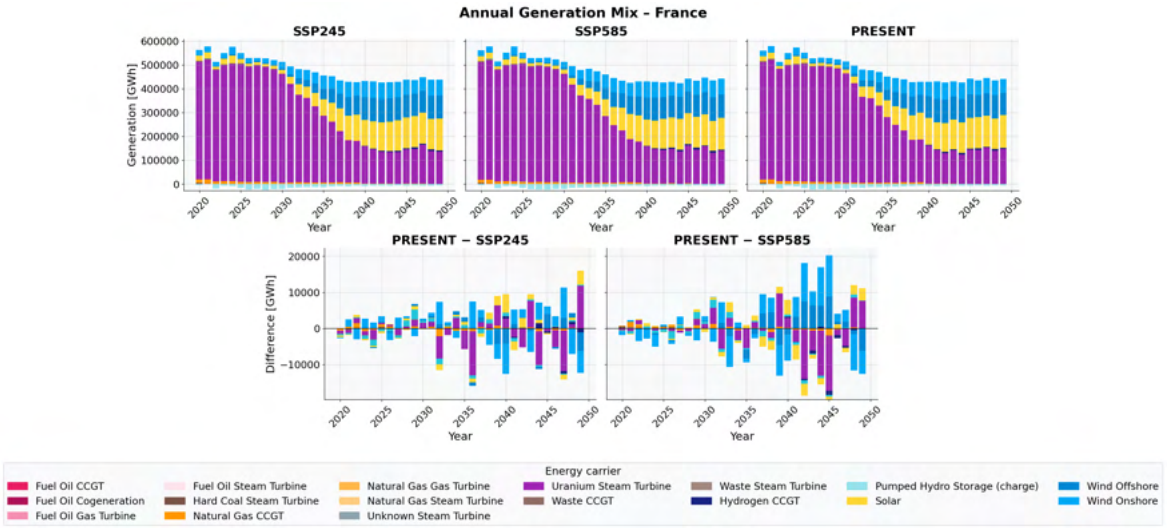

Figure 4.36.: Annual generation mix for France (2020–2049). Nuclear generation (purple) dominates the early period and declines substantially from the late 2020s. The growing solar and wind contributions partially offset this decline. Difference plots highlight the sensitivity of nuclear dispatch in the transition period.

4.2.2.6. Netherlands

The Netherlands (Figure 4.37) starts from a generation mix in which natural gas CCGT (orange) contriibutes 35 000–45 000 GWh annually in 2020, supplemented by hard coal steam turbines at roughly 15 000–20 000 GWh. A small contribution from uranium steam turbines (nuclear, purple) is visible in the very early simulation years, which declines steadily and is absent by the late 2020s. Waste CCGT, waste steam turbines, and natural gas internal combustion engines each add minor contributions in the range of 1 000–5 000 GWh that persist for a few years before fading. Hard coal is phased out relatively quickly, effectively exiting the generation mix by the late 2020s.

Wind onshore (bright blue) and solar PV (yellow) are already present in 2020 and expand continuously throughout the projection period. Wind offshore (dark blue) constitutes a growing and ultimately dominant contribution from the late 2020s onwards. By 2040–2049, offshore wind alone contributes an estimated 40 000–60 000 GWh, making it the single largest generation source. Solar PV grows in parallel to reach approximately 30 000–40 000 GWh. Natural gas CCGT declines progressively through the 2030s and 2040s, retaining a residual peaking role until the late 2040s. Hydrogen CCGT emerges as a low-carbon dispatchable technology from around 2033–2035, growing steadily to approximately 10 000–15 000 GWh by 2049. Total annual generation increases from roughly 90 000 GWh in 2020 to approximately 130 000–140 000 GWh by 2049.

The difference plots show moderate deviations in the range of ±4 000–7 000 GWh, with contributions primarily from wind onshore, offshore wind, solar, and natural gas. Under both SSP scenarios, the natural gas contribution is lower compared to Present-day. Solar dispatch is also lower in most years under both SSP scenarios, with the exception of the late

2030s and early 2040s; this effect is slightly more pronounced under SSP5-8.5. Conversely, wind contributions are lower under the SSP scenarios in most years, with the exception of a period in the late 2030s and early 2040s.

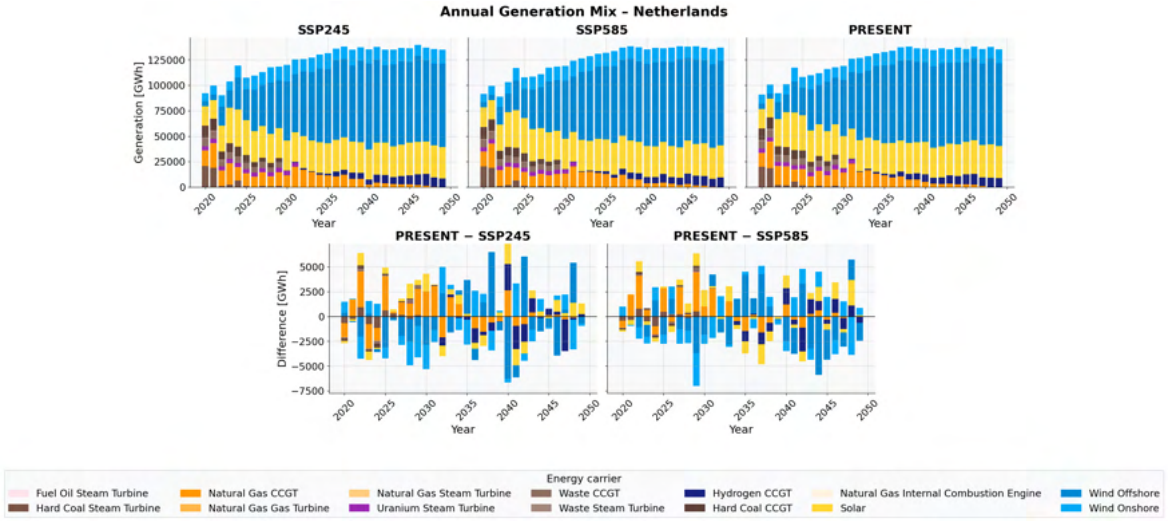

Figure 4.37.: Annual generation mix for the Netherlands (2020–2049). Natural gas is progressively replaced by offshore wind and solar PV. Hydrogen CCGT emerges as a dispatchable backup technology from the mid-2030s onwards.

4.2.2.7. Poland

Poland (Figure 4.38) presents the slowest decarbonisation trajectory among all modelled countries, and its generation mix reflects the structural legacy of a highly coal-dependent power system. In 2020, hard coal steam turbines and hard coal CCGT together contribute approximately 60 000–80 000 GWh, while lignite steam turbines and lignite CCGT add a further 40 000–60 000 GWh, such that coal and lignite together account for well over half of the approximately 160 000 GWh produced annually. Natural gas CCGT and natural gas gas turbines contribute a relatively modest share of around 10 000–20 000 GWh, serving primarily as mid-merit and peaking capacity. Minor contributors visible only in the first years include fuel oil CCGT and biofuel CCGT, both of which disappear by the mid-2020s. A small contribution from biofuel CCGT also exits the mix within the first decade.

The transition away from coal is slow but consistent across all three scenarios. Hard coal steam turbines begin declining noticeably from the mid-2020s, falling from their 2020 peak to approximately 20 000–30 000 GWh by 2035 and continuing to decline, though they remain visible throughout the simulation period at a residual level of 5 000–15 000 GWh by 2049. Lignite shows a similar pattern, declining more gradually and remaining a non-trivial contributor of approximately 10 000–20 000 GWh even in 2049. Natural gas CCGT declines in parallel with coal but retains a peaking role longer. Wind onshore and solar PV grow consistently throughout, with solar PV expanding particularly rapidly from the late 2020s

onwards. Wind offshore begins to appear from approximately 2030, adding a growing contribution that reaches an estimated 20 000–30 000 GWh by the late 2040s.

A notable structural feature is the introduction of nuclear power (uranium steam turbine, purple) from approximately 2033–2035. Nuclear generation grows from a few thousand GWh at introduction to approximately 30 000–50 000 GWh by 2049, becoming one of the primary baseload contributors in the later decades alongside wind and solar. Lignite CCGT and hard coal CCGT are present as minor carriers that phase out progressively through the 2020s and 2030s.

The difference plots for Poland show large alternating deviations of up to approximately ±10 000 GWh per year, with contributions from wind, nuclear dispatch, and residual coal and lignite. In years where Present-day conditions provide more wind resources than the SSP scenarios – which is the case in most years from 2025 onwards, particularly for SSP5-8.5 – coal and lignite are partially displaced, generating a negative fossil-fuel difference offset by a positive wind difference. During a few years, mainly around 2030, the opposite is the case. For solar power, no clear trend is discernible.

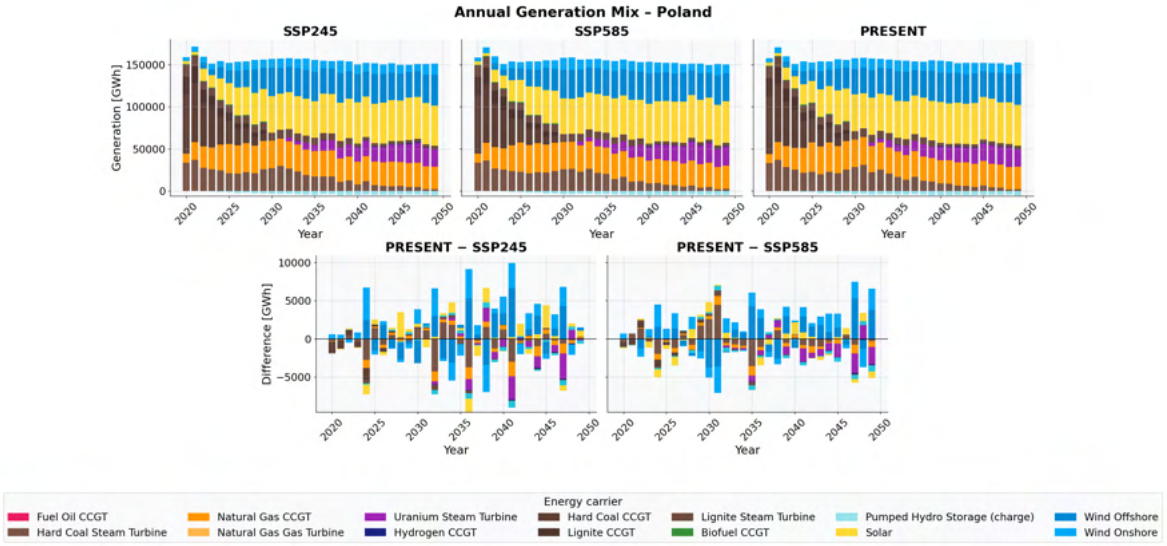

Figure 4.38.: Annual generation mix for Poland (2020–2049). The fossil-heavy initial mix dominated by hard coal and lignite declines gradually, while wind and solar expand. Nuclear (uranium steam turbine) enters the mix from the mid-2030s. Decarbonisation is the slowest among all modelled countries.

4.2.2.8. Portugal

Portugal (Figure 4.39) is one of the smaller markets in the dataset, with total annual generation rising from approximately 45 000–50 000 GWh in 2020 to 60 000–65 000 GWh by 2049. The generation mix in 2020 is already comparatively clean by European standards, with wind onshore (light blue) and solar PV (yellow) constituting a meaningful share alongside natural gas CCGT (orange) as well as hard coal (brown). Fuel oil CCGT, fuel oil gas turbines,

and fuel oil steam turbines are present as minor carriers in 2020, each contributing only a few hundred to low thousands of GWh; these fossil oil-based units are progressively decommissioned and are entirely absent from the mix by the late 2020s. Gasoil internal combustion engines similarly appear only fleetingly in the earliest simulation years before disappearing. A small contribution from waste steam turbines provides a minor but consistent baseload of around 500–1 000 GWh throughout most of the period.

Natural gas CCGT declines steadily from the early 2020s onwards, falling from approximately 10 000–15 000 GWh to near zero by around 2033–2035, after which natural gas generation is essentially absent from the Portuguese mix. Wind onshore expands robustly to compensate, and solar PV grows even more rapidly, ultimately becoming the single largest generation source by the late 2030s. Pumped hydro storage charging (teal, negative domain) grows progressively as the renewable fleet expands and the need for intraday flexibility increases, reaching approximately −5 000 to −8 000 GWh per year by the 2040s.

The difference plots show a broadly moderate pattern for most of the simulation period, with typical annual deviations in the range of ±1 000–2 000 GWh attributed primarily to wind and solar fluctuations. A striking exception is a very large positive excursion in Present-day–SSP2-4.5 concentrated around 2037–2040, where individual years show wind-dominated differences reaching approximately +4 000–5 000 GWh. For most of the years in the SSP5-8.5 scenario as well as from the mid 2030s for the SSP2-4.5 scenario wind contributions tend to be higher than during Present-day conditions. Solar ciontributions are mostly smaller than during Present-day conditions, especially for the SSP5-8.5 scenario. SSP2-4.5 shows some stronger exceptions like, 2034, 2038, 2047 and 2048.

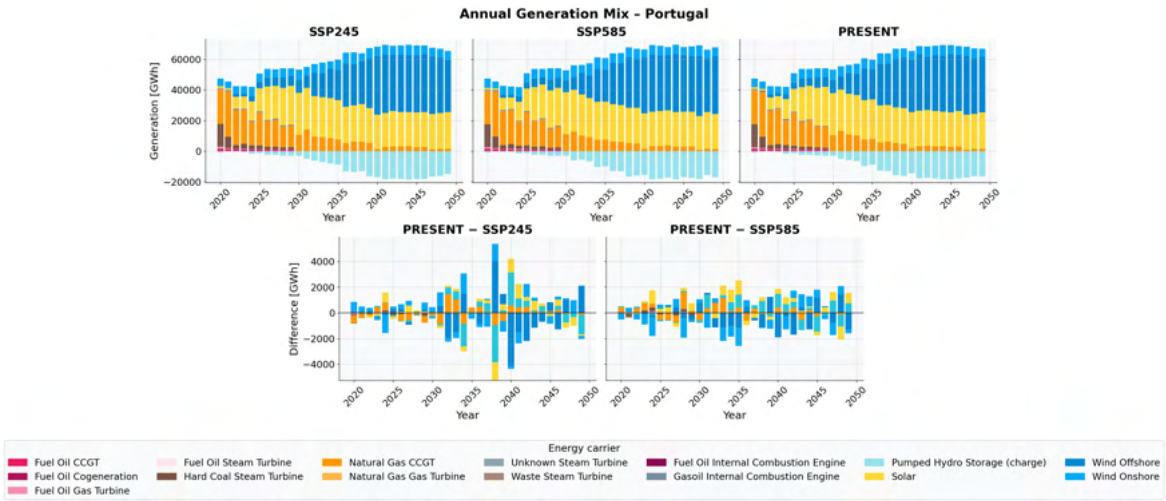

Figure 4.39.: Annual generation mix for Portugal (2020–2049). Wind onshore and solar PV dominate throughout. The Present-day–SSP2-4.5 difference plot shows a pronounced positive wind excursion around 2037–2040, indicative of a period of anomalously high wind yield under Present-day climate forcing.

4.2.3. Renewable Energy Share

4.2.3.1. Annual Renewable Energy Share – All Countries by Scenario

Figure 4.40 presents the annual renewable energy share (wind and solar relative to total positive generation) for all eight countries under each of the three scenarios. The three panels (SSP2-4.5, SSP5-8.5, Present-day) share a common y-axis ranging from 0 to 100%.

Several structural observations emerge. First, the trajectories of the three scenarios are remarkably similar within each country, confirming that the decarbonisation pathway is predominantly driven by assumed capacity expansion rather than climate-induced resource variability. Second, Germany-Luxembourg (brown) consistently leads the transition, reaching above 80% renewable share already by the late 2020s and stabilising near 90–95% from 2030 onwards. Switzerland (purple) shows a step-change structure reflecting the nuclear phaseout, with renewable share rising abruptly from around 40% to near 100% after approximately 2038 as nuclear retires and solar expands. Austria (green) and Netherlands (orange) follow broadly similar S-shaped trajectories, converging towards 90–95% by the mid-2040s.

France (blue) is the clear outlier, maintaining an unusually low renewable share of approximately 5–10% through the 2020s owing to its large nuclear fleet, then rising steeply from around 2028–2030 as nuclear capacity declines and renewables scale up, ultimately converging towards 65% by 2049 – the lowest endpoint among all countries. Belgium (grey) and Portugal (cyan) both show intermediate trajectories reaching approximately 90% by 2049. Poland (olive) is the slowest transition, reaching only 55–65% renewable share by 2049 under all scenarios, consistent with the continued presence of coal and lignite in the generation mix.

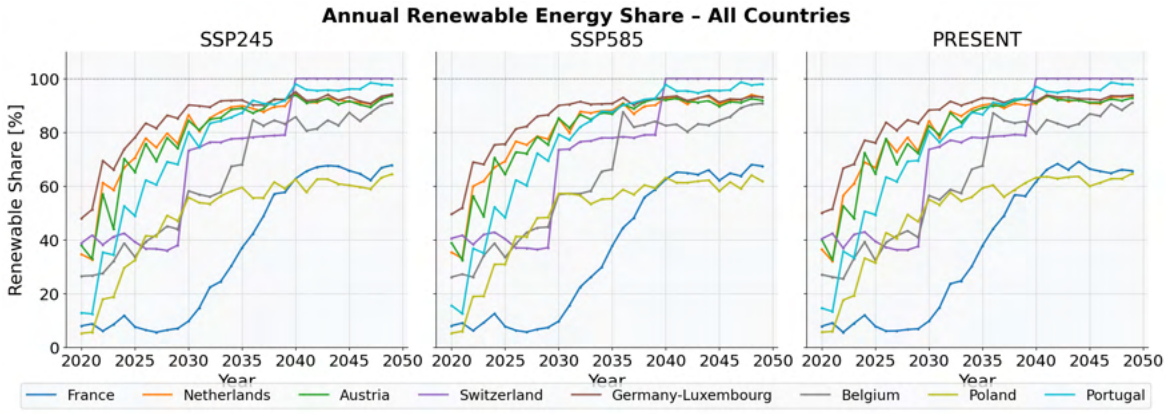

Figure 4.40.: Annual renewable energy share for all countries under each scenario (2020–2049). Each line represents one country. France (blue) stands out with the lowest renewable share early in the period due to its nuclear fleet, while Germany-Luxembourg (brown) leads the transition. All scenarios yield near-identical country trajectories.

4.2.3.2. Renewable Energy Share – Per Country, All Scenarios

Figure 4.41 shows the same renewable share data reorganised by country, with all three scenarios overlaid in each panel (SSP2-4.5 in blue, SSP5-8.5 in red, Present-day in green).

The close agreement between the three scenario lines in every country panel reinforces the conclusion that the renewable energy share is structurally determined. In most countries and years, the three lines are nearly indistinguishable, with small divergences typically within ±5 percentage points even in the most variable years. The inter-annual fluctuations (saw-tooth patterns) visible in several countries reflect weather-driven variability in wind and solar output, which shifts the share year to year even when installed capacity grows monotonically. Switzerland's step-change around 2038 is again clearly reproduced in all three scenarios simultaneously, confirming that it is a model assumption rather than a climate-driven phenomenon. France shows the widest year-to-year fluctuations relative to the trend, consistent with the high sensitivity of the renewable share to nuclear availability in a period of fleet transition.

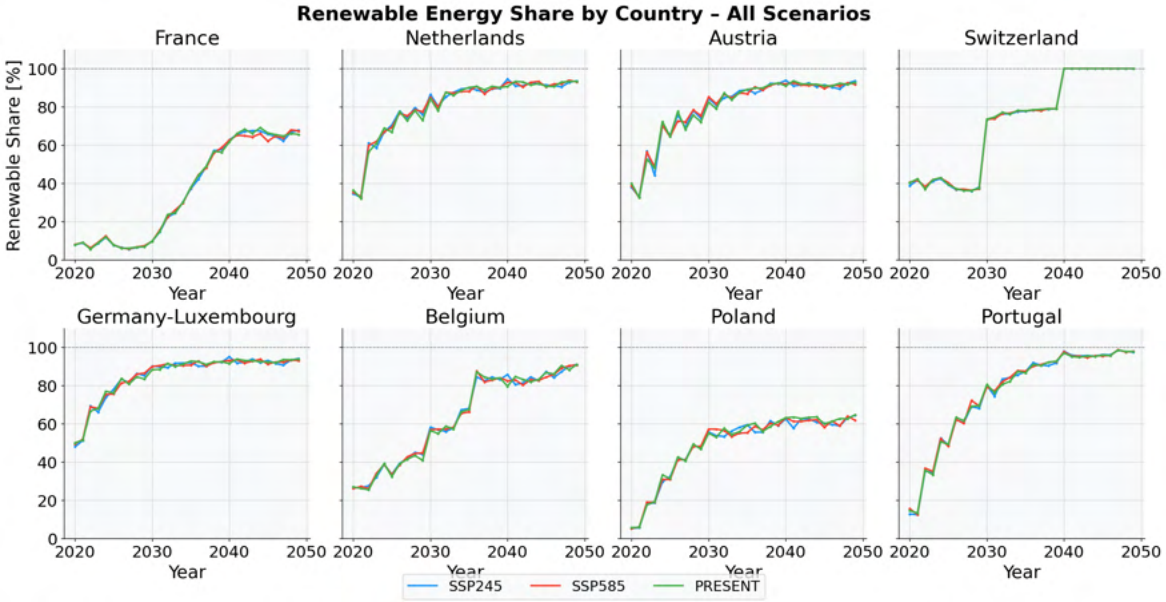

Figure 4.41.: Annual renewable energy share per country for all three scenarios (2020–2049). SSP2-4.5 (blue), SSP5-8.5 (red), and Present-day (green) are overlaid in each panel. The near-perfect alignment of the three lines confirms that the decarbonization trajectory is predominantly scenario-independent within this model framework.

4.3. Discussion

4.3.1. Energy System Relevant Climate Variables

The meteorological results from the ICON-SmART simulation, presented in this study, reveal a spatially heterogeneous and scenario-dependent response of renewable-energy-relevant meteorological variables across Europe over the 2020–2049 period. A central and recurring feature of the simulations is that SSP2-4.5 and SSP5-8.5 do not merely differ in the magnitude of their projected changes but in several regions produce trends of opposite sign, indicating that the level of radiative forcing influences not only the intensity but also the direction of regional climate responses. This qualitative scenario divergence is most clearly expressed in the 10 m wind speed over Southern and Northern Europe and in the shortwave surface irradiance over Central and Eastern Europe, and should be kept in mind when interpreting any single-scenario projection for energy system planning purposes. A further cross-cutting observation is that many of the identified trends, while physically plausible, do not survive autocorrelation correction uniformly across all temporal aggregations. The 30-year simulation window is sufficient to characterize the near-term evolution of the climate boundary conditions for energy systems, but is at the boundary of what is required to robustly separate forced trends from the substantial multi-decadal internal variability of European atmospheric circulation. Changes in the temporal variance of key variables – not only in their mean – would deserve attention in this context.

4.3.1.1. Wind Speed and Atmospheric Circulation

Regarding near-surface wind speed, the most robust and statistically significant signal in the entire dataset is the consistent negative trend in Eastern Europe under SSP2-4.5, which survives autocorrelation correction across all temporal aggregations and is confirmed by both and Mann-Kendall tests. This finding suggests that under the moderate emissions pathway a persistent reduction in near-surface wind speeds may emerge in this region over the coming decades, with potential implications for the wind energy yield of countries in that area. In Northern Europe, a similarly directed but somewhat weaker negative trend is found under SSP2-4.5, while SSP5-8.5 produces a weakly positive tendency, leading to a growing scenario separation from the mid-2030s onwards. The depicted case of Southern Europe, where the two scenarios diverge in sign at the 5-year rolling mean level with statistical significance, needs further investigation; the AR1-corrected significance is not retained in all aggregations, however, and the underlying dynamical mechanisms cannot be unambiguously attributed from the available simulation output alone. Western and Central Europe show no statistically robust wind speed trends, though the high interannual variability in the Atlantic-influenced western region is itself an important characteristic: for energy system planning, it is arguably this variability rather than a long-term mean trend that poses the greater operational challenge.

Summarizing the trends regarding the first central question in the introduction (see chapter 1) of this thesis referring to the analysis of temporal and spatial evolution of wind and

solar irradiance fields, most of the trends of SSP scenarios are negative, independent from being statistically significant. Exceptions can be found in southern Europe for the SSP2-4.5 scenario and in Eastern Europe for the SSP5-8.5 scenario. Present-day trends are mainly positive, except in northern and eastern Europe.

Comparing the wind speed trends obtained in this study with those reported by Carvalho et al. (2021), introduced in Chapter 1, reveals a consistent overall tendency towards decreasing wind speeds. In both studies, pronounced negative trends are found across large parts of Eastern Europe, while some regions further east exhibit positive trends. A similar pattern can be observed in areas adjacent to the Baltic Sea, where positive anomalies occur despite predominantly negative anomalies in the surrounding regions. These findings highlight one of the limitations of the present study, namely the use of relatively large analysis regions, which may mask or offset local-scale trends. Future studies could therefore focus on individual countries or smaller regions to investigate whether the positive anomalies identified around the Baltic Sea, in parts of the Balkan Peninsula, eastern Ukraine, and eastern Turkey can be confirmed, particularly under the SSP2-4.5 scenario. It is also noteworthy that the differences between SSP2-4.5 and SSP5-8.5 reported by Carvalho et al. (2021) are mainly confined to specific regions. In the eastern regions mentioned above, the projected changes under the two scenarios often exhibit opposite signs. In contrast, other regions show negative trends under both scenarios, with the signal generally being stronger under SSP5-8.5 than under SSP2-4.5. This behaviour can be partly confirmed by the results of the present study, for example in parts Western Europe, whereas SSP2-4.5 in Carvalho et al. (2021) even exhibit stronger negative trends. In other regions, however, only the overall negative signal is reproduced, while SSP2-4.5 occasionally exhibits an even stronger negative trend than SSP5-8.5. It should be noted that Carvalho et al. (2021) compare two future periods (2046–2065 and 2081–2100) against a historical reference period (1995–2014), whereas the present study does not employ such a baseline comparison. This methodological difference may contribute to some of the discrepancies between the results. Nevertheless, incorporating a comparison against a historical baseline period in future work could further improve the spatial analysis. Additionally it is important to mention that Carvalho et al. (2021) employ an ensemble of 16 CMIP6 climate models for the analysis.

The present analysis is limited to 10 m wind speed as a scalar quantity averaged over broad climate zones. A natural extension would be to examine wind direction distributions and surface pressure fields at selected locations, for example through windrose analyses or geopotential height composites. Such analyses would allow the large-scale circulation changes that underlie the identified regional wind speed signals to be characterized more concretely, without requiring causal attribution beyond what the data support. This is particularly relevant for the scenario-dependent divergences in Southern and Northern Europe, where the opposing trend signs suggest a sensitivity of the regional flow regime to the emissions pathway that cannot be resolved from wind speed magnitude alone. In a similar vein, a disaggregation of the results to individual countries rather than broad climate zones would enable more targeted statements about the wind resource evolution in specific national energy markets.

4.3.1.2. Shortwave Irradiance, Dust, and Photovoltaic Boundary Conditions

The picture for shortwave surface irradiance reveals pronounced scenario dependence, particularly in Central and Eastern Europe. Under SSP2-4.5, both regions exhibit a robust negative trend in incoming radiation, confirmed at monthly resolution even after autocorrelation correction, while SSP5-8.5 produces near-zero or weakly positive tendencies in the same areas. This contrast – where the moderate mitigation pathway is associated with a stronger reduction in solar resource than the high-radaiative forcing pathway – is a notable and perhaps counterintuitive result. In contrast, Northern and Southern Europe shows a positive irradiance tendency under both future scenarios and represents a potentially favourable development for photovoltaic energy generation in this area.

Summarizing the trends regarding the first central question in the introduction (see chapter 1) of this thesis referring to the analysis of temporal and spatial evolution of wind and solar irradiance fields, most of the trends of SSP scenarios are positive, independent from being statistically significant. Exceptions can be found in western, central and southern Europe for the SSP2-4.5 scenario and in Eastern Europe for the SSP5-8.5 scenario. Present-day trends are mainly positive, except in northern and eastern Europe. Similar to the wind analysis, eastern Europe seems to be a little bit of a special region where trends diverge from the rest of the trends. Further research for this region to understand the underlying processes can be interesting here.

Comparing these results with those of Hou et al. (2021), the predominantly positive trends under SSP5-8.5 are evident in both studies. SSP2-4.5 was not investigated in Hou et al. (2021); however, for the weaker scenario SSP1-2.6 considered therein, generally weak positive trends are found over Scandinavia, whereas SSP5-8.5 exhibits slightly weaker trends in this region. This negative trend cannot be confirmed in the present study. Interestingly, this study also shows negative trends for SSP2-4.5 in Western and Central Europe, and for both SSP2-4.5 and SSP5-8.5 in Eastern Europe, which, at least for the lower radiative forcing scenario in Hou et al. (2021), are not reproduced. It is important to recognize that Carvalho et al. (2021) evaluate future conditions in a timeframe from 2081-2100 to a historical reference period (1995–2014), while the present study does not apply a comparable baseline approach. This methodological discrepancy may partly explain some of the differences observed between the results. Future work could therefore benefit from including a historical reference period to further enhance the spatial interpretation of the findings. Moreover, Carvalho et al. (2021) base their analysis on an ensemble of 28 CMIP6 climate models.

Near-surface dust mass concentration shows a broadly decreasing tendency across most regions, but the dominant feature in Northern and Eastern Europe is a step-like reduction that occurs synchronously across all three scenarios in the early part of the record. The scenario-independent character of this transition suggests that it is driven by a common external factor rather than a scenario-specific forcing, though whether this reflects a genuine atmospheric reorganization or a feature of the model initialization cannot be resolved from the current analysis alone. In Southern Europe, future scenario dust loadings remain near-neutral or show weakly positive tendencies, in contrast to the general decrease seen elsewhere. Since mineral dust affects photovoltaic panel efficiency through soiling and

modifies the incoming radiation. While near-surface mineral dust concentrations show a general decline across most regions, the associated shortwave direct radiative effect becomes stronger under future SSP scenarios compared to Present-Day conditions. This contrast emphasizes the potentially increasing climatic significance of mineral dust in the future, especially related o photovoltaic energy.

Future analyses in this direction should broaden the set of dust-related variables – for instance by including aerosol optical depth or column-integrated dust burden alongside near-surface mass concentration.

Temperature represents a further variable of dual energy-system relevance that has not been examined in the present study: it governs heating and cooling demand on the load side and simultaneously affects photovoltaic module efficiency through thermal derating on the generation side. Given that the general warming tendency is well established in the literature, analyses building on the present work could focus on the fine-scale spatial patterns of temperature change and their direct translation into load profiles, as well as on the co-occurrence of temperature extremes with periods of low renewable energy supply – a combination that is particularly stressful for the energy system.

4.3.1.3. Energy-System-Relevant Events and Spatial Co-occurrence Patterns

The case studies of energy-system-relevant meteorological conditions provide a perspective that bridges the variable-level analysis and the spatiotemporal structure of critical energy system events. For dark doldrums, the analysis demonstrates that the pronounced annual cycle – with event counts peaking in winter and individual event lifetimes being longest during the same season – is robustly preserved across all scenarios and decades, reflecting the fundamental role of solar geometry in driving low-irradiance periods. While the aggregate statistics of event frequency, spatial extent, and lifetime show no dramatic scenario-driven changes, the spatial distribution of occurrence frequency is not static: under SSP5-8.5, a clear intensification of dark doldrum conditions emerges over the Iberian Peninsula in the 2040s, a region where renewable energy deployment is expanding rapidly. The marginally significant positive trend in dark doldrum frequency under SSP2-4.5, despite this being the milder scenario, provides a further illustration of the non-monotonic relationship between emissions pathway and regional impact that characterises several results of this study.

Light breeze events show a spring-centred seasonal maximum and are characterised by overall stability in frequency, spatial extent, and lifetime across all scenarios and decades. The absence of statistically significant trends in any of the three event metrics is itself a meaningful result, suggesting that the synoptic configurations that simultaneously drive high wind and photovoltaic capacity factors are not systematically altered by the projected climate change over the period under consideration. The more pronounced decade-to-decade swings in light breeze occurrence under SSP5-8.5 indicate, however, that higher radiative forcing may be associated with stronger low-frequency atmospheric variability, which would pose additional challenges for medium-term energy system planning even in the absence of a monotonic trend.

Both case studies also highlight the scope for methodological development. The capacity-factor-based definitions and fixed thresholds applied here represent one possible operationalization among several. Complementary approaches could include definitions based directly on meteorological variables rather than capacity factors, criteria with varied threshold values, or supplementary conditions that restrict event identification to a minimum spatial extent or minimum lifetime. Combining the identified events with actual energy yield estimates – for example computed with the atlite tool – would allow the meteorologically defined events to be expressed directly in energy terms. The geographical scope of the case study approach could furthermore be extended to other European countries beyond the western European focus adopted here, generating a broader set of region-specific energy meteorological indicators under different climate scenarios.

The coexistence scenario analysed in Case 3, in which light breeze conditions over the Iberian Peninsula coincide with dark doldrum conditions over Central Europe, is of direct relevance to the question of cross-border transmission adequacy given the limited interconnection capacity across the Pyrenees. The finding that no statistically significant trend exists in the combined co-occurrence area does not imply a static risk: the dominant role of high interannual variability means that peak stress situations govern the challenge for grid operators and planners even though it was shown that the occurrence of this case is only taking place during a few time steps. The bimodal distribution of dark-country area during co-occurrence events suggests the presence of two physically distinct regimes of Central European dark doldrum conditions, possibly associated with different synoptically driven circulation states, though a more detailed investigation of the underlying flow patterns would be required to substantiate this interpretation. A natural extension of this analysis would be to incorporate the total energy flows associated with co-occurrence events as well as the installed renewable capacity distribution, in order to move from a frequency-based assessment towards a quantification of the actual grid stress potential. The installed capacity perspective is also relevant beyond the Iberian coexistence scenario: an analogous analysis applied to Germany, for example, could address the concurrent evolution of offshore and onshore wind conditions in the north and photovoltaic conditions in the south, weighted by the respective installed capacity distributions, thereby providing information directly relevant to internal North–South transmission requirements. Such analyses could be generalized to other countries with similarly polarized renewable resource and capacity geographies, and would benefit from the extended simulation period, ensemble approach, and country-level spatial resolution discussed above.

4.3.2. Future Energy System Progressions

The energy market simulations with PowerACE reveal a picture in which the overarching decarbonization trajectory of each country is predominantly shaped by the assumed capacity expansion pathways. Across all eight modeled market areas, the renewable energy share follows closely similar time trajectories under SSP2-4.5, SSP5-8.5, and the Present-day reference, with differences between scenarios rarely exceeding a few percentage points in any given year. This structural invariance reflects the fact that installed capacity is

prescribed exogenously in the current model setup, meaning that climate-induced differences in resource availability modulate the output of existing plants but do not alter the overall capacity mix. The implication is that the long-term decarbonization pathway as modeled here is robust to the climate scenarios considered, while the climate signal manifests primarily at the level of interannual variability in dispatch, prices, and the residual fossil contribution in any given year. For some time frames there are still trends with small magnitude visible.

4.3.2.1. Climate Signal in the Generation Mix

While the structural trajectories are scenario-invariant, the difference plots between Present-day and the two climate scenarios reveal meaningful signals in the year-to-year dispatch of individual generation technologies that can be interpreted in the light of the climate variable trends discussed in the previous section. The most consistent cross-country pattern concerns solar PV: in the majority of years and across most market areas, solar dispatch is somewhat lower under the SSP scenarios than under Present-day conditions. This tendency is most consistently visible in Switzerland, Austria, and the Netherlands, where Present-day–SSP differences in solar generation are predominantly positive over the course of the simulation period. This finding is in line with the negative shortwave irradiance trends identified under SSP2-4.5 in Central Europe in the climate analysis, where a robust decline in incoming radiation is projected over the 2020–2050 period. The SSP5-8.5 scenario tends to produce somewhat more pronounced solar differences than SSP2-4.5 in several countries and periods, consistent with the stronger scenario divergence in shortwave irradiance found in Central Europe under the higher-radiative forcing pathway.

Wind dispatch differences between scenarios are more variable in sign and magnitude than those for solar and show a stronger country- and period-specific character, reflecting the regional heterogeneity of wind speed trends identified in the climate analysis. For Germany-Luxembourg, wind deviations between Present-day and the SSP scenarios are among the largest in absolute terms, reaching up to ±40 000 GWh in individual years, and they shift in direction over time: in the period around 2030, both SSP scenarios tend to yield more wind dispatch than Present-day, while from the mid-2030s onwards, Present-day conditions produce higher wind output than either SSP scenario in most years, with the effect being somewhat stronger under SSP5-8.5. This temporal inversion is broadly consistent with the rolling-mean wind speed evolution in Western and Central Europe identified in the climate simulations, where SSP5-8.5 starts above SSP2-4.5 in the early 2020s and subsequently declines more rapidly. For Belgium and the Netherlands, wind differences are similarly large in relative terms, driven primarily by offshore wind variability, and also tend towards lower wind dispatch in the SSP scenarios compared to Present-day in the later decades, again with SSP5-8.5 showing the more pronounced reduction. In Poland, a country particularly exposed to the negative wind trend under SSP2-4.5 identified in the Eastern European climate zone, wind dispatch in the SSP scenarios is lower than under Present-day conditions in most years from 2025 onwards, especially for SSP5-8.5. For Portugal, wind contributions are higher in the SSP scenarios compared to Present-day in most years, a pattern that aligns broadly with

the positive or near-neutral wind tendencies found in the Southern European climate zone. The negative trends of dispatch in other countries are however in line with the negative trends found for the SSP scenarios in most of the regions.

The interplay between wind and solar differences and the compensating adjustments in dispatchable generation is a further cross-cutting feature of the difference plots. In years where wind and solar dispatch is lower in the SSP scenarios than under Present-day conditions, the shortfall is compensated by higher utilisation of gas-fired or – progressively from the mid-2030s – hydrogen-fired capacity. This compensation mechanism is most clearly visible in Germany-Luxembourg, Belgium, and the Netherlands, where natural gas CCGT and later hydrogen CCGT appear as positive contributors in the Present-day minus SSP difference plots in years of reduced renewable dispatch. In Austria and Switzerland, where the fossil backup fleet is largely retired by the early 2030s, the same compensation signal manifests through reduced pumped hydro storage charging, indicating a lower intraday surplus of renewable energy available for storage. These dispatch adjustments illustrate how the climate-induced variability in renewable resource propagates through the energy market model: it does not alter the long-term technology mix, but it continuously reshapes the merit order and the utilisation of flexible capacities on an interannual basis. It is also important to note that replacing some dispatch of renewable energies with thermal capacities can contribute to higher electricity market prices.

4.3.2.2. Market Prices, Scarcity Events, and Their Meteorological Origin

Across most modelled countries, prices remain broadly similar across scenarios during the early 2020s but begin to diverge more noticeably from the late 2020s and particularly into the 2030s and 2040s, consistent with the growing scenario separation in the underlying climate variables over the same period. The price response is characterised by a bidirectional pattern: in some years the Present-day scenario yields higher prices than the climate scenarios, while in others the reverse holds, reflecting the stochastic nature of weather-driven generation imbalances. The differences between Present-day and SSP5-8.5 tend to be somewhat more sustained over time, while the differences between Present-day and SSP2-4.5 show higher peak excursions in individual years, consistent with the stronger low-frequency variability associated with the higher-radiative forcing pathway found in the climate analysis. Caution is warranted in drawing direct causal links, however, given the complexity of the market model response and the limited statistical sample available from a single model realisation per scenario.

A particularly notable feature of the price evolution is the progressive intensification of episodic price spikes from the late 2020s onwards, concentrated predominantly in the winter months. This seasonal concentration is not coincidental: it corresponds directly to the seasonal structure of dark doldrum conditions identified in the climate case studies, where event counts peak in December and January and individual event lifetimes are longest during the same period. The energy market model reproduces – through the mechanism of reduced wind and solar dispatch leading to scarcity pricing – the meteorological pattern of winter low-production episodes identified independently in the climate analysis. The

intensification of these spikes over time reflects the increasing penetration of variable renewables and the growing sensitivity of the residual load to meteorological conditions as the fossil backup fleet is progressively retired. This connection between the climatological characterisation of dark doldrum events and the price dynamics emerging from the market model represents one of the most direct and interpretable cross-model links in the present study.
Another important aspect regarding the comparably high prices from 2030 onwards, which can reach values of up to 4000 €/MWh, is that the demand specified by TYNDP cannot always be met during these periods. One reason for this ihat TYNDP assumes a high degree of electrification in the industrial, mobility, and household sectors, resulting in a substantial increase in electricity demand. This assumption is justified by the ambitious decarbonization and electrification targets for the aforementioned sectors across European countries on which the TYNDP projections are based. However, an analysis of the projected demand development suggests that this strong increase in electricity demand is not fully reflected in current real-world trends. This discrepancy may arise from both political and practical constraints. In particular, permitting, planning, and construction processes for new infrastructure can require many years and often proceed at different rates across regions. As a result, producing reliable forecasts of future electricity demand and generation capacity expansion over the coming decades remains highly challenging. If such demand levels were actually reached, additional power plants would likely be constructed to maintain security of supply and prevent excessively high prices. Furthermore, demand response, i.e., the flexibility of electricity demand, is not represented in PowerACE. As a consequence, time periods with assumed extreme demand levels can distort mean daily and annual electricity prices. Several approaches can be considered to address these very high prices in the subsequent analysis. On the one hand, a threshold value could be introduced to cap extreme prices and thereby exclude scarcity-driven price peaks. On the other hand, all hours during which demand cannot be met could be identified explicitly, improving the interpretability of the results for the reader.

4.3.2.3. Open Questions and Directions for Future Work

Several directions emerge for extending and refining the energy market component of the modelling chain. The load profiles used in the present study are derived from pre-calculated loads. A more physically consistent approach would link load profiles directly to climate model output, particularly near-surface temperature, which governs heating demand in winter and cooling demand in summer. As warming progresses, the seasonal load profile is expected to shift in a scenario-dependent manner, and incorporating this feedback would improve the overall consistency of the modelling chain and could reveal interactions between the climate effects on the supply and demand sides simultaneously.

Capacity expansion decisions represent another dimension currently treated exogenously. Allowing additions to be determined through interactive investment decisions, would make it possible to assess whether the climate-induced differences in resource availability and price signals are of sufficient magnitude to steer investment towards different technology

or location choices. It should be acknowledged, however, that investment decisions depend on a wide range of factors, including financing conditions, policy incentives, and grid access besides meteorological factors, so that the scope for a purely meteorologically driven endogenous framework is inherently limited. The role of storage systems also warrants more explicit treatment: under climate conditions that increase the frequency or duration of low-generation periods, the value of flexibility assets rises, and their contribution to managing residual load under dark doldrum conditions could be substantial and would be a natural extension of the present analysis. However, with regard to the high market prices, this analysis also highlights the need for additional generation capacity to meet future electricity demand, assuming that the demand projections of the TYNDP and the associated policy-driven targets are realized in practice. At the same time, sufficient grid capacity will be required to transmit the additional electricity generation and ensure reliable supply.

A further variable not yet included but of direct relevance to several of the modelled market areas is hydropower. Reservoir and run-of-river generation depends on precipitation, snowmelt timing, and glacier mass balance, all of which are sensitive to the climate scenario. For countries with significant hydropower shares, projected changes in the seasonal distribution of runoff – driven by earlier snowmelt and potential increases in summer drought frequency under warming – could alter the dispatchable capacity available during periods of low wind and solar output. Incorporating precipitation and temperature-derived runoff projections from the climate simulations into the hydropower representation of the market model would therefore improve both the physical consistency and the regional relevance of the integrated modeling chain.

4.4. Results and Outlook of Power Flow Model Output when coupling Climate- and Energy Market Models

An additional way to do further analysis on the energy grid as well as mitigation actions due to climate change can be done with a power flow model. This section presents the first attempt to merge these two simulation types with a third model representing the energy market. As described in section 3.4.2, climate data have been calculated to energy yields and these renewable generation profiles as well as thermal power generation profiles have been mapped on IIP nodes. Loads per IIP node were already pre calculated by Slednev, 2024, and have only been scaled such that they match the loads given by PowerACE. After mapping the data on IAI nodes of the model described in section 3.4.1, a power flow analysis has been performed for 23 December 2026, 12 UTC. Mapping and power flow calculations have been carried out by IAI employees for licensing reasons. The results of the power flow analysis with PowerFactory are displayed in figure 4.42. The colour of the filled circles displays voltage operating limits. Most of them are green, respresenting stable conditions. Rings outside the circles determines occupancy of grid assets (Transformators and Generators), lines and arrows determine transmission lines. Noticeably, there is a red ring around the site in Flamanville. It represents a slack generator, that compensates grid losses, balance errors and unbalanced generators and loads by adjusting its generations. Due to occupancy

of 560 %, this shows a dispatch error. Other red rings mainly represent transformer with an occupancy of 120 %. This can happen due to a mechanism, triggered due to high loads or long transmittance ways. As a consequence, voltage decreases locally and generators as well as transformer try to maintain the voltage. Because the occupancy of a transformer is typically described as apparent power, consisting of active and reactive power. Here, high amounts of reactive power is formed, flows increase and the transformer is thermally overloaded. In reality on the short term this would lead to a couple of actions by the grid operator like redispatching, adjusting voltage levels, redirecting the grid and transmission lines and in extreme cases also load shedding to prevent defects in the transformers on the intermediate time scale. Note that load and generation data from the other models is scaled to 25 % that a power flow can take place due to voltage limits as well as too high demand data. This shows the current incompatibilty with the current model version of PowerACE and FowerFactory due to many inconsistencies. The base is that PowerFactory simulates an AC power flow and PowerACE does not calculate any grid physics, also no DC power flow. It simply reads a pathway of Net Transfer Capacities (NTCs), only modeling how much power should flow between the market areas but not how exactly the exact power flow within and between market zones. That only results in market situations that are economically reasonable but not necessarily physically. One could think that externally given NTCs by the TYNDP should contain realistic exchange values. This is also the case but they are only valid for certain grid assumptions and conditions and scenarios and act as system boundaries but do not contain information about the power flow in transmission line inside of a market zone. Additionally, it is possible that there are differences between the Power Flow Model that ENTSO-E has used to calculate the NTCs and the PowerFactory model that is used within this study. More simplicity, other assumptions and locations of power plants and small structural differences can lead to quite large divergence. Moreover its not only the ENTSO-E model and the here used model has to be compared. Also uncertainties occur when mapping the capacities and generations from PowerACE to the IIP nodes. Also these mapped power plants already have different locations because of the assumed extension of power plants at similar locations like already existing ones resulting in changing flows. The mapping on most likely different substation regions than in this study (see 3.4.2.1), leads to different uncertainties. A similar argumentation yields for the loads since they are also not directly obtained by TYNDP data (see section 3.4.2.2). Electrically an NTC model only optimizes the active power P, whereas the additional reactive power Q and losses is considered in an AC model like PowerFactory.

Options how to deal with that perspectively would be either implementing at least a DC power flow or creating a coupled iterative market-AC model process. Note that for DC power flow models the estimated power could still be incorrect due to simplified assumptions (e.g. no apparent power, no phase angles,...). Probably developing a coupled process between market model and AC model would be the most effective process. In the following this process is quickly depicted.

In a first step, a market model calculates the power plant dispatches as well as cross-zone exchanges as well as spot market prices with NTCs but without any physics. Afterwards a mapping on the IAI nodes takes place to distribute the results on nodes and buses. In a third step the power flow analysis is performed and grid violations are identified. These four steps mainly summarize the steps performed during this study and could directly be used

in the whole process. Subsequently a feedback to the market model has to take place. From redispatch perspective the market model has to examine which plants are worth activating and deactivating from a market perspective. Furthermore adjustments at the NTCs but also at the minimum and maximum plant used capacities could be made in order to force less overload at certain regions. Sixth, the energy market is recalculated and the Power Flow is then checked iteratively afterwards. Still, problems can occur due to no direct convergence of the power flow model. Moreover, the mapping process from the market model to certain node regions can be challenging and yields many potential uncertainties as already pointed out in this section and further presented in section 4.5.
Another option could work the other way around that an Optimal Power Flow model is used to determine the optimal redispatch actions. For that an objective function has to be found that considers the costs of redispatch. A third option might be applying the newly developed PROcess Orchestration Framework (PROOF, see Liu et al. (2023)) that enables the coupling of several executables that are originally not developed dependantly. With that, it enables the automation of computational workflows and conduction of co-simulations.

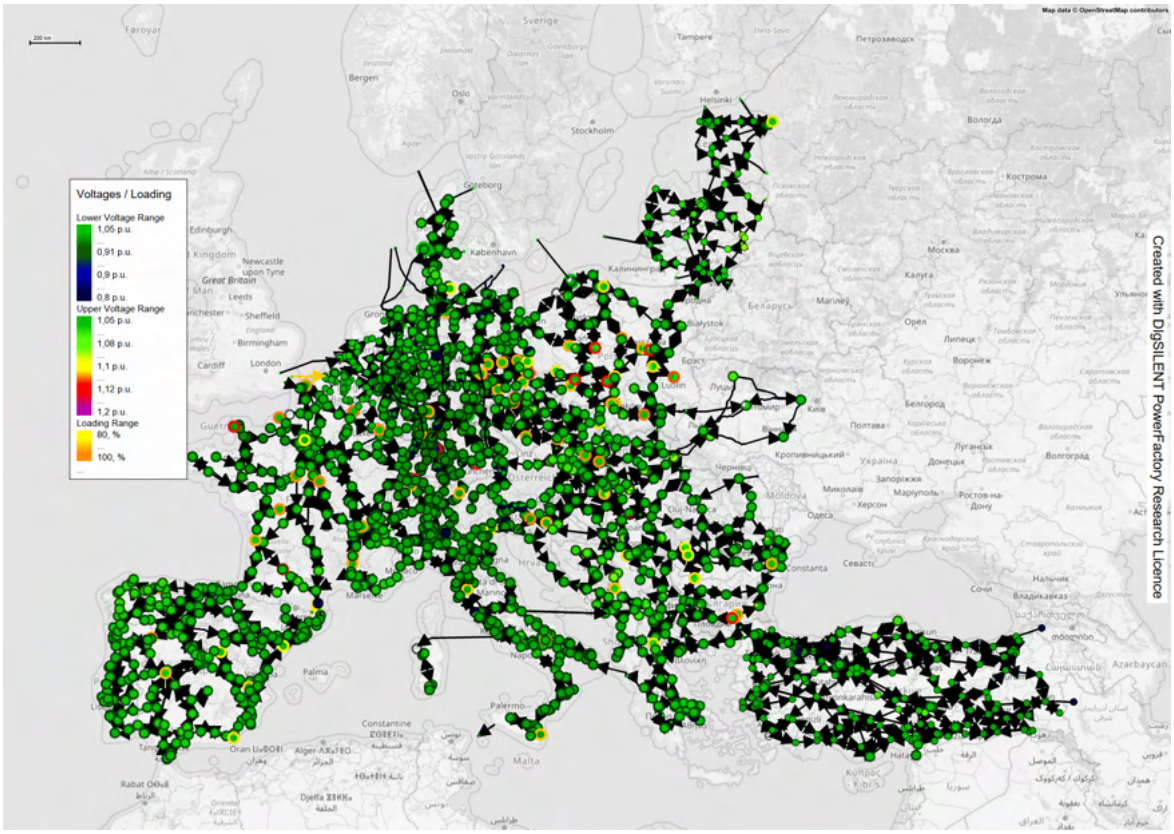

Figure 4.42.: Result of Power Flow Analysis with PowerFactory on 23 December 2026, 12 UTC: Geographic depiction. The colour of the filled circles displays voltage operating limits, rings outside the circles determines occupancy of grid assets (Transformators and Generators), lines and arrows determine transmission lines.

4.5. Limitations of the presented methods in regards to the research problem

Given the chain of simulations and calculations linked within the described workflow, a number of assumptions, simplifications, and deliberate neglects were necessary to arrive at a solution that is as accurate as possible while remaining practically feasible. This section addresses the resulting qualitative uncertainties and proposes improvements for future studies, with specific reference to the field examined here. To this end, all methods introduced in chapter 3 are reviewed in turn and potential improvements are identified.

4.5.1. Climate Data

As explained in chapter 3.1, the current ICON-SmART configuration uses an R2B05 grid with a spatial resolution of approximately 78.9 km. This is a relatively coarse resolution not only for convective systems, but also for applications involving hydropower plants and associated runoff or, more generally, precipitation in further energy-meteorological studies. Wind fields, turbulence, and irradiance fields are also affected within this study. For wind in particular, the coarse resolution can have a pronounced effect in mountainous regions that do not extend over hundreds of kilometres spatially but may still be suitable for wind farms and are thus underrepresented. An example is the Black Forest, which reaches wind power densities of only around 250 $\frac{\mathrm{W}}{\mathrm{m}^2}$ in the model but can attain values up to 400 $\frac{\mathrm{W}}{\mathrm{m}^2}$ in certain areas according to the Windatlas Baden-Württemberg, which employs models at finer resolution.
A limited-area model (LAM) simulation with ICON at finer grid resolution could therefore be performed for specific regions. It is important to note that global simulation data of the same configuration type (such as the SmART-dust case used in this study) are required as boundary conditions for the LAM simulation, and nudging towards these boundary data must be activated. In the context of climate simulation, nudging refers to a technique in which the model is gently pushed towards prescribed boundary condition data rather than allowing the simulated fields to evolve freely. Without activating nudging in a LAM simulation, the model will crash after only a few time steps. This occurs primarily for numerical reasons: in a global simulation, the entire model system – including all interactions and processes related to the various components of the climate system – is approximately in balance. When simulating only a sub-region of the climate system, meteorological fields diverge both numerically and spatially. A further important consideration is that the finer grid inside the pre-defined LAM region should be only one refinement level finer than the global resolution (e.g. an R2B06 LAM grid when using a global R2B05 grid).
Since ICON-SmART is still at an early stage of development, other global grid resolutions that could provide finer global boundary data (see table 3.1) have not yet been tested and may require further adjustments to the model configuration to maintain numerical stability. Until such resolutions have been validated, one possible workaround would be to remap the R2B05 grid data to an R2B06 grid, use the remapped dataset as global boundary conditions,

and define an R2B07 LAM grid with a resolution of approximately 19.7 km within the target region. Uncertainties arising from the remapping process and the absence of directly simulated data on the R2B06 grid are to be expected, since the data effectively retain the spatial resolution of the original R2B05 grid.
Additionally, incorporating a broader range of aerosols through ART, or using pre-defined time series analogous to those used for greenhouse gases, could improve the accuracy of the simulation, particularly with respect to irradiance and absorption processes, as currently only mineral dust is considered as an aerosol.
Further improvements in the forecasting of significant weather events with implications for energy load or generation in specific regions – such as heat waves, strong wind events, or dust episodes – could be achieved by performing ensemble simulations for selected reference years. Several studies have already conducted comparable simulations in the climate context. Such an approach would also help to smooth out model errors. If ensemble simulations are performed, the appropriate magnitude of initial condition perturbations for each ensemble member should be carefully examined.
Examining additional SSP scenarios could further improve the understanding of potential climate trends. The corresponding data are freely available for download from the CMIP6 websites.
Simulating over longer time frames could result in clearer signals between the scenarios since in 2050 the radiative forcing is still rather moderate (see chapter 1). However, this would be rather relevant for meteorological studies since simulating on longer time frames than 2050 with energy system models becomes increasingly difficult due to the uncertain boundary conditions (described in section 3.3.2). Multi-chunk simulations of the ICON-SmART configuration with auto-icon are currently problematic, as each chunk does not automatically restart the simulation at its starting time step. Further work is needed to assess whether a manual restart with auto-icon yields physically reasonable results, and the restart functionality should be reviewed more generally to ensure reliable operation across all experiment types.

4.5.2. Capacity Factors and Energy Yields

Calculating renewable capacity factors and energy yields with *atlite* provides a convenient way to transform meteorological fields directly into energy quantities within the Python xarray framework. One aspect that is simultaneously an advantage and a limitation is that a specific wind turbine type or panel type must be selected for each renewable technology. On the one hand, this makes it possible to incorporate the actual performance characteristics of each technology, resulting in more accurate yield values. On the other hand, only a limited number of solar panels and wind turbine models are natively available in *atlite*, and most of these are relatively outdated and would no longer be deployed in new installations. If other technologies are required, they would need to be added manually to the source code. Alternatively, the module could be extended by creating a fork or using a wrapper of *atlite*. Data availability may still pose a challenge, however, since information on the exact turbine or panel type and installed capacity at a specific site is not available in every country. In

Germany, this information is accessible via the Marktstammdatenregister. When using the node regions defined in Slednev (2024) in particular, capacity factors and energy yields could be quantified with considerable precision, and their aggregation to the country level would then be straightforward. Where information on technology types is unavailable, a single technology type must be assumed, which introduces additional uncertainty into the calculations, since the performance characteristics of different technologies vary.
The higher grid resolutions suggested in section 4.5.1 would also lead to improved spatial accuracy when calculating capacity factors and energy yields with *atlite* (see sections 3.2.2 and 3.2.3), yielding more accurate renewable generation values both at the country level for the energy market simulation and at the IIP node level for the power flow analysis input data.
For future studies, it may also be worthwhile to explore the use of the simulated meteorological fields as boundary conditions for high-resolution Computational Fluid Dynamics (CFD) simulations, such as RANS simulations (based on Reynolds-averaging theory, described in chapter 2.1.3) or LES simulations. Using widely adopted CFD software in the renewable energy community – such as *Meteodyn* (see *Meteodyn - L'Ingénierie du vent, de la Climatologie et de la Météorologie* (2026) or *WindSim* (see *WindSim Home* - (2026) – energy yields can be quantified at metre-scale resolution. With a digital elevation model and precise information on turbine and solar collector locations and types, this would likely represent the most accurate approach for quantifying yields from renewable farm layouts. This option may be particularly worth considering for local power flow studies, for example the analysis of specific renewable farms under changing climatic conditions and their influence on the local energy grid.

4.5.3. Energy System Analysis

The energy market simulation relies on a number of assumptions that make the overall setup more tractable. Many parameters that could in principle be calculated in advance or determined interactively during the simulation are provided as fixed input data. Nearly all of these are drawn from the TYNDP. Nevertheless, studies could be conducted in which, for example, load data are explicitly derived from the pre-simulated meteorological output – in particular from temperature and radiation fields – to calculate demand profiles based on season, heat waves, or other climatic conditions, and to link these directly with the simultaneously available renewable generation. Conditions for dark doldrums or light breezes could also be defined in more detail within this framework. As described in section 4.5.2, the calculated capacity factors could be made more accurate if additional technology-specific data were available. The sensitivity of the entire market to capacity factor values at a given time step is illustrated in section 4.2, which demonstrates how different capacity factors affect the whole market through the merit-order-based dispatch of renewables (see section 2.3.2).
Estimating the exact properties of a future energy system over long time horizons is inherently difficult. Many driving factors are strongly influenced by political decisions and the

choices of decision-makers. A central example is the expansion of renewable energy capacity and grid infrastructure. Even projecting these developments over the next ten years is ambitious. One reason is that renewables and new transmission lines are subject to complex approval processes (see e.g. Ciupuliga et al. (2011)) in which it is often difficult to predict how long individual projects will take. Land-use planning, securing of property areas, dealing with citizens' initiatives, and carrying out environmental and technical inspections, as well as the construction process itself, can extend a project by several years. Uncertainties also arise in the assumptions about energy demand. (Slednev, 2024) If it is assumed that society will adopt more electric vehicles, battery storage systems, heat pumps, and data centres, and that industry will become more electrified, greater quantities of electricity will need to be transmitted through the grid and the need for grid expansion will be high. A more conservative trajectory involving lower uptake of electrification technologies would result in significantly lower grid loads. New technological developments are not considered at this stage. Beyond these structural factors, market behaviour can change rapidly in response to external economic or geopolitical events. (Nonnenmacher et al., 2023) Rising energy prices may, for example, stimulate individual investment in photovoltaic systems, while a general economic contraction may suppress overall investment. New tariff structures or funding schemes can likewise determine whether a given technology expands or stagnates. (Azhgaliyeva et al., 2024)

To explore different market and technological scenarios more thoroughly, one option would be to run additional scenarios. The TYNDP offers several alternatives, and custom scenarios could also be created by generating new model input data.

The same considerations apply to the power flow analysis, where assumptions about grid capacities become even more uncertain for future scenarios. Furthermore, the process of connecting PowerACE and PowerFactory has not been completed within this study; only a first approach is presented and substantial further work remains. To enable analyses for years other than 2026, additional load data would need to be produced. As discussed earlier, improving the spatial resolution of the meteorological data is necessary to calculate more reliable renewable power generation values. The loss factor for photovoltaic generation – which accounts for shading from surrounding buildings, trees, or terrain and is currently defined only at the country level – could be quantified with considerably greater spatial and temporal precision. The widely used renewable energy software *WindPRO* (see EMD (2026)) provides modules for quantifying topographic shadows, panel self-shading, and shading from obstacles, based on digital elevation models and three-dimensional representations of panels and shading objects. Similar to the CFD simulations mentioned earlier, this tool could be applied for small-scale analyses or, with considerable effort, for medium- to large-scale projects. Geographic information systems could also be used to calculate and visualise such losses. For further challenges to be addressed in future research on power flow analysis, it is referred to the discussion of the power flow results within this study (see section 4.4).

Summary

This thesis develops an end-to-end modelling workflow coupling long-term climate projections with renewable energy market simulation and physical power flow analysis, applied to Europe over the period 2020–2049 under the SSP2-4.5 and SSP5-8.5 emissions scenarios alongside a Present-Day reference. The modelling chain proceeds from the global climate model ICON-SmART, which couples the ICON dynamical core with the ART aerosol module and the SmART land-surface and ocean extension, through the Python module atlite for the derivation of hourly wind and photovoltaic capacity factors, to the agent-based electricity market model PowerACE, and finally to a first coupling attempt with DIgSILENT PowerFactory for power flow analysis.

The first purpose of this study was to examine the changes of renewable energy system relevant variables from 2020 tot 2049 temporally and spatially. The climate simulations reveal that near-surface wind speed trends across Europe are both spatially heterogeneous and scenario-dependent, with SSP2-4.5 and SSP5-8.5 producing partly trends of opposite sign in several regions — indicating that radiative forcing influences not only the magnitude but also the direction of regional responses. The most robust signal is a statistically significant negative wind speed trend in Eastern Europe under SSP2-4.5, with a similar tendency in Northern Europe, while SSP5-8.5 produces a weakly positive tendency there, leading to a growing scenario separation from the mid-2030s onward. Generally, independent from being statistically significant, most of the trends of SSP scenarios are negative, exceptions can be found in southern Europe for the SSP2-4.5 scenario and in Eastern Europe for the SSP5-8.5 scenario. Present-day trends are mainly positive, except in northern and eastern Europe.

For shortwave surface irradiance, Central and Eastern Europe exhibit a robust negative trend under SSP2-4.5 but near-neutral or weakly positive tendencies under SSP5-8.5. Southern Europe shows positive irradiance tendencies under both future scenarios. Regarding mineral dust, while near-surface mass concentrations broadly decrease across most regions, the shortwave direct radiative effect of dust shows a scenario-dependent intensification especially under the SSP scenarios relative to Present-Day, emphasizing the increasing role of mineral dust in the course of climate change. Generally, most of the trends of SSP scenarios are positive, independent from being statistically significant. Exceptions can be found in western, central and southern Europe for the SSP2-4.5 scenario and in Eastern Europe for the SSP5-8.5 scenario. Present-day trends are mainly positive, except in northern and eastern Europe.

Two categories of energy-system-relevant meteorological events were analysed in dedicated case studies. Dark doldrum conditions — periods of simultaneously low wind speed and

low solar irradiance — exhibit a robust winter-centred seasonal cycle across all scenarios and decades, with only weak changes in overall event frequency. However, their spatial distribution shifts: under SSP5-8.5, a clear intensification emerges over the Iberian Peninsula, south-western France, and northern Germany and Poland in the 2040s, while under SSP2-4.5 the signal is more confined, with intensification primarily over Poland and weaker signals elsewhere. Light breeze events — periods of simultaneously elevated wind and solar generation — show a spring-centred maximum and no statistically significant long-term trends overall, though regional changes are identifiable over central Iberia, western France, and the North Sea coast, with higher forcing under SSP5-8.5 associated with stronger decadal variability. Analysis of the co-occurrence of Iberian light breezes with Central European dark doldrums reveals no significant trend in the total combined area, but a spatial redistribution: under SSP conditions, events of co-occurrences increases in parts of western Europe linked to the Iberian Peninsula, while it decreases in Central Europe — a pattern with direct implications for cross-border transmission adequacy across the Pyrenees.

The second goal of this thesis was to analyze potential impacts on the future energy system due to changing renewable energy yields. The energy market simulations show that the long-term decarbonisation trajectory of each modelled country is predominantly shaped by the prescribed capacity expansion pathways. The climate signal manifests at the level of interannual dispatch variability: solar PV output is consistently somewhat lower under the SSP scenarios than under Present-Day conditions in mainly central european market areas, consistent with the identified negative irradiance trends, while wind dispatch shows reductions under SSP conditions particularly visible in Poland, France, and partly in Germany. In years of reduced renewable dispatch, fossil and later hydrogen-fired capacity compensates the shortfall. Day-ahead electricity prices show a progressive intensification of wintertime price spikes from the late 2020s onward, directly mirroring the winter-centred seasonality of dark doldrum events identified in the climate analysis — one of the most interpretable cross-model connections established in this study. High market prices could be identified due to demand that could not be fulfilled at certain time steps. All dispatch differences are modest and do not determine the system trajectory; extracting more robust signals would require ensemble simulations and additional targeted analyses.

As a third goal, the first coupling of climate and market model outputs into a power flow analysis with DIgSILENT PowerFactory was conducted which demonstrates the general feasibility of the three-tier workflow but exposes fundamental incompatibilities between the NTC-based market model and the full AC power flow solver, requiring data to be scaled to 25 % for convergence and resulting in local transformer overloads. The path forward is an iterative coupled market–AC process in which dispatch and network constraints are resolved jointly.

Key uncertainties span all tiers: the coarse climate model resolution (~79 km) limits spatial precision for wind and irradiance fields; atlite capacity factors rely on a limited set of turbine and panel models; installed capacity and load profiles are treated exogenously; and hydropower is not driven by the simulated meteorological fields. These limitations point to concrete directions for future work: limited-area model refinement, ensemble approaches, endogenous capacity and load coupling, a fully iterative market–grid framework, and —

for meteorological research — extended time horizons to 2100 to capture clearer long-term trends.

Acknowledgements

I would like to express my deepest gratitude to my first supervisor TT-Prof. Dr. Martina Klose-Albinger for her unwavering support, insightful critiques, frequent meetings and excellent supervision in this interdisciplinary study – especially when problems occurred. I also greatly appreciate that this project in cooperation with IIP and IAI has been facilitated from the meteorological side, as this is not something to be taken for granted.
The same appreciation goes to my second supervisor Prof. Veit Hagenmeyer from IAI, who has always been an important contact for energy-related topics and supported me in challenging phases. I am deeply thankful for his collaboration in this joint project.
Big thanks go to the whole mineral dust working group at IMKTRO for their constant support and open ear. Special gratitude goes to Noel Chawang for support with the in-development ICON-SmART, Rumeng Li for her pragmatism in finding solutions, and Andreas Bär, the absolute expert in nearly every ICON and HPC related topic. Thank you, Patrick Ludwig for the introduction in climate modeling with CMIP6 data.
From IIP, I am especially grateful to Thorben Sandmeier for his help in nearly every PowerACE and energy system related topic, as well as Thorsten Weiskopf as a PowerACE expert and Johannes Schuhmacher and Eric Jahnke for their support on analytical topics related to the energy market. Special thanks also go to Victor Slednev, who calculated the load data and defined the substation regions used in this study.
From IAI, I address my deepest gratitude to Julian Hoffmann for his important input and support regarding PowerFactory. Big thanks also go to Jakob Geiges for the mapping from IIP to IAI nodes, as well as Arjun Madhusoodhanan and Jismon Stanly for conducting the power flow analysis.
I would also like to thank Martina Klose, Thorben Sandmeier, and Julian Hoffmann for carefully reviewing my thesis and for their valuable comments, which greatly contributed to improving my scientific writing.
Besides Prof. Hagenmeyer, I want to express my gratitude to Prof. Stefan Emeis (IMK-IFU) and Dr.-Ing. Rainer Koch (ITS) for their excellent lectures in energy informatics, energy meteorology, and CFD modelling, which motivated me to merge meteorology and energy technology in this thesis and study program.
Last but not least, I thank my family, my girlfriend, and my friends for constantly motivating and supporting me throughout my studies. Their encouragement has been invaluable – without them, many things would have been much more challenging. Thank you all!

AI declaration

The following parts within his thesis were conducted with help of AI tools:

- code development for the following topics:
  - improvement of performance and parallelizing of existing code
  - improvements of Plots
  - trouble shooting with Python, ICON, HPC-System Levante, LaTeX, HeidiSQL,
  - development and improvement of performance of Region Tracking Algorithm
  - creating shape data from .csv data
  - dealing with geodata and .csv-tables
  - adjusting input tables for PowerACE and PoweFactoory
- stylistic rephrasing of written thesis
- (with self-cross-checks) search engine for thesis related topics and literature

The main AI tool used in this thesis was Claude Sonnet 4.6. For quick research about thesis related topics, ChatGPT as well as Perplexity was used.

Bibliography

/www.hans-ertel-zentrum.de/Projekte/ICON-SmART.html (Nov. 2023). de. URL: https://www.hans-ertel-zentrum.de/Projekte/ICON-SmART.html (visited on 05/28/2026).

Ai, Bin et al. (July 2003). "Calculation of the hourly and daily radiation incident on three step tracking planes". In: *Energy Conversion and Management* 44.12, pp. 1999–2011. ISSN: 0196-8904. DOI: 10.1016/S0196-8904(02)00229-7. URL: https://www.sciencedirect.com/science/article/pii/S0196890402002297 (visited on 05/28/2026).

Albrecht, Bruce A. (Sept. 1989). "Aerosols, Cloud Microphysics, and Fractional Cloudiness". In: *Science* 245.4923, pp. 1227–1230. DOI: 10.1126/science.245.4923.1227. URL: https://www.science.org/doi/10.1126/science.245.4923.1227 (visited on 05/29/2026).

Alfaro, Stéphane C. and Laurent Gomes (2001). "Modeling mineral aerosol production by wind erosion: Emission intensities and aerosol size distributions in source areas". en. In: *Journal of Geophysical Research: Atmospheres* 106.D16. _eprint: https://agupubs.onlinelibrary.wiley.com/d pp. 18075–18084. ISSN: 2156-2202. DOI: 10.1029/2000JD900339. URL: https://onlinelibrary.wiley.com/doi/abs/10.1029/2000JD900339 (visited on 05/29/2026).

Antonov, John et al. (1998). *World ocean atlas 1998. Volume 1, Temperature of the Atlantic Ocean*. en. URL: https://repository.library.noaa.gov (visited on 05/29/2026).

Arino, Olivier et al. (2008). "The Most Detailed Portrait of Earth". en. In: *ESA Bulletin*. URL: https://publications.jrc.ec.europa.eu/repository/handle/JRC49370 (visited on 05/29/2026).

Ataş, İsa (Jan. 2023). "Performance Evaluation of Jaccard-Dice Coefficient on Building Segmentation from High Resolution Satellite Images". en. In: *Balkan Journal of Electrical and Computer Engineering* 11.1, pp. 100–106. ISSN: 2147-284X, 2147-284X. DOI: 10.17694/bajece.1212563. URL: https://dergipark.org.tr/en/pub/bajece/article/1212563 (visited on 05/29/2026).

Atmospheric circulation (Jan. 2026). en. Page Version ID: 1334449903. URL: https://en.wikipedia.org/w/index.php?title=Atmospheric_circulation&oldid=1334449903 (visited on 06/01/2026).

Aydin, Nazli Yonca, Elcin Kentel, and Sebnem Duzgun (Jan. 2010). "GIS-based environmental assessment of wind energy systems for spatial planning: A case study from Western Turkey". In: *Renewable and Sustainable Energy Reviews* 14.1, pp. 364–373. ISSN: 1364-0321. DOI: 10.1016/j.rser.2009.07.023. URL: https://www.sciencedirect.com/science/article/pii/S1364032109001610 (visited on 05/28/2026).

Azhgaliyeva, Dina et al. (Nov. 2024). "Renewable energy investments and feed-in tariffs: Firm-level evidence from Southeast Asia1". In: *Applied Energy* 374, p. 123986. ISSN: 0306-2619. DOI: 10.1016/j.apenergy.2024.123986. URL: https://www.sciencedirect.com/science/article/pii/S0306261924013692 (visited on 06/01/2026).

Baer, Andreas et al. (Jan. 2025). *auto-icon: seamless management of ICON model runs with Autosubmit*. Language: eng. DOI: 10.5281/zenodo.15019211. URL: https://zenodo.org/records/15019211 (visited on 05/29/2026).

Bechtold, P. et al. (2001). "A mass-flux convection scheme for regional and global models". en. In: *Quarterly Journal of the Royal Meteorological Society* 127.573. _eprint: https://rmets.onlinelibrary.wiley.com pp. 869–886. ISSN: 1477-870X. DOI: 10.1002/qj.49712757309. URL: https://onlinelibrary.wiley.com/doi/abs/10.1002/qj.49712757309 (visited on 05/29/2026).

Benyadry, Sara, Mohammed Halimi, and Ahmed Khouya (May 2024). "Soiling impact and cleaning techniques for optimizing photovoltaic and concentrated solar power power production: A state-of-the-art review". EN. In: *Energy & Environment* 35.3, pp. 1637–1669. ISSN: 0958-305X. DOI: 10.1177/0958305X241230624. URL: https://doi.org/10.1177/0958305X241230624 (visited on 05/28/2026).

Bergen, A. R. and D. J. Hill (Jan. 1981). "A structure preserving model for power system stability analysis". English. In: *IEEE Transactions on Power Apparatus and Systems* PAS-100.1, pp. 25–35. ISSN: 0018-9510. DOI: 10.1109/TPAS.1981.316883. URL: https://research.monash.edu/en/publications/a-structure-preserving-model-for-power-system-stability-analysis/ (visited on 05/28/2026).

Bergin, Mike H. et al. (Aug. 2017). "Large Reductions in Solar Energy Production Due to Dust and Particulate Air Pollution". en. In: *Environmental Science & Technology Letters* 4.8, pp. 339–344. ISSN: 2328-8930, 2328-8930. DOI: 10.1021/acs.estlett.7b00197. URL: https://pubs.acs.org/doi/10.1021/acs.estlett.7b00197 (visited on 05/28/2026).

Borchert, Sebastian et al. (Aug. 2019). "The upper-atmosphere extension of the ICON general circulation model (version: ua-icon-1.0)". English. In: *Geoscientific Model Development* 12.8, pp. 3541–3569. ISSN: 1991-959X. DOI: 10.5194/gmd-12-3541-2019. URL: https://gmd.copernicus.org/articles/12/3541/2019/ (visited on 05/30/2026).

Botha, Nicolene et al. (July 2025). *Power Generation Time Series for Solar Energy Generation: Modelling with ATlite in South Africa*. URL: https://www.mdpi.com/2673-9941/5/1/8 (visited on 05/28/2026).

Brandkamp, Simon (Feb. 2025). "Hedging households against extreme electricity prices". en. In: *Working Paper Series in Economics*. Number: 106. URL: https://ideas.repec.org//p/kls/series/0106.html (visited on 05/28/2026).

Carvalho, D. et al. (Nov. 2021). "Wind energy resource over Europe under CMIP6 future climate projections: What changes from CMIP5 to CMIP6". In: *Renewable and Sustainable Energy Reviews* 151, p. 111594. ISSN: 1364-0321. DOI: 10.1016/j.rser.2021.111594. URL: https://www.sciencedirect.com/science/article/pii/S1364032121008716 (visited on 05/28/2026).

Ciupuliga, Ana Roxana et al. (May 2011). "Approval procedures and consensus for building transmission lines: Obstacles and solutions". In: *2011 8th International Conference on the European Energy Market (EEM)*. ISSN: 2165-4093, pp. 426–431. DOI: 10.1109/EEM.2011.5953123. URL: https://ieeexplore.ieee.org/abstract/document/5953123 (visited on 06/01/2026).

Collatz, GJ, M. Ribas-Carbo, and JA Berry (Jan. 1992). "Coupled Photosynthesis-Stomatal Conductance Model for Leaves of C4 Plants". In: *Functional Plant Biology* 19. ADS Bibcode: 1992FunPB..19..519C, p. 519. DOI: 10.1071/PP9920519. URL: https://ui.adsabs.harvard.edu/abs/1992FunPB..19..519C (visited on 05/28/2026).

Deng, S. J. and S. S. Oren (May 2006). "Electricity derivatives and risk management". In: *Energy*. Electricity Market Reform and Deregulation 31.6, pp. 940–953. ISSN: 0360-5442. DOI: 10.1016/j.energy.2005.02.015. URL: https://www.sciencedirect.com/science/article/pii/S0360544205000496 (visited on 05/28/2026).

Directive (EU) 2018/2001 of the European Parliament and of the Council of 11 December 2018 on the promotion of the use of energy from renewable sources (recast) (Text with EEA relevance.) (Dec. 2018). en. URL: http://data.europa.eu/eli/dir/2018/2001/oj (visited on 05/28/2026).

Directorate-General for Energy (European Commission) and Frontier Economics (2019). *METIS technical note T4: overview of European electricity markets*. eng. Publications Office of the European Union. ISBN: 978-92-76-08956-8. URL: https://data.europa.eu/doi/10.2833/65488 (visited on 05/28/2026).

Dutta, Riya, Kironmala Chanda, and Rajib Maity (Feb. 2022). "Future of solar energy potential in a changing climate across the world: A CMIP6 multi-model ensemble analysis". In: *Renewable Energy* 188. DOI: 10.1016/j.renene.2022.02.023.

EEG 2023 - nichtamtliches Inhaltsverzeichnis (2026). URL: https://www.gesetze-im-internet.de/eeg_2014/ (visited on 05/28/2026).

EMD (2026). *windPRO*. en. URL: https://www.emd-international.com/software/windpro (visited on 06/01/2026).

Energy Transition Model (2026). URL: https://energytransitionmodel.com/ (visited on 05/31/2026).

EnergyMap - Auf dem Weg zu 100% EE (2026). URL: http://www.energymap.info/ (visited on 05/29/2026).

ENTSO-E (Mar. 2009). *ENTSO-E Operation Handbook (Load-Frequency Control and Performance)*. Tech. rep.

– (Jan. 2025). *Entso-e | Planning the future grid - TYNDP*. en. URL: https://tyndp.entsoe.eu/ (visited on 05/28/2026).

– (2026). *ERAA - European Resource Adequacy Assessment*. en-us. URL: https://www.entsoe.eu/eraa/ (visited on 05/28/2026).

Environmental Working Group, Norbert Untersteiner (1997). *Environmental Working Group Joint U.S.-Russian Atlas of the Arctic Ocean*. DOI: 10.7265/N5H12ZX4. URL: http://nsidc.org/data/G01961.html (visited on 05/29/2026).

Eriksson, Sandra, Hans Bernhoff, and Mats Leijon (June 2008). "Evaluation of different turbine concepts for wind power". In: *Renewable and Sustainable Energy Reviews* 12.5, pp. 1419–1434. ISSN: 1364-0321. DOI: 10.1016/j.rser.2006.05.017. URL: https://www.sciencedirect.com/science/article/pii/S1364032107000111 (visited on 05/29/2026).

esa (2026). *Earth radiation budget*. en. URL: https://www.esa.int/ESA_Multimedia/Images/2024/01/Earth_radiation_budget (visited on 06/01/2026).

ESGF MetaGrid (2026). URL: https://esgf-metagrid.cloud.dkrz.de/search/cmip6-dkrz/ (visited on 05/29/2026).

Etling, Dieter, ed. (2008). *Theoretische Meteorologie: Eine Einführung*. ger. 3. erweiterte und aktualisierte Auflage. SpringerLink Bücher. Berlin, Heidelberg: Springer-Verlag Berlin Heidelberg. ISBN: 978-3-540-75979-9. DOI: 10.1007/978-3-540-75979-9.

Farquhar, G. D., S. von Caemmerer, and J. A. Berry (June 1980). "A biochemical model of photosynthetic CO2 assimilation in leaves of C3 species". en. In: *Planta* 149.1, pp. 78–90.

ISSN: 1432-2048. DOI: 10.1007/BF00386231. URL: https://doi.org/10.1007/BF00386231 (visited on 05/28/2026).

Fécan, F., B. Marticorena, and G. Bergametti (Jan. 1999). "Parametrization of the increase of the aeolian erosion threshold wind friction velocity due to soil moisture for arid and semi-arid areas". English. In: *Annales Geophysicae* 17.1, pp. 149–157. ISSN: 0992-7689. DOI: 10.1007/s00585-999-0149-7. URL: https://angeo.copernicus.org/articles/17/149/1999/ (visited on 05/29/2026).

Frank, Stephen, Ingrida Steponavice, and Steffen Rebennack (Sept. 2012). "Optimal power flow: a bibliographic survey I". en. In: *Energy Systems* 3.3, pp. 221–258. ISSN: 1868-3975. DOI: 10.1007/s12667-012-0056-y. URL: https://doi.org/10.1007/s12667-012-0056-y (visited on 05/29/2026).

Fraunholz, Christoph (2021). *Market Design for the Transition to Renewable Electricity Systems*. de. DOI: 10.5445/IR/1000133282. URL: https://publikationen.bibliothek.kit.edu/1000133282 (visited on 05/29/2026).

Gassmann, Almut and Hans-Joachim Herzog (2008). "Towards a consistent numerical compressible non-hydrostatic model using generalized Hamiltonian tools". en. In: *Quarterly Journal of the Royal Meteorological Society* 134.635. _eprint: https://onlinelibrary.wiley.com/doi/pdf/10.1002/qj.297, pp. 1597–1613. ISSN: 1477-870X. DOI: 10.1002/qj.297. URL: https://onlinelibrary.wiley.com/doi/abs/10.1002/qj.297 (visited on 02/22/2023).

Glossar - energieforschung.de (2026). URL: https://www.energieforschung.de/de/glossar/Dunkelflaute (visited on 06/01/2026).

Grainger, John J. and William D. Stevenson (1994). *Power system analysis*. eng. McGraw-Hill series in electrical and computer engineering Power and energy. New York, NY ; St. Louis ; San Francisco: McGraw-Hill, Inc. ISBN: 978-0-07-061293-8 978-0-07-113338-8.

Häberlin, Heinrich (Sept. 2007). *Photovoltaik*. de-DE. ISBN: 978-3-8007-3003-2. URL: https://www.isbn.de/buch/9783800730032/photovoltaik (visited on 05/28/2026).

Hagenmeyer, Veit (Feb. 2024). *Optimierung in Energiesystemen*. Karlsruhe Institut of Technology.

Hau, Erich (2016). *Windkraftanlagen*. en. URL: https://link.springer.com/book/10.1007/978-3-662-53154-9 (visited on 05/28/2026).

Heussaff, C. and G. Zachmann (Apr. 2024). *The changing dynamics of European electricity markets and the supply-demand mismatch risk*. en. URL: https://www.bruegel.org/policy-brief/changing-dynamics-european-electricity-markets-and-supply-demand-mismatch-risk (visited on 05/28/2026).

Hofmann, Fabian et al. (June 2021). *atlite: A Lightweight Python Package for Calculating Renewable Power Potentials and Time Series*. Tech. rep.

Hogan, Robin J. and Alessio Bozzo (2018). "A Flexible and Efficient Radiation Scheme for the ECMWF Model". en. In: *Journal of Advances in Modeling Earth Systems* 10.8. _eprint: https://agupubs.onlinelibrary.wiley.com/doi/pdf/10.1029/2018MS001364, pp. 1990–2008. ISSN: 1942-2466. DOI: 10.1029/2018MS001364. URL: https://onlinelibrary.wiley.com/doi/abs/10.1029/2018MS001364 (visited on 05/29/2026).

Home | Global Energy Monitor (2026). en. URL: https://globalenergymonitor.org/ (visited on 05/29/2026).

Hoshyaripour, Gholam Ali et al. (Feb. 2026). "The atmospheric composition component of the ICON modeling framework: ICON-ART version 2025.10". English. In: *Geoscientific Model*

Development 19.4, pp. 1645–1681. ISSN: 1991-959X. DOI: 10.5194/gmd-19-1645-2026. URL: https://gmd.copernicus.org/articles/19/1645/2026/ (visited on 05/29/2026).

Hou, Xinyuan et al. (Nov. 2021). "Climate change impacts on solar power generation and its spatial variability in Europe based on CMIP6". English. In: *Earth System Dynamics* 12.4, pp. 1099–1113. ISSN: 2190-4979. DOI: 10.5194/esd-12-1099-2021. URL: https://esd.copernicus.org/articles/12/1099/2021/ (visited on 05/28/2026).

Hufschmid, Markus (2021). *Grundlagen der Elektrotechnik: Einführung für Studierende der Ingenieur- und Naturwissenschaften*. de. Wiesbaden: Springer Fachmedien. ISBN: 978-3-658-30385-3 978-3-658-30386-0. DOI: 10.1007/978-3-658-30386-0. URL: http://link.springer.com/10.1007/978-3-658-30386-0 (visited on 05/28/2026).

Hurtt, George C. et al. (Nov. 2020). "Harmonization of global land use change and management for the period 850–2100 (LUH2) for CMIP6". English. In: *Geoscientific Model Development* 13.11, pp. 5425–5464. ISSN: 1991-959X. DOI: 10.5194/gmd-13-5425-2020. URL: https://gmd.copernicus.org/articles/13/5425/2020/ (visited on 05/29/2026).

institute, energy (2024). *Statistical Review of Worrld Energy 2024 (73rd edition)*. Tech. rep. energy institute.

Introduction — atlite 0.6 documentation (2026). URL: https://atlite.readthedocs.io/en/master/introduction.html (visited on 05/28/2026).

JRC Data Catalogue - Collection - European Commission (2026). URL: https://data.jrc.ec.europa.eu/collection/id-0110 (visited on 05/31/2026).

Kinne, Stefan (Aug. 2019). "Aerosol radiative effects with MACv2". English. In: *Atmospheric Chemistry and Physics* 19.16, pp. 10919–10959. ISSN: 1680-7316. DOI: 10.5194/acp-19-10919-2019. URL: https://acp.copernicus.org/articles/19/10919/2019/ (visited on 05/29/2026).

Kok, Jasper F. et al. (Feb. 2023). "Mineral dust aerosol impacts on global climate and climate change". en. In: *Nature Reviews Earth & Environment* 4.2, pp. 71–86. ISSN: 2662-138X. DOI: 10.1038/s43017-022-00379-5. URL: https://www.nature.com/articles/s43017-022-00379-5 (visited on 05/28/2026).

Konstantin, Panos and Margarete Konstantin (2023a). "Energierechtliche Rahmenbedingungen". de. In: *Praxisbuch Energiewirtschaft: Energieumwandlung, -transport und -beschaffung, Übertragungsnetzausbau und Kernenergieausstieg*. Ed. by Panos Konstantin and Margarete Konstantin. Berlin, Heidelberg: Springer, pp. 517–570. ISBN: 978-3-662-67335-5. DOI: 10.1007/978-3-662-67335-5_9. URL: https://doi.org/10.1007/978-3-662-67335-5_9 (visited on 05/28/2026).

– (2023b). *Praxisbuch Energiewirtschaft: Energieumwandlung, -transport und -beschaffung, Übertragungsnetzausbau und Kernenergieausstieg*. ger. 5., aktualisierte Auflage. Berlin ; [Heidelberg]: Springer Vieweg. ISBN: 978-3-662-67335-5. DOI: 10.1007/978-3-662-67335-5.

Korn, P. et al. (2022). "ICON-O: The Ocean Component of the ICON Earth System Model—Global Simulation Characteristics and Local Telescoping Capability". en. In: *Journal of Advances in Modeling Earth Systems* 14.10. _eprint: https://agupubs.onlinelibrary.wiley.com/doi/pdf/10.1029/2021M e2021MS002952. ISSN: 1942-2466. DOI: 10.1029/2021MS002952. URL: https://onlinelibrary.wiley.com/doi/abs/10.1029/2021MS002952 (visited on 05/28/2026).

Kriegler, Elmar et al. (Feb. 2014). "A new scenario framework for climate change research: the concept of shared climate policy assumptions". en. In: *Climatic Change* 122.3, pp. 401–414.

ISSN: 1573-1480. DOI: 10.1007/s10584-013-0971-5. URL: https://doi.org/10.1007/s10584-013-0971-5 (visited on 05/29/2026).

Kühnapfel, Uwe and Veit Hagenmeyer (2025). "On the Art of Electric Power System Modelling and Simulation for Integrated Transmission-Distribution Analysis". en. In: *Modelling the Energy Transition: Cultures, Visions, Narratives*. Ed. by Robert Matthias Erdbeer, Veit Hagenmeyer, and Klaus Stierstorfer. Cham: Springer Nature Switzerland, pp. 117–133. ISBN: 978-3-031-69031-0. DOI: 10.1007/978-3-031-69031-0_7. URL: https://doi.org/10.1007/978-3-031-69031-0_7 (visited on 05/29/2026).

Kühnapfel, Uwe G. (2025). "European RMS PowerFactory Model". de. In: URL: https://publikationen.bibliothek.kit.edu/1000183486 (visited on 05/29/2026).

Kundur, Prabha S. and Om P. Malik (2022). *Power system stability and control*. eng. Second edition. New York ; Chicago ; San Francisco ; Athens ; London ; Madrid ; Mexico City ; Milan ; New Delhi ; Singapore ; Sydney ; Toronto: McGraw Hill. ISBN: 978-1-260-47354-4.

Lei, Yadong et al. (July 2023). "Co-benefits of carbon neutrality in enhancing and stabilizing solar and wind energy". en. In: *Nature Climate Change* 13.7, pp. 693–700. ISSN: 1758-6798. DOI: 10.1038/s41558-023-01692-7. URL: https://www.nature.com/articles/s41558-023-01692-7 (visited on 05/28/2026).

Leuenberger, Daniel et al. (Sept. 2010). "A Generalization of the SLEVE Vertical Coordinate". EN. In: *Monthly Weather Review* 138.9, pp. 3683–3689. ISSN: 1520-0493, 0027-0644. DOI: 10.1175/2010MWR3307.1. URL: https://journals.ametsoc.org/view/journals/mwre/138/9/2010mwr3307.1.xml (visited on 02/22/2023).

Levante HPC System — DKRZ Documentation documentation (2026). URL: https://docs.dkrz.de/doc/levante/index.html (visited on 05/28/2026).

Li, Charles, Denise Mauzerall, and Mike Bergin (Sept. 2020). "Global reduction of solar power generation efficiency due to aerosols and panel soiling". In: *Nature Sustainability* 3, pp. 1–8. DOI: 10.1038/s41893-020-0553-2.

Li, Xingpeng and Qianxue Xia (Oct. 2020). "Stochastic Optimal Power Flow with Network Reconfiguration: Congestion Management and Facilitating Grid Integration of Renewables". In: *2020 IEEE/PES Transmission and Distribution Conference and Exposition (T&D)*. ISSN: 2160-8563, pp. 1–5. DOI: 10.1109/TD39804.2020.9299954. URL: https://ieeexplore.ieee.org/abstract/document/9299954 (visited on 05/28/2026).

Liebensteiner, Mario, Fabian Ocker, and Anas Abuzayed (2025). "High electricity price despite expansion in renewables: How market trends shape Germany's power market in the coming years". en. In: *Energy Policy* 198.C. URL: https://ideas.repec.org//a/eee/enepol/v198y2025ics0301421524004683.html (visited on 05/28/2026).

Liu, Jianlei et al. (Mar. 2023). "Introducing PROOF - A PROcess Orchestration Framework for the Automation of Computational Scientific Workflows and Co-Simulations". In: *2023 Open Source Modelling and Simulation of Energy Systems (OSMSES)*, pp. 1–6. DOI: 10.1109/OSMSES58477.2023.10089680. URL: https://ieeexplore.ieee.org/document/10089680 (visited on 05/30/2026).

Lott, François and Martin J. Miller (1997). "A new subgrid-scale orographic drag parametrization: Its formulation and testing". en. In: *Quarterly Journal of the Royal Meteorological Society* 123.537. _eprint: https://rmets.onlinelibrary.wiley.com/doi/pdf/10.1002/qj.49712353704, pp. 101–127. ISSN: 1477-870X. DOI: 10.1002/qj.49712353704. URL: https://onlinelibrary.wiley.com/doi/abs/10.1002/qj.49712353704 (visited on 05/29/2026).

Marti, Luisa and Rosa Puertas (Jan. 2022). "Sustainable energy development analysis: Energy Trilemma". In: *Sustainable Technology and Entrepreneurship* 1.1, p. 100007. ISSN: 2773-0328. DOI: 10.1016/j.stae.2022.100007. URL: https://www.sciencedirect.com/science/article/pii/S2773032822000074 (visited on 05/28/2026).

Masson-Delmotte, Valérie et al., eds. (2021). *Climate Change 2021: The Physical Science Basis. Contribution of Working Group I to the Sixth Assessment Report of the Intergovernmental Panel on Climate Change*. Cambridge, United Kingdom and New York, NY, USA: Cambridge University Press. DOI: 10.1017/9781009157896.

Maysun (Feb. 2025). *Der Einfluss der Temperatur auf photovoltaische Kraftwerke*. de. URL: https://www.maysunsolar.de/blog/der-einfluss-der-temperatur-auf-photovoltaische-kraftwerke (visited on 05/28/2026).

McLinden, C. A. et al. (2000). "Stratospheric ozone in 3-D models: A simple chemistry and the cross-tropopause flux". en. In: *Journal of Geophysical Research: Atmospheres* 105.D11. _eprint: https://agupubs.onlinelibrary.wiley.com/doi/pdf/10.1029/2000JD900124, pp. 14653–14665. ISSN: 2156-2202. DOI: 10.1029/2000JD900124. URL: https://onlinelibrary.wiley.com/doi/abs/10.1029/2000JD900124 (visited on 05/29/2026).

Mellor, George L. and Tetsuji Yamada (1982). "Development of a turbulence closure model for geophysical fluid problems". en. In: *Reviews of Geophysics* 20.4. _eprint: https://agupubs.onlinelibrary.wile pp. 851–875. ISSN: 1944-9208. DOI: 10.1029/RG020i004p00851. URL: https://onlinelibrary.wiley.com/doi/abs/10.1029/RG020i004p00851 (visited on 05/29/2026).

Meteodyn - L'Ingénierie du vent, de la Climatologie et de la Météorologie (2026). fr-FR. URL: https://meteodyn.fr/ (visited on 06/01/2026).

Mignacca, B. and G. Locatelli (Feb. 2020). "Economics and finance of Small Modular Reactors: A systematic review and research agenda". In: *Renewable and Sustainable Energy Reviews* 118, p. 109519. ISSN: 1364-0321. DOI: 10.1016/j.rser.2019.109519. URL: https://www.sciencedirect.com/science/article/pii/S1364032119307270 (visited on 05/28/2026).

Miura, Hiroaki and William Skamarock (2013). *An Upwind-Biased Transport Scheme Using a Quadratic Reconstruction on Spherical Icosahedral Grids in: Monthly Weather Review Volume 141 Issue 2 (2013)*. URL: https://journals.ametsoc.org/view/journals/mwre/141/2/mwr-d-11-00355.1.xml (visited on 05/31/2026).

Moss, Richard H. et al. (Feb. 2010). "The next generation of scenarios for climate change research and assessment". en. In: *Nature* 463.7282, pp. 747–756. ISSN: 1476-4687. DOI: 10.1038/nature08823. URL: https://www.nature.com/articles/nature08823 (visited on 05/28/2026).

Müller, Wolfgang A. et al. (Dec. 2025). "The ICON-based Earth System Model for climate predictions and projections (ICON XPP v1.0)". English. In: *Geoscientific Model Development* 18.23, pp. 9385–9415. ISSN: 1991-959X. DOI: 10.5194/gmd-18-9385-2025. URL: https://gmd.copernicus.org/articles/18/9385/2025/ (visited on 05/28/2026).

Nachtergaele, F. and N. Batjes (2012). *Harmonized world soil database v1.2 | FAO SOILS PORTAL | Food and Agriculture Organization of the United Nations*. URL: https://www.fao.org/soils-portal/data-hub/soil-maps-and-databases/harmonized-world-soil-database-v12/en/ (visited on 05/29/2026).

Nejla, Essaddi, Khaoula Saidani, and Mongi Besbes (Dec. 2025). "Overcoming the integration bottleneck: a global review of renewable energy and grid adaptation strategies". In: *International Journal of Sustainable Energy* 44.1. _eprint: https://doi.org/10.1080/14786451.2025.2569922,

p. 2569922. ISSN: 1478-6451. DOI: 10.1080/14786451.2025.2569922. URL: https://doi.org/10.1080/14786451.2025.2569922 (visited on 05/28/2026).

Nonnenmacher, Tom, Jenny Nelson, and Benedict Winchester (Oct. 2023). *Maximum Return on Investment for a Domestic Photovoltaic Installation*. arXiv:2310.09323 [math.OC]. DOI: 10.48550/arXiv.2310.09323. URL: http://arxiv.org/abs/2310.09323 (visited on 06/01/2026).

O'Neill, Brian C. et al. (Sept. 2016). "The Scenario Model Intercomparison Project (ScenarioMIP) for CMIP6". English. In: *Geoscientific Model Development* 9.9, pp. 3461–3482. ISSN: 1991-959X. DOI: 10.5194/gmd-9-3461-2016. URL: https://gmd.copernicus.org/articles/9/3461/2016/ (visited on 05/28/2026).

Ohlendorf, Nils and Wolf-Peter Schill (Aug. 2020). "Frequency and duration of low-wind-power events in Germany". en. In: *Environmental Research Letters* 15.8, p. 084045. ISSN: 1748-9326. DOI: 10.1088/1748-9326/ab91e9. URL: https://doi.org/10.1088/1748-9326/ab91e9 (visited on 06/01/2026).

Organization, World Meteorological (Mar. 2025). *Report: How climate insights drive a more reliable renewable energy transition*. en. URL: https://wmo.int/news/media-centre/report-how-climate-insights-drive-more-reliable-renewable-energy-transition (visited on 05/28/2026).

Orr, Andrew et al. (Nov. 2010). "Improved Middle Atmosphere Climate and Forecasts in the ECMWF Model through a Nonorographic Gravity Wave Drag Parameterization". EN. In: *Journal of Climate* 23.22, pp. 5905–5926. ISSN: 0894-8755, 1520-0442. DOI: 10.1175/2010JCLI3490.1. URL: https://journals.ametsoc.org/view/journals/clim/23/22/2010jcli3490.1.xml (visited on 05/29/2026).

Peixoto, José P. and Abraham H. Oort (1992). *Physics of climate*. eng. New York ; Berlin ; Heidelberg: AIP; Springer. ISBN: 978-0-88318-712-8 978-0-88318-711-1.

Prill, F. et al. (Aug. 2025). *Working wih the ICON Model - ICON Tutorial 2025*. Tech. rep. Offenbach: Deutscher Wetterdienst (DWD). URL: https://www.dwd.de/EN/ourservices/nwp_icon_tutorial/pdf_volume/icon_tutorial2025_en.pdf (visited on 05/29/2026).

Quaschning, Volker (2025). *Regenerative Energiesysteme: Technologie, Berechnung, Klimaschutz*. ger. 13., aktualisierte Auflage. Hanser eLibrary. München: Hanser. ISBN: 978-3-446-48466-5. DOI: 10.3139/9783446484665.

R Owens, Tim Hewson (2018). *ECMWF Forecast User Guide*. eng. text. URL: https://www.ecmwf.int/en/elibrary/81307-ecmwf-forecast-user-guide (visited on 05/29/2026).

Rappaport, Paul (Dec. 1959). "The photovoltaic effect and its utilization". en. In: *Solar Energy* 3.4, pp. 8–18. ISSN: 0038092X. DOI: 10.1016/0038-092X(59)90002-7. URL: https://linkinghub.elsevier.com/retrieve/pii/0038092X59900027 (visited on 05/28/2026).

Raupach, M. (1993). *Dry deposition of gases and particles to vegetation*. Tech. rep. 27.

Reick, Christian H. et al. (2021). *JSBACH 3 - The land component of the MPI Earth System Model: documentation of version 3.2 | Ansicht | MPG.PuRe*. URL: https://pure.mpg.de/view/item_3279802 (visited on 05/29/2026).

Reinert, D et al. (n.d.). "ICON Database Reference Manual". en. In: ().

Riahi, Keywan et al. (Jan. 2017). "The Shared Socioeconomic Pathways and their energy, land use, and greenhouse gas emissions implications: An overview". In: *Global Environmental Change* 42, pp. 153–168. ISSN: 0959-3780. DOI: 10.1016/j.gloenvcha.2016.05.009. URL:

https://www.sciencedirect.com/science/article/pii/S0959378016300681 (visited on 05/28/2026).

Rieger, D., M. Bangert, et al. (June 2015). "ICON–ART 1.0 – a new online-coupled model system from the global to regional scale". English. In: *Geoscientific Model Development* 8.6, pp. 1659–1676. ISSN: 1991-959X. DOI: 10.5194/gmd-8-1659-2015. URL: https://gmd.copernicus.org/articles/8/1659/2015/ (visited on 04/24/2026).

Rieger, D., Martin Köhler, et al. (Jan. 2019). *ecRad in ICON - Details on the Implementation and First Results | Request PDF*. en. DOI: 10.5676/DWD_pub/nwv/icon_004. URL: https://www.researchgate.net/publication/338424386_ecRad_in_ICON_-_Details_on_the_Implementation_and_First_Results (visited on 05/29/2026).

Rieger, Daniel et al. (Nov. 2017). "Impact of the 4 April 2014 Saharan dust outbreak on the photovoltaic power generation in Germany". English. In: *Atmospheric Chemistry and Physics* 17.21, pp. 13391–13415. ISSN: 1680-7316. DOI: 10.5194/acp-17-13391-2017. URL: https://acp.copernicus.org/articles/17/13391/2017/ (visited on 05/28/2026).

Roy, F. Ruby Vincy et al. (Jan. 2026). "A systematic review of congestion management strategies in renewable-integrated power systems". en. In: *Electrical Engineering* 108.2, p. 130. ISSN: 1432-0487. DOI: 10.1007/s00202-025-03477-x. URL: https://doi.org/10.1007/s00202-025-03477-x (visited on 05/28/2026).

Schneck, Rainer et al. (Nov. 2022). "Assessment of JSBACHv4.30 as a land component of ICON-ESM-V1 in comparison to its predecessor JSBACHv3.2 of MPI-ESM1.2". English. In: *Geoscientific Model Development* 15.22, pp. 8581–8611. ISSN: 1991-959X. DOI: 10.5194/gmd-15-8581-2022. URL: https://gmd.copernicus.org/articles/15/8581/2022/ (visited on 05/28/2026).

Schneider, C. et al. (Jan. 2013). "How will climate change modify river flow regimes in Europe?" English. In: *Hydrology and Earth System Sciences* 17.1, pp. 325–339. ISSN: 1027-5606. DOI: 10.5194/hess-17-325-2013. URL: https://hess.copernicus.org/articles/17/325/2013/hess-17-325-2013.html (visited on 05/30/2026).

Schwab, Adolf J. (2017). *Elektroenergiesysteme: Erzeugung, Übertragung und Verteilung elektrischer Energie*. ger. 5. Aufl. 2017. SpringerLink Bücher. Berlin, Heidelberg: Springer Vieweg. ISBN: 978-3-662-55316-9. DOI: 10.1007/978-3-662-55316-9.

Seifert, Axel and Klaus D. Beheng (Oct. 2001). "A double-moment parameterization for simulating autoconversion, accretion and selfcollection". In: *Atmospheric Research*. 13th International Conference on Clouds and Precipitation 59-60, pp. 265–281. ISSN: 0169-8095. DOI: 10.1016/S0169-8095(01)00126-0. URL: https://www.sciencedirect.com/science/article/pii/S0169809501001260 (visited on 05/29/2026).

Sensfuß, Frank (2007). *Assessment of the impact of renewable electricity generation on the German electricity sector: An agent-based simulation approach*. de. DOI: 10.5445/IR/1000007777. URL: https://publikationen.bibliothek.kit.edu/1000007777 (visited on 05/29/2026).

Shao, Yaping (2001). "A model for mineral dust emission". en. In: *Journal of Geophysical Research: Atmospheres* 106.D17. _eprint: https://agupubs.onlinelibrary.wiley.com/doi/pdf/10.1029/2001JD90 pp. 20239–20254. ISSN: 2156-2202. DOI: 10.1029/2001JD900171. URL: https://onlinelibrary.wiley.com/doi/abs/10.1029/2001JD900171 (visited on 05/29/2026).

Shao, Yaping, Andreas H. Fink, and Martina Klose (2010). "Numerical simulation of a continental-scale Saharan dust event". en. In: *Journal of Geophysical Research: Atmospheres*

115.D13. _eprint: https://agupubs.onlinelibrary.wiley.com/doi/pdf/10.1029/2009JD012678. ISSN: 2156-2202. DOI: 10.1029/2009JD012678. URL: https://onlinelibrary.wiley.com/doi/abs/10.1029/2009JD012678 (visited on 05/29/2026).

Shao, Yaping and Hua Lu (2000). "A simple expression for wind erosion threshold friction velocity". en. In: *Journal of Geophysical Research: Atmospheres* 105.D17. _eprint: https://agupubs.onlinelibrary.wiley.com/doi/pdf/10.1029/2000JD900304, pp. 22437–22443. ISSN: 2156-2202. DOI: 10.1029/2000JD900304. URL: https://onlinelibrary.wiley.com/doi/abs/10.1029/2000JD900304 (visited on 05/29/2026).

Shepherd, Dennis G. (Dec. 1990). *Historical development of the windmill*. Tech. rep. NASA-CR-4337. NTRS Author Affiliations: Sverdrup Technology, Inc., Brook Park NTRS Document ID: 19910012312 NTRS Research Center: Legacy CDMS (CDMS). URL: https://ntrs.nasa.gov/citations/19910012312 (visited on 05/28/2026).

Shu, Han, Siva Visvesvaran, and Jacob Mays (Dec. 2025). "Operational uncertainty and the missing money problem". In: *Energy Economics* 152, p. 108948. ISSN: 0140-9883. DOI: 10.1016/j.eneco.2025.108948. URL: https://www.sciencedirect.com/science/article/pii/S0140988325007753 (visited on 05/28/2026).

Slednev, Viktor (2024). *Development of a techno-economic energy system model considering the highly resolved conversion and multimodal transmission of energy carriers on a global scale*. de. DOI: 10.5445/IR/1000170863. URL: https://publikationen.bibliothek.kit.edu/1000170863 (visited on 05/29/2026).

Slednev, Viktor et al. (2017). "Regionalizing Input Data for Generation and Transmission Expansion Planning Models". en. In: *Advances in Energy System Optimization*. Ed. by Valentin Bertsch et al. Cham: Springer International Publishing, pp. 205–217. ISBN: 978-3-319-51795-7. DOI: 10.1007/978-3-319-51795-7_13.

Sokolovsky, Yuli and Vladimir Rotkin (Aug. 2017). *THEORETICAL AND TECHNICAL BASIS FOR THE OPTIMIZATION OF WIND ENERGY PLANTS*. ISBN: 978-1-387-33326-4.

Staniforth, Andrew and Nigel Wood (Mar. 2008). "Aspects of the dynamical core of a nonhydrostatic, deep-atmosphere, unified weather and climate-prediction model". In: *Journal of Computational Physics*. Predicting weather, climate and extreme events 227.7, pp. 3445–3464. ISSN: 0021-9991. DOI: 10.1016/j.jcp.2006.11.009. URL: https://www.sciencedirect.com/science/article/pii/S0021999106005626 (visited on 05/30/2026).

Steele, Michael, Rebecca Morley, and Wendy Ermold (May 2001). "PHC: A Global Ocean Hydrography with a High-Quality Arctic Ocean". EN. In: *Journal of Climate* 14.9, pp. 2079–2087. ISSN: 0894-8755, 1520-0442. DOI: 10.1175/1520-0442(2001)014<2079:PAGOHW>2.0.CO;2. URL: https://journals.ametsoc.org/view/journals/clim/14/9/1520-0442_2001_014_2079_pagohw_2.0.co_2.xml (visited on 05/29/2026).

Stull, Roland B. (2009). *An introduction to boundary layer meteorology*. eng. Reprinted. Atmospheric and oceanographic sciences library 13. Dordrecht: Springer. ISBN: 978-90-277-2769-5.

Tegen, Ina et al. (1997). "Contribution of different aerosol species to the global aerosol extinction optical thickness: Estimates from model results". en. In: *Journal of Geophysical Research: Atmospheres* 102.D20. _eprint: https://agupubs.onlinelibrary.wiley.com/doi/pdf/10.1029/97JD01864, pp. 23895–23915. ISSN: 2156-2202. DOI: 10.1029/97JD01864. URL: https://onlinelibrary.wiley.com/doi/abs/10.1029/97JD01864 (visited on 05/29/2026).

Tiedtke, M. (Jan. 1989). “A Comprehensive Mass Flux Scheme for Cumulus Parameterization in Large-Scale Models”. In: *Monthly Weather Review* 117. ADS Bibcode: 1989MWRv..117.1779T, p. 1779. ISSN: 0027-0644. DOI: 10.1175/1520-0493(1989)117<1779:ACMFSF>2.0.CO;2. URL: https://ui.adsabs.harvard.edu/abs/1989MWRv..117.1779T (visited on 05/29/2026).

Twomey, S. (July 1977). “The Influence of Pollution on the Shortwave Albedo of Clouds”. EN. In: *Journal of the Atmospheric Sciences* 34.7, pp. 1149–1152. ISSN: 0022-4928, 1520-0469. DOI: 10.1175/1520-0469(1977)034<1149:TIOPOT>2.0.CO;2. URL: https://journals.ametsoc.org/view/journals/atsc/34/7/1520-0469_1977_034_1149_tiopot_2_0_co_2.xml (visited on 05/29/2026).

Vallis, Geoffrey K. (2017). *Atmospheric and Oceanic Fluid Dynamics: Fundamentals and Large-Scale Circulation*. 2nd ed. Cambridge: Cambridge University Press. ISBN: 978-1-107-06550-5. DOI: 10.1017/9781107588417. URL: https://www.cambridge.org/core/books/atmospheric-and-oceanic-fluid-dynamics/41379BDDC4257CBE11143C466F6428A4 (visited on 05/28/2026).

Vidmachenko, A. (Jan. 2026). “PHYSICAL PARAMETERS AND ORBITAL CHARACTERISTICS OF MARS AND THEIR COMPARISON WITH EARTH”. In: *European Open Science Space*, pp. 234–240. DOI: 10.70286/EOSS-12.01.2026.006.234-240.

Vogel, Helmut and Christian Gerthsen (1994). *Probleme aus der Physik: Aufgaben und Lösungen zur 17. Auflage von Gerthsen, Vogel: Physik ; mit über 1150 Aufgaben und ausführlichen Lösungen und 16 Tabellen*. ger. Springer-Lehrbuch. Berlin ; Heidelberg [u.a.]: Springer. ISBN: 978-3-540-56632-8.

Wagner, Thomas and Walter Roedel (2024). “Strahlung und Energie in dem System Atmosphäre/Erdoberfläche”. de. In: *Physik unserer Umwelt: Die Atmosphäre*. Ed. by Walter Roedel and Thomas Wagner. Berlin, Heidelberg: Springer, pp. 1–67. ISBN: 978-3-662-68944-8. DOI: 10.1007/978-3-662-68944-8_1. URL: https://doi.org/10.1007/978-3-662-68944-8_1 (visited on 05/28/2026).

Wan, H. et al. (June 2013). “The ICON-1.2 hydrostatic atmospheric dynamical core on triangular grids – Part 1: Formulation and performance of the baseline version”. English. In: *Geoscientific Model Development* 6.3, pp. 735–763. ISSN: 1991-959X. DOI: 10.5194/gmd-6-735-2013. URL: https://gmd.copernicus.org/articles/6/735/2013/ (visited on 03/16/2023).

Weimer, Michael et al. (June 2017). “An emission module for ICON-ART 2.0: implementation and simulations of acetone”. English. In: *Geoscientific Model Development* 10.6, pp. 2471–2494. ISSN: 1991-959X. DOI: 10.5194/gmd-10-2471-2017. URL: https://gmd.copernicus.org/articles/10/2471/2017/gmd-10-2471-2017.html (visited on 05/30/2026).

Weiskopf, Thorsten et al. (2026). “PowerACE - An Agent-based Electricity Market Model”. de. In: URL: https://publikationen.bibliothek.kit.edu/1000192771 (visited on 05/28/2026).

White, B. R. (Aug. 1979). “Soil transport by winds on Mars”. In: *Journal of Geophysical Research* 84. NTRS Author Affiliations: California, University NTRS Document ID: 19790064513 NTRS Research Center: Legacy CDMS (CDMS). URL: https://ntrs.nasa.gov/citations/19790064513 (visited on 05/29/2026).

Wild, Oliver, Xin Zhu, and Michael J. Prather (Nov. 2000). “Fast-J: Accurate Simulation of In- and Below-Cloud Photolysis in Tropospheric Chemical Models”. en. In: *Journal of*

Atmospheric Chemistry 37.3, pp. 245–282. ISSN: 1573-0662. DOI: 10.1023/A:1006415919030. URL: https://doi.org/10.1023/A:1006415919030 (visited on 05/29/2026).

WindSim Home - (2026). en-US. URL: https://windsim.com/ (visited on 06/01/2026).

Zängl, Günther (Oct. 2023). *ICON Namelists*. en. DOI: 10.1002/qj.4535. URL: https://docs.icon-model.org/documentation/buildrun/buildrun_namelist_overview.html (visited on 05/29/2026).

Zängl, Günther et al. (2015). "The ICON (ICOsahedral Non-hydrostatic) modelling framework of DWD and MPI-M: Description of the non-hydrostatic dynamical core". en. In: *Quarterly Journal of the Royal Meteorological Society* 141.687. _eprint: https://onlinelibrary.wiley.com/doi/pdf/10.1002/qj. pp. 563–579. ISSN: 1477-870X. DOI: 10.1002/qj.2378. URL: https://onlinelibrary.wiley.com/doi/abs/10.1002/qj.2378 (visited on 03/16/2023).

Zender, Charles S., Huisheng Bian, and David Newman (2003). "Mineral Dust Entrainment and Deposition (DEAD) model: Description and 1990s dust climatology". en. In: *Journal of Geophysical Research: Atmospheres* 108.D14. _eprint: https://agupubs.onlinelibrary.wiley.com/doi/pdf/10.1029/ ISSN: 2156-2202. DOI: 10.1029/2002JD002775. URL: https://onlinelibrary.wiley.com/doi/abs/10.1029/2002JD002775 (visited on 05/29/2026).

Zhu, Ziqing et al. (May 2025). "Designing the future electricity spot market with high renewables via reliable simulations". en. In: *Nature Reviews Electrical Engineering* 2.5, pp. 320–337. ISSN: 2948-1201. DOI: 10.1038/s44287-025-00163-9. URL: https://www.nature.com/articles/s44287-025-00163-9 (visited on 05/28/2026).

Zimmermann, Florian (2024). *Effekte von Kapazitätsmechanismen in gekoppelten Strommärkten*. de. DOI: 10.5445/IR/1000168525. URL: https://publikationen.bibliothek.kit.edu/1000168525 (visited on 05/29/2026).

A. Appendix

A.1. Results (Annual and 5-year mean timeseries)

A.1.1. 10 m wind speed

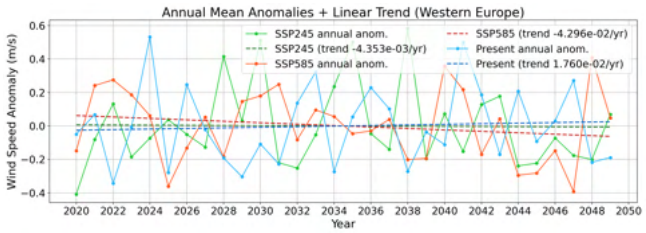

(a) Western Europe

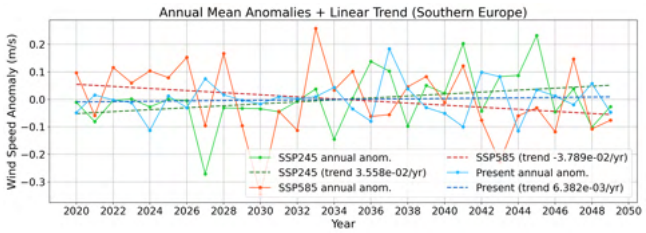

(b) Southern Europe

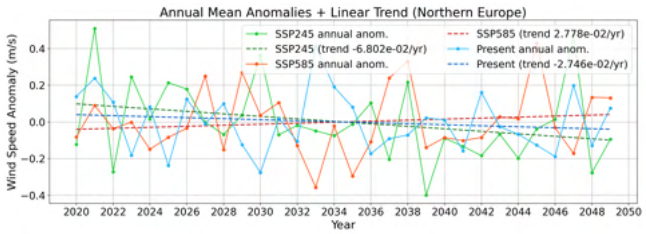

(c) Northern Europe

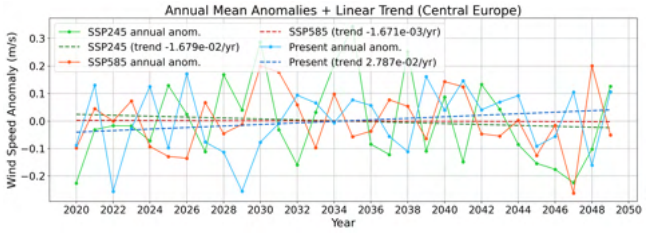

(d) Central Europe

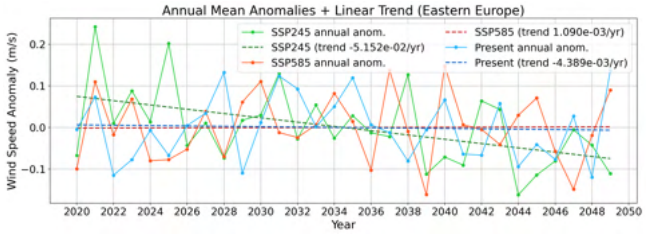

(e) Eastern Europe

Figure A.1.: Annual mean anomalies and linear trends of 10 m wind speed (m s^{-1}) in different climate zones, 2020–2049.

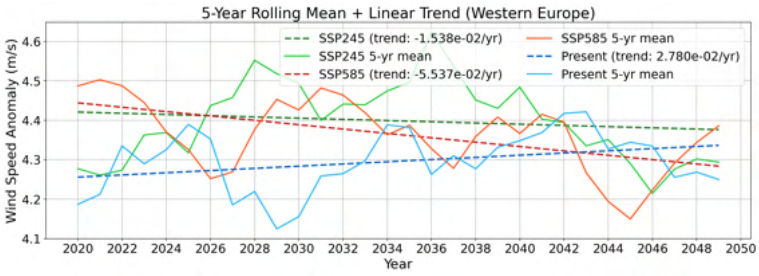

(a) Western Europe

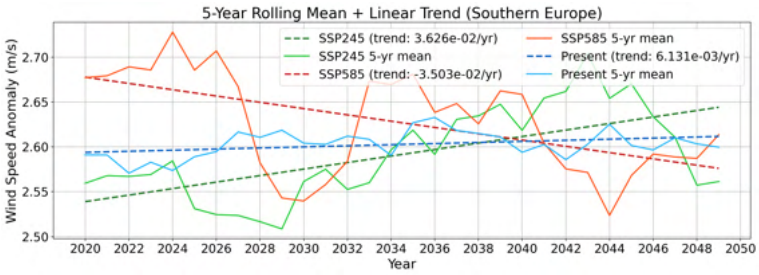

(b) Southern Europe

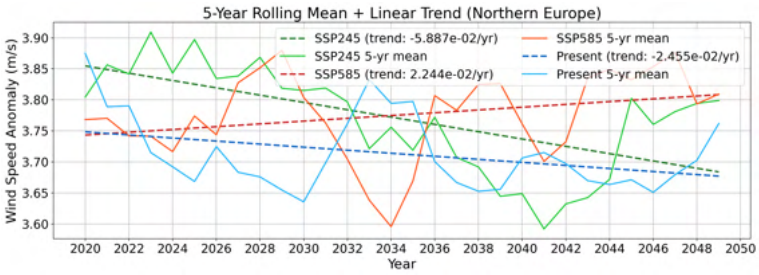

(c) Northern Europe

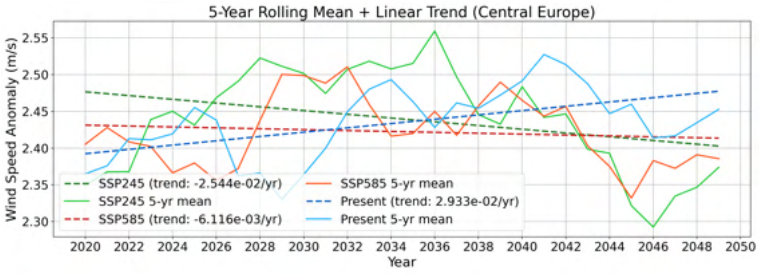

(d) Central Europe

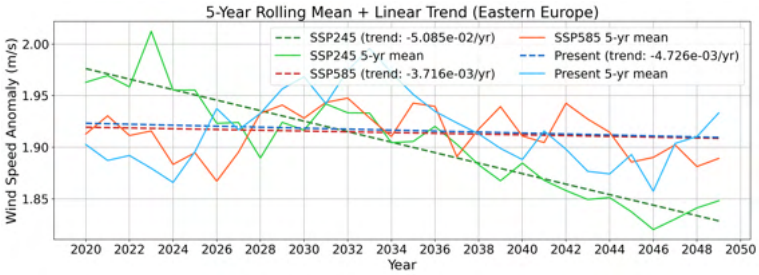

(e) Eastern Europe

Figure A.2.: Five-year rolling mean of 10 m wind speed ($m\,s^{-1}$) with linear trend in different climate zones, 2020–2049.

A.1.2. Shortwave irradiance

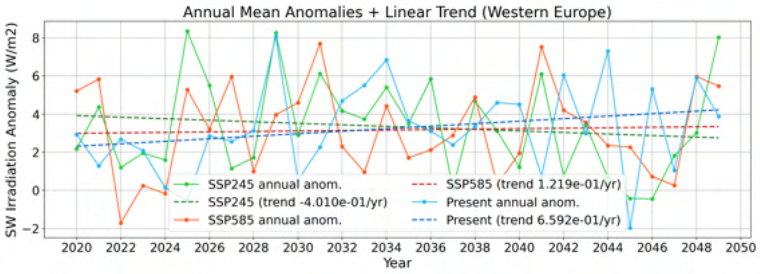

(a) Western Europe

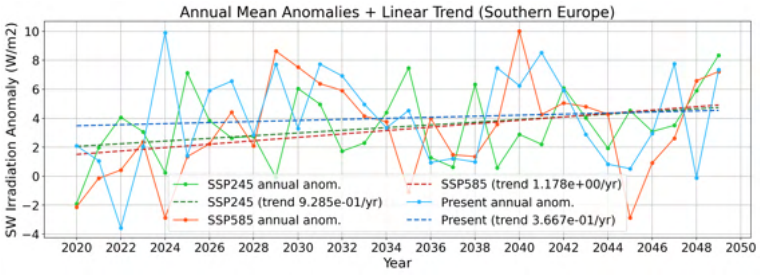

(b) Southern Europe

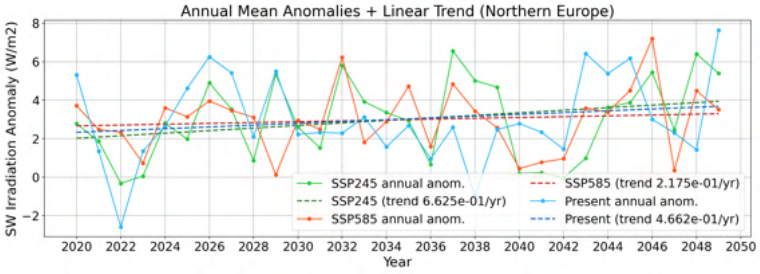

(c) Northern Europe

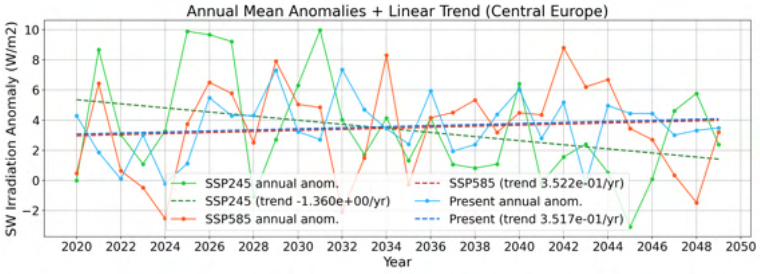

(d) Central Europe

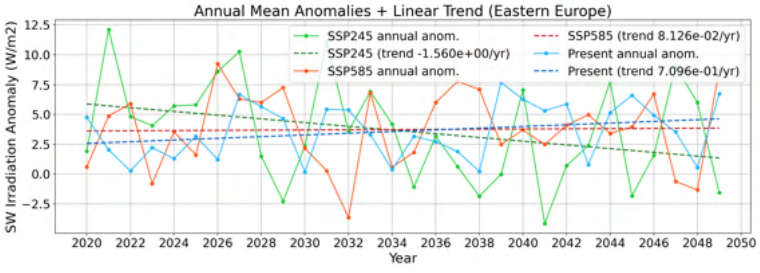

(e) Eastern Europe

Figure A.3.: Annual mean anomalies and linear trends of shortwave irradiance (W m^{-2}) in different climate zones, 2020–2049.

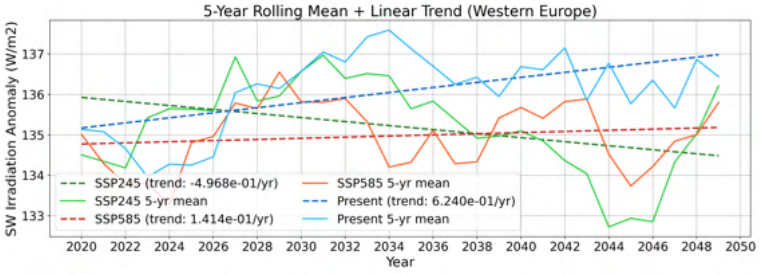

(a) Western Europe

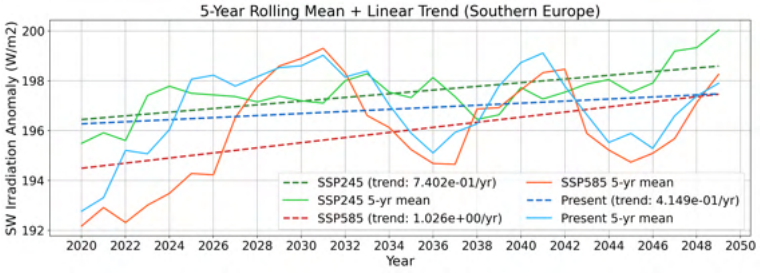

(b) Southern Europe

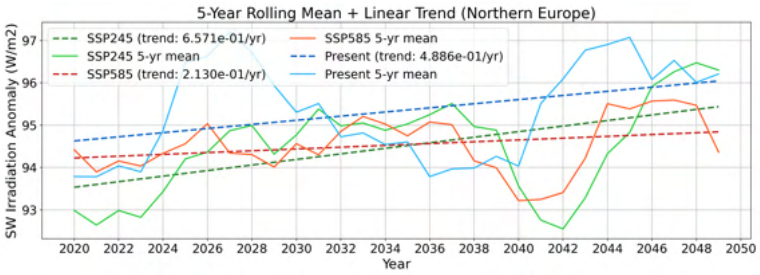

(c) Northern Europe

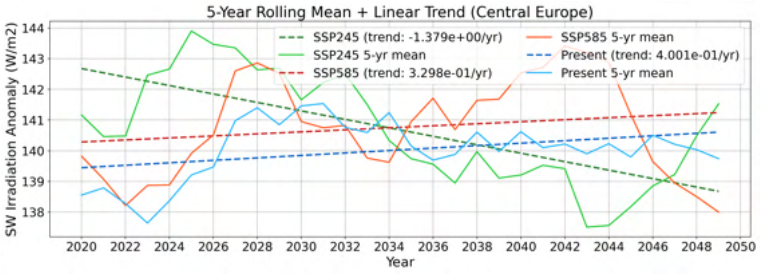

(d) Central Europe

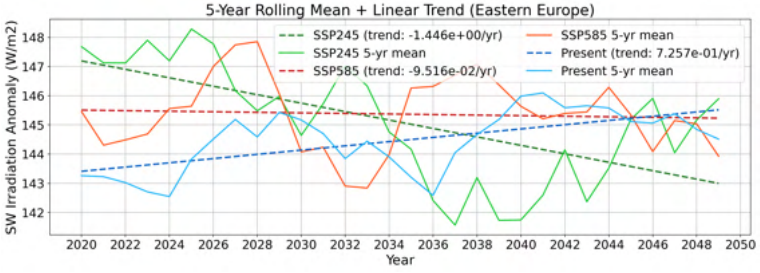

(e) Eastern Europe

Figure A.4.: Five-year rolling mean of shortwave irradiance ($W\,m^{-2}$) with linear trend in different climate zones, 2020–2049.

A.1.3. Near-Surface Dust Mass Concentation

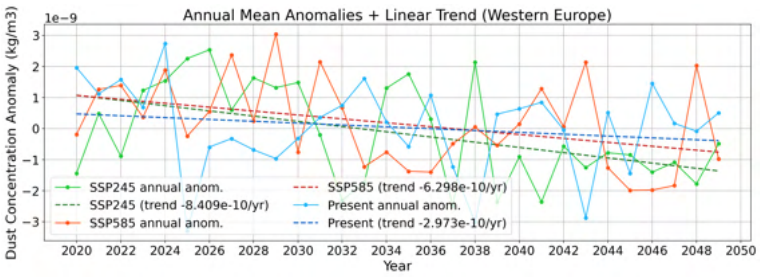

(a) Western Europe

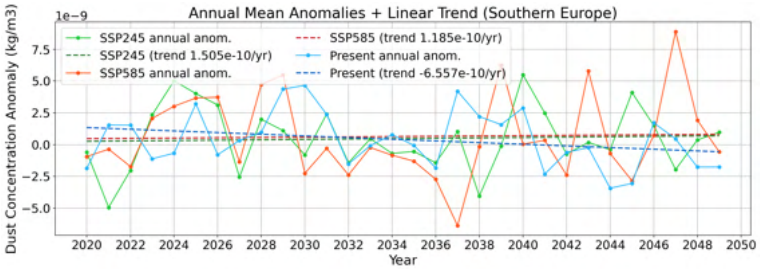

(b) Southern Europe

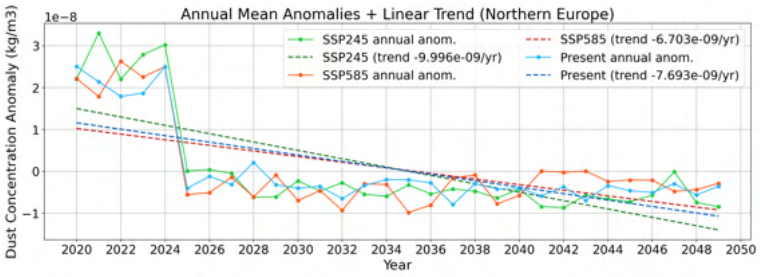

(c) Northern Europe

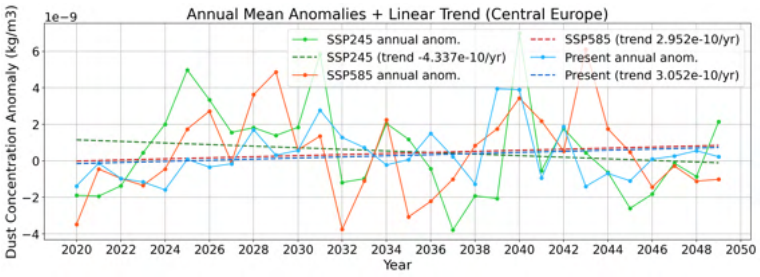

(d) Central Europe

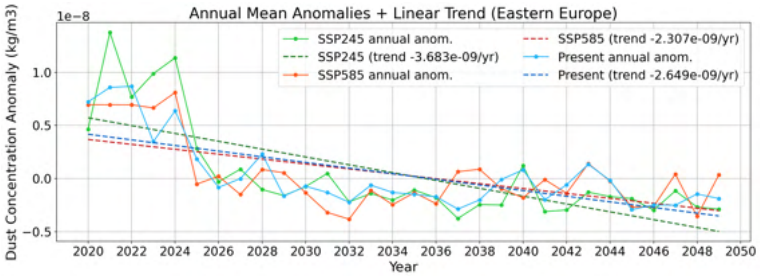

(e) Eastern Europe

Figure A.5.: Annual mean anomalies and linear trends of near-surface dust mass concentration ($kg\,m^{-3}$) in different climate zones, 2020–2049. Scale 10^{-8} for (c), 10^{-9} elsewhere.

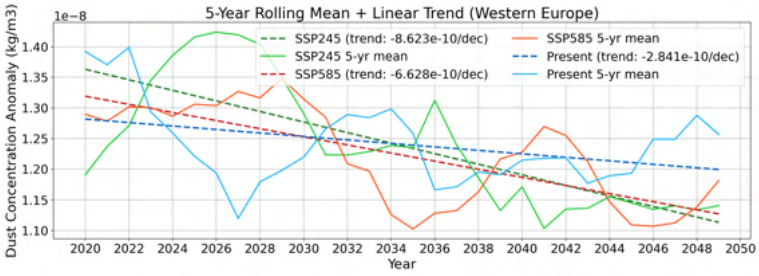

(a) Western Europe

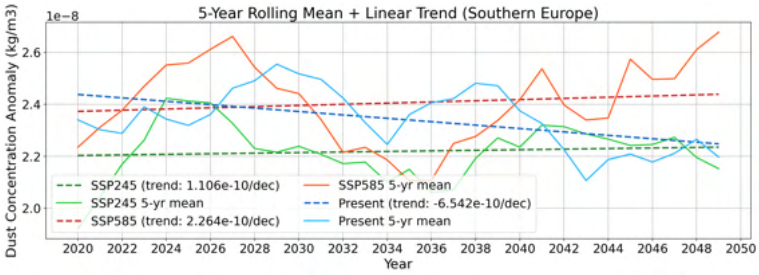

(b) Southern Europe

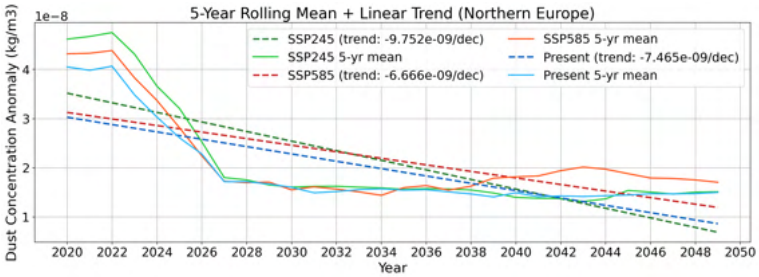

(c) Northern Europe

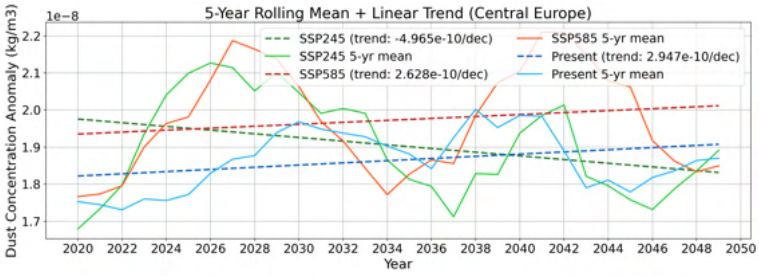

(d) Central Europe

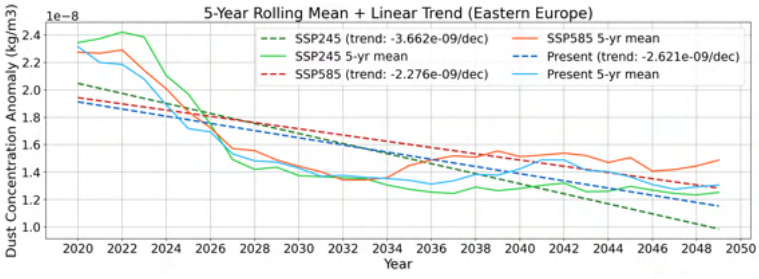

(e) Eastern Europe

Figure A.6.: Five-year rolling mean of near-surface dust mass concentration (kg m^{-3}, scale 10^{-8}) with linear trend in different climate zones, 2020–2049.